UNIVERSITY OF CALIFORNIA, SAN DIEGO

Cloud Microphysical Effects of Aerosol Particle Sources and Marine Boundary Layer Processes

A dissertation submitted in partial satisfaction of the
requirements for the degree
Doctor of Philosophy

in

Earth Sciences

by

Kevin J. Sanchez

Committee in charge:

Professor Lynn M. Russell, Chair
Professor Gregory C. Roberts, Co-Chair
Professor Lihini I. Aluwihare
Professor Andrew C. Kummel
Professor Joel R. Norris

2017

The Dissertation of Kevin J. Sanchez is approved, and it is acceptable in quality and form for publication on microfilm and electronically:

_____

_____

_____

_____
Co-Chair

_____
Chair

University of California, San Diego

2017

TABLE OF CONTENTS

LIST OF FIGURES

LIST OF TABLES

ACKNOWLEDGEMENTS

First, I want to thank Professor Lynn Russell and Greg Roberts for their encouragement throughout my graduate studies. I appreciate the time and effort they spent on guiding my development as a researcher. The knowledge passed to me will be valuable throughout my career. Second, I thank the members of the Russell Group as well as GMEI at Météo France for their support and assistance throughout my graduate career. I also want to thank all the collaborators that have made measurements and contributed to my publications, making it possible for me to write this dissertation. Last, I thank my family and friends for all of their support.

Chapter 1, in full, is a reprint of the material as it appears in the *Journal of Geophysical Research: Atmospheres* 2016 with slight modifications. Sanchez, K.J., L.M. Russell, R.L. Modini, A.A. Frossard, L. Ahlm, C.E. Corrigan, G.C. Roberts, L.N. Hawkins, J.C. Schroder, A.K. Bertram, R. Zhao, A.K.Y. Lee, J.J. Lin, A. Nenes, Z. Wang, A. Wonaschütz, A. Sorooshian, K.J. Noone, H. Jonsson, D. Toom, A.M. Macdonald, W.R. Leaitch, and J.H. Seinfeld. "Meteorological and aerosol effects on marine cloud microphysical properties." *Journal of Geophysical Research. Atmospheres*, 121 (8), pp. 4142-4161, doi:10.1002/2015JD024595, 2016. The dissertation author was the primary investigator and author of this paper.

Chapter 2, in full, is a reprint of the material as it appears in the *Atmospheric Chemistry and Physics* 2017 with slight modifications. Sanchez, K.J., G.C. Roberts, R. Calmer, K. Nicoll, E. Hashimshoni, D. Rosenfeld, J. Ovadnevaite, J. Preissler, D. Ceburnis, C. O'Dowd, and L.M. Russell, "Top-down and bottom-up aerosol–cloud

closure: towards understanding sources of uncertainty in deriving cloud shortwave radiative flux." *Atmos. Chem. Phys*., 17, 9797-9814, https://doi.org/10.5194/acp-17-9797-2017, 2017. The dissertation author was the primary investigator and author of this paper.

Chapter 3, in full, has been submitted for publication to *Nature: Scientific Reports*. Sanchez, K.J., C. Chen, L.M. Russell, R. Betha, J. Liu, D.J. Price, P. Massoli, L.D. Ziemba, E.C. Crosbie, R.H. Moore, M. Müller, S.A. Schiller, A. Wisthaler, A.K.Y. Lee, P.K. Quinn, T.S. Bates, J. Porter, T.G. Bell, E.S. Saltzman, R.D. Vaillancourt, M.J. Behrenfeld, "Higher Contributions of Marine Sulfate than Sea Spray to Cloud Condensation Nuclei in Late Spring than in Late Autumn." (In Review). The dissertation author was the primary investigator and author of this paper.

VITA

2012 B. S. in Meteorology, The Pennsylvania State University
2014 M. S. in Earth Sciences, University of California, San Diego
2016 Graduate Teaching Assistant, University of California, San Diego
2017 Graduate Teaching Assistant, University of California, San Diego
2017 Ph. D. in Earth Sciences, University of California, San Diego

PUBLICATIONS

Sanchez, K.J., C. Chen, L.M. Russell, R. Betha, J. Liu, D.J. Price, P. Massoli, L.D. Ziemba, E.C. Crosbie, R.H. Moore, M. Müller, S.A. Schiller, A. Wisthaler, A.K.Y. Lee, P.K. Quinn, T.S. Bates, J. Porter, T.G. Bell, E.S. Saltzman, R.D. Vaillancourt, M.J. Behrenfeld. (in review), Higher Contributions of Marine Sulfate than Sea Spray to Cloud Condensation Nuclei in Late Spring than in Late Autumn.

Betha, R., L.M. Russell, C. Chen, J. Liu, D.J. Price, **K.J. Sanchez**, S. Chen, A.K.Y. Lee, S.C. Collier, Q. Zhang, X. Zhang, and C.D. Cappa. (Accepted) Larger submicron particles for emissions with residential burning in wintertime San Joaquin Valley (Fresno) than for vehicle combustion in summertime South Coast Air *J. Geophys. Res.*

Chen, C., S. Chen, L.M. Russell, J. Liu, D.J. Price, R. Betha, **K.J. Sanchez**, A.K.Y. Lee, S.C. Collier, Q.Zhang, A. Kumar, M. Kleeman, X. Zhang, and C.D. Cappa. (in preparation) Organic aerosol particle chemical properties associated with residential burning and fog in wintertime San Joaquin Valley (Fresno) and with vehicle and firework emissions in summertime South Coast Air Basin (Fontana). *J. Geophys. Res*.

Sanchez, K.J., G.C. Roberts, R. Calmer, K. Nicoll, E. Hashimshoni, D. Rosenfeld, J. Ovadnevaite, J. Preissler, D. Ceburnis, C. O'Dowd, and L.M. Russell (2017), Top-down and Bottom-up aerosol-cloud-closure: towards understanding sources of uncertainty in deriving cloud radiative flux, *Atmos. Chem. Phys.*, 17, 9797-9814, https://doi.org/10.5194/acp-17-9797-2017.

Price, D.J., C. Chen, L.M. Russell, M.A. Lamjiri, R. Betha, **K.J. Sanchez**, J. Liu, A.K.Y. Lee, and D.R. Cocker. (2017) More unsaturated, cooking-type hydrocarbon-like organic aerosol particle emissions from renewable diesel compared to ultra low sulfur diesel in at-sea operations of a research vessel. *Aerosol Science And Technology*. Vol. 51 , Iss. 2.

Betha, R., L.M. Russell, **K.J. Sanchez**, J. Liu, D.J. Price, M.A. Lamjiri, C. Chen, X.M. Kuang, G.O. da Rocha, S.E. Paulson, J.W. Miller, and D.R. Cocker. (2017) Lower NOx but higher particle and black carbon emissions from renewable diesel compared to

ultra low sulfur diesel in at-sea operations of a research vessel. *Aerosol Science And Technology*. Vol. 51 , Iss. 2.

Sanchez, K.J., L.M. Russell, R.L. Modini, A.A. Frossard, L. Ahlm, C.E. Corrigan, G.C. Roberts, L.N. Hawkins, J.C. Schroder, A.K. Bertram, R. Zhao, A.K.Y. Lee, J.J. Lin, A. Nenes, Z. Wang, A. Wonaschütz, A. Sorooshian, K.J. Noone, H. Jonsson, D. Toom, A.M. Macdonald, W.R. Leaitch, and J.H. Seinfeld. (2016), Meteorological and aerosol effects on marine cloud microphysical properties, *J. Geophys. Res. Atmos.*, 121, 4142–4161, doi:10.1002/2015JD024595.

ABSTRACT OF THE DISSERTATION

Cloud Microphysical Effects of Aerosol Particle Sources and Marine Boundary Layer Processes

by

Kevin J. Sanchez

Doctor of Philosophy in Earth Sciences

University of California, San Diego, 2017

Professor Lynn M. Russell, Chair
Professor Greg C. Roberts, Co-Chair

Marine boundary layer (MBL) clouds are an important, though uncertain, part of Earth's radiative budget. Previous studies have shown sources of aerosol particles in the remote MBL consist of primary sea spray, secondary organic and inorganic vapors derived from the ocean, entrainment from the free troposphere, and anthropogenic pollution. The potential for these particles to become cloud condensation nuclei (CCN) is largely dependent on their hygroscopic properties. Furthermore, when clouds form, physical processes can alter the optical properties of the cloud. This dissertation aims to identify variations in aerosol sources that affect MBL CCN concentrations and physical

processes throughout the cloud lifetime that influence cloud optical properties. Ambient measurements of marine particles and clouds were made throughout two campaigns in the north Pacific and four campaigns in the north Atlantic. Both clean marine and polluted clouds were sampled. Dry MBL particles were measured to identify their chemical composition and size distribution, which is necessary to identify their potential to be CCN active. The organic hygroscopicity influenced CCN concentrations and cloud optical properties significantly for particles that were mostly organic, such as ship stack and generated smoke particles. For a typical range of organic hygroscopicity the amount of reflected solar radiation varied by 0.02-0.07 for polluted conditions and less than 0.01 for clean conditions (where 1.0 reflects all solar radiation). Simulated droplet spectral width was shown to be more representative of observations when using a weighted distribution of cloud base heights and updraft velocities, and increased the albedo up to 0.02. Cloud top entrainment and decoupling of the MBL were found to account for a decrease in cloud radiative forcing. Cloud top entrainment was corrected for homogeneous entrainment and accounted for a decrease in radiative forcing of up to 50 Wm^{-2}. Clustering of individual marine aerosol particles resulted in the identification of particle types derived from dimethyl-sulfide (DMS) oxidation. Two particle types were identified to come from DMS oxidation products and accounted for approximately 25% and 65% of CCN at 0.1% supersaturation during the winter and summer, respectively.

Introduction

Aerosol particles play an important role in the global radiative balance due to their ability to absorb and reflect light, and act as cloud condensation nuclei (CCN). Furthermore, marine aerosol particles are of particular importance because of their role in regulating the energy budget over the oceans, which cover over 70% of the earth. In the marine boundary layer, clouds are often formed by weak updrafts that cause the air to cool, leading to water vapor supersaturation. The water vapor then condenses onto particles to form cloud droplets. As the albedo, or reflectivity, of the ocean is below 0.1 under most conditions [*Li et al.*, 2006], most solar radiation that reaches the ocean surface is absorbed; an albedo of 1.0 means that all solar radiation is reflected. By contrast, marine clouds have high albedos and significantly reduce the amount of shortwave radiation that reaches the ocean surface. Since, marine clouds are a significant part of the global radiative balance, it is critical to accurately model them to predict future changes in climate.

Marine cloud shortwave radiative forcing is influenced by a range of variables, such as cloud droplet number concentration (CDNC), droplet size, entrainment drying, drizzle and meteorological conditions. To simulate the CDNC, many case studies assume the boundary layer is well mixed, though, studies have shown, this is not always the case [*Bates et al.*, 1998; *Kunz et al.*, 2002; *Milroy et al.*, 2012; *Raes et al.*, 2000; *Russell et al.*, 1998]. If the boundary layer is decoupled, then the boundary layer is not

well-mixed, and the particle distribution measured at the sea surface is not representative of the particle distribution that activate to form a cloud in the decoupled layer. For a particle to activate and become a cloud droplet, the supersaturation must reach the critical supersaturation of the particle. The atmosphere is considered supersaturated when the relative humidity exceeds its equilibrium value (100%). A particle's critical supersaturation is dependent on its chemical composition and size [*Kohler*, 1936]. Furthermore, the cloud supersaturation must remain at or above the critical supersaturation for a sufficient amount of time for the particle to grow to droplet sizes [*Chuang et al.*, 1997]. Ultimately, the evolution of the supersaturation in a cloud is a function of the adiabatic cooling rate and the condensation rate. The cooling rate is affected by the updraft velocity, where high updraft velocities enhance the rate of adiabatic cooling and lead to higher water vapor supersaturations in the cloud. Models have shown that the CDNC and cloud droplet size distributions are better represented by a distribution of updraft velocities rather than a single updraft velocity [*Conant et al.*, 2004; *Peng et al.*, 2005; *Snider et al.*, 2003]. Previous work has also shown that correctly reproducing the cloud droplet size distribution is important to accurately simulate the cloud optical properties [*Hsieh et al.*, 2009; *West et al.*, 2014]. There are several processes that can alter the cloud microphysical properties. For example, drizzle scavenges droplets, coalescence alters the size distribution and concentration, and cloud top entrainment warms and dries out the top of the cloud, leading to droplet evaporation [*Burnet and Brenguier*, 2007; *Mellado*, 2017]. All of these processes reduce the CDNC and some reduce the cloud liquid water content, both of which decrease the cloud

albedo. Models are often used to identify what physical and chemical processes are important for reproducing observations. To accurately model cloud radiative forcing, models must account for the processes altering cloud microphysical properties.

Particle and CCN concentrations in the marine boundary layer are typically small, relative to continental or polluted air. Pollution in the marine boundary layer from ship stacks or continental air can greatly enhance particle concentrations [*Chuang*, 2006; *Hegg et al.*, 2010; *Hudson and Noble*, 2014; *McFiggans et al.*, 2006; *Russell et al.*, 2013; *Sanchez et al.*, 2016; *Twohy et al.*, 2013]. Particles derived from pollution and continental sources typically contain mostly organic components and have low hygroscopicities relative to inorganic constituents [*Hawkins et al.*, 2010; *Hegg et al.*, 2010; *Leaitch et al.*, 2010]. However, the high particle concentrations, produced by pollution and continental sources, often result in higher CCN concentrations than in clean marine conditions.

Natural sources of marine particles include sea salt, organic components, and dimethyl sulfide (DMS) [*Frossard et al.*, 2014a; *Quinn and Bates*, 2011]. The sea salt particles are emitted directly from the ocean as primary aerosol particles and are highly hygroscopic and readily active CCN [*Bates et al.*, 2012; *Frossard et al.*, 2014a; *Frossard et al.*, 2014b; *Middlebrook et al.*, 1998; *Murphy et al.*, 1998; *Quinn et al.*, 2014; *Quinn et al.*, 2017; *Rinaldi et al.*, 2010]. DMS is emitted from the ocean as a gas that can form methansulfonic acid and sulfur dioxide through photochemical oxidation and aqueous processing [*Ayers et al.*, 1991; *Pandis et al.*, 1994]. These DMS oxidation products enhance CCN concentrations by condensing onto existing particles, increasing

their size and enhancing their hygroscopicity by the addition of sulfate mass [*Riipinen et al.*, 2012; *Russell et al.*, 1994]. DMS oxidation products also nucleate to form new particles that will subsequently grow to CCN-size aerosol particles [*Almeida et al.*, 2013; *Clarke et al.*, 1998; *Covert et al.*, 1992; *Pirjola et al.*, 2000; *Warren and Seinfeld*, 1985]. These nucleation events have been observed to typically occur in the free troposphere above the marine boundary layer [*Clarke*, 1993; *Clarke et al.*, 1998; *Raes et al.*, 1997]. The organic component of marine particles can be directly emitted from the ocean as primary particles or condense to form secondary particles. Organics have low hygroscopicities compared to sulfate and sea salt; however, they can account for a significant fraction of the CCN concentrations [*Leaitch et al.*, 2010]. Marine CCN concentrations are often limited by the low particle concentrations in the marine boundary layer.

This dissertation focuses on three key aspects of aerosol interactions with marine clouds including, source apportionment of aerosols and CCN, microphysical processes that affect the CDNC, and physical processes that alter cloud optical properties. One chapter focuses on both polluted marine conditions and clean marine conditions (marine air that is not influenced by anthropogenic pollution or continental aerosol) and the other two chapters focus only on clean marine conditions. The first two chapters utilize an aerosol-cloud-parcel model (ACPM) [*Russell and Seinfeld*, 1998] to identify processes important for accurately simulating the CDNC and cloud droplet size distributions, which are necessary to calculate the cloud optical properties. The third chapter uses Köhler theory to estimate the CCN concentration, which uses particle size distribution

and chemical composition to estimate CCN concentrations. Köhler theory assumes the particles are in equilibrium with water vapor, such that kinetic limitations (i.e., water vapor diffusion) of activated CCN particles are ignored [*Chuang et al.*, 1997; *Kohler*, 1936; *Russell and Seinfeld,* 1998].

Chapter 1 utilizes measurements collected in the marine boundary layer off the coast of California and on Mt. Soledad in San Diego as part of the Eastern Pacific Emitted Aerosol Cloud Experiment (EPEACE) and the Stratocumulus Observations of Los-Angeles Emission Derived Aerosol-Droplets (SOLEDAD) campaigns. The main objective that tied these two projects together was to identify the contribution of continental and anthropogenic aerosol particle emissions on marine clouds and identify differences in observed and simulated cloud microphysical and optical properties. In this chapter, simulated droplet size distributions from the ACPM are compared with observed droplet size distributions from clean marine and polluted marine conditions. Also, the effect of the organic hygroscopicity and particle size distribution on both clean marine and polluted conditions were examined to identify changes in CCN concentration and overall cloud albedo [*Sanchez et al.,* 2016].

Chapter 2 utilizes the ACPM for a closure study that combines ground-based, satellite, and unmanned aerial vehicle (UAV) measurements collected during the Impact of Biogenic versus Anthropogenic emissions on Clouds and Climate: towards a Holistic UnderStanding (BACCHUS) campaign. The objective of this study was to compare observed cloud optical properties with simulations and identify physical processes that promote closure. Cloud shortwave radiative forcing was overestimated for cases with

cloud-top entrainment or at the top of a decoupled boundary layer. Closure of cloud optical properties was improved after accounting for these processes [*Sanchez et al.*, 2017].

Chapter 3 focuses on the source apportionment of different marine particle types that are identified by their measured individual particle chemical composition. The measurements were collected during the second Western Atlantic Climate Study (WACS2) and the first and second North Atlantic Aerosol and Marine Ecosystems Study (NAAMES1 and NAAMES2). A similar objective between these studies was to identify marine biological contributions to marine aerosol particle concentrations. Two particle types are shown to form from DMS oxidation products and be an important source of CCN. One DMS particle type is the result of the condensation of DMS oxidation products onto existing particles, and the other is from the nucleation of DMS oxidation products to form new sulfate particles. The contribution of DMS derived particles to the CCN concentration is found to vary by season [*Sanchez et al.*, Submitted].

References

Almeida, J., Schobesberger, S., Kurten, A., Ortega, I. K., Kupiainen-Maatta, O., Praplan, A. P., Adamov, A., Amorim, A., Bianchi, F., Breitenlechner, M., David, A., Dommen, J., Donahue, N. M., Downard, A., Dunne, E., Duplissy, J., Ehrhart, S., Flagan, R. C., Franchin, A., Guida, R., Hakala, J., Hansel, A., Heinritzi, M., Henschel, H., Jokinen, T., Junninen, H., Kajos, M., Kangasluoma, J., Keskinen, H., Kupc, A., Kurten, T., Kvashin, A. N., Laaksonen, A., Lehtipalo, K., Leiminger, M., Leppa, J., Loukonen, V., Makhmutov, V., Mathot, S., McGrath, M. J., Nieminen, T., Olenius, T., Onnela, A., Petaja, T., Riccobono, F., Riipinen, I., Rissanen, M., Rondo, L., Ruuskanen, T., Santos, F. D., Sarnela, N., Schallhart, S., Schnitzhofer, R., Seinfeld, J. H., Simon, M., Sipila, M., Stozhkov, Y., Stratmann, F., Tome, A., Trostl, J., Tsagkogeorgas, G., Vaattovaara, P., Viisanen, Y., Virtanen, A., Vrtala, A., Wagner, P. E., Weingartner, E., Wex, H., Williamson, C., Wimmer, D., Ye, P. L., Yli-Juuti, T., Carslaw, K. S., Kulmala, M., Curtius, J., Baltensperger, U., Worsnop, D. R., Vehkamaki, H., and Kirkby, J.: Molecular understanding of sulphuric acid-amine particle nucleation in the atmosphere, Nature, 502, 359-+, 10.1038/nature12663, 2013.

Ayers, G. P., Ivey, J. P., and Gillett, R. W.: COHERENCE BETWEEN SEASONAL CYCLES OF DIMETHYL SULFIDE, METHANESULFONATE AND SULFATE IN MARINE AIR, Nature, 349, 404-406, 10.1038/349404a0, 1991.

Bates, T. S., Kapustin, V. N., Quinn, P. K., Covert, D. S., Coffman, D. J., Mari, C., Durkee, P. A., De Bruyn, W. J., and Saltzman, E. S.: Processes controlling the distribution of aerosol particles in the lower marine boundary layer during the First Aerosol Characterization Experiment (ACE 1), Journal of Geophysical Research-Atmospheres, 103, 16369-16383, 10.1029/97jd03720, 1998.

Bates, T. S., Quinn, P. K., Frossard, A. A., Russell, L. M., Hakala, J., Petaja, T., Kulmala, M., Covert, D. S., Cappa, C. D., Li, S. M., Hayden, K. L., Nuaaman, I., McLaren, R., Massoli, P., Canagaratna, M. R., Onasch, T. B., Sueper, D., Worsnop, D. R., and Keene, W. C.: Measurements of ocean derived aerosol off the coast of California, Journal of Geophysical Research-Atmospheres, 117, 13, 10.1029/2012jd017588, 2012.

Burnet, F., and Brenguier, J.-L.: Observational study of the entrainment-mixing process in warm convective clouds, Journal of the Atmospheric Sciences, 64, 1995-2011, 10.1175/jas3928.1, 2007.

Chuang, P. Y., Charlson, R. J., and Seinfeld, J. H.: Kinetic limitations on droplet formation in clouds, Nature, 390, 594-596, 1997.

Chuang, P. Y.: Sensitivity of cloud condensation nuclei activation processes to kinetic parameters, Journal of Geophysical Research-Atmospheres, 111, 10.1029/2005jd006529, 2006.

Clarke, A. D.: ATMOSPHERIC NUCLEI IN THE PACIFIC MIDTROPOSPHERE - THEIR NATURE, CONCENTRATION, AND EVOLUTION, Journal of Geophysical Research-Atmospheres, 98, 20633-20647, 10.1029/93jd00797, 1993.

Clarke, A. D., Davis, D., Kapustin, V. N., Eisele, F., Chen, G., Paluch, I., Lenschow, D., Bandy, A. R., Thornton, D., Moore, K., Mauldin, L., Tanner, D., Litchy, M., Carroll, M. A., Collins, J., and Albercook, C.: Particle nucleation in the tropical boundary layer and its coupling to marine sulfur sources, Science, 282, 89-92, 10.1126/science.282.5386.89, 1998.

Conant, W. C., VanReken, T. M., Rissman, T. A., Varutbangkul, V., Jonsson, H. H., Nenes, A., Jimenez, J. L., Delia, A. E., Bahreini, R., Roberts, G. C., Flagan, R. C., and Seinfeld, J. H.: Aerosol-cloud drop concentration closure in warm cumulus, Journal of Geophysical Research-Atmospheres, 109, 10.1029/2003jd004324, 2004.

Covert, D. S., Kapustin, V. N., Quinn, P. K., and Bates, T. S.: NEW PARTICLE FORMATION IN THE MARINE BOUNDARY-LAYER, Journal of Geophysical Research-Atmospheres, 97, 20581-20589, 10.1029/92jd02074, 1992.

Frossard, A. A., Russell, L. M., Burrows, S. M., Elliott, S. M., Bates, T. S., and Quinn, P. K.: Sources and composition of submicron organic mass in marine aerosol particles, Journal of Geophysical Research-Atmospheres, 119, 12977-13003, 10.1002/2014jd021913, 2014a.

Frossard, A. A., Russell, L. M., Massoli, P., Bates, T. S., and Quinn, P. K.: Side-by-Side Comparison of Four Techniques Explains the Apparent Differences in the Organic Composition of Generated and Ambient Marine Aerosol Particles, Aerosol Science and Technology, 48, V-X, 10.1080/02786826.2013.879979, 2014b.

Hawkins, L. N., Russell, L. M., Covert, D. S., Quinn, P. K., and Bates, T. S.: Carboxylic acids, sulfates, and organosulfates in processed continental organic aerosol over the southeast Pacific Ocean during VOCALS-REx 2008, Journal of Geophysical Research-Atmospheres, 115, 10.1029/2009jd013276, 2010.

Hegg, D. A., Covert, D. S., Jonsson, H. H., and Woods, R. K.: The contribution of anthropogenic aerosols to aerosol light-scattering and CCN activity in the California coastal zone, Atmospheric Chemistry and Physics, 10, 7341-7351, 10.5194/acp-10-7341-2010, 2010.

Hsieh, W. C., Nenes, A., Flagan, R. C., Seinfeld, J. H., Buzorius, G., and Jonsson, H.: Parameterization of cloud droplet size distributions: Comparison with parcel models

and observations, Journal of Geophysical Research-Atmospheres, 114, 10.1029/2008jd011387, 2009.

Hudson, J. G., and Noble, S.: CCN and Vertical Velocity Influences on Droplet Concentrations and Supersaturations in Clean and Polluted Stratus Clouds, Journal of the Atmospheric Sciences, 71, 312-331, 10.1175/jas-d-13-086.1, 2014.

Kohler, H.: The nucleus in and the growth of hygroscopic droplets, Transactions of the Faraday Society, 32, 1152-1161, 10.1039/tf9363201152, 1936.

Kunz, G. J., de Leeuw, G., Becker, E., and O'Dowd, C. D.: Lidar observations of atmospheric boundary layer structure and sea spray aerosol plumes generation and transport at Mace Head, Ireland (PARFORCE experiment), Journal of Geophysical Research-Atmospheres, 107, 10.1029/2001jd001240, 2002.

Leaitch, W. R., Lohmann, U., Russell, L. M., Garrett, T., Shantz, N. C., Toom-Sauntry, D., Strapp, J. W., Hayden, K. L., Marshall, J., Wolde, M., Worsnop, D. R., and Jayne, J. T.: Cloud albedo increase from carbonaceous aerosol, Atmospheric Chemistry and Physics, 10, 7669-7684, 10.5194/acp-10-7669-2010, 2010.

Li, J., Scinocca, J., Lazare, M., McFarlane, N., von Salzen, K., and Solheim, L.: Ocean surface albedo and its impact on radiation balance in climate models, Journal of Climate, 19, 6314-6333, 10.1175/jcli3973.1, 2006.

McFiggans, G., Artaxo, P., Baltensperger, U., Coe, H., Facchini, M. C., Feingold, G., Fuzzi, S., Gysel, M., Laaksonen, A., Lohmann, U., Mentel, T. F., Murphy, D. M., O'Dowd, C. D., Snider, J. R., and Weingartner, E.: The effect of physical and chemical aerosol properties on warm cloud droplet activation, Atmospheric Chemistry and Physics, 6, 2593-2649, 2006.

Mellado, J. P.: Cloud-Top Entrainment in Stratocumulus Clouds, Annual Review of Fluid Mechanics, Vol 49, 49, 145-169, 10.1146/annurev-fluid-010816-060231, 2017.

Middlebrook, A. M., Murphy, D. M., and Thomson, D. S.: Observations of organic material in individual marine particles at Cape Grim during the First Aerosol Characterization Experiment (ACE 1), Journal of Geophysical Research-Atmospheres, 103, 16475-16483, 10.1029/97jd03719, 1998.

Milroy, C., Martucci, G., Lolli, S., Loaec, S., Sauvage, L., Xueref-Remy, I., Lavric, J. V., Ciais, P., Feist, D. G., Biavati, G., and O'Dowd, C. D.: An Assessment of Pseudo-Operational Ground-Based Light Detection and Ranging Sensors to Determine the Boundary-Layer Structure in the Coastal Atmosphere, Advances in Meteorology, 10.1155/2012/929080, 2012.

Murphy, D. M., Anderson, J. R., Quinn, P. K., McInnes, L. M., Brechtel, F. J., Kreidenweis, S. M., Middlebrook, A. M., Posfai, M., Thomson, D. S., and Buseck, P. R.: Influence of sea-salt on aerosol radiative properties in the Southern Ocean marine boundary layer, Nature, 392, 62-65, 10.1038/32138, 1998.

Pandis, S. N., Russell, L. M., and Seinfeld, J. H.: THE RELATIONSHIP BETWEEN DMS FLUX AND CCN CONCENTRATION IN REMOTE MARINE REGIONS, Journal of Geophysical Research-Atmospheres, 99, 16945-16957, 10.1029/94jd01119, 1994.

Peng, Y. R., Lohmann, U., and Leaitch, R.: Importance of vertical velocity variations in the cloud droplet nucleation process of marine stratus clouds, Journal of Geophysical Research-Atmospheres, 110, 10.1029/2004jd004922, 2005.

Pirjola, L., O'Dowd, C. D., Brooks, I. M., and Kulmala, M.: Can new particle formation occur in the clean marine boundary layer?, Journal of Geophysical Research-Atmospheres, 105, 26531-26546, 10.1029/2000jd900310, 2000.

Quinn, P. K., and Bates, T. S.: The case against climate regulation via oceanic phytoplankton sulphur emissions, Nature, 480, 51-56, 10.1038/nature10580, 2011.

Quinn, P. K., Bates, T. S., Schulz, K. S., Coffman, D. J., Frossard, A. A., Russell, L. M., Keene, W. C., and Kieber, D. J.: Contribution of sea surface carbon pool to organic matter enrichment in sea spray aerosol, Nature Geoscience, 7, 228-232, 10.1038/ngeo2092, 2014.

Quinn, P. K., Coffman, D. J., Johnson, J. E., Upchurch, L. M., and Bates, T. S.: Small fraction of marine cloud condensation nuclei made up of sea spray aerosol, Nature Geoscience, 10.1038/ngeo3003, 2017.

Raes, F., VanDingenen, R., Cuevas, E., VanVelthoven, P. F. J., and Prospero, J. M.: Observations of aerosols in the free troposphere and marine boundary layer of the subtropical Northeast Atlantic: Discussion of processes determining their size distribution, Journal of Geophysical Research-Atmospheres, 102, 21315-21328, 10.1029/97jd01122, 1997.

Raes, F., Bates, T., McGovern, F., and Van Liedekerke, M.: The 2nd Aerosol Characterization Experiment (ACE-2): general overview and main results, Tellus Series B-Chemical and Physical Meteorology, 52, 111-125, 10.1034/j.1600-0889.2000.00124.x, 2000.

Riipinen, I., Yli-Juuti, T., Pierce, J. R., Petaja, T., Worsnop, D. R., Kulmala, M., and Donahue, N. M.: The contribution of organics to atmospheric nanoparticle growth, Nature Geoscience, 5, 453-458, 10.1038/ngeo1499, 2012.

Rinaldi, M., Decesari, S., Finessi, E., Giulianelli, L., Carbone, C., Fuzzi, S., O'Dowd, C. D., Ceburnis, D., and Facchini, M. C.: Primary and Secondary Organic Marine Aerosol and Oceanic Biological Activity: Recent Results and New Perspectives for Future Studies, Advances in Meteorology, 10.1155/2010/310682, 2010.

Russell, L. M., Pandis, S. N., and Seinfeld, J. H.: AEROSOL PRODUCTION AND GROWTH IN THE MARINE BOUNDARY-LAYER, Journal of Geophysical Research-Atmospheres, 99, 20989-21003, 10.1029/94jd01932, 1994.

Russell, L. M., Lenschow, D. H., Laursen, K. K., Krummel, P. B., Siems, S. T., Bandy, A. R., Thornton, D. C., and Bates, T. S.: Bidirectional mixing in an ACE 1 marine boundary layer overlain by a second turbulent layer, Journal of Geophysical Research-Atmospheres, 103, 16411-16432, 10.1029/97jd03437, 1998.

Russell, L. M., and Seinfeld, J. H.: Size- and composition-resolved externally mixed aerosol model, Aerosol Science and Technology, 28, 403-416, 10.1080/02786829808965534, 1998.

Russell, L. M., Sorooshian, A., Seinfeld, J. H., Albrecht, B. A., Nenes, A., Ahlm, L., Chen, Y.-C., Coggon, M., Craven, J. S., Flagan, R. C., Frossard, A. A., Jonsson, H., Jung, E., Lin, J. J., Metcalf, A. R., Modini, R., Muelmenstaedt, J., Roberts, G. C., Shingler, T., Song, S., Wang, Z., and Wonaschuetz, A.: EASTERN PACIFIC EMITTED AEROSOL CLOUD EXPERIMENT, Bulletin of the American Meteorological Society, 94, 709-+, 10.1175/bams-d-12-00015.1, 2013.

Sanchez, K. J., Russell, L. M., Modini, R. L., Frossard, A. A., Ahlm, L., Corrigan, C. E., Roberts, G. C., Hawkins, L. N., Schroder, J. C., Bertram, A. K., Zhao, R., Lee, A. K. Y., Lin, J. J., Nenes, A., Wang, Z., Wonaschutz, A., Sorooshian, A., Noone, K. J., Jonsson, H., Toom, D., Macdonald, A. M., Leaitch, W. R., and Seinfeld, J. H.: Meteorological and aerosol effects on marine cloud microphysical properties, Journal of Geophysical Research-Atmospheres, 121, 4142-4161, 10.1002/2015jd024595, 2016.

Sanchez, K. J., Roberts, G. C., Calmer, R., Nicoll, K., Hashimshoni, E., Rosenfeld, D., Ovadnevaite, J., Preissler, J., Ceburnis, D., O'Dowd, C., and Russell, L. M.: Top-down and bottom-up aerosol-cloud closure: towards understanding sources of uncertainty in deriving cloud shortwave radiative flux, Atmospheric Chemistry and Physics, 17, 9797-9814, 10.5194/acp-17-9797-2017, 2017.

Sanchez, K.J., C. Chen, L.M. Russell, R. Betha, J. Liu, D.J. Price, P. Massoli, L.D. Ziemba, E.C. Crosbie, R.H. Moore, M. Müller, S.A. Schiller, A. Wisthaler, A.K.Y. Lee, P.K. Quinn, T.S. Bates, J. Porter, T.G. Bell, E.S. Saltzman, R.D. Vaillancourt, M.J. Behrenfeld. (in review), Higher Contributions of Marine Sulfate than Sea Spray to Cloud Condensation Nuclei in Late Spring than in Late Autumn.

Snider, J. R., Guibert, S., Brenguier, J. L., and Putaud, J. P.: Aerosol activation in marine stratocumulus clouds: 2. Kohler and parcel theory closure studies, Journal of Geophysical Research-Atmospheres, 108, 10.1029/2002jd002692, 2003.

Twohy, C. H., Anderson, J. R., Toohey, D. W., Andrejczuk, M., Adams, A., Lytle, M., George, R. C., Wood, R., Saide, P., Spak, S., Zuidema, P., and Leon, D.: Impacts of aerosol particles on the microphysical and radiative properties of stratocumulus clouds over the southeast Pacific Ocean, Atmospheric Chemistry and Physics, 13, 2541-2562, 10.5194/acp-13-2541-2013, 2013.

Warren, D. R., and Seinfeld, J. H.: PREDICTION OF AEROSOL CONCENTRATIONS RESULTING FROM A BURST OF NUCLEATION, Journal of Colloid and Interface Science, 105, 136-142, 10.1016/0021-9797(85)90356-x, 1985.

West, R. E. L., Stier, P., Jones, A., Johnson, C. E., Mann, G. W., Bellouin, N., Partridge, D. G., and Kipling, Z.: The importance of vertical velocity variability for estimates of the indirect aerosol effects, Atmospheric Chemistry and Physics, 14, 6369-6393, 10.5194/acp-14-6369-2014, 2014.

Chapter 1

Meteorological and Aerosol Effects on Marine Cloud Microphysical Properties

Meteorology and microphysics affect cloud formation, cloud droplet distributions and shortwave reflectance. The Eastern Pacific Emitted Aerosol Cloud Experiment (E-PEACE) and the Stratocumulus Observations of Los-Angeles Emissions Derived Aerosol-Droplets (SOLEDAD) studies provided measurements in six case studies of cloud thermodynamic properties, initial particle number distribution and composition, and cloud drop distribution. In this study, we use simulations from a chemical and microphysical aerosol-cloud parcel (ACP) model with explicit kinetic drop activation to reproduce observed cloud droplet distributions of the case studies. Four cases had sub-adiabatic lapse rates, resulting in fewer activated droplets, lower liquid water content (LWC) and higher cloud base height than an adiabatic lapse rate. A weighted ensemble of simulations that reflect measured variation in updraft velocity and cloud base height was used to reproduce observed droplet distributions. Simulations

show organic hygroscopicity in internally mixed cases causes small effects on cloud reflectivity (CR) (<0.01), except for cargo ship and smoke plumes, which increased CR by 0.02 and 0.07, respectively, owing to their high organic mass fraction. Organic hygroscopicity had larger effects on droplet concentrations for cases with higher aerosol concentrations near the critical diameter (namely polluted cases with a modal peak near 0.1 μm). Differences in simulated droplet spectral widths (k) caused larger differences in CR than organic hygroscopicity in cases with organic mass fractions of 60% or less for the cases shown. Finally, simulations from a numerical parameterization of cloud droplet activation suitable for GCMs compared well with the ACP model, except under high organic mass fraction.

1.1 Introduction

Clouds play an essential role in the climate system. Cloud reflectivity (CR) is determined by microphysical properties, such as cloud droplet number concentration (CDNC), size distribution, cloud thickness, and liquid water content (LWC). Atmospheric chemical transport models and aerosol-cloud modules embedded in General Circulation Models (GCMs) predict CDNC and a single volumetric or effective droplet size resulting from the activation of aerosols. Though knowledge of the cloud droplet size distribution is important for accurately estimating CR, many atmospheric models do not include this level of detail. Clouds form when aerosols undergo activation in conditions of water vapor supersaturation. The aerosol characteristics that are important in cloud droplet activation are size, concentration, and chemical composition. A key property of aerosol-cloud interactions related to aerosol chemical composition is hygroscopicity.

The basis of microscale models for simulating the formation of liquid-phase clouds is a solution of the conservation equations for energy and water vapor. As an air parcel cools to below the dew point, water vapor becomes supersaturated, and droplets start forming on those particles that can act as cloud condensation nuclei (CCN). Not all aerosol particles are CCN. Particles with greater mass have more soluble mass and reduced curvature effects, enhancing their ability to become CCN; hydrophilic particles are more water soluble, increasing their effectiveness as CCN. Each particle therefore requires exposure to a characteristic level of supersaturation to act as a CCN. The supersaturation, *s*, that develops in clouds is set by a dynamic balance between adiabatic

cooling (that increases *s*) and condensation upon existing droplets (that decreases *s*). During the initial phases of cloud formation, cooling dominates, *s* increases and drives the formation of droplets. A point is reached, however, where water vapor condensation becomes dominant, *s* is reduced and droplet nucleation ceases. The point of maximum supersaturation, s_{max}, is therefore the quantity that determines how many particles can act as a CCN. Because of this, CDNC and size are dependent on updraft velocity, aerosol size distribution, and chemical composition. Globally, regimes have been identified in which cloud formation is controlled mainly by updraft velocity and others in which formation is governed by CCN properties [*Reutter et al.*, 2009]. For example, at high aerosol number concentrations characteristic of polluted conditions and low updraft conditions, CDNC is more sensitive to changes in updraft velocity or supersaturation [*McFiggans et al.*, 2006]. Previous work has shown that CDNC is better represented in models with a more realistic distribution of updraft velocities, rather than a single updraft value [*Conant et al.*, 2004; *Peng et al.*, 2005; *Snider et al.*, 2003]. *Hudson et al.* [2014] found strong evidence from measurements showing variations in CDNC that were due to the steep slope of the CCN concentration with supersaturation, providing observational evidence for a case in which CDNC is sensitive to updraft velocity. Global climate models have also been used to show that a characteristic velocity cannot reproduce the indirect aerosol effects of a distribution of updraft velocities and that the uncertainty in the width of the vertical velocity distribution can perturb the radiative flux by up to 0.4 W m^{-2} [*West et al.*, 2014]. Variations in updraft velocity can contribute to the broadening of the cloud droplet distribution [*Hsieh et al.*, 2009], as each updraft

leads to a different droplet size distribution. The droplet size distribution needs to be modeled accurately to estimate cloud optical properties. The droplet size is also a function of LWC, so the resolution of LWC is important for accurate modeling of cloud systems. Finally, since cloud thickness is also important for cloud optical properties, cloud base height needs to be simulated accurately. Cloud base height is a function of several variables, one of which is lapse rate [*Li et al.*, 2013]. The value of the lapse rate varied to show the sensitivity of cloud droplet distribution to both lapse rate and cloud base height.

Activation of inorganic salt particles is a well-understood parameterized process in models. In general, however, organic compounds constitute a substantial fraction of atmospheric aerosols. Studies focusing on analysis of organic aerosol properties have shown that organic components exhibit a wide range of water solubility. Unlike that of most inorganic aerosol components, the hygroscopicities of organic compounds are less constrained. Laboratory studies have demonstrated that purely organic particles can act as CCN [*Cruz and Pandis*, 1997; *Novakov and Corrigan*, 1996; *Raymond and Pandis*, 2002]. Studies have also shown that organic hygroscopicity can increase when internally mixed with even a small fraction of inorganic components if the inorganic water content modifies slightly soluble organic compounds into dissolved compounds [*Collins et al.*, 2013; *Shulman et al.*, 1996]. *Cruz and Pandis* [2000] showed evidence of several organic-salt mixtures in which there was no change in the individual water absorption of each component, indicating that simple volume mixing rules could be applied. *Wang et al.* [2010] showed that CCN concentrations were within 20% when an

internal mixture was assumed. However, these lab experiments investigating internal mixture thermodynamic interactions have used mixtures containing only a few known compounds. The thermodynamics of more complex organic-containing mixtures is not well understood, although several approaches have been used with success [*Ming and Russell*, 2004; *Petters et al.*, 2015]. In addition, the available measurements of organic ambient aerosol composition are typically not quantified by individual molecules. Given this support for volume mixing and the lack of organic molecular composition that would be needed to support another approach, the ACP model simulations have relied on the assumption of volume mixing.

Modeling the cloud droplet activation of mixed inorganic-organic aerosols representative of real-world air masses remains a frontier area of cloud physics. This is in part owing to compositional heterogeneity of particle types, leading to an externally-mixed aerosol population. Near urban regions, Tandem Differential Mobility Analyzer (TDMA) [*Massling et al.*, 2009; *Tiitta et al.*, 2010], single particle mass spectrometry [*Healy et al.*, 2014], and optical microscopy [*Moffet et al.*, 2010] show evidence of multiple particle populations, especially in regard to their carbonaceous content. In continental outflow [*Hawkins et al.*, 2010; *Hegg et al.*, 2010; *Leaitch et al.*, 2010], free tropospheric air masses and fresh biogenic aerosol production [*Allan et al.*, 2009; *Hersey et al.*, 2009; *Mochida et al.*, 2011], less hygroscopic and hydrophobic modes of particles are observed. To accurately represent the effects of aerosol chemical composition on activation of cloud droplets, it is important to know the contribution of organic mass to each population. In understanding cloud formation and properties in

different regions of the atmosphere, it is important to compare the results of detailed simulations with actual measured aerosol and cloud properties.

In this work, the comparison of models of marine cloud formation with actual field measurements of organic aerosols and cloud droplets is of particular interest. We focus on observations from two field studies, the Eastern Pacific Emitted Aerosol Cloud Experiment (E-PEACE) and Stratocumulus Observations of Los-Angeles Emissions Derived Aerosol-Droplets (SOLEDAD). Each of these experiments was carried out in the Eastern Pacific off the coast of California, in a region characterized by ship exhaust and smoke from land-based fires, as well as natural marine aerosol sources, such as bubble bursting at the ocean surface [*Facchini et al.*, 2008; *Frossard*, 2014; *Leck and Bigg*, 2005; *Quinn et al.*, 2014] and oxidation of dimethyl sulfide (by hydroxyl radicals) to produce sulfuric acid.

We use a detailed chemical and microphysical aerosol-cloud parcel (ACP) model with explicit kinetic droplet activation to simulate observed cloud droplet distribution and composition. Novel aspects of this modeling study include the extensive nature of the measured constraints (on not only cloud thermodynamic properties but also initial particle number distribution and composition) as well as resulting cloud drop distribution and composition that are available from these two eastern Pacific stratocumulus experiments. These detailed case studies allow evaluation of the extent to which the model effectively represents processes of cloud droplet formation. To identify the effect of lapse rate and updraft variation on droplet spectral widths (k), distributions of each are used as model inputs. Also, to identify

the contribution of organic components to droplet formation, we simulate the effect of smoke-generated plumes, a cargo ship plume, and background aerosol. We then evaluate the sensitivity of the predictions to the organic aerosol fraction and to the hygroscopicity of the aerosol. In addition, ACP model simulations are compared to those from a numerical GCM parameterization of cloud droplet activation [*Betancourt and Nenes*, 2014; *Fountoukis and Nenes*, 2005; *Nenes and Seinfeld*, 2003] to evaluate the accuracy of the more efficient approach in the GCM. Finally, to put the meteorological and microphysical effects in context of radiative forcing, we investigate the sensitivity of cloud reflectance (at measurement heights) to simulated droplet spectra for six cases.

1.2 Methods

This section summarizes measurements from two field campaigns, E-PEACE off the coast of California in July and August of 2011 and SOLEDAD in May and June of 2012 located 1km from the coast, and the models used to simulate the observations.

1.2.1 E-PEACE

E-PEACE consisted of a 12-day research cruise on the R/V *Point Sur* (12 to 23 July) and 30 research flights on the Center for Interdisciplinary Remotely-Piloted Aircraft Studies (CIRPAS) Twin Otter aircraft (8 July to 18 August). Both the ship and aircraft were equipped with an array of instruments to provide detailed meteorological and aerosol measurements [*Russell et al.*, 2013]. The two E-PEACE case studies considered here occurred on 16 July (EJL16) and 10 August (EAG10). Each case

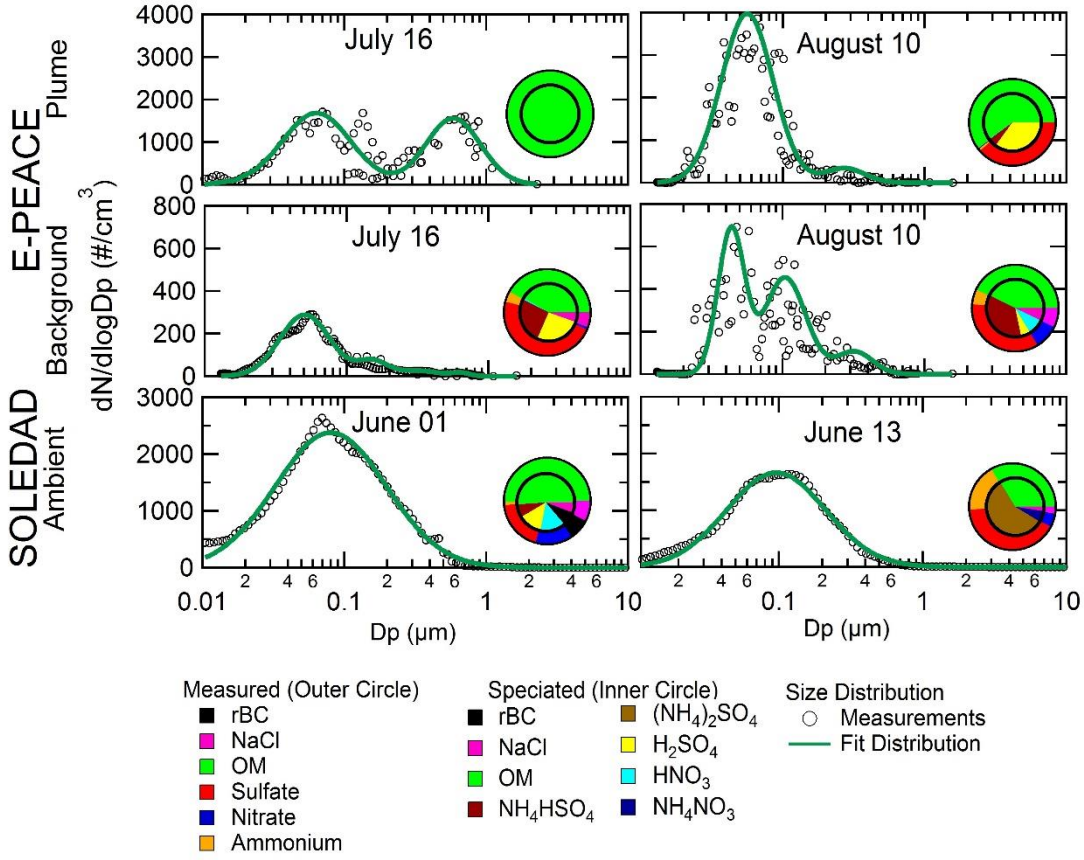

Figure 1.1: Below-cloud dried particle number distributions with log normal fits for each case study. The pie charts show measured submicron and molecular composition from an SP2, refractory Black Carbon (rBC), and an AMS with scaled NaCl [Modini et al., 2015] and organic mass (OM). The 16 July submicrometer measurements of aerosol size and composition were collected on the R/V Point Sur (1717-1722 LT) with a SEMS and HR-ToF-AMS, respectively; 10 August submicrometer measurements of aerosol size and composition were collected on the CIRPAS Twin Otter (1710-1716 LT) with a scanning DMA and C-ToF-AMS respectively. The SOLEDAD submicrometer measurements of aerosol size and composition from 01 (1200-1650 LT) and 13 (0800-1050 LT) June were collected on Mt. Soledad with a SEMS and HR-ToF-AMS, respectively. E-PEACE measurements also include PCASP measurements for supermicron aerosol sizes (0.1-10 μm). The size distribution and composition in this figure are used as input for the cases shown in Table 1.

includes a background ‘B’ case (EJL16B, EAG10B) and a plume ‘P’ case (EJL16P, EAG10P). The EJL16P case included release of organic smoke from two U.S. Army-issued smoke generators to produce concentrated plumes of particles consisting of vaporized and condensed paraffin oil [*Russell et al.*, 2013; *Wonaschuetz et al.*, 2013]. In the EAG10P case the Twin Otter aircraft sampled exhaust from a cargo ship.

1.2.1.1 R/V *Point Sur* Ship Measurements

A vertical inlet, shielded from sea spray, on the forward deck of the R/V *Point Sur* was used to sample air. Aerosols were dried in diffusion driers before delivery to instruments. A Scanning Electrical Mobility Sizer (SEMS, Model 138, 2002, BMI, Hayward, CA) was used to measure the number size distribution of submicrometer (0.01 - 0.9 μm diameter) particles. Supermicrometer particle size distributions were measured using an Aerodynamic Particle Sizer (APS 3321, TSI Inc., St. Paul, MN, size range 0.5–20 μm). The total number concentration of aerosol particles was tracked with a condensation particle counter (CPC 3010, TSI Inc., St. Paul, MN) to monitor contamination from the R/V *Point Sur* stack and from nearby ships. Submicrometer particles were separated from supermicrometer particles with a cyclone (sharp cut cyclone SCC 2.229, BGI Inc. US), then analyzed with a high-resolution time-of-flight aerosol mass spectrometer (HR-ToF-AMS, Aerodyne Research Inc., Billerica, MA) to measure non-refractory inorganic (sulfate, ammonium, nitrate, chloride) and organic components [*DeCarlo et al.*, 2006]. For the HR-ToF-AMS, a collection efficiency of 0.6 and a detection limit of 0.01 μg m^{-3} were applied [*Wonaschuetz et al.*, 2013]. Refractory black carbon was measured with a single-particle soot photometer (SP2,

DMT, Boulder, CO), which has a particle size range of 80-300 nm; refractory black carbon concentrations were negligible during E-PEACE and are not included. In the absence of fresh emissions from ships [*Wonaschuetz et al.*, 2013], past measurements in the same study region have suggested that the aerosol is internally mixed in the size range of 150-200 nm [*Hersey et al.*, 2009]. Plumes were considered to be a second (internally mixed) aerosol population separate from the background populations [*Modini et al.*, 2015]. Figure 1.1 (upper two panels) shows surface-level measurements of aerosol size distribution and chemical composition during E-PEACE.

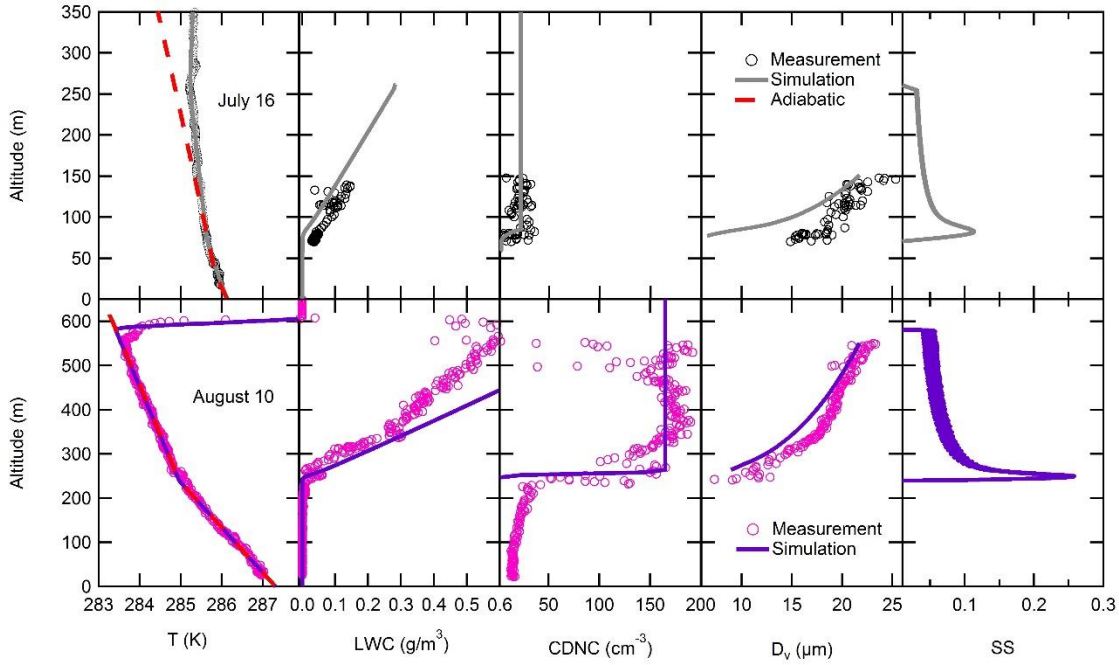

Figure 1.2: Measured, fitted and simulated profiles of temperature (T), liquid water content (LWC), cloud droplet number concentration (CDNC), volume mean diameter (Dv), and supersaturation (SS) profiles for the CIRPAS Twin Otter flights and ACP model runs for the 10 August and 16 July cases during E-PEACE. The simulations shown are the EJL16B-sa and EAG10B-ad cases from Table 1. For comparison, the adiabatic lapse rate is also shown as a red dashed line. The observations did not include cloud top for 16 July.

1.2.1.2 CIRPAS Twin Otter Flight Measurements

On the CIRPAS Twin Otter, similar instruments as those on the R/V *Point Sur* were used to measure dried aerosol concentrations and properties at various heights (Figure 1.2). Cloud droplet residuals were sampled with a Counter-flow Virtual Impactor (CVI) inlet. Details of this inlet are provided by [*Shingler et al.*, 2012]. Scanning Differential Mobility Analyzers (models 3081 and 3010, TSI, Inc., St. Paul, MN), with time resolutions of 110 s, and a passive cavity aerosol spectrometer probe (PCASP 0.1 – 10 μm, PMS Inc., Boulder, Co) were used to measure aerosol size distributions. Multiple CPCs (model 3010 and 3025, TSI, Inc., St. Paul, MN) measured total aerosol concentration. A compact time-of-flight aerosol mass spectrometer (C-ToF-AMS, Aerodyne Research Inc., Billerica, MA) measured inorganic and organic composition in mass spectrum mode. The C-ToF-AMS had a time resolution of 8-12 s, a size range of 60-600 nm, and a collection efficiency of 0.53 [*Coggon et al.*, 2012]. A CCN counter operating in Scanning Flow CCN Analysis mode [*Moore and Nenes*, 2009] was used to estimate the maximum supersaturation by comparing the measured CDNC to the CCN at supersaturations between 0.1% - 0.8%. A cloud aerosol spectrometer (CAS) and cloud droplet probe (CDP, DMT, Boulder, CO, [*Lance et al.*, 2010]) measured in-cloud droplet number distributions. *Feingold et al.* [2013] showed that autoconversion and accretion rates are negligible for values of LWC and CDNC that are lower than 0.3 g m^{-3} and 50 - 200 cm^{-3} (respectively) or 0.5 g m^{-3} and 200 - 700 cm^{-3} (respectively). Thus, since the values of LWC and CDNC are lower for the case studies used here, droplet number loss by collision-coalescence can be neglected.

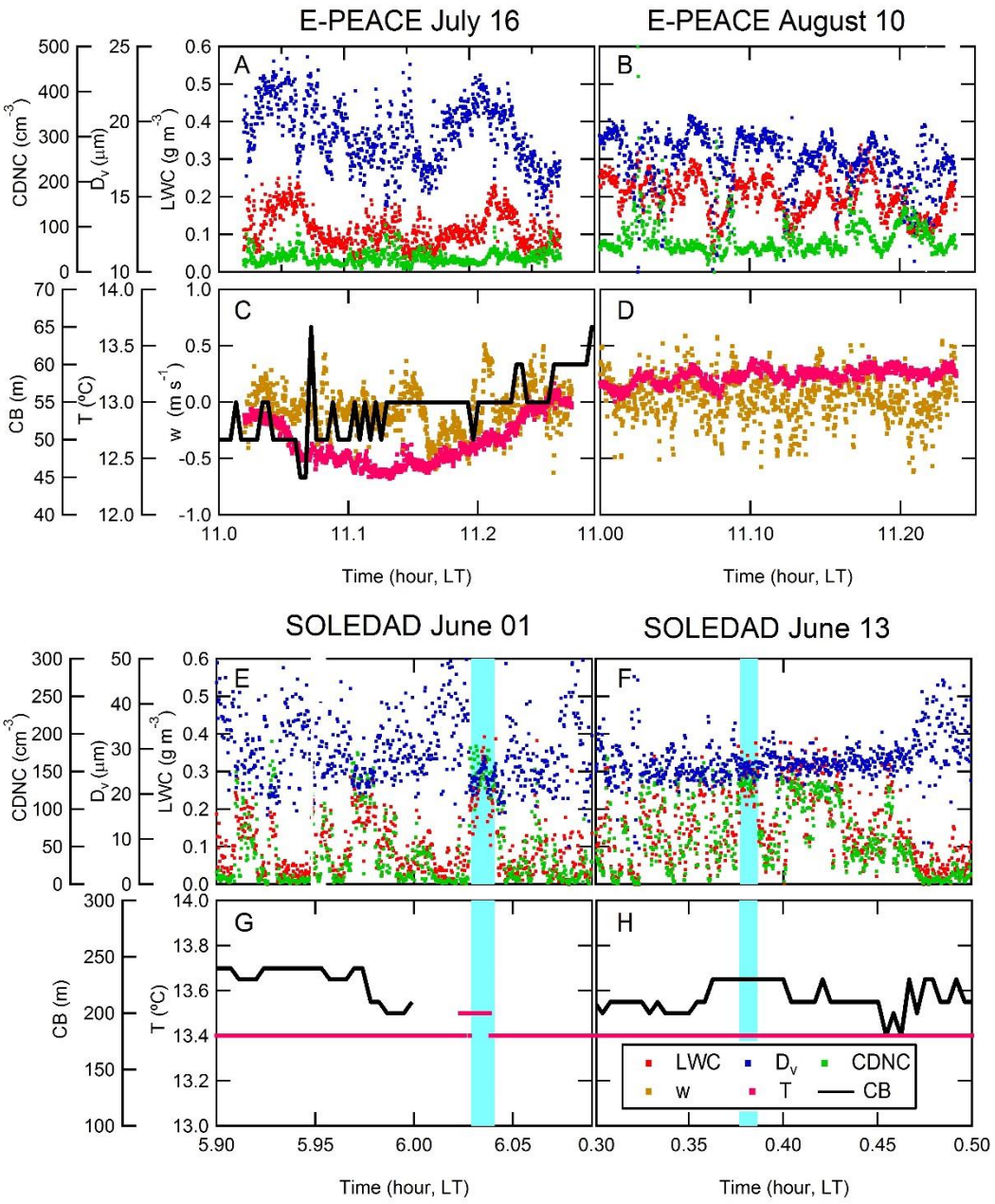

Figure 1.3: In cloud measurements of CDNC, LWC, D_v, w, T and CB for each case. CDP and CAS measured CDNC, D_v and LWC for E-PEACE 16 July and 10 August cases, respectively. Fog Monitor measurements are used for SOLEDAD CDNC, D_v and LWC. Cloud base measurements for both SOLEDAD and E-PEACE cases are detected with a ceilometer. Cloud base (CB) measurements for E-PEACE 10 August and vertical velocity measurements for SOLEDAD are not available. Only about 2% of all in-cloud measurements are shown here as these times were identified as consistent conditions for use in initializing the SOLEDAD and E-PEACE cases. Due to the high variability in SOLEDAD cloud measurements, only the cyan-highlighted sections were used for the SOLEDAD cases.

Table 1.1: Observations and ACP Simulation Results.

	E-PEACE 16 Jul Background (EJL16B)	**E-PEACE 16 Jul Smoke Plume (EJL16P)**	**E-PEACE 10 Aug Background (EAG10B)**	**E-PEACE 10 Aug Cargo Plume (EAG10P)**	**SOLEDAD 01 Jun Ambient (SJN01A)**	**SOLEDAD 13 Jun Ambient (SJN13A)**
Simulation Run	ad[1] / al / sa	ad / al / sa	ad / sa	ad / sa	ad / sa	ad / sa
Cloud Base (m)	61±9[2] (28) / <70> / <70>	61±9 (28) / <70> / <70>	240 <240> / (295)	240 <240> / (295)	205±23 (160) / (225)	170±34 (145) / (200)
Measurement Height (m)	145	145	325	325	250	250
Dry Lapse Rate (K km^{-1})	[-9.8] / [-9.8] / <-7.0>	[-9.8] / [-9.8] / <-7.0>	<-9.8> / [-8.0]	<-9.8> / [-8.0]	[-9.8] / (-7.0)	[-9.8] / (-7.0)
Moist Lapse Rate (K km^{-1})	- / - / -2.2 (-4.4) / (-4.4) / <-2.2>	- / - / -2.2 (-4.4) / (-4.4) / <-2.2>	-4.5 / - <-4.5> / (-3.4)	-4.5 / - <-4.5> / (-3.4)	- (-4.1) / (-2.7)	- (-4.0) / (-2.8)
Liquid Water Content (g m^{-3})	- (0.34) / (0.24) / (0.11)	- / - / 0.08±0.08 (0.34) / (0.24) / (0.09)	0.24±0.05 / - (0.25) / (0.08)	0.19±0.06 / - (0.25) / (0.08)	0.25±0.07 (0.28) / (0.06)	0.28±0.04 (0.32) / (0.10)
Mean D_v (µm)	- / - / 19.7±2.0 (37.2) / (26.8) / (21.0)	- / - / 18.6±2.0 (17.7) / (15.3) / (15.2)	14.1±1.1 / - (14.0) / (8.8)	12.2±1.1 / - (12.1) / (7.9)	15.5±0.3 (15.5) / (8.8)	16.7±0.2 (16.8) / (12.6)
Updraft (m s^{-1})	[0.06]	[0.06]	[0.31]	[0.31]	[0.05]	[0.05]
CDNC for a Single Updraft (cm^{-3})	- / - / 21±6 (37) / (37) / (22)	- / - / 49±14 (86) / (86) / (50)	156±30 / - (165)/(165)	277±85 / - (241)/(241)	148±19 (146) / (108)	137±8 (129) / (95)
CDNC for a PDF of Updrafts (cm^{-3})	- / - / 21±6 - / - / (23)	- / - / 49±14 - / - / (207)	156±30 / - (160) / -	277±85 / - (296) / -	- -	- -

[1] The simulation runs use an adiabatic lapse rate with adiabatic cloud base (ad), an adiabatic lapse rate with measured cloud base (al), and a sub-adiabatic lapse rate with measured cloud base (sa)

[2] Observations (not in brackets) and ACP simulation, inputs from observations <in triangle brackets>, modified inputs [in square brackets], and simulation results (in parentheses)

Standard meteorological variables (temperature, wind speed and direction, relative humidity, pressure) were measured. Relevant cloud measurements are shown in Figure 1.3, wherein the altitude at which observations were made is compared to model predictions (145 m and 325 m for EJL16 and EAG10), shown in Table 1.1. Of these measurements, only those within one standard deviation of mean CDNC were averaged to represent the observed droplet distribution to reduce errors in distribution width associated with non-representative (high or low) CDNC. Consequently, for EJL16, 42% and 21% of the measurements in the time series match the background and plume, respectively. For EAG10, 68% and 16% of the measurements in the time series match the criterion used for the background and plume, respectively.

1.2.2 SOLEDAD

The SOLEDAD campaign consisted of ground-based measurements located near the peak of Mt. Soledad, 251 m above sea level, and about 1 km from the Pacific coast. Measurements collected for 49 days (1 May to 18 June, 2012) include: particle-cloud partitioning of refractory black carbon [*Schroder et al.*, 2014], and salt particle contributions to cloud droplets [*Modini et al.*, 2015]. Measurements on 1 June and 13 June, 2012, of two cloud events contained sufficient observations for characterizing droplet size and composition of the stratocumulus clouds. Chemical composition and aerosol size distribution (Figure 1.1) used to initialize the models were collected inside the instrument container; instruments for cloud measurements were mounted on top. We assumed particle composition was internally mixed and independent of size because size-dependent AMS measurements were below detection limit for the relevant

sampling periods and no measurements of bulk mixing state were carried out. Two inlets were used to sample ambient aerosols: the high-flow rate isokinetic inlet continuously collected air containing both interstitial aerosols and cloud droplets and a counterflow virtual impactor (CVI) was used to sample only cloud droplet residuals [*Noone et al.*, 1988; *Schroder et al.*, 2014]. The CVI inlet for droplet residuals was mounted atop the container and was only used during cloud events. During periods with no clouds, all instruments sampled through the isokinetic inlet. Two single-particle soot photometers (SP2, DMT, Boulder, CO) were used to measure refractory black carbon: one continuously measured from the isokinetic inlet and the other measured from the residual inlet during cloud events.

The SEMS measured submicrometer particle number size distributions from the total inlet at all times, while a Scanning Mobility Particle Sizer (SMPS Model 3034, TSI, St. Paul, MN) was used on the CVI inlet during cloud periods and on the total inlet during non-cloud periods. The same HR-ToF-AMS used on E-PEACE was used on Mt. Soledad to measure aerosol composition on the residual inlet during cloud events to obtain the chemical composition of cloud droplet residuals and on the total inlet during non-cloud periods. A fog monitor (FM-100, model 100, DMT, Boulder, CO) was mounted on top of the instrument container to provide cloud in-situ measurements of droplet size and concentration, as well as LWC. Figure 1.3 shows time series of LWC and CDNC for both the SOLEDAD June 1 ambient 'A' (SJN01A) case and the June 13 ambient (SJN13A) case. Both LWC and CDNC are highly variable with maximum hourly standard deviations of 0.09 g m^{-3} and 52 cm^{-3} for SJN01A and 0.13 g m^{-3} and 58

cm^{-3} for SJN13A, respectively. The short, cyan-highlighted periods in Figure 1.3 represent the time periods averaged and compared to model simulations. These time periods were selected because LWC and CDNC were above the detection limit and fairly constant, whereas the remainder of the measurements were quite variable. From the selected time periods, the mean and standard deviation in CDNC was 148±19 $cm^{-3}$and 137±8 cm^{-3} for the SJN01 and SJN13 cases, respectively. CDNC was within one standard deviation of the subset mean for SJN01 (6.4%) and SJN13 (9.8%), respectively. The measurements were made close to the cloud base. Consequently, small changes in the cloud base height caused large changes in CDNC and LWC. The higher CDNC was chosen because it was more consistent and likely represented the CDNC after maximum supersaturation (Figure 1.10).

1.2.3 Aerosol-Cloud Parcel (ACP) Model

The aerosol dynamics model is based on a fixed-sectional approach to represent the (dry) particle size domain, with internally-mixed chemical components and externally-mixed types of particles. Using measured aerosol types (or "populations"), the model is described by the number of particles each with an internal mixture of compounds at each size. The model employs a dual moment (number and mass) algorithm to calculate particle growth from one size section to the next for non-evaporating compounds (namely, all components other than water) using an accommodation coefficient of 1.0 [*Raatikainen et al.*, 2013]. The dual moment method is based on *Tzivion et al.* [1987] to allow accurate accounting of both aerosol number and mass. This algorithm incorporates independent calculations of the change in

particle number and mass for all processes other than growth. The model includes a dynamic scheme for activation of particles to cloud droplets. Liquid water is treated in a moving section representation, similar to the approach of *Jacobson et al.* [1994], to allow the accurate calculation of evaporation and condensation of water in conditions of varying humidity. In subsaturated conditions, aerosol particles below the cloud base are considered to be in local equilibrium with water vapor. The initial relative humidity at sea level for the simulations ranged from 91%-98%.

In E-PEACE and SOLEDAD, we assumed there was no gas-to-particle growth below cloud, so below-cloud condensation was neglected, with the exception of water for which subsaturated liquid-vapor equilibrium was assumed. For the relatively short simulations used here (<2 h) at marine concentrations (<400 cm^{-3}), coagulation, scavenging, and deposition of the aerosol were included in the model but their effects were negligible. The particle size distributions of the background aerosol for the E-PEACE and SOLEDAD cases were modeled as one internally mixed particle type. The plumes were included in the models as separate particle types from the background aerosol. The inorganic ion (NH_4^+, NO_3^-, SO_4^{2-}) mass fractions measured with the HR-ToF-AMS were apportioned to molecular mass fractions of ammonium nitrate, ammonium sulfate, ammonium bisulfate, sulfuric acid, or nitric acid using the simplified ion pairing scheme of *Gysel et al.*, [2007]. Inorganic ion concentrations and molecule concentrations for each case study are in Tables 1.4 and 1.5, respectively.

The parcel model is constrained by measured temperature profiles, cloud base height, and updraft velocities whenever available (Figures 1.2 and 1.3). The simulations

used fixed updraft velocities, based on the calculation that at low updrafts, there is a negligible feedback effect due to small evolved heat of condensation and negligible density and viscosity changes in the non-drizzling air parcel below 500 m. For E-PEACE, vertical profiles of temperature and pressure measured by the CIRPAS Twin Otter were used to provide measured lapse rates. For SOLEDAD, lapse rates were not measured so both adiabatic and sub-adiabatic conditions were simulated. To account for release of latent heat in the cloud, the vertical temperature gradient was calculated as

$$dT = -\left(\frac{gwdt+Ldw_l}{c_p}\right), \quad (1.1)$$

where dT is change in temperature, g is acceleration due to gravity, w is updraft velocity, dt is time step, L is latent heat of water condensation, w_l is liquid water mixing ratio, and c_p is specific heat of water [*Bahadur et al.*, 2012]. A ceilometer (Model CL31, Vaisala) was used to measure cloud base height on the R/V *Point Sur* during E-PEACE and on Scripps Pier (1 km west of the sampling site) during SOLEDAD. Updraft velocities used for E-PEACE simulations were measured on the CIRPAS Twin Otter during E-PEACE; for SOLEDAD, updraft velocities were estimated (as described in section 1.3.1.1). More detailed model mechanics are given by *Russell and Seinfeld* [1998] and *Russell et al.* [1999].

1.2.4 GCM Parameterization

The second model used in this study is the parameterization of cloud droplet formation [*Betancourt and Nenes*, 2014; *Fountoukis and Nenes*, 2005; *Nenes and Seinfeld*, 2003] that was designed to be numerically efficient for use in GCMs. It is

based on a generalized sectional representation of aerosol size and composition. The parameterization can be used with internally or externally mixed aerosols with size-varying composition, and it can include the effects of surface-active compounds, insoluble compounds, and slightly soluble compounds. The model uses minimal empirical information and is applied in a two-step process. It first accounts for the aerosol number and chemical composition modeled with modified Kohler theory to provide critical supersaturations for each aerosol bin; it next uses an updraft velocity to express a cooling rate and compute the maximum supersaturation using a semi-analytical approach. To calculate the condensation rate of water vapor in the supersaturation balance equation, the "population splitting" approach is adopted – which determines the size of droplets at the point of maximum supersaturation in the cloudy updraft. This differential growth of the larger droplets relative to the smaller droplets is important because it affects the estimated surface area for water vapor condensation and supersaturation. Once the maximum supersaturation, s_{max}, is computed, the CDNC is then equal to the CCN with critical supersaturation less than s_{max}. The model takes into account the "inertial" mechanism for kinetic limitation described by *Nenes et al.* [2001], as well as a series of corrections to account for the effects of large particles to preclude errors in maximum supersaturation [*Barahona et al.*, 2010; *Betancourt and Nenes*, 2014]. For a large range of CCN activation conditions, the parameterization does not require empirical information.

1.2.5 Model Initialization

Both the ACP model and GCM parameterization are initialized by measurements below or before cloud occurrences and are compared to in-cloud measurements from the two field campaigns. The initial and simulated values are provided in Table 1.6. To initialize the E-PEACE case studies, number concentrations were obtained from merged APS and SMPS measurements on 16 July and from merged scanning DMA and PCASP measurements on 10 August. The method described by *Khlystov et al.* [2001] was used to merge the distributions from submicrometer and supermicrometer instruments. Consistent with the available chemical and physical measurements, these simulations were initialized with one internally mixed aerosol population except for the plume cases which consisted of an external mixture of the background (marine) aerosol population and the plume aerosol population. The modeled aerosol chemical constituents are ammonium sulfate, ammonium bisulfate, ammonium nitrate, nitric acid, sulfuric acid, sodium chloride, refractory black carbon, and organic carbon.

Aerosol compositions were obtained from 30-minute averaged bulk submicron MS mode HR and C ToF-AMS measurements. Salt concentrations of NaCl, were calculated from the components measured by the AMS, scaled by XRF and IC sea salt concentrations for E-PEACE and SOLEDAD, respectively [*Modini et al.*, 2015]. Sulfate molecules were apportioned using the molar ratio of sulfate to ammonium ions [*Nenes et al.*, 1998]. SP2 measurements, averaged over 5 h, were used for refractory black carbon mass concentrations. Aerosol hygroscopicities as represented by the

kappa parameter (κ) were calculated from CCN spectra measurements. Inorganic hygroscopicities (κ_{inorg}) have been measured in laboratory experiments [*Petters and Kreidenweis*, 2007] using the molecular concentrations to then calculate the inorganic contribution to particle hygroscopicity. The organic hygrospopicity (κ_{org}) was then evaluated from the equation

$$\kappa_{measured} = \kappa_{inorg}\chi_{inorg} + \kappa_{org}\chi_{org} \quad (1.2)$$

where χ_{org} and χ_{inorg} are the organic and inorganic volume fractions, respectively. There is uncertainty in the hygroscopicity of the organic fraction because its components are not specific identified molecular compounds and because the hygroscopicity of many organic molecules (or their mixtures) has not been measured [*Petters et al.*, 2015]. For these reasons, we consider a range of values for $\kappa_{org}\chi_{org}$ in different simulations. Refractory black carbon has a hygroscopicity of zero and would have no contribution to the measured hygroscopicity. Finally, meteorological inputs consisted of observed temperature, pressure and relative humidity profiles were used to initialize the model. The meteorological profiles determined the cloud base temperature and pressure as well as the subsequent forcing on the cloud supersaturation.

1.2.6 Cloud Reflectivity

Cloud reflectivity (CR) was estimated using the following equation [*Bohren and Battan*, 1980; *Geresdi et al.*, 2006]

$$CR = \frac{(\sqrt{3}(1-g)\tau)}{(2+\sqrt{3}(1-g)\tau)}, \quad (1.3)$$

where τ is the cloud optical depth defined as

$$\tau = 2hCDNC\pi r_e^2; \quad (1.4)$$

and h is the cloud height or thickness r_e is the cloud effective radius, and g, the asymmetric scattering parameter, is approximated as 0.85 based on Mie scattering calculations for supermicron cloud drops. A CR of 1.0 reflects all visible light and a CR of 0.0 reflects no visible light.

Cloud reflectivity (CR) is largely dependent on CDNC and cloud droplet size distributions. Cloud droplet effective radius can be approximated as a weighted mean radius of the cloud droplet size distribution

$$r_e = \left(\frac{3LWC}{4\pi kCDNC\rho_w}\right), \quad (1.5)$$

where LWC is liquid water content, ρ_w is density of water, and k is the spectral parameter that represents the reciprocal of the cloud droplet spectrum width [*Hsieh et al.*, 2009]. For example, a monodisperse droplet distribution would have k=1 and a broader droplet distribution is characterized by k <1. The spectral parameter k is calculated as

$$k = \left(\frac{r_v}{r_e}\right)^3 \quad (1.6)$$

where r_v is the effective volume radius and r_e is the effective radius [*Hsieh et al.*, 2009]. In this manuscript, cloud reflectivity calculations are calculated from cloud base to the measurement height (Table 1.1) in the cloud and thus do not represent cloud-top-reflectivity. This approach provides values that are more representative of average cloud properties and avoids the influence of cloud-top-entrainment.

1.3 Results

1.3.0 Initialization of Case Studies

These case studies included six different measured compositions and aerosol size distributions to identify different CCN distributions that initialize the modeled droplet activation. The aerosol composition and aerosol number size distributions with lognormal fits are shown in Figure 1.1.

Each of the two SOLEDAD cases was internally mixed in one approximately-lognormal aerosol mode, which was consistent with a mixture of coastal pollution and sea spray particles suspended in the atmosphere long enough (*i.e.* "aged") to be internally mixed. The higher concentration of nitrate in cloud than out of cloud shows that secondary aerosol formation from cloud processing contributes to the overall aerosol population. The SJN01A case contained over 50% organics by mass and a concentration of 2290 cm^{-3}. The SOLEDAD June 13 ambient (SJN13A) case was less polluted with 1430 cm^{-3}, a much lower organic mass fraction and was primarily ammonium sulfate by mass. SJN01A was the only case with a significant amount of refractory black carbon (8% by mass).

The E-PEACE particle number distributions contained multiple modes that were fit to lognormal distributions (Figure 1.1) and used to initialize the two models. The EJL16B and EAU10B cases had compositions with a large mass fraction of NaCl and lower aerosol number concentrations (160 and 360 cm^{-3}, respectively). The EAG10P contained mostly organic components with sulfuric acid and particle concentrations of 1940 cm^{-3}. The E-PEACE intentionally-generated smoke plume case (EJL16P)

consisted of nearly 100% organic components with a mean particle concentration of 1790 cm^{-3}. The composition of the E-PEACE background aerosol was modeled as an internally mixed distribution of the chemical compounds (Figure 1.1). The E-PEACE "background" cases consisted of one particle type, and the "plume" cases had two particle types that represented the generated smoke or cargo ship emissions and the background aerosol.

The vertical temperature profiles for initializing simulations were linear fits of the observed temperatures for the E-PEACE cases (Figure 1.2). The meteorological profiles determined the cloud base temperature and pressure as well as the subsequent forcing on the cloud supersaturation. The same temperature profile was used for the background and plume cases on each day. The observed temperature profile for EJL16B and EJL16P (on 16 July 2011) was sub-adiabatic, but the temperature profile for EAU10B and EAU10P (on 10 August 2011) was adiabatic. For the SOLEDAD cases, temperature was only measured at Scripps Pier (14m ASL) and at the summit (251 m ASL), so the temperature profile below and in-cloud was calculated for both adiabatic and sub-adiabatic conditions. Temperature soundings at airports to the north and south were not consistent with measured surface temperatures at the Mt. Soledad site due to local differences and could not be used. Figure 1.2 also shows LWC, CDNC, and mean volumetric cloud droplet diameter (D_v) for both measurements and simulations of the background cases. The CDNC profile for the EJL16B in Figure 1.2 stopped at 145 m because the droplet concentration decreased to zero above 145 m, indicating that the Twin Otter aircraft left the cloud. Based on measured lapse rates and observed mean

cloud base height, the ACP model reproduced the observed LWC in both E-PEACE cases (Table 1.1). CDNC increased rapidly in observations and model simulations above cloud base and remained relatively constant throughout the rest of the cloud. The D_v increased with height and agreed well between observations and model simulations, as summarized in Table 1.1. Table 1.1 also shows three different simulations for each of the two July 16 E-PEACE cases to illustrate the effect of assuming an adiabatic lapse rate, compared to the observed sub-adiabatic lapse rate. These are discussed further in section 1.3.1.1.

1.3.1 Thermodynamic Constraints on Cloud Droplet Formation, Growth, and Distribution

The ACP model predicted activation and condensational growth of cloud droplets in clouds formed for each case study. In the ACP simulation, the parcel rose vertically at a fixed updraft velocity from the ocean surface to cloud top, with cooling controlled by the measured lapse rate. Changes in updraft velocity due to condensation had negligible effects on drop distributions for the cases studied here, so fixing the updraft velocity had little effect on the predicted drop distribution. The particles took up water and grew in diameter as the relative humidity increased below cloud, sometimes increasing the diameter by a factor of 2 from dry conditions to 90% relative humidity, consistent with measurements [*Wonaschuetz et al.*, 2013]. Differences in droplet number and size relative to equilibrium calculations emerge because faster-growing particles reduce the water vapor available for slower-growing particles. Within the first several meters above the cloud base, the particles activate rapidly, and the

maximum supersaturation is reached (Figure 1.2). For the remainder of the in-cloud ascent, activated droplets continued to grow to larger sizes but no additional particles were activated (Figure 1.2). The detailed measurements of thermodynamic and microphysical properties sufficiently constrain the simulated cloud droplet size distributions to match the mean measured CDNC within 6% and the mean diameter within 10% for five of the six cases (Table 1.1), thus demonstrating "closure" or consistency of the measured composition with the measured CCN spectra and the inferred and modeled supersaturation.

To understand the role of cloud thermodynamic variability on cloud reflectivity, one can evaluate the sensitivity of each simulated drop distribution to the measured cloud base height (and associated lapse rate) and updraft velocity. CDNC greatly influences cloud reflectivity, and CDNC is sensitive to other variables, such as updraft velocity, aerosol concentration, the hygroscopicity parameter κ, and aerosol distribution parameters [*McFiggans et al.*, 2006; *Reutter et al.*, 2009; *Rissman et al.*, 2004; *Twomey*, 1977]. Table 1.2 includes CDNC relative sensitivities to aerosol concentration (N_a) and updraft velocity (w), as well as sensitivities to κ_{org}, and the dry lapse rate (Γ_d). The LWC, CDNC, D_v, and CR are shown in Figure 1.4 as a function of lapse rate, updraft velocity, and organic hygroscopicity ($\kappa_{org}\chi_{org}$, Equation 1.2). Error bars in Figure 1.4 represent 25th and 75th quartiles. SOLEDAD updraft velocities were not measured and are therefore estimated from measurements (this is further explained in section 1.3.1.1). Lapse rate measurements, organic hygroscopicity ($\kappa_{org}\chi_{org}$) for EAG10P and EJL16P, and updraft velocity for SJN01A and SJN13A, have insufficient measurements to define

quartiles. The effects of lapse rate and updraft velocity on droplet distribution for the case studies are discussed below.

Table 1.2: Calculated sensitivities of *CDNC* to X_i ($\partial \ln CDNC / \partial \ln X_i$), where X_i is κ_{org}, Γ_d, w, S_{max}, or N_a.

	Polluted (N_a > 1000 cm^{-3})				**Clean (Na < 1000 cm^{-3})**	
	EJL16P	**EAG10P**	**SJN01A**	**SJN13A**	**EJL16B**	**EAG10B**
κ_{org} (0.05 to 0.20)	0.4	0.10	0	0	0.07	0.05
Γ_d (-7 to -9.8 K km^{-1})	1.61	0	0.91	.90	1.54	0
W (0.1 to 0.3 m s^{-1})	0.74	0.58	0.60	0.68	0.24	0.51
	July 16 (N_a range:160-1790 cm^{-3})				**August 10 (N_a range: 360-1940 cm-3)**	
N_a	0.35				0.34	

1.3.1.1 Variability in Lapse Rate

As a non-entraining air parcel rises through the atmosphere, temperature decreases adiabatically. At the cloud base, the parcel reaches saturation and water condenses and releases latent heat, which decreases the magnitude of the lapse rate. The reduced moist (in-cloud) lapse rate is caused by cooling which also provides additional water for condensation as the parcel rises above the cloud base.

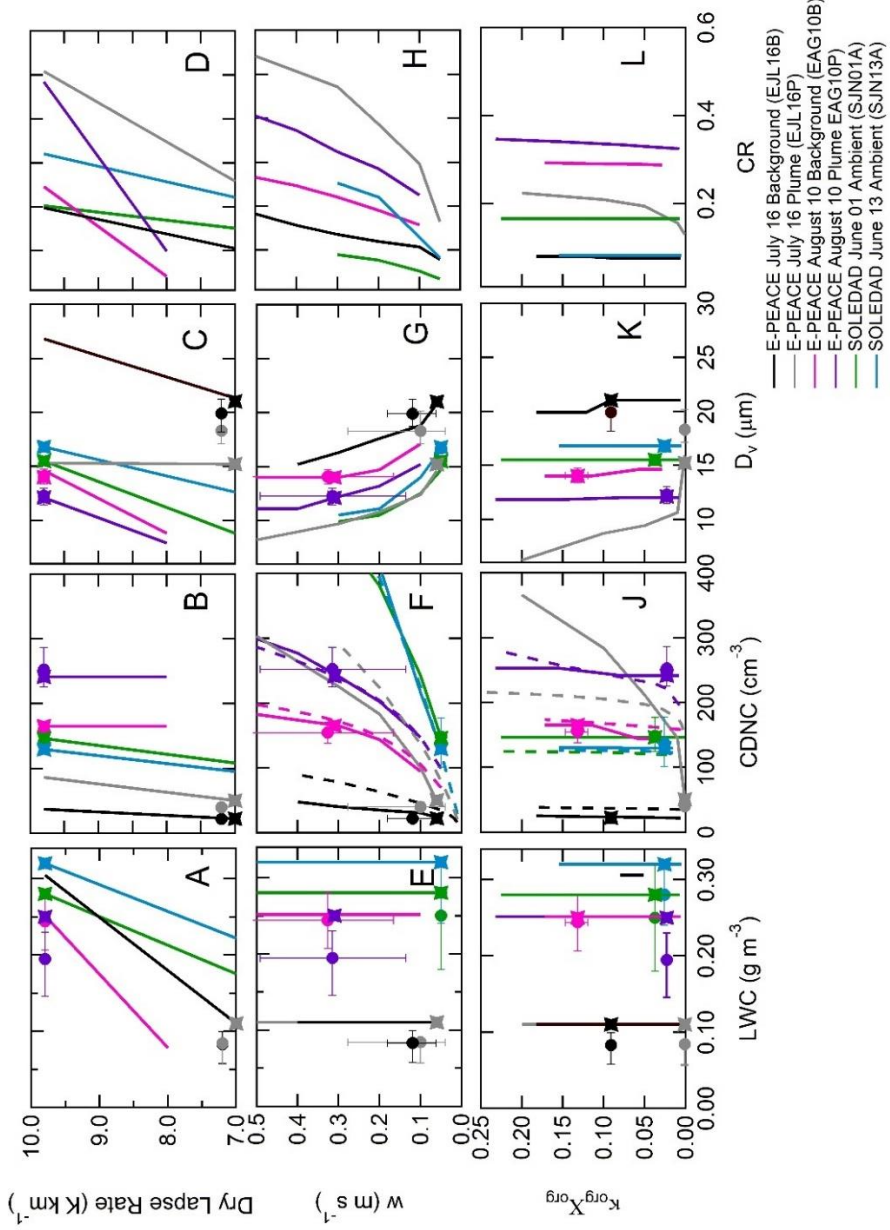

Figure 1.4: Simulations of LWC, CDNC, Dv, and CR for different values of lapse rate, updraft velocity (w) and organic hygroscopicity ($\kappa_{org}\chi_{org}$) for the six cases in Table 1. Dashed lines represent the GCM parameterization, and solid lines represent the ACP model. The circles represent the measured 50th quartile and error bars represent observed 25th and 75th percentiles. The stars represent the simulation runs from Table 1. The $\kappa_{org}\chi_{org}$ standard deviation is only due to changes in κ_{org} while χ_{org} is held constant. Measurements are from the same instruments in Figures 1-3.

To show the relationship between different lapse rates and cloud base heights, the lapse rate was varied for the sub-adiabatic E-PEACE cases EJL16P and EJL16B to be adiabatic (Table 1.1); the other cases were tested with a sub-adiabatic lapse rate (Table 1.1). Equation 1.1 was used to estimate the moist adiabatic lapse rate for E-PEACE cases. SOLEDAD cases used a prescribed lapse rate that resulted in the measured LWC at the height of measurement. To simulate a sub-adiabatic lapse rate, part of the first term in Equation 1.1, which represents an adiabatic lapse rate of -9.8 K/km $\left(g/c_p\right)$, was changed to be sub-adiabatic (> -9.8 K/km). The measured in cloud lapse rate (-2.2 K/km) and cloud base height (70 m) are used for EJL16P-sa ("sa" for "sub-adiabatic lapse rate") and EJL16B-sa cases. These simulations both reproduce measured mean CDNC and LWC within one standard deviation. In EJL16P-al and EJL16B-al (where "al" indicates "adiabatic lapse rate"), the measured cloud base height of 70 m was used but the in-cloud lapse rate was set to be adiabatic (a moist lapse rate of -4.4K/km as calculated by Equation 1.1). In both EJL16P-al and EJL16B-al simulations, CDNC and LWC are much larger than measured values. Simulations EJL16P-ad and EJL16B-ad (where "ad" indicates "adiabatic lapse rate and cloud base height") used both the adiabatic cloud base height of 28 m and moist lapse rate of -4.4 K/km. The adiabatic lapse rate simulated a much lower cloud base height, consistent with the findings of *Craven et al.* [2002]. These simulations produced an even larger LWC but similar CDNC as for runs EJL16P-al and EJL16B-al. The simulations also showed that the measured sub-adiabatic lapse rate, used in simulations EJL16B-sa and EJL16P-sa, caused the parcel of air to reach saturation at a higher altitude and produced

a corresponding decrease in the moist lapse rate. This sub-adiabatic moist lapse rate resulted in lower supersaturations, which caused the measured CDNC and LWC to be lower than that of an adiabatic case. The reduction in CDNC due to sub-adiabatic lapse rates was consistent with *Leaitch et al.* [1996], who compared the maximum CDNC (associated with parcels having adiabatic lapse rates to the observed average CDNC) and observed CDNC associated with sub-adiabatic lapse rates for stratocumulus clouds in the North Atlantic. This result also explains why the adiabatic form of the simplified GCM parameterization [*Betancourt et al.*, 2012; *Nenes and Seinfeld*, 2003] produces larger CDNC than was measured for sub-adiabatic cases (EJL16B-sa and EJL16P-sa), as shown in Figure 1.4 F,J. Another reason the [*Nenes and Seinfeld*, 2003] parameterization does not compare well to the ACP model for the EJL16P case is that this is an unusual case with comparatively high concentrations of large (~1 micron diameter) organic smoke particles. In this case, the empirical data used in the parameterization when CDNC is sensitive to kinetic limitations [*Nenes and Seinfeld*, 2003] was not a good representation of the EJL16P aerosol, specifically of the smoke plume particles. The ACP model and GCM parameterization agree well for the EAG10B-ad and EAG10P-ad cases, largely because the lapse rate measured was adiabatic. However, the GCM parameterization could be adjusted to use a sub-adiabatic lapse rate. The simulations EAG10B-sa and EAG10P-sa, using a sub-adiabatic lapse rate of -8 K/km, produced a lower moist lapse rate and resulted in underestimating D_v and LWC. A sub-adiabatic lapse rate of -7 K/km could not be used to compare to measurements for the 10 August cases because it led to cloud formation above the

Table 1.3: Observed and Simulated Spectral Parameter (k).

	E-PEACE 16 Jul Background (EJL16B)	E-PEACE 16 Jul Smoke Plume (EJL16P)	E-PEACE 10 Aug Background (EAG10B)	E-PEACE 10 Aug Cargo Plume (EAG10P)	SOLEDAD 01 Jun Ambient (SJN01A)	SOLEDAD 13 Jun Ambient (SJN13A)
Observations	0.84±0.05	0.87±0.04	0.90±0.03	0.93±0.02	0.71±0.03	0.72±0.01
Simulations						
Single Updraft Velocity	0.98	0.98	1.00	1.00	0.72	0.89
PDF of Updraft Velocities	0.96	0.87	0.96	0.93	-	-
PDF of Cloud Bases	0.98	0.96	0.97	0.96	0.62	0.81
PDF of Updraft Velocities and Cloud Bases	0.89	0.81	0.93	0.87	-	-

observed cloud base height. These sub-adiabatic cases had the same CDNC as the "al" case. This result differs from the other cases because the lapse rate is closer to adiabatic and because the updraft velocity is higher. Figure 1.4F shows that CDNC is less sensitive at higher updraft velocities, as seen in *Rissman et al.* [2004]. The SOLEDAD cases used simulated updraft velocity and lapse rate because there were no measured updraft velocities or meteorological profiles. This information was estimated with the ACP model by matching the simulated results of LWC and CDNC to the observed values. The results from a pure adiabatic lapse rate and a sub-adiabatic lapse rate of -7 K/km were simulated and are also shown in Table 1.1. For both SOLEDAD cases, the simulations with sub-adiabatic lapse rate predicted fewer cloud droplets and less LWC

than simulations with an adiabatic lapse rate, similar to the E-PEACE cases. CDNC is most sensitive to changes in lapse rate for the EJL16P, EJL16B, SJN01A and SJN13A cases as shown in Table 1.3.The remaining cases, EAG10P and EAG10B, show no sensitivity to lapse rate possibly due to the low aerosol bin resolution.

The sub-adiabatic lapse rates may result from mixing. Cloud top-entrainment can cause deviations from the moist adiabatic profile, but typically those effects are most evident close to the top of the cloud [*Nicholls and Leighton*, 1986]. The sub-adiabatic temperature profile in the cases shown here extends to below cloud base. Also, the clouds were only simulated up to the measurement heights, which were several tens of meters below the cloud top, so that cloud top effects were likely minimal. Therefore, effects of cloud top entrainment are small but the reflectivity is biased slightly low.

In Figure 1.4A-D, different simulated lapse rates are shown to vary CDNC, LWC, and CR. The reasons for these dependencies are the same as in the previous paragraph. Variation of CDNC and LWC cause variation in D_v (Figure 1.4C) and CR (Figure 1.4D). Measurements from SOLEDAD were taken close to cloud base at an average of 45 m and 80 m above cloud base for SJN01A and SJN13A, respectively. LWC and CDNC correlated well on both days (Figure 1.10), which further suggests that measurements were taken near cloud base because, as shown in Figure 1.2 for EJL16B and EAG10B, CDNC quickly reached its maximum value above cloud base. It is possible that the decreased cooling rate was caused by a sub-adiabatic lapse rate, leading to a decrease in CDNC. The sub-adiabatic cases for both SOLEDAD cases (Table 1.1) had simulated LWC and CDNC that were within one standard deviation of observations

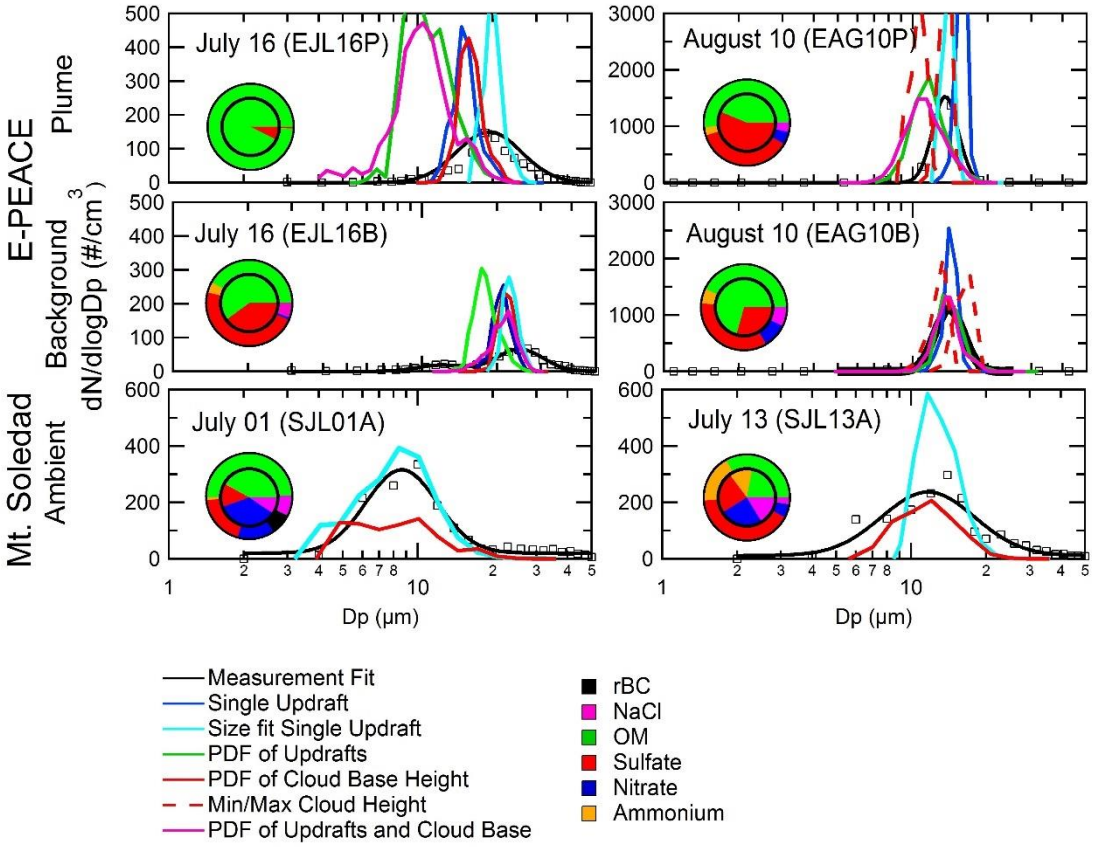

Figure 1.5: Cloud droplet size distributions are presented for the cases in Table 1. Each case contains cloud droplet distribution measurements as black squares with a lognormal fit. Blue distributions are simulation results based on a single updraft (constrained by CCN spectra behind the CVI, equivalent to the measured CDNC). Light blue distributions also use the same single updraft velocity; however, the cloud base in the simulation is adjusted so the peak measured fits correspond to simulation peaks. Green and solid red distributions are simulation results for a probability distribution of updrafts and cloud base respectively. Dashed red distributions simulated droplet distributions using minimum and maximum measured cloud base heights for cases without ceilometer measurements. Finally, magenta distributions are simulation results for the combined probability distribution of updrafts and cloud base heights. The inner pie represents the simulated composition and the outer pie represents the measured composition.

for 6% of all in-cloud droplet measurements, consistent with sub-adiabatic lapse rates. E-PEACE cases had a much smaller variation in number concentration (Figure 1.3); however, they had significant variations in LWC and cloud base height. To identify the effect of LWC variation due to lapse rate variation, a probability distribution function (PDF) of measured cloud base heights (Figure 1.12) was used in the ACP model to estimate *k* (Table 1.3). Variability in cloud base height (or lapse rate) alone broadens the cloud droplet distribution, but it is still narrower than observed for all cases with the exception of the SJN01A case (Table 1.3, Figure 1.5). Table 1.3 shows that four of the six cases are estimated to have droplet spectral widths within observed error when using a distribution of updrafts or cloud base heights rather than a single updraft and cloud base height. The SJL13A case does not have updraft measurements, so variability in *k* with cloud base height could not be calculated. The SJL01A case had a simulated *k* value from a single updraft and cloud base height that was within 2% of the observed *k* value.

The SJL01A case had measurements close to cloud base where supersaturation is at maximum. *Hsieh et al* [2009] found that the *k* value at the height of maximum supersaturation is a good representation of the *k* value throughout the cloud; therefore, that constant updraft simulation *k* is comparable to observations for SJL01A, consistent with the result of *Hsieh et al* [2009].

1.3.1.2 Variability in Updraft Velocity

Variations in updraft velocity have the potential to broaden the cloud droplet distribution. Updraft velocity controls the maximum supersaturation, which in turn

determines the smallest (and least hygroscopic) particles that can activate. In fast updrafts, there is less time available for water vapor uptake by aerosols, which causes higher supersaturation and activation of more particles. CDNC increases with updraft velocity, as shown in Figure 1.4F. As noted by *Chuang* [2006] and *McFiggans et al.* [2006], CDNC is more sensitive to updraft velocity variation in polluted cases (Table 1.2). Updraft velocity also affects droplet size (D_v in Figure 1.4G) as a consequence of increased CDNC for a given constant LWC.

Since updraft velocity affects CDNC (and, for constant LWC, drop size), variability in updraft velocity results in broadening of the observed cloud drop distribution. Simulated cloud droplet distributions always produce narrower droplet distributions (larger *k*) than measured when applying a constant updraft and lapse rate. Figure 1.5 consists of droplet size distributions from the ACP model for each case, as well as the observed cloud droplet distribution. Figure 1.5 shows that using an ensemble of updrafts instead of a single updraft to simulate observed *k* values is better at reproducing the droplet spectral parameter *k* than a single updraft, which agrees with the findings of *Hsieh et al.* [2009]. Since the SOLEDAD cases did not include vertical velocity measurements, it was not possible to include a droplet distribution using a PDF of measured updraft velocities. The simulated distribution with a single updraft velocity for SJL01A in Figure 1.5 matched the observed droplet distribution width well, unlike the other cases. This is possibly because the measurements were close to cloud base, and the broadening of the droplet distributions due to variations in updraft velocity and lapse rate at cloud base is not significant till higher altitudes.

1.3.1.3 Combined Variability of Cloud Base Height (Lapse Rate) and Updraft Velocity

We have shown that updraft velocity variability and cloud base height variability both increase droplet distribution width (decrease *k*). However, using either a distribution of cloud base heights or updraft velocities, but not both, is not sufficient to broaden the distribution of *k* values to observed values for the E-PEACE background cases (Table 1.3). By incorporating variability of both cloud base height and updraft velocity, the simulated droplet distributions best approximate the observed distributions and spectral parameter for background cases. The combined influence of both variables on the distribution width creates a broader distribution than when each is considered separately. Simulated E-PEACE plume cases have distributions broader than those observed. It is possible that the measured updraft velocity and cloud base height distributions are not representative because the small horizontal area may include only a subset of the measured updraft distribution. *Chuang* [2006] showed that in polluted cases small variations in the updraft velocity can cause large variations in CDNC. For the EJL16P case, for example, the distribution of updrafts produced a simulated CDNC that exceeded the measured values by a factor of three. However, for all other cases a distribution of updrafts produced CDNC within one standard deviation of the measured CDNC.

1.3.2 Effects of Organic Composition and Hygroscopicity on Cloud Droplet Formation, Growth, and Distributions

Aerosol hygroscopicity can also play a role in determining CDNC [*Petters and Kreidenweis,* 2007]. Figure 1.5 shows in-cloud droplet composition as measured and

simulated (inner and outer circles, respectively) in the cloud. The inorganic and organic fractions of the measured and simulated compositions are of roughly similar magnitude, but noticeable differences exist in each case. In-cloud aqueous uptake or production of sulfate, nitrate, and organic compounds can explain discrepancies between predicted and measured composition [*Charlson et al.*, 1987; *Hayden et al.*, 2008; *Modini et al.*, 2015; *Prabhakar et al.*, 2014; *Sorooshian et al.*, 2015; *Sorooshian et al.*, 2013; *Youn et al.*, 2015]. The lack of gas-phase measurements precludes a detailed analysis; however, we note that during E-PEACE Twin Otter cloud droplet residual particle measurements, downstream of the CVI, suggest dissolution of precursor vapors and in-cloud production of such compounds [*Prabhakar et al.*, 2014; *Sorooshian et al.*, 2015; *Sorooshian et al.*, 2013; *Youn et al.*, 2015].

Organic aerosol component hygroscopicity has been shown to have a small effect on CDNC in non-polluted situations [*Dusek et al.*, 2006], whereas in polluted cases CDNC can be strongly affected [*Hegg et al.*, 2010; *Twohy et al.*, 2013]. To investigate the sensitivity of CDNC to the organic component, the GCM parameterization and ACP model were initialized with a range of typically observed κ_{org} values (0.01-0.3). These were multiplied by the organic aerosol volumetric fraction to obtain the hygroscopicity due to organics ($\kappa_{org}X_{org}$, Figure 1.4I-L). The CDNC sensitivity to κ_{org} is largest for the EJL16P and EAG10P cases (Figure 1.4J, Table 1.2). All of the calculated sensitivity values to κ_{org} are all smaller than κ sensitivities reported by *Reutter et al.* [2009], likely because κ_{org} represents only a small fraction of the total κ. The only exception is the EJL16P case, which consists entirely of organic

components, such that $\kappa_{org} = \kappa_{.}$ The plume cases exhibit the largest effect because of a high organic volume fraction, a high aerosol concentration, and the largest degree of external mixing from the background aerosol. EJL16P, for which the aerosol was entirely organic (Figure 1.1), showed the greatest change in simulated CDNC (increasing by a factor of 6) with organic hygroscopicity. EAG10P exhibited the second greatest increase in CDNC at 34%. Background aerosol organic hygroscopicity has little effect on CDNC, with an increase of only 17% and 10% over the tested κ_{org} range for EJL16B and EAG10B, respectively, because the background aerosols were mostly inorganic and internally mixed. The highly hygroscopic salt and sulfate particles produce high total hygroscopicity, even when the organic hygroscopicity is low, because the organic volume fraction itself was low. High aerosol hygroscopicity caused rapid uptake of water, preventing further activation of droplets despite increases in organic hygroscopicity [*Modini et al.*, 2015]. The variation in CDNC due to κ_{org} significantly affects other cloud properties such as D_v and CR (Figure 1.4I-L). *Ervens et al.* [2010] found that different assumptions for organic solubility and mixing state for marine conditions often lead to similar CDNCs, so reasonable closure could be achieved with assumptions that were not representative of the actual aerosol composition. This is in agreement with our results for the ambient background cases in which the organic hygroscopicity has little effect on the CDNC. Results from *VanReken et al.* [2003] show that closure was observed within 20% with the broad assumption that all the aerosol was composed entirely of ammonium sulfate, indicating that in the cases they studied the CDNC is not very sensitive to even the total hygroscopicity of marine

aerosols. External mixtures are necessary for the plume cases because assuming a completely internally mixed aerosol population was shown to overestimate droplet concentration in polluted conditions where there is a greater fraction of less hygroscopic aerosol [*West et al.,* 2014].

The organic composition and hygroscopicity are important if the organic volume fraction is sufficiently large and mainly externally mixed. κ_{org} does not have a strong influence on changes in CDNC for background cases because of low concentrations just below critical diameters. CDNC is not predicted to increase much in the background cases; the change in critical diameter for all cases was 5 nm or less for an increase in κ_{org} of 0.1, except for EJL16P. In fact, the EJL16B case exhibited the largest change in critical diameter (5 nm), for an increase in κ_{org} of 0.1, even though CDNC increased the least in the E-PEACE cases. In terms of the effect of κ_{org} on CDNC, the CDNC can increase only as much as the concentration between the two critical diameters representing the two different κ_{org} values (Figure 1.11). To test the effect of aerosol concentrations in this narrow size range (marked on Figure 1.11) on CDNC, the bin concentrations were changed to be a fraction of the measured value for size bins below the critical diameter for κ_{org} = 0.01. Figure 1.6 illustrates how aerosol number concentration between the critical diameters (indicated in Figure 1.11) is essential in understanding the effect κ_{org} can have on CDNC. In Figure 6a, the EAG10P case represents the maximum concentration presented, while the lowest concentration represents a 95% decrease in the sub-critical diameter concentration at a κ_{org} of 0.01. Figure 1.6a illustrates that an increase in CDNC due to a change in κ_{org} is largely

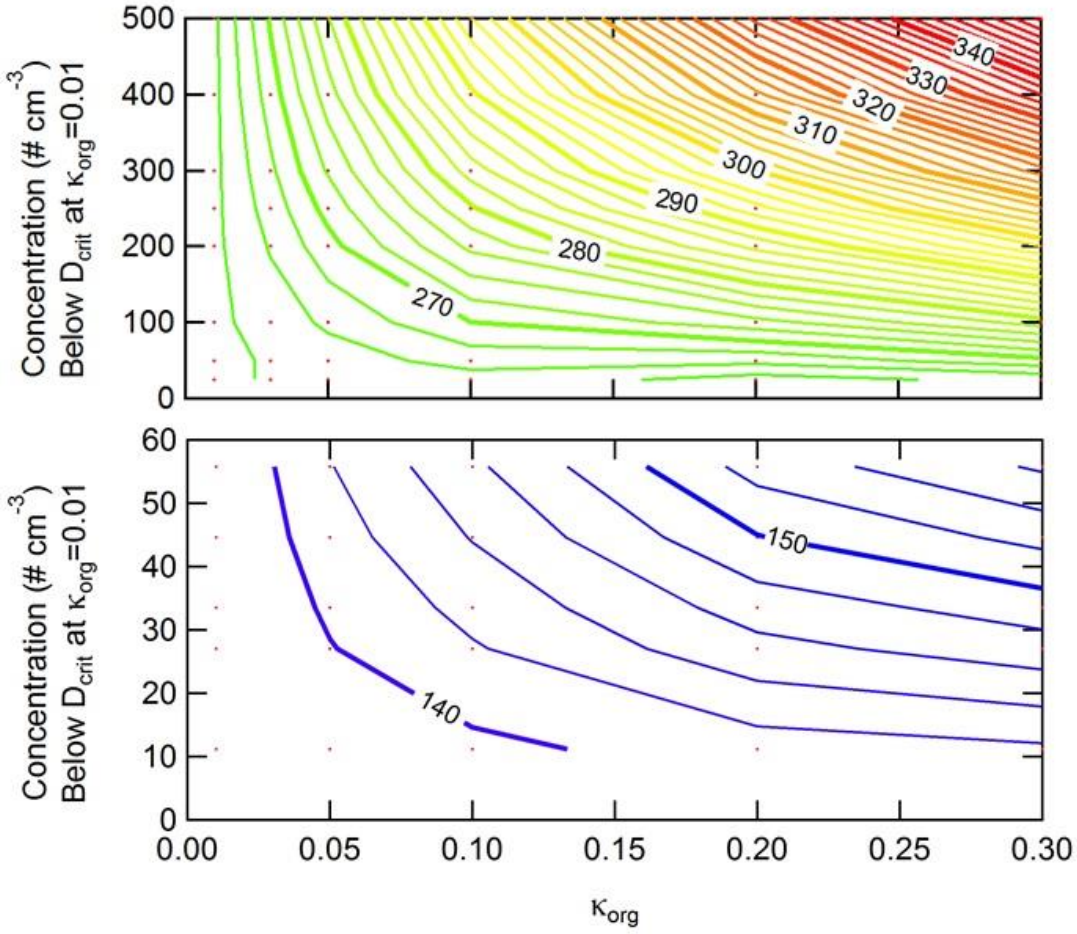

Figure 1.6: Simulated cloud droplet number concentrations for 10 August cargo ship plume (top) and Background (bottom) are shown as a function of κorg and concentration in bins below critical diameter when κorg =0.01. Red dots indicate the combination of κorg and concentration in bins below critical diameter for each simulation.

dependent on the concentration between the two critical diameters associated with the two κ_{org} values, as shown in Figure 1.11. Figure 1.6b represents the EAG10B case. The change in CDNC with κ_{org} is also shown to decrease with a below-critical-diameter concentration at a κ_{org} of 0.01. From overall concentrations tested in Figure 1.6b, the change in CDNC is much smaller than in the plume case (Figure 1.6a) because there are

fewer particles in the bins below the critical diameter. This suggests that κ_{org} is most influential on CDNC for plumes or polluted areas in which the critical diameter falls near the peak of an aerosol mode.

In the two E-PEACE background cases and two SOLEDAD ambient cases, the uncertainty and variability in organic composition and hygroscopity are unlikely to contribute significantly to differences between the measured and simulated droplet number distribution (and its spectral width, *k*) or the droplet concentration. The organic fraction was largest in plume sources, wherein organic hygroscopicity exhibits a larger effect than in background and ambient aerosol cases. Furthermore, the low aerosol concentrations in the background cases were such that changes in hygroscopicity have little effect on droplet concentration. Even with high aerosol concentrations, such as in the ambient SOLEDAD cases where the inorganic fraction is high and the inorganic contribution to the aerosol hygroscopicity is much larger than the organic contribution, any change in organic hygroscopicity had no significant effect on CDNC and size.

1.3.3 Impacts of Thermodynamic and Composition Properties on Cloud Reflectivity

Updraft velocity, organic aerosol hygroscopicity, and lapse rate can affect CDNC and LWC, both of which influence ultimate CR. CR calculations were completed for each case corresponding to variations in κ_{org} and *k*. Spectral parameter comparisons were calculated from a single ACP model run with one updraft velocity, several model runs from a PDF of updrafts, a PDF of cloud base heights, and the *k* value of measured distributions (Table 1.3). For all cases, droplets above 2 μm in diameter were used to

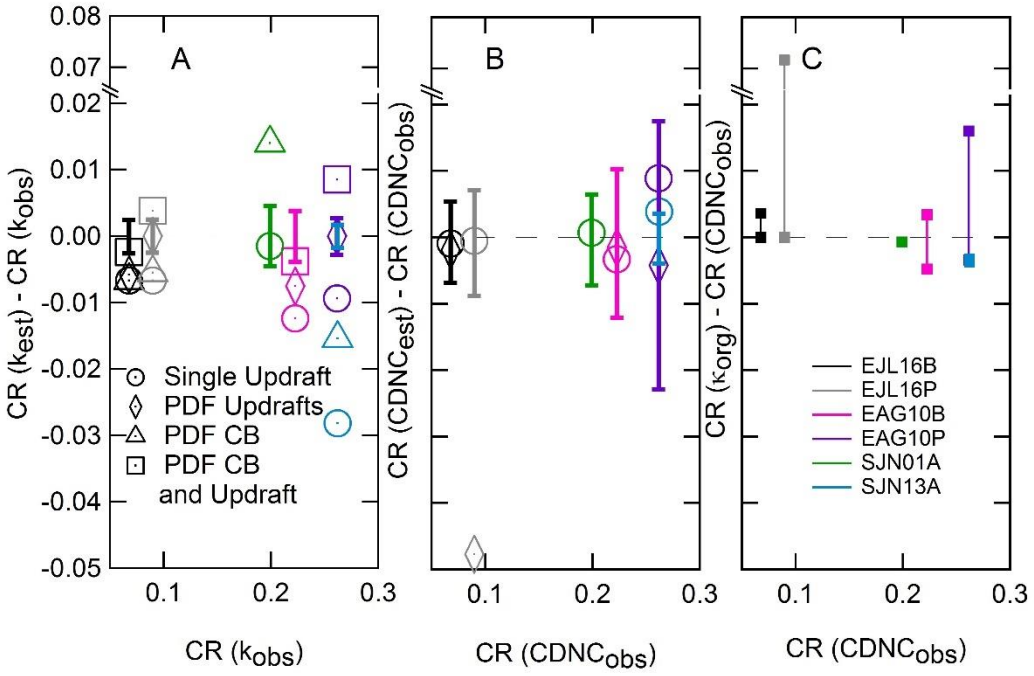

Figure 1.7: Calculated cloud reflectivity (CR) as a function of the spectral parameter (k) using the observed CDNC (panel A) and as a function of CDNC using the observed k (panel B). Error bars represent the CR as a function of k_{obs} ± one standard deviation (panel A) and $CDNC_{obs}$ ± one standard deviation (panel B). CR is calculated as a function of κ_{org} (κ_{org} values of 0.01 and 0.3 shown as higher and lower CR, respectively) using the observed k (panel C). CR was unaffected by κ_{org} for the SJN01A and SJN13A cases, resulting in a single point instead of a range. Each case is represented by the same colors as in Figure 4.

calculate *k* except for the EJL16P case. In the EJL16P only droplets above 5 µm in diameter were used to calculate *k* because some aerosol particles exceeded 2 µm, but did not activate and were not counted as cloud droplets.

k values are mainly constant in model predictions and observations, with the exception of those near cloud base where particles activate and their classification as droplet or interstitial is ambiguous. The SOLEDAD measurements were carried out near

cloud base, which is thought to be why the observed spectral parameter *k* was lower than in the E-PEACE cases (Table 1.3).

Applying a PDF of updrafts and cloud base heights (due to variable lapse rates) instead of a single value improves the agreement between observed and simulated *k* and improves CR estimates. Applying a PDF of updrafts and cloud base heights also affects CDNC, even though it can be modeled well with a single updraft and cloud base height. To observe the influence of *k* and CDNC separately, in Figure 1.7a we used the observed CDNC and simulated *k* to calculate CR; in Figure 1.7b, we used the simulated CDNC and observed *k*. Error bars in each plot express one standard deviation of the observed CDNC or *k*. As shown in Figure 1.7b, all cases lie within the error bars, except the EJL16P case because CDNC is highly sensitive to updraft velocity. When the CR is a function of *k*, many cases lie outside the error bars. The influence of *k* on CR can also be compared to the κ_{org} effect on CR (Figure 1.7c). With the exception of the two plume cases, the change in CR for κ_{org} from 0.01 to 0.3 is much smaller than the effect of the simulated range of *k* on CR. Overall, the use of a distribution of updrafts and lapse rates broadened the droplet spectral width, reducing differences between observed and simulated CR, with the exception of the SJL01A, in which measurements were close to cloud base [*Hsieh et al.*, 2009].

1.4 Conclusions

This work presents a comparison of predictions of two models of aerosol activation and subsequent cloud droplet evolution with measurements from two field studies carried out over the Pacific Ocean off the coast of California and on the

California Pacific coast, E-PEACE in 2011 and SOLEDAD in 2012. One model is a comprehensive size-resolved aerosol-cloud parcel model (ACP), and the second is a global climate model (GCM) parameterization of aerosol activation and cloud formation. Four aerosol cases were analyzed from E-PEACE: a generated organic smoke plume, a cargo ship plume, and two cases of background marine aerosols. The two SOLEDAD cases had aerosol compositions and concentrations characteristic of polluted marine conditions. The model was initialized with aerosol composition taken from HR-ToF-AMS and size distribution measurements. Vertical profiles of meteorological parameters and aerosol size distributions were also used as model inputs. Four of the cases were characterized by a sub-adiabatic lapse rate, which led to fewer droplets owing to decreased maximum supersaturation, lower LWC, and higher cloud base height. Such comparisons are important in order to assess the extent to which models can replicate actual atmospheric conditions. Predictions of cloud microphysical properties depend on a number of key variables, including ambient lapse rate, aerosol size distribution, chemical composition, and updraft velocity; the lack of agreement between predictions and observations often reveals uncertainties in the governing physical processes because these variables are not sufficiently constrained by measurements.

For the E-PEACE cases, a weighted ensemble of simulations that reflect the measured variation in updraft velocity and cloud base height reproduced the observed droplet distributions within 9%, excluding the case of the generated organic smoke plume. Vertical velocity was not measured in SOLEDAD, so an estimated updraft of

0.05 m s^{-1} was used (reproducing CDNC observations with errors of 1% and 6%). A distribution of cloud base heights and updraft velocities produced simulations with a broader cloud droplet distribution than achieved using a single updraft or cloud base height.

In comparing simulated and measured cloud droplet composition, differences suggest a possible role of in-cloud uptake or production of sulfate, nitrate, and organic components. To examine the CDNC sensitivity to the aerosol organic fraction, simulations were initialized with a range of organic hygroscopicities (Table 1.2). The organic fraction in marine background aerosols tends to be too low for organic hygroscopicity to affect CDNC because background particles contain internally mixed hygroscopic salts. However, generated smoke and cargo ship plume aerosols, which have a substantial organic fraction and a large aerosol concentration near the critical diameter of cloud active aerosol, exert a large effect on CDNC. CDNC in such plumes is strongly dependent on the value of the aerosol hygroscopicity, $\kappa_{org}\chi_{org}$, due to both the high organic fraction and aerosol concentration. $\kappa_{org}\chi_{org}$ in the SOLEDAD experiment showed no effect on CDNC, even at the high aerosol concentrations present, because the prevalent inorganic hygroscopic fraction dominates cloud activation. To explore the role of aerosol size and its combined effect with $\kappa_{org}\chi_{org}$, we varied the aerosol concentration in the size bin(s) just below the critical diameters to show that an increase in CDNC, due to a change in $\kappa_{org}\chi_{org}$ is largely dependent on the difference in concentration near the critical diameters. In other words, $\kappa_{org}\chi_{org}$ has the strongest influence on CDNC when the critical diameter falls near the peak of an aerosol mode.

In addition, droplet size, CDNC, and droplet distribution width (*k*) affect cloud reflectivity (CR). Changes in organic hygroscopicity are found to have little or no effect on CR, with the exception of a case with a fresh smoke plume (EJL16P; section 3.3), in which CDNC increased by a factor of 6 (to 300 cm-3 from 49 cm^{-3}), causing an increase in CR from 0.09 to 0.16 (where a CR of 1.0 reflects all visible light), due to its high fraction of externally mixed organics. A case with a cargo ship plume (EAG10P; section 3.3) had the second greatest increase in CDNC with increasing κ_{org}. However, the cloud droplet concentration was already high (277 cm^{-3}) compared to other cases so the increase in CDNC of 35% had little effect on CR, increasing it from 0.26 to 0.28. The difference in cloud *k* values caused a change in CR ranging from ~0.01 to 0.03 for all case, when the CDNC is equal to the observed value, while organic hygroscopicity caused a difference of <0.01 in CR for the cases without fresh plumes.

1.5 Acknowledgements

This work was funded by NSF AGS-1013423, NSF AGS-1360645, NSF AGS-1008848, DOE DE-SC0006679, ONR grants N00014-11-1-0783, N00014-10-1-0200, N00014-10-1-0811 and EC Finance ID #1300359. Kevin J. Sanchez appreciates the support of the San Diego Foundation. We gratefully acknowledge the help and support of the crew and staff of the R/V *Point Sur* and the CIRPAS Twin Otter, as well as assistance from Bill Shull and Ken Duff of Scripps Institution of Oceanography. Finally, we thank Bruce Albrecht for the ceilometer measurements taken on both the SOLEDAD and E-PEACE campaigns. Corresponding data can be found at: http://aerosols.ucsd.edu/SANCHEZetal2016_data.html.

Chapter 1, in full, is a reprint of the material as it appears in the *Journal of Geophysical Research: Atmospheres* 2016 with slight modifications. Sanchez, K.J., L.M. Russell, R.L. Modini, A.A. Frossard, L. Ahlm, C.E. Corrigan, G.C. Roberts, L.N. Hawkins, J.C. Schroder, A.K. Bertram, R. Zhao, A.K.Y. Lee, J.J. Lin, A. Nenes, Z. Wang, A. Wonaschütz, A. Sorooshian, K.J. Noone, H. Jonsson, D. Toom, A.M. Macdonald, W.R. Leaitch, and J.H. Seinfeld. "*Meteorological and aerosol effects on marine cloud microphysical properties.*" *Journal of Geophysical Research. Atmospheres*, 121 (8), pp. 4142-4161, doi:10.1002/2015JD024595, 2016. The dissertation author was the primary investigator and author of this paper.

1.6 Appendix

Table 1.4: Measured chemical components used in the *Gysel et al.* [2007] ion pairing scheme.

	EJL16B	**EJL16P**	**EAG10B**	**EAG10P**	**SJN01A**	**SJN13A**
NO_3^-	0.02	0.00	0.32	0.34	1.04	0.32
NH_4^+	0.10	0.00	0.20	0.66	0.08	1.24
SO_4^{2-}	1.26	0.00	1.20	34.82	1.44	2.8

Table 1.5: Molecular composition derived from AMS chemical composition using the *Gysel et al.* [2007] ion pairing scheme, ion chromatography (NaCl), and SP2 measurements (BC).

	EJL16B	**EJL16P**	**EAG10B**	**EAG10P**	**SJN01A**	**SJN13A**
OM	1.12	22.34	1.46	54.53	3.76	2.24
$(NH_4)_2SO_4$	0.00	0.00	0.00	0.00	0.00	3.86
NH_4HSO_4	0.70	0.00	1.23	4.26	0.55	0.00
H_2SO_4	0.70	0.00	0.18	31.93	0.99	0.00
HNO_3	0.03	0.00	0.32	0.35	1.05	0.00
NH_4NO_3	0.00	0.00	0.00	0.00	0.00	0.41
rBC	0.00	0.00	0.00	0.00	0.56	0.00
NaCl	0.14	0.00	0.24	0.00	0.16	0.17

1.6.1 Model initialization and simulation values

Measurements used to initialize the ACP model and GCM parameterization are given in Table 1.6. Also, simulated values from the ACP model and GCM parameterization are given in Table 1.6. The aerosol distribution parameters used for each case is presented in Table 1.7, using the equation:

$$\frac{dN}{dlnDp} = \frac{N}{(2\pi)^{1/2} ln(\sigma_g)} exp\left(-\frac{\left(\ln(D_p)-\ln(\bar{D}_{pg})\right)^2}{2ln^2(\sigma_g)}\right) \quad (1.7)$$

where D_p is diameter, $\bar{D}_{pg}$ is the geometric mean diameter, N is the total droplet concentration, and σ_g is the geometric mean diameter.

Table 1.6: ACP model and GCM parameterization initial conditions and simulated values.

Initial conditions

	ACP model	**GCM parameterization**
Temperature	Vertical profile (Figure 1.8)	At cloud base (Figure 1.8)
Relative humidity	Vertical profile (Figure 1.8)	-
Pressure	Vertical profile (Figure 1.8)	At cloud base (Figure 1.8)
Updraft velocity	Yes (Table 1.1, Figure 1.10)	Yes (Table 1.1)
Cloud Base	Yes (Table 1.1)	-
Aerosol distribution	Mass size distribution (Figure 1.9)	Number size distribution (Figure 1.1)
Aerosol chemical composition	Compound specific mass size distributions (Figure 1.9)	Aerosol hygroscopicity (κ) (Table 1.5)

Simulated values

	ACP model	**GCM parameterization**
Supersaturation	Vertical profile	Maximum value
Cloud droplet	Vertical profile of particle and drop size distributions	Number concentration

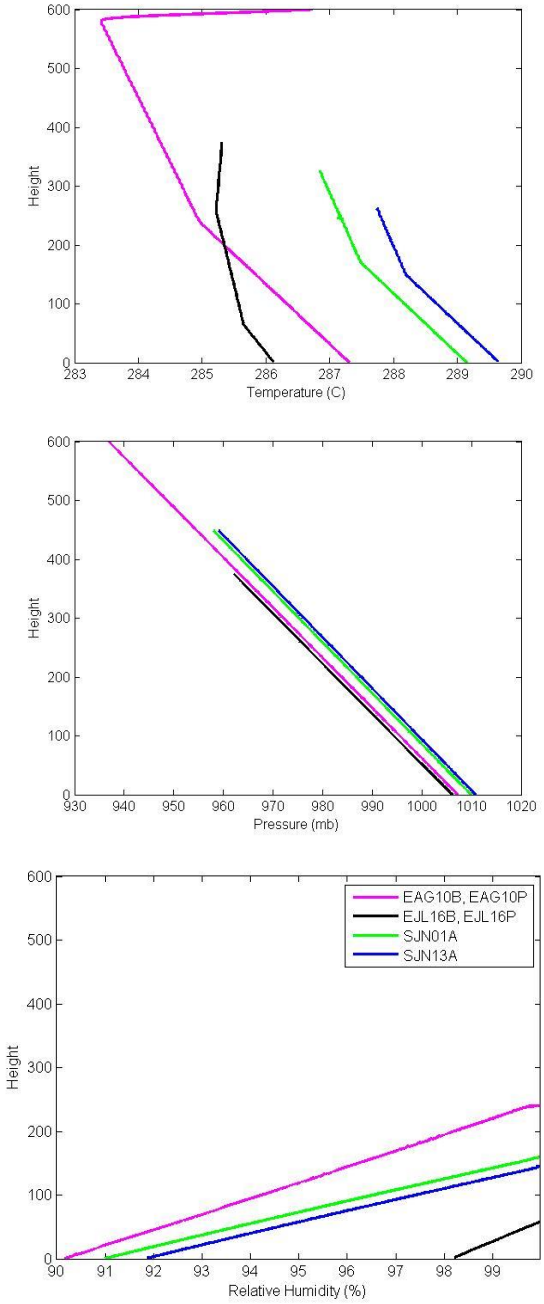

Figure 1.8: Temperature (top left), pressure (top right) and relative humidity (bottom) vertical profiles.

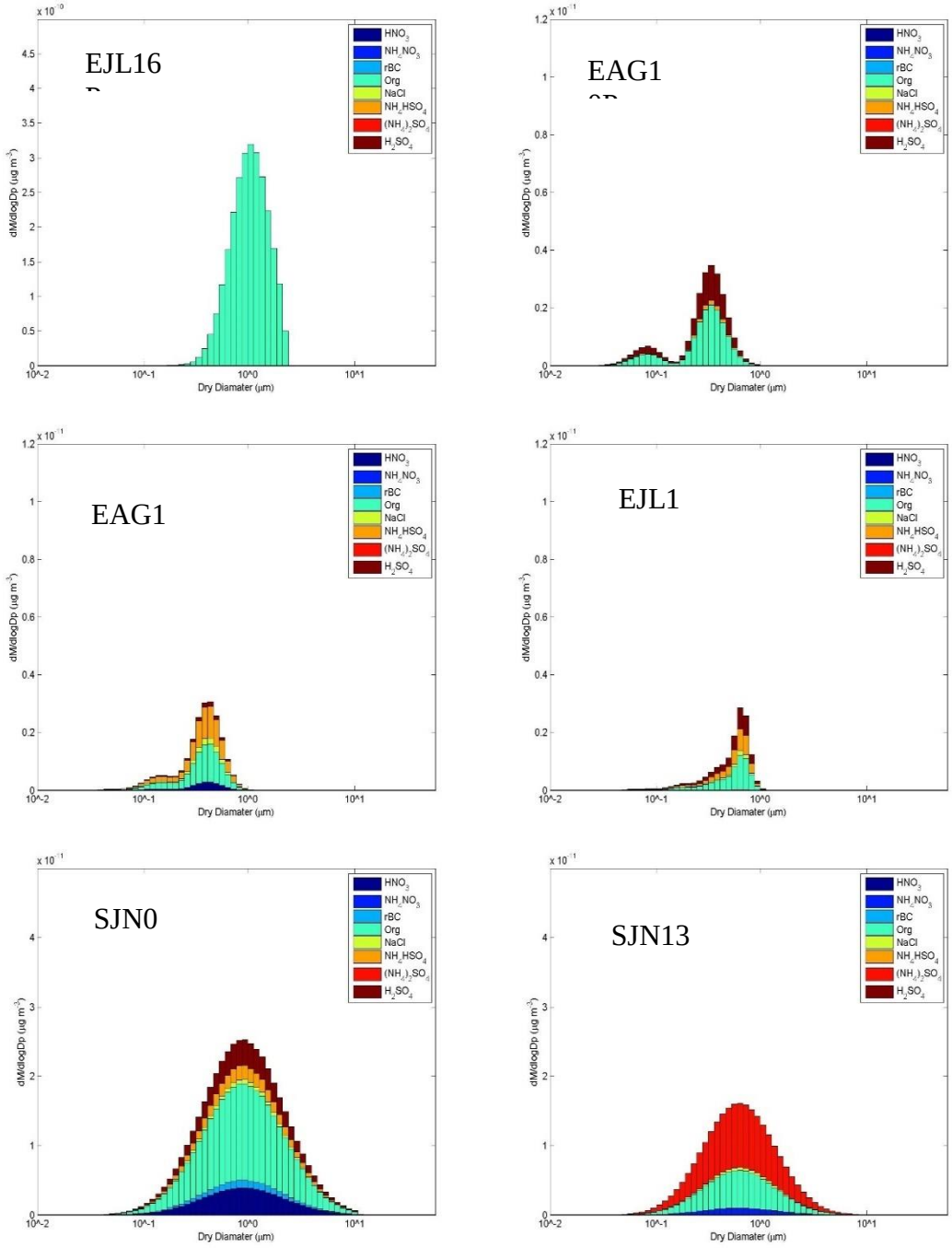

Figure 1.9: Mass size distributions for each molecular species included.

Table 1.7: Lognormal fit parameters for measured initial aerosol number size distributions; the E-PEACE particle size distributions were fit with multiple aerosol modes.

	Mode total concentration (cm^{-3})	**Geometric mean diameter (nm)**	**Geometric dispersion**
EJL16B	128,19,9,6	51,152,318,633	1.50,1.28,1.37,1.16
EJL16P	860,740	65,586	1.73,1.56
EAG10B	160,170,33	44,104,318	1.24,1.40,1.34
EAG10P	1500, 80	53, 265	1.48,1.36
SJN01A	2310	80	2.45
SJN13A	1440	95	2.2

1.6.2 SOLEDAD LWC and CDNC measurements

Figure 1.10 shows measured LWC vs CDNC for the SJL01A and SJL13A cases. LWC increases with altitude so many of the low LWC measurements are close to cloud base.

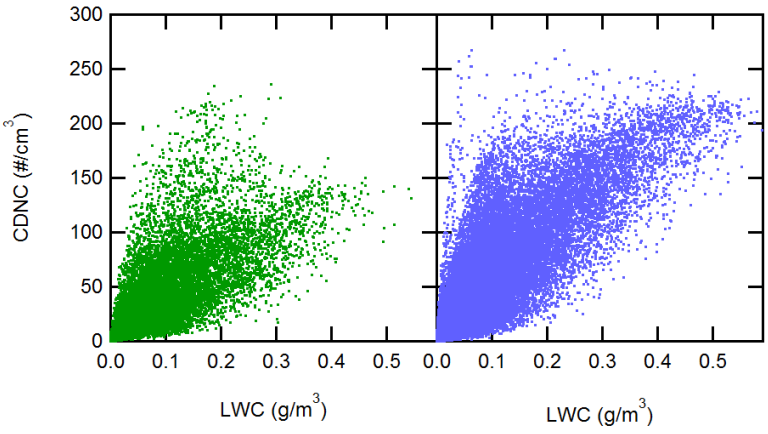

Figure 1.10: Measured CDNC and LWC correlate for the SJL01A (left) and SJL13A (right) cases.

Figure 1.11 illustrates the measured and modified distributions to show how the measured distribution was adjusted to decrease concentrations and add higher resolution at aerosol sizes close to the critical diameter in Figure 1.6. $D1_{crit}$ represents a critical diameter for κ_{org}=0.01 (the lowest simulated κ_{org} in Figure 1.6). $D2_{crit}$ represents a critical diameter for κ_{org} > 0.01.

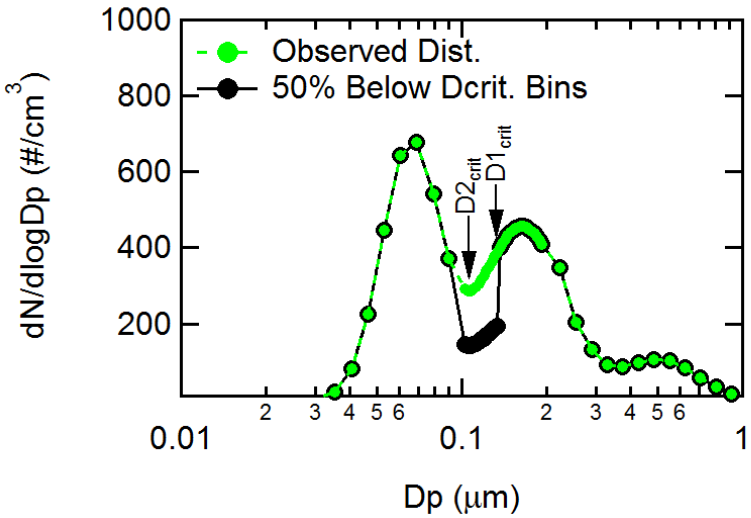

Figure 1.11: Observed aerosol size distribution for EAG10B (green). Modified aerosol size distribution for EAG10B, decreasing the concentration of aerosol below D1crit to 50% of the observed value.

1.6.3 EPEACE measured updraft velocity distribution.

Updraft velocity was measured at a frequency of 1 Hz for the EPEACE cases. Histograms of the updraft velocity are shown for each day in Figure 1.12. The measurements show a negative bias for the 16 July cases. The 10 August case has a

positive bias in updraft measurements. Both cases are consistent with the ranges observed in past observational studies [*Lenschow and Stephens*, 1980].

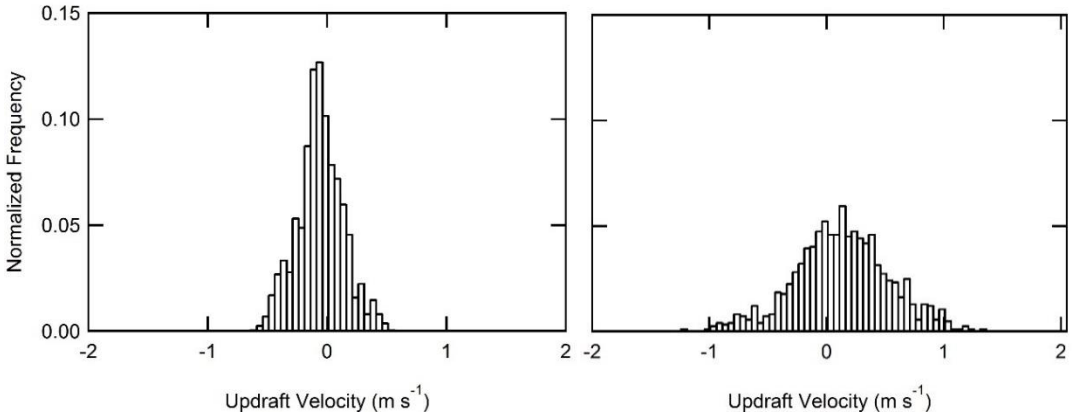

Figure 1.12: In cloud measured updraft velocity distribution for EPEACE cases on July 16 (left) and August 10 (right). Measurements were corrected for the motion of the Twin Otter aircraft. Aircraft velocity was consistent throughout horizontal legs, minimizing spatial bias. Model was initialized with updraft velocities at values > 0.05 m s^{-1}.

Table 1.8: Relevant findings from previous publications relating to vertical velocity variability in stratocumulus cloud regimes.

Publication	**Relevant Findings**
	Observations
Lenschow and Stephens [1980]	Convective thermals are found to cover 40% of area and have a large divergence in vertical velocity.
Nicholls [1989]	Variance in convective motion due to cloud top radiative cooling and entrainment mixing is similar to motion in other convective layers.
Snider and Brenguier [2000]	Positive correlation of updraft velocity and droplet concentration in level-flight traverse; larger correlation for larger CCN.
Feingold et al. [2003]	Droplet size is correlated with cloud turbulence.
[*McFiggans et al.*, [2006]	CDNC sensitivity to updraft velocity was higher for polluted conditions.
Ghate et al. [2010]	Surface buoyancy effects vertical velocity distribution skewness.
Hudson and Noble [2014]	Strong dependence of CCN on supersaturation indicates large CDNC dependency on vertical velocity.
	Modeling
Stevens et al. [1996]	Droplet diameter dispersion was explained by updraft velocities.
Rissman et al. [2004]	Composition can be more influential on CDNC than updraft velocity, in particular in clouds with higher supersaturations.
Erlick et al. [2005]	Vertical velocity fluctuations cause droplet spectrum broadening in stratocumulus due to updraft acceleration.

Table 1.8 (Continued): Relevant findings from previous publications relating to vertical velocity variability in stratocumulus cloud regimes.

Reutter et al. [2009]	Distinguished aerosol and updraft-limited regimes; changes in CDNC are more sensitive to vertical velocity than other variables.
Hsieh et al. [2009]	Observed droplet spectral widths were better represented by a distribution of updraft velocities rather than a single value.
Zhu et al. [2010]	Variance and skewness in vertical velocity can depend on internal and external forcing on the boundary layer.
Feingold et al. [2013]	Updraft variance has strong effects on autoconversion rates.
West et al. [2014]	Single characteristic velocity cannot reproduce the cloud radiative effects of a distribution of vertical velocities.
This work	Observed lapse rate and distribution of updraft velocity reproduced observed droplet spectrum for constrained case studies. Updraft distribution and lapse rate affected cloud droplet distributions more than organic hygroscopicity.

References

Allan, J. D., Topping, D. O., Good, N., Irwin, M., Flynn, M., Williams, P. I., Coe, H., Baker, A. R., Martino, M., Niedermeier, N., Wiedensohler, A., Lehmann, S., Mueller, K., Herrmann, H., and McFiggans, G.: Composition and properties of atmospheric particles in the eastern Atlantic and impacts on gas phase uptake rates, Atmospheric Chemistry and Physics, 9, 9299-9314, 2009.

Bahadur, R., Russell, L. M., Jacobson, M. Z., Prather, K., Nenes, A., Adams, P., and Seinfeld, J. H.: Importance of composition and hygroscopicity of BC particles to the effect of BC mitigation on cloud properties: Application to California conditions, Journal of Geophysical Research-Atmospheres, 117, 10.1029/2011jd017265, 2012.

Barahona, D., West, R. E. L., Stier, P., Romakkaniemi, S., Kokkola, H., and Nenes, A.: Comprehensively accounting for the effect of giant CCN in cloud activation parameterizations, Atmospheric Chemistry and Physics, 10, 2467-2473, 2010.

Betancourt, R. M., Lee, D., Oreopoulos, L., Sud, Y. C., Barahona, D., and Nenes, A.: Sensitivity of cirrus and mixed-phase clouds to the ice nuclei spectra in McRAS-AC: single column model simulations, Atmospheric Chemistry and Physics, 12, 10679-10692, 10.5194/acp-12-10679-2012, 2012.

Betancourt, R. M., and Nenes, A.: Droplet activation parameterization: the population-splitting concept revisited, Geoscientific Model Development, 7, 2345-2357, 10.5194/gmd-7-2345-2014, 2014.

Bohren, C. F., and Battan, L. J.: RADAR BACKSCATTERING BY INHOMOGENEOUS PRECIPITATION PARTICLES, Journal of the Atmospheric Sciences, 37, 1821-1827, 10.1175/1520-0469(1980)037<1821:rbbipp>2.0.co;2, 1980.

Charlson, R. J., Lovelock, J. E., Andreae, M. O., and Warren, S. G.: OCEANIC PHYTOPLANKTON, ATMOSPHERIC SULFUR, CLOUD ALBEDO AND CLIMATE, Nature, 326, 655-661, 10.1038/326655a0, 1987.

Chuang, P. Y.: Sensitivity of cloud condensation nuclei activation processes to kinetic parameters, Journal of Geophysical Research-Atmospheres, 111, 10.1029/2005jd006529, 2006.

Coggon, M. M., Sorooshian, A., Wang, Z., Metcalf, A. R., Frossard, A. A., Lin, J. J., Craven, J. S., Nenes, A., Jonsson, H. H., Russell, L. M., Flagan, R. C., and Seinfeld, J. H.: Ship impacts on the marine atmosphere: insights into the contribution of shipping emissions to the properties of marine aerosol and clouds, Atmospheric Chemistry and Physics, 12, 8439-8458, 10.5194/acp-12-8439-2012, 2012.

Collins, D. B., Ault, A. P., Moffet, R. C., Ruppel, M. J., Cuadra-Rodriguez, L. A., Guasco, T. L., Corrigan, C. E., Pedler, B. E., Azam, F., Aluwihare, L. I., Bertram, T. H., Roberts, G. C., Grassian, V. H., and Prather, K. A.: Impact of marine biogeochemistry on the chemical mixing state and cloud forming ability of nascent sea spray aerosol, Journal of Geophysical Research-Atmospheres, 118, 8553-8565, 10.1002/jgrd.50598, 2013.

Conant, W. C., VanReken, T. M., Rissman, T. A., Varutbangkul, V., Jonsson, H. H., Nenes, A., Jimenez, J. L., Delia, A. E., Bahreini, R., Roberts, G. C., Flagan, R. C., and Seinfeld, J. H.: Aerosol-cloud drop concentration closure in warm cumulus, Journal of Geophysical Research-Atmospheres, 109, 10.1029/2003jd004324, 2004.

Craven, J. P., Jewell, R. E., and Brooks, H. E.: Comparison between observed convective cloud-base heights and lifting condensation level for two different lifted parcels, Weather and Forecasting, 17, 885-890, 10.1175/1520-0434(2002)017<0885:cboccb>2.0.co;2, 2002.

Cruz, C. N., and Pandis, S. N.: A study of the ability of pure secondary organic aerosol to act as cloud condensation nuclei, Atmospheric Environment, 31, 2205-2214, 10.1016/s1352-2310(97)00054-x, 1997.

Cruz, C. N., and Pandis, S. N.: Deliquescence and hygroscopic growth of mixed inorganic-organic atmospheric aerosol, Environmental Science & Technology, 34, 4313-4319, 10.1021/es9907109, 2000.

DeCarlo, P. F., Kimmel, J. R., Trimborn, A., Northway, M. J., Jayne, J. T., Aiken, A. C., Gonin, M., Fuhrer, K., Horvath, T., Docherty, K. S., Worsnop, D. R., and Jimenez, J. L.: Field-deployable, high-resolution, time-of-flight aerosol mass spectrometer, Analytical Chemistry, 78, 8281-8289, 10.1021/ac061249n, 2006.

Dusek, U., Frank, G. P., Hildebrandt, L., Curtius, J., Schneider, J., Walter, S., Chand, D., Drewnick, F., Hings, S., Jung, D., Borrmann, S., and Andreae, M. O.: Size matters more than chemistry for cloud-nucleating ability of aerosol particles, Science, 312, 1375-1378, 10.1126/science.1125261, 2006.

Erlick, C., Khain, A., Pinsky, M., and Segal, Y.: The effect of wind velocity fluctuations on drop spectrum broadening in stratocumulus clouds, Atmospheric Research, 75, 15-45, 10.1016/j.atmosres.2004.10.007, 2005.

Ervens, B., Cubison, M. J., Andrews, E., Feingold, G., Ogren, J. A., Jimenez, J. L., Quinn, P. K., Bates, T. S., Wang, J., Zhang, Q., Coe, H., Flynn, M., and Allan, J. D.: CCN predictions using simplified assumptions of organic aerosol composition and mixing state: a synthesis from six different locations, Atmospheric Chemistry and Physics, 10, 4795-4807, 10.5194/acp-10-4795-2010, 2010.

Facchini, M. C., Rinaldi, M., Decesari, S., Carbone, C., Finessi, E., Mircea, M., Fuzzi, S., Ceburnis, D., Flanagan, R., Nilsson, E. D., de Leeuw, G., Martino, M., Woeltjen, J., and O'Dowd, C. D.: Primary submicron marine aerosol dominated by insoluble organic colloids and aggregates, Geophysical Research Letters, 35, 10.1029/2008gl034210, 2008.

Feingold, G., Eberhard, W. L., Veron, D. E., and Previdi, M.: First measurements of the Twomey indirect effect using ground-based remote sensors, Geophysical Research Letters, 30, 10.1029/2002gl016633, 2003.

Feingold, G., McComiskey, A., Rosenfeld, D., and Sorooshian, A.: On the relationship between cloud contact time and precipitation susceptibility to aerosol, Journal of Geophysical Research-Atmospheres, 118, 10544-10554, 10.1002/jgrd.50819, 2013.

Fountoukis, C., and Nenes, A.: Continued development of a cloud droplet formation parameterization for global climate models, Journal of Geophysical Research-Atmospheres, 110, 10.1029/2004jd005591, 2005.

Frossard, A. A.: Investigation of the sources and composition of submicron organic aerosol particles in marine environments through artificial generation and atmospheric measurements, Doctor of Philosophy in Oceanography, Scripps Institution of Oceanography, University of California, San Diego, La Jolla, CA, 243 pp., 2014.

Geresdi, I., Meszaros, E., and Molnar, A.: The effect of chemical composition and size distribution of aerosol particles on droplet formation and albedo of stratocumulus clouds, Atmospheric Environment, 40, 1845-1855, 10.1016/j.atmosenv.2005.11.012, 2006.

Ghate, V. P., Albrecht, B. A., and Kollias, P.: Vertical velocity structure of nonprecipitating continental boundary layer stratocumulus clouds, Journal of Geophysical Research-Atmospheres, 115, 10.1029/2009jd013091, 2010.

Gysel, M., Crosier, J., Topping, D. O., Whitehead, J. D., Bower, K. N., Cubison, M. J., Williams, P. I., Flynn, M. J., McFiggans, G. B., and Coe, H.: Closure study between chemical composition and hygroscopic growth of aerosol particles during TORCH2, Atmospheric Chemistry and Physics, 7, 6131-6144, 2007.

Hawkins, L. N., Russell, L. M., Covert, D. S., Quinn, P. K., and Bates, T. S.: Carboxylic acids, sulfates, and organosulfates in processed continental organic aerosol over the southeast Pacific Ocean during VOCALS-REx 2008, Journal of Geophysical Research-Atmospheres, 115, 10.1029/2009jd013276, 2010.

Hayden, K. L., Macdonald, A. M., Gong, W., Toom-Sauntry, D., Anlauf, K. G., Leithead, A., Li, S. M., Leaitch, W. R., and Noone, K.: Cloud processing of nitrate, Journal of Geophysical Research-Atmospheres, 113, 10.1029/2007jd009732, 2008.

Healy, R. M., Evans, G. J., Murphy, M., Juranyi, Z., Tritscher, T., Laborde, M., Weingartner, E., Gysel, M., Poulain, L., Kamilli, K. A., Wiedensohler, A., O'Connor, I. P., McGillicuddy, E., Sodeau, J. R., and Wenger, J. C.: Predicting hygroscopic growth using single particle chemical composition estimates, Journal of Geophysical Research-Atmospheres, 119, 9567-9577, 10.1002/2014jd021888, 2014.

Hegg, D. A., Covert, D. S., Jonsson, H. H., and Woods, R. K.: The contribution of anthropogenic aerosols to aerosol light-scattering and CCN activity in the California coastal zone, Atmospheric Chemistry and Physics, 10, 7341-7351, 10.5194/acp-10-7341-2010, 2010.

Hersey, S. P., Sorooshian, A., Murphy, S. M., Flagan, R. C., and Seinfeld, J. H.: Aerosol hygroscopicity in the marine atmosphere: a closure study using high-time-resolution, multiple-RH DASH-SP and size-resolved C-ToF-AMS data, Atmospheric Chemistry and Physics, 9, 2543-2554, 2009.

Hsieh, W. C., Nenes, A., Flagan, R. C., Seinfeld, J. H., Buzorius, G., and Jonsson, H.: Parameterization of cloud droplet size distributions: Comparison with parcel models and observations, Journal of Geophysical Research-Atmospheres, 114, 10.1029/2008jd011387, 2009.

Hudson, J. G., and Noble, S.: CCN and Vertical Velocity Influences on Droplet Concentrations and Supersaturations in Clean and Polluted Stratus Clouds, Journal of the Atmospheric Sciences, 71, 312-331, 10.1175/jas-d-13-086.1, 2014.

Jacobson, M. Z., Turco, R. P., Jensen, E. J., and Toon, O. B.: MODELING COAGULATION AMONG PARTICLES OF DIFFERENT COMPOSITION AND SIZE, Atmospheric Environment, 28, 1327-1338, 10.1016/1352-2310(94)90280-1, 1994.

Lance, S., Brock, C. A., Rogers, D., and Gordon, J. A.: Water droplet calibration of the Cloud Droplet Probe (CDP) and in-flight performance in liquid, ice and mixed-phase clouds during ARCPAC, Atmospheric Measurement Techniques, 3, 1683-1706, 10.5194/amt-3-1683-2010, 2010.

Leaitch, W. R., Banic, C. M., Isaac, G. A., Couture, M. D., Liu, P. S. K., Gultepe, I., Li, S. M., Kleinman, L., Daum, P. H., and MacPherson, J. I.: Physical and chemical observations in marine stratus during the 1993 North Atlantic Regional Experiment: Factors controlling cloud droplet number concentrations, Journal of Geophysical Research-Atmospheres, 101, 29123-29135, 10.1029/96jd01228, 1996.

Leaitch, W. R., Lohmann, U., Russell, L. M., Garrett, T., Shantz, N. C., Toom-Sauntry, D., Strapp, J. W., Hayden, K. L., Marshall, J., Wolde, M., Worsnop, D. R., and Jayne, J. T.: Cloud albedo increase from carbonaceous aerosol, Atmospheric Chemistry and Physics, 10, 7669-7684, 10.5194/acp-10-7669-2010, 2010.

Leck, C., and Bigg, E. K.: Source and evolution of the marine aerosol - A new perspective, Geophysical Research Letters, 32, 10.1029/2005gl023651, 2005.

Lenschow, D. H., and Stephens, P. L.: THE ROLE OF THERMALS IN THE CONVECTIVE BOUNDARY-LAYER, Boundary-Layer Meteorology, 19, 509-532, 10.1007/bf00122351, 1980.

Li, X., Wang, L., Chen, D., Yang, K., Xue, B., and Sun, L.: Near-surface air temperature lapse rates in the mainland China during 1962-2011, Journal of Geophysical Research-Atmospheres, 118, 7505-7515, 10.1002/jgrd.50553, 2013.

Massling, A., Stock, M., Wehner, B., Wu, Z. J., Hu, M., Brueggemann, E., Gnauk, T., Herrmann, H., and Wiedensohler, A.: Size segregated water uptake of the urban submicrometer aerosol in Beijing, Atmospheric Environment, 43, 1578-1589, 10.1016/j.atmosenv.2008.06.003, 2009.

McFiggans, G., Artaxo, P., Baltensperger, U., Coe, H., Facchini, M. C., Feingold, G., Fuzzi, S., Gysel, M., Laaksonen, A., Lohmann, U., Mentel, T. F., Murphy, D. M., O'Dowd, C. D., Snider, J. R., and Weingartner, E.: The effect of physical and chemical aerosol properties on warm cloud droplet activation, Atmospheric Chemistry and Physics, 6, 2593-2649, 2006.

Ming, Y., and Russell, L. M.: Organic aerosol effects on fog droplet spectra, Journal of Geophysical Research-Atmospheres, 109, 10.1029/2003jd004427, 2004.

Mochida, M., Nishita-Hara, C., Furutani, H., Miyazaki, Y., Jung, J., Kawamura, K., and Uematsu, M.: Hygroscopicity and cloud condensation nucleus activity of marine aerosol particles over the western North Pacific, Journal of Geophysical Research-Atmospheres, 116, 10.1029/2010jd014759, 2011.

Modini, R. L., Frossard, A. A., Ahlm, L., Russell, L. M., Corrigan, C. E., Roberts, G. C., Hawkins, L. N., Schroder, J. C., Bertram, A. K., Zhao, R., Lee, A. K. Y., Abbatt, J. P. D., Lin, J., Nenes, A., Wang, Z., Wonaschuetz, A., Sorooshian, A., Noone, K. J., Jonsson, H., Seinfeld, J. H., Toom-Sauntry, D., Macdonald, A. M., and Leaitch, W. R.: Primary marine aerosol-cloud interactions off the coast of California, Journal of Geophysical Research-Atmospheres, 120, 4282-4303, 10.1002/2014jd022963, 2015.

Moffet, R. C., Henn, T., Laskin, A., and Gilles, M. K.: Automated Chemical Analysis of Internally Mixed Aerosol Particles Using X-ray Spectromicroscopy at the Carbon K-Edge, Analytical Chemistry, 82, 7906-7914, 10.1021/ac1012909, 2010.

Moore, R. H., and Nenes, A.: Scanning Flow CCN Analysis-A Method for Fast Measurements of CCN Spectra, Aerosol Science and Technology, 43, 1192-1207, 10.1080/02786820903289780, 2009.

Nenes, A., Pandis, S. N., and Pilinis, C.: ISORROPIA: A new thermodynamic equilibrium model for multiphase multicomponent inorganic aerosols, Aquatic Geochemistry, 4, 123-152, 10.1023/a:1009604003981, 1998.

Nenes, A., Ghan, S., Abdul-Razzak, H., Chuang, P. Y., and Seinfeld, J. H.: Kinetic limitations on cloud droplet formation and impact on cloud albedo, Tellus Series B-Chemical and Physical Meteorology, 53, 133-149, 10.1034/j.1600-0889.2001.d01-12.x, 2001.

Nenes, A., and Seinfeld, J. H.: Parameterization of cloud droplet formation in global climate models, Journal of Geophysical Research-Atmospheres, 108, 10.1029/2002jd002911, 2003.

Nicholls, S., and Leighton, J.: AN OBSERVATIONAL STUDY OF THE STRUCTURE OF STRATIFORM CLOUD SHEETS .1. STRUCTURE, Quarterly Journal of the Royal Meteorological Society, 112, 431-460, 10.1002/qj.49711247209, 1986.

Nicholls, S.: THE STRUCTURE OF RADIATIVELY DRIVEN CONVECTION IN STRATOCUMULUS, Quarterly Journal of the Royal Meteorological Society, 115, 487-511, 10.1002/qj.49711548704, 1989.

Noone, K. J., Ogren, J. A., Heintzenberg, J., Charlson, R. J., and Covert, D. S.: DESIGN AND CALIBRATION OF A COUNTERFLOW VIRTUAL IMPACTOR FOR SAMPLING OF ATMOSPHERIC FOG AND CLOUD DROPLETS, Aerosol Science and Technology, 8, 235-244, 10.1080/02786828808959186, 1988.

Novakov, T., and Corrigan, C. E.: Cloud condensation nucleus activity of the organic component of biomass smoke particles, Geophysical Research Letters, 23, 2141-2144, 10.1029/96gl01971, 1996.

Peng, Y. R., Lohmann, U., and Leaitch, R.: Importance of vertical velocity variations in the cloud droplet nucleation process of marine stratus clouds, Journal of Geophysical Research-Atmospheres, 110, 10.1029/2004jd004922, 2005.

Petters, M. D., and Kreidenweis, S. M.: A single parameter representation of hygroscopic growth and cloud condensation nucleus activity, Atmospheric Chemistry and Physics, 7, 1961-1971, 2007.

Petters, M. D., Kreidenweis, S. M., and Ziemann, P. J.: Prediction of cloud condensation nuclei activity for organic compounds using functional group contribution methods, Geoscientific Model Development, 8, 7445-7475, 10.5194/gmdd-8-7445-2015, 2015, 2015.

Prabhakar, G., Ervens, B., Wang, Z., Maudlin, L. C., Coggon, M. M., Jonsson, H. H., Seinfeld, J. H., and Sorooshian, A.: Sources of nitrate in stratocumulus cloud water: Airborne measurements during the 2011 E-PEACE and 2013 NiCE studies, Atmospheric Environment, 97, 166-173, 10.1016/j.atmosenv.2014.08.019, 2014.

Quinn, P. K., Bates, T. S., Schulz, K. S., Coffman, D. J., Frossard, A. A., Russell, L. M., Keene, W. C., and Kieber, D. J.: Contribution of sea surface carbon pool to organic matter enrichment in sea spray aerosol, Nature Geoscience, 7, 228-232, 10.1038/ngeo2092, 2014.

Raatikainen, T., Nenes, A., Seinfeld, J. H., Morales, R., Moore, R. H., Lathem, T. L., Lance, S., Padro, L. T., Lin, J. J., Cerully, K. M., Bougiatioti, A., Cozic, J., Ruehl, C. R., Chuang, P. Y., Anderson, B. E., Flagan, R. C., Jonsson, H., Mihalopoulos, N., and Smith, J. N.: Worldwide data sets constrain the water vapor uptake coefficient in cloud formation, Proceedings of the National Academy of Sciences of the United States of America, 110, 3760-3764, 10.1073/pnas.1219591110, 2013.

Raymond, T. M., and Pandis, S. N.: Cloud activation of single-component organic aerosol particles, Journal of Geophysical Research-Atmospheres, 107, 10.1029/2002jd002159, 2002.

Reutter, P., Su, H., Trentmann, J., Simmel, M., Rose, D., Gunthe, S. S., Wernli, H., Andreae, M. O., and Poeschl, U.: Aerosol- and updraft-limited regimes of cloud droplet formation: influence of particle number, size and hygroscopicity on the activation of cloud condensation nuclei (CCN), Atmospheric Chemistry and Physics, 9, 7067-7080, 2009.

Rissman, T. A., Nenes, A., and Seinfeld, J. H.: Chemical amplification (or dampening) of the Twomey effect: Conditions derived from droplet activation theory, Journal of the Atmospheric Sciences, 61, 919-930, 10.1175/1520-0469(2004)061<0919:caodot>2.0.co;2, 2004.

Russell, L. M., and Seinfeld, J. H.: Size- and composition-resolved externally mixed aerosol model, Aerosol Science and Technology, 28, 403-416, 10.1080/02786829808965534, 1998.

Russell, L. M., Seinfeld, J. H., Flagan, R. C., Ferek, R. J., Hegg, D. A., Hobbs, P. V., Wobrock, W., Flossmann, A. I., O'Dowd, C. D., Nielsen, K. E., and Durkee, P. A.: Aerosol dynamics in ship tracks, Journal of Geophysical Research-Atmospheres, 104, 31077-31095, 10.1029/1999jd900985, 1999.

Russell, L. M., Sorooshian, A., Seinfeld, J. H., Albrecht, B. A., Nenes, A., Ahlm, L., Chen, Y.-C., Coggon, M., Craven, J. S., Flagan, R. C., Frossard, A. A., Jonsson, H., Jung, E., Lin, J. J., Metcalf, A. R., Modini, R., Muelmenstaedt, J., Roberts, G. C., Shingler, T., Song, S., Wang, Z., and Wonaschuetz, A.: EASTERN PACIFIC

EMITTED AEROSOL CLOUD EXPERIMENT, Bulletin of the American Meteorological Society, 94, 709-+, 10.1175/bams-d-12-00015.1, 2013.

Schroder, J. C., Hanna, S. J., Modini, R. L., Corrigan, A. L., Macdonald, A. M., Noone, K. J., Russell, L. M., Leaitch, W. R., and Bertram, A. K.: Size-resolved observations of refractory black carbon particles in cloud droplets at a marine boundary layer site, Atmospheric Chemistry and Physics Discussions, 14, 11447-11491, 10.5194/acpd-14-11447-2014, 2014.

Shingler, T., Dey, S., Sorooshian, A., Brechtel, F. J., Wang, Z., Metcalf, A., Coggon, M., Muelmenstaedt, J., Russell, L. M., Jonsson, H. H., and Seinfeld, J. H.: Characterisation and airborne deployment of a new counterflow virtual impactor inlet, Atmospheric Measurement Techniques, 5, 1259-1269, 10.5194/amt-5-1259-2012, 2012.

Shulman, M. L., Jacobson, M. C., Carlson, R. J., Synovec, R. E., and Young, T. E.: Dissolution behavior and surface tension effects of organic compounds in nucleating cloud droplets, Geophysical Research Letters, 23, 277-280, 10.1029/95gl03810, 1996.

Snider, J. R., and Brenguier, J. L.: Cloud condensation nuclei and cloud droplet measurements during ACE-2, Tellus Series B-Chemical and Physical Meteorology, 52, 828-842, 10.1034/j.1600-0889.2000.00044.x, 2000.

Snider, J. R., Guibert, S., Brenguier, J. L., and Putaud, J. P.: Aerosol activation in marine stratocumulus clouds: 2. Kohler and parcel theory closure studies, Journal of Geophysical Research-Atmospheres, 108, 10.1029/2002jd002692, 2003.

Sorooshian, A., Wang, Z., Coggon, M. M., Jonsson, H. H., and Ervens, B.: Observations of Sharp Oxalate Reductions in Stratocumulus Clouds at Variable Altitudes: Organic Acid and Metal Measurements During the 2011 E-PEACE Campaign, Environmental Science & Technology, 47, 7747-7756, 10.1021/es4012383, 2013.

Sorooshian, A., Crosbie, E., Maudlin, L. C., Youn, J.-S., Wang, Z., Shingler, T., Ortega, A. M., Hersey, S., and Woods, R. K.: Surface and airborne measurements of organosulfur and methanesulfonate over the western United States and coastal areas, Journal of Geophysical Research-Atmospheres, 120, 8535-8548, 10.1002/2015jd023822, 2015.

Stevens, B., Feingold, G., Cotton, W. R., and Walko, R. L.: Elements of the microphysical structure of numerically simulated nonprecipitating stratocumulus, Journal of the Atmospheric Sciences, 53, 980-1006, 10.1175/1520-0469(1996)053<0980:eotmso>2.0.co;2, 1996.

Tiitta, P., Miettinen, P., Vaattovaara, P., Joutsensaari, J., Petaja, T., Virtanen, A., Raatikainen, T., Aalto, P., Portin, H., Romakkaniemi, S., Kokkola, H., Lehtinen, K. E.

J., Kulmala, M., and Laaksonen, A.: Roadside aerosol study using hygroscopic, organic and volatility TDMAs: Characterization and mixing state, Atmospheric Environment, 44, 976-986, 10.1016/j.atmosenv.2009.06.021, 2010.

Twohy, C. H., Anderson, J. R., Toohey, D. W., Andrejczuk, M., Adams, A., Lytle, M., George, R. C., Wood, R., Saide, P., Spak, S., Zuidema, P., and Leon, D.: Impacts of aerosol particles on the microphysical and radiative properties of stratocumulus clouds over the southeast Pacific Ocean, Atmospheric Chemistry and Physics, 13, 2541-2562, 10.5194/acp-13-2541-2013, 2013.

Twomey, S.: Atmospheric Aerosols (Developments in atmospheric science), Elsevier Science Ltd, 316 pp., 1977

Tzivion, S., Feingold, G., and Levin, Z.: An efficient numerical solution to the stochastic collection equation, Journal of the Atmospheric Sciences, 44, 3139-3149, 10.1175/1520-0469(1987)044<3139:aenstt>2.0.co;2, 1987.

VanReken, T. M., Rissman, T. A., Roberts, G. C., Varutbangkul, V., Jonsson, H. H., Flagan, R. C., and Seinfeld, J. H.: Toward aerosol/cloud condensation nuclei (CCN) closure during CRYSTAL-FACE, Journal of Geophysical Research-Atmospheres, 108, 10.1029/2003jd003582, 2003.

Wang, J., Cubison, M. J., Aiken, A. C., Jimenez, J. L., and Collins, D. R.: The importance of aerosol mixing state and size-resolved composition on CCN concentration and the variation of the importance with atmospheric aging of aerosols, Atmospheric Chemistry and Physics, 10, 7267-7283, 10.5194/acp-10-7267-2010, 2010.

West, R. E. L., Stier, P., Jones, A., Johnson, C. E., Mann, G. W., Bellouin, N., Partridge, D. G., and Kipling, Z.: The importance of vertical velocity variability for estimates of the indirect aerosol effects, Atmospheric Chemistry and Physics, 14, 6369-6393, 10.5194/acp-14-6369-2014, 2014.

Wonaschuetz, A., Coggon, M., Sorooshian, A., Modini, R., Frossard, A. A., Ahlm, L., Muelmenstaedt, J., Roberts, G. C., Russell, L. M., Dey, S., Brechtel, F. J., and Seinfeld, J. H.: Hygroscopic properties of smoke-generated organic aerosol particles emitted in the marine atmosphere, Atmospheric Chemistry and Physics, 13, 9819-9835, 10.5194/acp-13-9819-2013, 2013.

Youn, J. S., Crosbie, E., Maudlin, L. C., Wang, Z., and Sorooshian, A.: *Dimethylamine* as a major alkyl amine species in particles and cloud water: Observations in semi-arid and coastal regions, in, Atmospheric Environment, 250-258, 2015.

Zhu, P., Albrecht, B. A., Ghate, V. P., and Zhu, Z.: Multiple-scale simulations of stratocumulus clouds, Journal of Geophysical Research-Atmospheres, 115, 10.1029/2010jd014400, 2010.

Chapter 2

Top-down and Bottom-up aerosol-cloud-closure: towards understanding sources of uncertainty in deriving cloud radiative flux

Top-down and bottom-up aerosol-cloud shortwave radiative flux closures were conducted at the Mace Head atmospheric research station in Galway, Ireland in August 2015. This study is part of the BACCHUS (Impact of Biogenic versus Anthropogenic emissions on Clouds and Climate: towards a Holistic UnderStanding) European collaborative project, with the goal of understanding key processes affecting aerosol-cloud shortwave radiative flux closures to improve future climate predictions and develop sustainable policies for Europe. Instrument platforms include ground-based,

unmanned aerial vehicles (UAV)[3], and satellite measurements of aerosols, clouds and meteorological variables. The ground-based and airborne measurements of aerosol size distributions and cloud condensation nuclei (CCN) concentration were used to initiate a 1D microphysical aerosol-cloud parcel model (ACPM). UAVs were equipped for a specific science mission, with an optical particle counter for aerosol distribution profiles, a cloud sensor to measure cloud extinction, or a 5-hole probe for 3D wind vectors. UAV cloud measurements are rare and have only become possible in recent years through the miniaturization of instrumentation. These are the first UAV measurements at Mace Head. ACPM simulations are compared to in-situ cloud extinction measurements from UAVs to quantify closure in terms of cloud shortwave radiative flux. Two out of seven cases exhibit sub-adiabatic vertical temperature profiles within the cloud, which suggests that entrainment processes affect cloud microphysical properties and lead to an overestimate of simulated cloud shortwave radiative flux. Including an entrainment parameterization and explicitly calculating the entrainment fraction in the ACPM simulations both improved cloud-top radiative closure. Entrainment reduced the difference between simulated and observation-derived cloud-top shortwave radiative flux (δRF) by between 25 W m^{-2} and 60 W m^{-2}. After accounting for entrainment, satellite-derived cloud droplet number concentrations (CDNC) were within 30% of simulated CDNC. In cases with a well-mixed boundary layer, δRF is no greater than 20 W m^{-2} after accounting for cloud-top entrainment, and up to 50 W m^{-2}

[3] The regulatory term for UAV is Remotely Piloted Aircraft (RPA).

when entrainment is not taken into account. In cases with a decoupled boundary layer, cloud microphysical properties are inconsistent with ground-based aerosol measurements, as expected, and δRF is as high as 88 W m^{-2}, even high (> 30 W m^{-2}) after accounting for cloud-top entrainment. This work demonstrates the need to take in-situ measurements of aerosol properties for cases where the boundary layer is decoupled as well as consider cloud-top entrainment to accurately model stratocumulus cloud radiative flux.

2.1 Introduction

One of the greatest challenges in studying cloud effects on climate are that the clouds are literally out of reach. Many ground-based measurement sites have a long historical record that are useful for identifying climatological trends, however, it is difficult to quantify such trends in cloud microphysical and radiative properties at these stations based solely on remote sensing techniques such as radar and lidar. *In-situ* aerosol measurements at the surface are often used to estimate cloud properties aloft, but the simulations used to estimate above surface conditions require many idealized assumptions such as a well-mixed boundary layer and adiabatic parcel lifting. Satellites have the advantage to infer cloud properties over a much larger area than ground-based observations; however, they can only see the upper most cloud layer and satellites need *in-situ* observations to improve their retrievals. In this study, we combine ground-based and airborne measurements with satellite observations to determine cloud radiative properties and compare these results to an aerosol-cloud parcel model (ACPM) to identify sources of uncertainty in aerosol-cloud interactions.

The atmospheric research station at Mace Head has been a research platform for studying trace gases, aerosols and meteorological variables since 1958 [*O'Connor et al.*, 2008]. The station is uniquely exposed to a variety of air masses, such as clean marine air and polluted European air. Over the long history of observations and numerous field-campaigns held at the Mace Head research station, few airborne field experiments have been conducted. During the PARFORCE campaign in September 1998, aerosol and trace gas measurements were made to map coastal aerosol formation [*C D O'Dowd et*

al., 2001]. During the second PARFORCE campaign in June 1999, measurements of sea spray plumes were made on an aircraft installed with a Lidar [*Kunz et al.*, 2002]. In the NAMBLEX campaign in August 2002, flights were conducted to measure aerosol chemical and physical properties in the vicinity of Mace Head [*Coe et al.*, 2006; *Heard et al.*, 2006; *Norton et al.*, 2006]None of the research flights thus far have studied aerosol-cloud interactions and cloud radiative properties at Mace Head.

For ground-based observations, it is often assumed that measured species are well-mixed throughout the boundary layer. Often this assumption is valid and many observational studies have shown that models which use ground-based measurements can accurately simulated cloud droplet number concentrations (CDNC) [*Conant et al.*, 2004; *Fountoukis et al.*, 2007; *Russell and Seinfeld*, 1998], making bottom-up closure a viable method for predicting cloud properties. Closure is defined here as the agreement between observations and model simulations of CDNC and cloud-top shortwave radiative flux. This well-mixed boundary layer simplification, however, has been shown to be inaccurate in many field experiments (e.g., the Atlantic Stratocumulus Transition Experiment (ASTEX) [*Albrecht et al.*, 1995]; and the Aerosol Characterization Experiments, ACE1 [*Bates et al.*, 1998] and ACE2 [*Raes et al.*, 2000]. Previous studies at Mace Head have shown that decoupled boundary layers were observed with scanning backscatter lidar measurements [*Kunz et al.*, 2002; *Milroy et al.*, 2012]. Such decoupled layers often contain two distinct cloud layers, distinguished as a lower layer within the well-mixed surface-mixed layer and a higher decoupled layer between the free troposphere and surface-mixed layer [*Kunz et al.*, 2002; *Milroy et al.*, 2012; *Stull*, 1988].

General characteristics associated with decoupled boundary layers are a weak inversion, a decrease in aerosol concentration relative to the surface-mixed layer, and more commonly occurring in relatively deep marine boundary layers (> 1400 m) [*Jones et al.,* 2011]. Dall'Osto et al [2010] showed the average height of the surface-mixed layer, over Mace Head, varies from 500 m to 2000 m, and the decoupled layers have heights ranging from 1500 m to 2500 m. Marine boundary layer decoupling is often seen in the tropics and has been attributed to processes that involve cloud heating from cloud-top entrainment, leading to decoupling of the boundary layer [*Albrecht et al.,* 1995; *Bates et al.*, 1998; *Bretherton et al.*, 1997; *Stevens*, 2002; *Zhou et al.*, 2015]. In addition, Bretherton and Wyant [1997] have shown that the decoupling structure is mainly driven by a high latent heat flux that results in a large buoyancy jump across the cloud base. This high latent heat flux is attributed to easterlies bringing air over increasing SST, where the boundary layer becomes deeper and more likely to decouple [*Albrecht et al.*, 1995]. The cloud layer drives the turbulent motion and a zone of negative buoyancy flux develops below cloud. The turbulent motion is driven by radiative cooling at cloud top, causing air to sink [*Lilly*, 1968]. The zone of negative buoyancy exists because the deepening of the boundary layer causes the lifting condensation level of the updraft and downdraft to separate. This is important because latent heating in the cloud contributes significantly to the buoyancy in the cloud [*Schubert et al.,* 1979]. If this zone of negative buoyancy flux becomes deep enough, it is dynamically favorable for the cloud layer to become decoupled from the cloud layer [*Bretherton et al.*, 1997]. Bretherton and Wyant [1997] also show that drizzle can have a substantial impact on enhancing the negative

buoyancy flux below cloud, but drizzle is not necessary for decoupling mechanism they proposed. Other factors, such as the vertical distribution of radiative cooling in the cloud, and sensible heat fluxes, play less important roles. Turton and Nicholls [1987] used a two-layer model to show that decoupling can also result from solar heating of the cloud layer; however, only during the day. Furthermore, Nicholls and Leighton [1986] showed observations of decoupled clouds with cloud-top radiative cooling and the resulting in-cloud eddies do not mix down to the surface (further suggesting radiative cooling plays a less important role). Russell et al. [1998] and Sollazzo et al. [2000] showed that, in a decoupled atmosphere the two distinct layers have similar characteristics (e.g., aerosol and trace gases composition), with different aerosol concentrations that gradually mix with each other, mixing air from the surface-mixed layer into the decoupled layer and vice versa. These previous studies also show that aerosol concentrations in the decoupled layer are lower than those in the surface-mixed layer implying an overestimation in cloud shortwave radiative flux when using ground-based aerosol measurements.

Satellite measurements of microphysical properties, such as CDNC, have the potential to be independent of ground-based measurements, and therefore be reliable for studying decoupled clouds. Satellite estimates of CDNC have only become possible recently due to the increased resolution in measurements [*Painemal and Zuidema*, 2011; *Rosenfeld et al.*, 2014; *Rosenfeld et al.*, 2012; *Rosenfeld et al.*, 2016]. Therefore, current measurements still require ground-based validation until the method is further developed.

The focus of this manuscript is on the top-down closure between satellite retrievals and airborne measurements of cloud microphysical properties, as well as, traditional bottom-up closure coupling below and in-cloud measurements of cloud condensation nuclei (CCN), updraft, and cloud microphysical properties. *In-situ* measurements of CDNC are not available so bottom-up closure is expressed in terms of cloud-top shortwave radiative flux rather than CDNC and top-down closure of satellite CDNC is compared to ACPM simulated CDNC. The methods section describes how observations were collected, as well as the methods for estimating CDNC with satellite measurements and calculating shortwave radiative flux with the ACPM. The results section summarizes the bottom-up and top-down closure for coupled and decoupled clouds and quantifies the differences in cloud shortwave radiative flux for cases that were affected by cloud-top entrainment.

2.2 Methods

The August 2015 campaign at the Mace Head research station (Galway, Ireland; 53.33ºN, 9.90ºW) focused on aerosol-cloud interactions at the north eastern Atlantic Ocean by coupling ground-based *in-situ* and remote sensing observations with airborne and satellite observations. This section summarizes the measurements used for this study and the model used to simulate the observations.

2.2.1 Ground-based measurements

At the Mace Head research site, aerosol instruments are located in the laboratory at about 100 m from the coastline. They are connected to the laminar flow community air sampling system, which is constructed from a 100 mm diameter stainless-steel pipe with the main inlet at 10 m above ground level, so that samples are not impacted by immediate coastal aerosol production mechanisms, such as wave breaking and biological activity [*Coe et al.*, 2006; *Norton et al.*, 2006; *C O'Dowd et al.*, 2014; *C D O'Dowd et al.*, 2004; *Rinaldi et al.*, 2009]. The performance of this inlet is described in Kleefeld et al.[2002]. Back trajectories during the period of the experiment show that the origin of air masses is predominantly from the North Atlantic; therefore, the air masses sampled at Mace Head generally represent clean open ocean marine aerosol. Mace Head contains a variety of aerosol sampling instrumentation, spanning particle diameter range of 0.02 μm and 20 μm. Size spectral measurements are performed at a relative humidity < 40% using Nafion driers. Supermicron particle size distributions were measured using an Aerodynamic Particle Sizer (APS, TSI model 3321, 0.5 < Dp < 20 μm). The remaining submicron aerosol size range was retrieved from a scanning mobility particle sizer (SMPS, 0.02 < Dp <0.5 μm), comprised of a differential mobility analyzer (DMA, TSI model 3071), a condensation particle counter (TSI model 3010, Dp > 10 nm), and a Kr-85 aerosol neutralizer (TSI 3077). Cloud condensation nuclei (CCN) measurements were performed with a miniature Continuous Flow Stream-wise Thermal Gradient Chamber, which measures the concentration of activated CCN over a range of supersaturations [*Roberts and Nenes*, 2005]. During this study, the

supersaturation range spanned 0.2% to 0.82%. Aerosol hygroscopicity was calculated using κ-Köhler theory [*Petters and Kreidenweis*, 2007] with the sampled CCN concentrations at a particular supersaturation and corresponding integrated aerosol number concentration at a critical diameter [*Roberts et al.*, 2001]. Figure 2.1 shows time series of CCN spectra and aerosol number size distributions throughout the campaign. The ground-based remote sensing measurements utilized in this study are the MIRA36, 35.5 GHz Ka-band Doppler cloud radar [*Goersdorf et al.*, 2015; *Melchionna et al.*, 2008] to obtain vertical velocity distributions at cloud-base and the Jenoptik CHM15K ceilometer [*Heese et al.*, 2010; *Martucci et al.*, 2010] to obtain cloud base height.

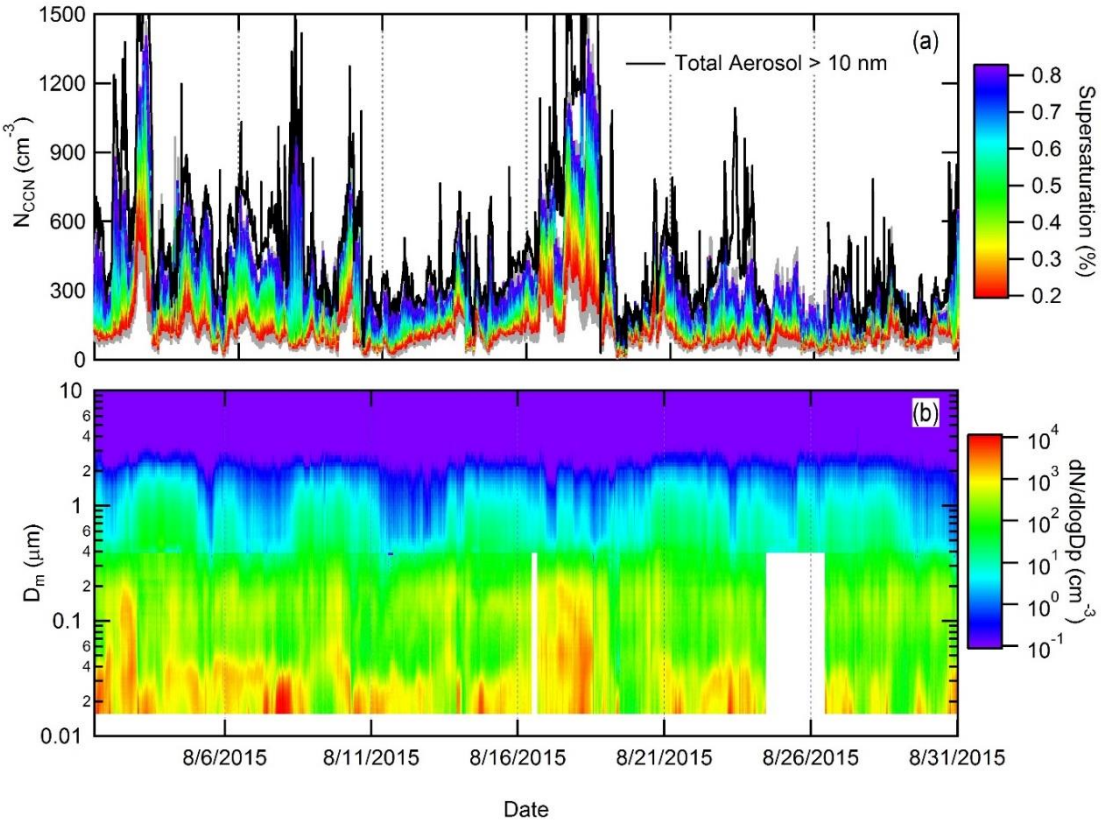

Figure 2.1: Time series for the month of August 2015 at Mace Head Ireland of ground-based CCN concentrations (top) and merged SMPS and APS number size distributions (bottom).

Table 2.1: UAV research flights conducted at Mace Head, Ireland and measured parameters in 2015. Flight start and end times are in UTC. Suomi NASA Polar-orbiting Partnership satellite overpasses occurred at approximately 13:00 UTC. Measurements include relative humidity (RH), temperature (T), pressure (P), 3-dimensional wind vectors (3D Winds), optical particle counter (OPC) and cloud sensor measurements of cloud droplet extinction.

Date	Flight	Start Time	End Time	RH	T	P	3D Winds	OPC	Cloud
30-Jul	4	12:41	13:19	x	x	x		x	
30-Jul	5	14:00	14:44	x	x	x			x
30-Jul	6	16:04	16:42	x	x	x		x	
01-Aug	7	11:30	12:13	x	x	x		x	
01-Aug	8	12:35	13:16	x	x	x			x
01-Aug	9	14:00	15:20	x	x	x	x		
01-Aug	10	15:54	16:43	x	x	x		x	
05-Aug	11	11:47	12:29	x	x	x			x
05-Aug	13	13:36	14:26	x	x	x	x		
05-Aug	14	14:42	15:29	x	x	x			x
06-Aug	16	11:55	12:37	x	x	x			x
06-Aug	17	13:51	15:16	x	x	x	x		
10-Aug	19	13:41	14:10	x	x	x			x
10-Aug	20	14:42	15:45	x	x	x	x		
10-Aug	21	16:00	16:45	x	x	x			x
11-Aug	23	12:00	12:47	x	x	x			x
11-Aug	24	13:11	14:05		x	x	x		
11-Aug	25	14:25	15:10	x	x	x			x
11-Aug	26	15:29	16:22		x	x	x		
11-Aug	27	16:58	17:33		x	x		x	
15-Aug	29	12:19	13:03	x	x	x		x	
15-Aug	30	13:46	14:31		x	x	x		
15-Aug	31	15:08	16:14	x	x	x			x
16-Aug	32	12:30	13:20	x	x	x		x	
16-Aug	33	13:40	14:00	x	x	x		x	
17-Aug	34	11:30	12:24	x	x	x			x
17-Aug	35	13:45	14:34	x	x	x		x	
21-Aug	36	12:21	13:12		x	x		x	
21-Aug	37	13:40	14:25	x	x	x			x
21-Aug	38	15:17	16:26	x	x	x	x		
21-Aug	39	16:53	17:27	x	x	x			x
22-Aug	40	9:29	10:12	x	x	x			x
22-Aug	41	10:47	11:37	x	x	x		x	
22-Aug	42	12:52	13:53	x	x	x	x		
22-Aug	43	14:22	14:59	x	x	x		x	
27-Aug	45	10:21	11:10	x	x	x		x	
27-Aug	46	11:27	12:13	x	x	x			x
27-Aug	47	13:11	13:45			x			x
27-Aug	48	15:09	15:23	x	x	x	x		
27-Aug	49	17:20	17:50	x	x	x		x	
28-Aug	50	14:25	14:49	x	x	x		x	

2.2.2 UAV vertical profiles

The UAV operations were conducted directly on the coast about 200 meters from the Mace Head research station. UAVs were used to collect vertical profiles of standard meteorological variables, temperature (IST, Model P1K0.161.6W.Y.010), pressure (Bs rep Gmbh, Model 15PSI-A-HGRADE-SMINI), and relative humidity (IST, P14 Rapid-W), as well as aerosol size distributions with an optical particle counter (OPC, Met One Model 212-2), cloud droplet extinction [*Harrison and Nicoll*, 2014], updraft velocity at cloud base with a 5-hole probe. A list of the various UAV flights and their instrumentation is given in Table 2.1. Measurement errors for the relative humidity and temperature sensors are ± 5% and ± 0.5 ºC respectively. As RH sensors are not accurate at high RH (> 90%), the measured values have been scaled such that RH measurements are 100% in a cloud. At altitudes where the UAV is known to be in-cloud (based on *in-situ* cloud extinction measurements) the air mass is considered saturated (RH ~ 100%). The temperature and relative humidity sensors are protected from solar radiative heating by a thin-walled aluminum shroud positioned outside of the surface layer of the UAV. A helical cone, mounted in front of the sensors, ejects droplets to protect the sensors. The temperature measurements for both cases in which cloud-top entrainment is explored (see section 2.3.2) are verified to remain in stratocumulus clouds throughout the ascents and descents, and are not affected by evaporative cooling. The temperature and relative humidity measurements were used to initialize the ACPM below cloud. The UAVs were flown individually in separate

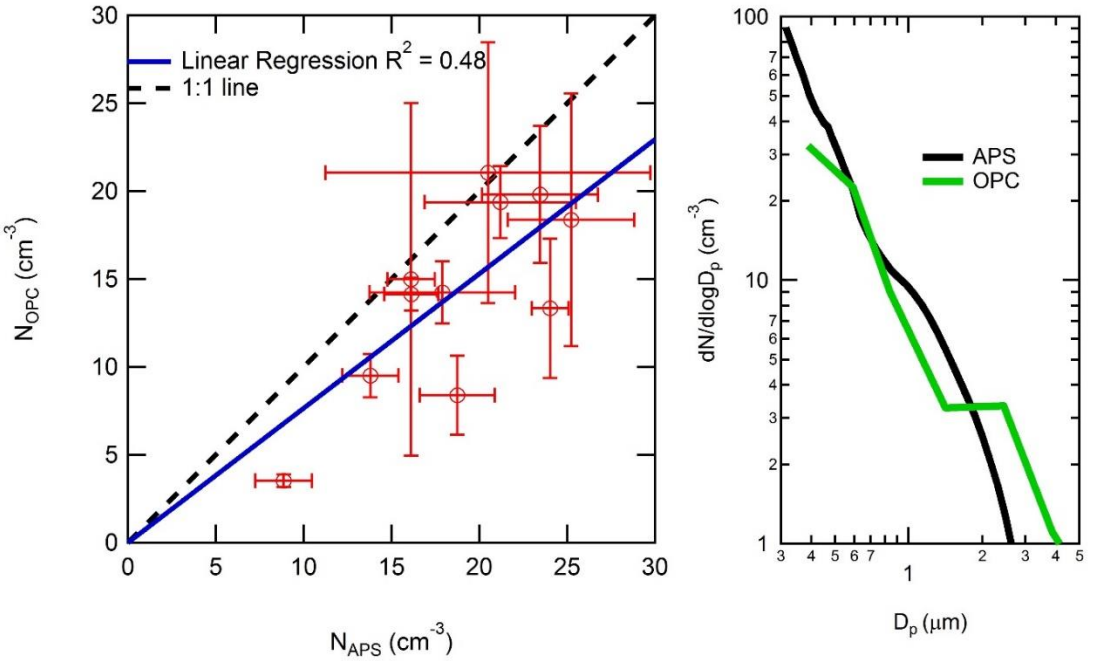

Figure 2.2: OPC concentrations with particle diameters (Dp) greater than 0.3 um (left) from 11 UAV research flights, listed in Table 2.1, plotted against APS concentrations (Dp > 0.3 um) at Mace Head Research Station (red circles). Error bars represent ±1 standard deviation. The points are fit with a linear regression (blue line). OPC data was averaged between 40 and 80 m asl. Averaged OPC and APS number size distributions averaged for the 11 flights (right).

missions up to 1.5 hours and each UAV was instrumented to perform a specific science mission (referred to here as aerosol, cloud, 3D winds).

The OPC measured aerosol number size distributions in eight size bins between 0.3 and 10 µm diameter. Aerosols were sampled via a quasi-isokinetic shrouded inlet mounted on the nose of the UAV. Aerosols samples were heated upon entering the UAV ($\Delta T > 5$ K due to internal heating by the electronics), reducing the relative humidity of the sampled air to less than 60% and decreased with height (< 50% above 150 m) before aerosol size was measured. Figure 2.2 shows a two-instrument

redundancy cross check between ground-based APS and UAV OPC measurements (collected between 40 m agl and 80 m agl) of aerosol sizes are in agreement ($r^2 = 0.48$).

In-cloud extinction was measured in-situ using a miniature optical cloud droplet sensor developed at the University of Reading [*Harrison and Nicoll*, 2014]. The sensor operates by a backscatter principle using modulated LED light which is backscattered into a central photodiode. Comparison of the sensor with a Cloud Droplet Probe (DMT) demonstrate good agreement for cloud droplet diameters >5µm [*Nicoll et al.*, 2016]. The extinction measurements were used to calculate cloud-top shortwave radiative flux and is further discussed in section 2.2.4.

Finally, a 5-hole probe for measuring 3-dimentional wind vectors was mounted on a third UAV. The 3D wind vectors are determined by subtracting the UAV motion given by an inertial measurement unit (IMU) from the total measured flow obtained by differential pressures in the 5-hole probe [*Calmer et al.*, 2017; *Lenschow and Spyers-Duran*, 1989; *Wildmann et al.*, 2014]. UAV 5-hole probe measurements were collected along 6 km long straight and level legs at cloud base. Normalized cloud radar vertical velocity distributions are compared to vertical wind distributions obtained from the UAV in Figure 2.3. The positive updraft velocities in Figure 2.3 are used to initialize the ACPM to produce simulated cloud droplet size distributions throughout the depth of the cloud. The droplet distributions for each updraft velocity are averaged and weighted by the probability distribution of the measured positive velocities. Differences in results when using the cloud radar updrafts versus the UAV 5-hole probe updrafts (Figure 2.3) are discussed in section 2.3.1.2.

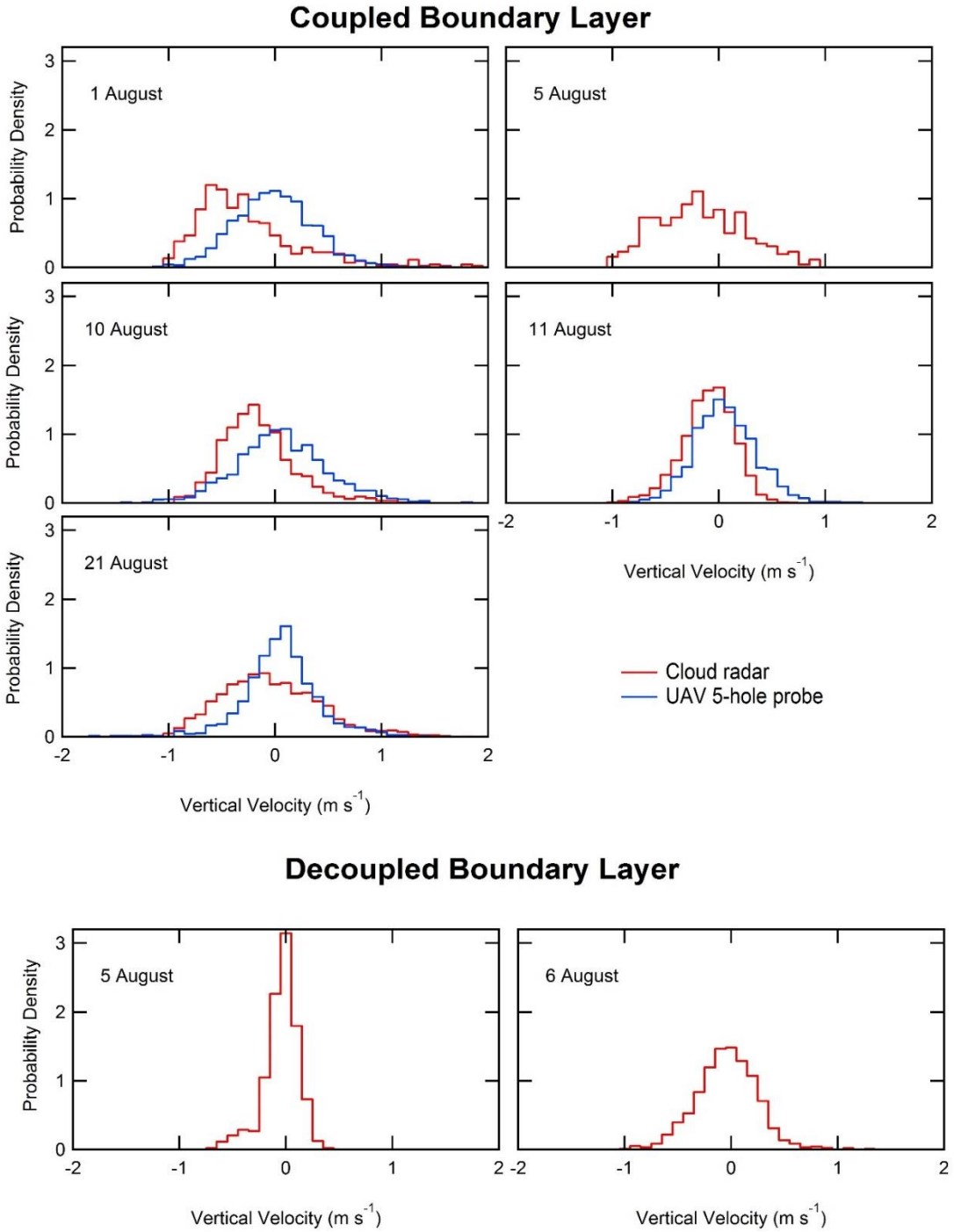

Figure 2.3: Normalized observed vertical velocity distributions measured by the cloud radar and UAV for each case presented in Table 2.2.

2.2.3 Satellite measurements

Research flights with the UAV were conducted in conjunction with satellite overpasses to compare retrieved CDNC and maximum supersaturation (S_{max}) with ACPM simulated values using the Suomi NASA Polar-orbiting Partnership satellite. The satellite estimations of CDNC and S_{max} are based on methods described by Rosenfeld et al.[2014; 2012; 2016], which are briefly summarized in the following paragraph. The case selection criteria for satellite observations required the overpass to occur at a zenith angle between 0º and 45º to the east of the ground track, to have convective development that spans at least 6 K of cloud temperature from base to top (~1 km thick), and to not precipitate significantly. In-situ observations were often of thin clouds (< 1 km thick), and the satellite observations consist primarily of the more developed clouds in the same system.

To obtain CDNC, cloud droplet effective radius profiles were extracted from the Suomi NASA Polar-orbiting Partnership satellite. Figure 2.4 shows an image from the Suomi visible infrared imaging radiometer suite on 21 August overlapped on a map of western Ireland. The vertical profile in figure 2.4 shows satellite retrieved and ACPM simulated effective radius. To estimate the CDNC, the satellite effective radius (Figure 2.4) is first converted to mean volume radius (r_v) using a linear relationship [*Freud et al.*, 2011]. Next, it is assumed that any mixing that occurred between the cloud and cloud-free air was inhomogeneous; this implies that the actual r_v is equal to the adiabatic r_v. CDNC can be calculated by dividing the adiabatic water content in the cloud by r_v [*Beals et al.*, 2015; *Rosenfeld et al.*, 2012]. The cloud base height and pressure was used

to calculate the adiabatic water content. Cloud base height and pressure were obtained from the height of the NCEP reanalysis of the cloud base temperature, as retrieved from satellite. The cloud base height was validated against the ceilometer. Freud et al. [2011] showed that the inhomogeneous assumption resulted in an average over-estimate in CDNC of 30%, so the CDNC is reduced by 30% to account for the bias with the assumption. Finally, to calculate S_{max} the cloud base updraft velocity, from the UAV or cloud radar, is needed and when paired with the CDNC, it can be used to empirically calculate S_{max} [*Pinsky et al.*, 2012; *Rosenfeld et al.*, 2012]. The methodology was validated by Rosenfeld et al. [2016].

2.2.4 Aerosol-cloud parcel model simulations

A detailed description of the aerosol-cloud parcel model (ACPM) is presented in Russell and Seinfeld [1998] and Russell et al. [1999]. The ACPM is based on a fixed-sectional approach to represent the (dry) particle size domain, with internally mixed chemical components. Aerosols are generally internally mixed at Mace Head because there were no immediate strong sources of pollution. The model employs a dual moment (number and mass) algorithm to calculate particle growth from one size section to the next for non-evaporating compounds (namely, all components other than water) using an accommodation coefficient of 1.0 [*Raatikainen et al.*, 2013]. The dual moment method is based on Tzivion et al. [1987] to allow accurate accounting of both aerosol number and mass, and incorporates independent calculations of the change in particle number and mass for all processes other than growth. The model includes a dynamic scheme for activation of particles to cloud droplets. Liquid water is treated in a moving

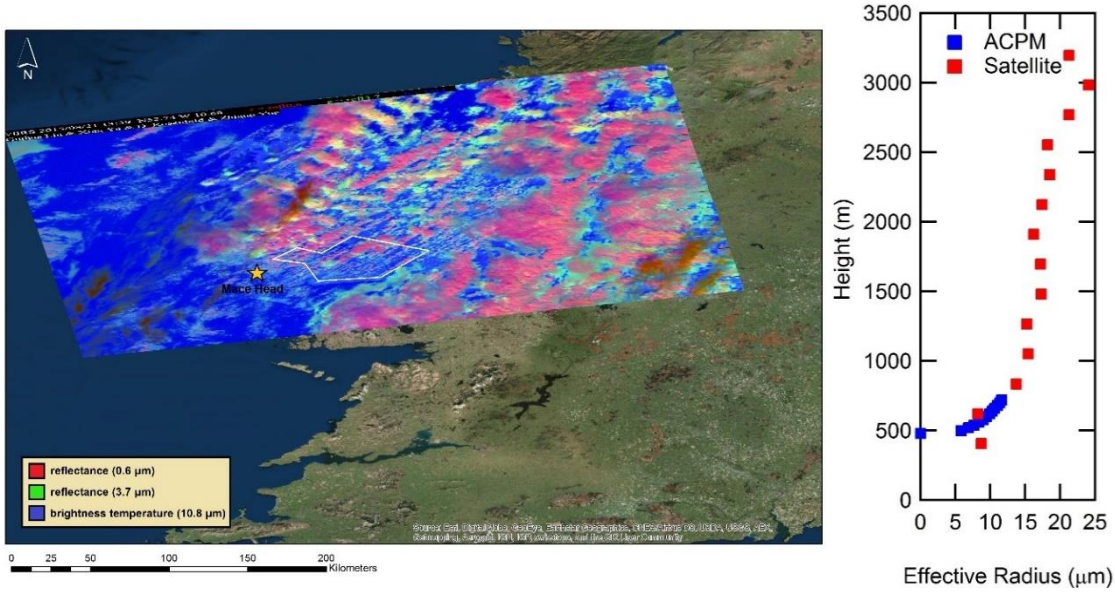

Figure 2.4: Suomi NPP satellite RGB composite image for 21 August 2015 (left). Mace Head Research Station and UAV flight location are indicated by the yellow star. The white polygon represents the zone for retrieving cloud properties – which is represented by the profile of cloud effective radius (right). Effective radius profiles are presented for both the Suomi NPP satellite (red) and the ACPM (blue).

section representation, similar to the approach of Jacobson et al. [1994], to account for evaporation and condensation of water in conditions of varying humidity. In sub-saturated conditions, aerosol particles below the cloud base are considered to be in local equilibrium with water vapor pressure (i.e., relatively humidity < 100%).

Coagulation, scavenging, and deposition of the aerosol were included in the model but their effects are negligible given the relatively short simulations used here (<2 h) and low marine total aerosol particle concentrations (<500 cm3; Dp > 10 nm). Feingold et al. [2013] showed that autoconversion and accretion rates are negligible for the simulated values of LWC and CDNC except for the C21Cu case, which had LWC

> 1 g m^{-3}. Thus, droplet number loss by collision coalescence can be neglected for all cases except for the C21Cu case. Aerosol hygroscopicity as a function of size (and supersaturation) is determined from CCN spectra and aerosol size distributions as mentioned in Section 2.3.1, and is used as model input. The ACPM is also constrained by measured temperature profiles, cloud base height, and updraft velocity distribution (Figure 2.3). The in-cloud lapse rate is assumed to be adiabatic, unless specified otherwise, so simulation results represent an upper bound on CDNC and liquid water content that is unaffected by entrainment. To account for release of latent heat in the cloud, the vertical temperature gradient is calculated as $dT = -(gwdt + Ldq_l)/c_p$, where *dT* is change in temperature for the vertical displacement of an air parcel, g is acceleration due to gravity, *w* is updraft velocity at cloud base, *dt* is time step, *L* is latent heat of water condensation, q_l is liquid water mixing ratio, and c_p is specific heat of water [*Bahadur et al.*, 2012]. A weighted ensemble of positive updraft velocities measured with the cloud radar and UAV 5-hole probe were applied to the ACPM [*Sanchez et al.*, 2016].

The simulated cloud droplet size distribution is used to calculate the shortwave cloud extinction. Cloud extinction is proportional to the total droplet surface area [*Hansen and Travis*, 1974; *Stephens*, 1978] and is calculated from,

$$\sigma_{ext} = \int_0^\infty Q_{ext}(r)\pi r^2 n(r)\, dr \qquad (2.1)$$

where r is the radius of the cloud droplet, $n(r)$ is the number of cloud droplets with a radius of r, and $Q_{ext}(r)$ is the Mie efficiency factor, which asymptotically approaches 2 for water droplets at large sizes (r > 2 um).

Finally, the shortwave radiative flux (RF) is calculated as RF = αQ, where Q is the daily-average insolation at Mace Head and α is the cloud albedo. α is estimated using the following equation [*Bohren and Battan*, 1980; *Geresdi et al.*, 2006]

$$\alpha = \frac{(\sqrt{3}(1-g)\tau)}{(2+\sqrt{3}(1-g)\tau)}; \quad (2.2)$$

where τ is the cloud optical depth defined as

$$\tau = \int_0^H \sigma_{ext}(h)\, dh; \quad (2.3)$$

and H is the cloud height or thickness and g, the asymmetric scattering parameter, is approximated as 0.85 based on Mie scattering calculations for supermicron cloud drops. RF is calculated for both, simulated cloud extinction and measured UAV extinction.

2.3 Results/Discussion

2.3.1 Closure of CDNC and cloud-top shortwave radiative flux

For this study, closure is defined as the agreement between observations and model simulations of CDNC and cloud-top shortwave radiative flux. In-situ measurements of clouds were made by UAVs on 13 days during the campaign. Of these, a subset of six are chosen here for further analysis, which includes comparison with satellite CDNC as well as simulation of cloud properties with the ACPM (Table 2.2). The remaining days with UAV measurements did not contain sufficient cloud measurements for analysis. A satellite overpass occurred on each of the six days, however only 4 of the days contained clouds that were thick enough to analyze with the satellite. The 10 August cases experienced a light drizzle, so ACPM simulations were not conducted for this case, however analysis with satellite imagery was still conducted.

On 5 August, two cloud layers were examined, for a total of 7 case studies shown in Table 2.2. Aerosols were occasionally influenced by anthropogenic sources, however, the cases shown consist of aerosol of marine origin with concentrations under 1000 cm^{-3} (Figure 2.1).

2.3.1.1 Ground-based measurement closure

The columns in Table 2.2 represent the different cases for both clouds that were (a) coupled with and (b) decoupled from the surface BL ("C" and "D" in case acronym, respectively). The first row in Table 2.2 includes the state of atmospheric mixing, the date, the type of cloud present, and the acronym used for each case. The top portion of Table 2.2 consists of *in-situ* airborne measurements, the bottom portion presents ACPM simulation results and their relation to *in-situ* cloud extinction and satellite-retrieved observations. The ground-based *in-situ* measurements in Table 2.2 include the Hoppel minimum diameter[4] (D_{min}), as well as the aerosol concentration of aerosol with diameters greater than the Hoppel D_{min} and the inferred in-cloud critical supersaturation (S_c) [*Hoppel*, 1979]. The dry aerosol particles with diameters greater than the Hoppel D_{min} have undergone cloud processing and are used here to estimate the CDNC. For each of the case study days, Figure 2.5 demonstrates the aerosol size distribution measurements, from the SMPS and APS, that are used to find the Hoppel D_{min}, Hoppel CDNC and used to initialize the ACPM. The Hoppel CDNC is calculated by integrating the SMPS and APS combined size distributions for aerosol sizes greater than Hoppel

[4] The Hoppel minimum diameter is the diameter with the lowest aerosol concentration between Aitken mode and accumulation mode.

Table 2.2: UAV observations of cloud heights and temperatures and cloud property estimates based on ground measurements. Ground-based Hoppel minimum diameter (D_{min}) is used to estimate CDNC. ACPM simulation and satellite results are also presented, as well as differences between simulated and observation-derived cloud-top extinction and cloud-top radiative flux. Case abbreviations include if they are coupled (C) or decoupled (D), the day of the month and cloud types, cumulus (Cu) or stratocumulus (Sc).

	Coupled BL					Decoupled BL	
	01Aug Cumulus (C01Cu)[a]	**05 Aug Cumulus (C05Cu)**	**10 Aug[b] Cumulus (C10Cu)**	**11 Aug[c] StratoCu (C11Sc)**	**21 Aug[d] Cumulus (C21Cu)**	**05 Aug[c] StratoCu (D05Sc)**	**06 Aug Cumulus (D06Cu)**
	***In-situ* Ground-based and UAV Measurements**						
Cloud-base height (m)	800	430	650	1200	460	1490	2180
Cloud-base temperature (ºC)	7.4 ±0.1	10.6 ±0.2	8.1 ±0.1	3.7 ±0.1	10.4 ±0.1	6.5 ±0.2	-2.1 ±0.2
Cloud-top height (m)	1040	710	1720	1460	960	1630	2400
Cloud-top temperature (ºC)	5.7 ±0.1	8.7 ±0.2	1.8 ±0.1	2.4 ±0.2	7.6 ±0.1	5.8 ±0.2	-3.1 ±0.4
Measured lapse rate in-cloud (K km^{-1})	5.7	6.1	5.1	4.7	6.0	4.1	6.3
Number of cloud layers	1	2[g]	1	1	1	2[h]	2[h]
Hoppel D_{min} (nm)	74 ±6	78 ±16	73 ±8	83 ±7	83 ±5	78 ±16	80 ±9
Hoppel D_{min} CDNC (> Hoppel D_{min}, cm^{-3})	129 ±5	69 ±8	105 ±11	87 ±5	94 ±12	69 ±8	164 ±13
Measured cloud τ	-	11.7	-	8.3	29.1	1.3	4.9
Hoppel minimum critical supersaturation (S_{crit})	0.43 ±0.03	0.61 ±0.10	0.37 ±0.11	0.37 ±0.05	0.41 ±0.10	0.61 ±0.10	0.31 ±0.06
	ACPM Simulation and Satellite-derived Cloud Properties[e]						
Simulated moist adiabatic lapse rate (K km^{-1})	5.0	4.5	4.9	5.7	4.5	5.1	6.4
Simulated cloud-top droplet r_e (μm)	10.3 ±0.1	14.4±0.3	-	11.3 ±0.2	14.2 ±0.4	10.0 ±0.1	8.2 ±0.2
Simulated cloud τ	-	13.2 ±1.9	-	18.7 ±2.7	42.1 ±11.2	4.4 ±0.5	9.0 ±1.1
Cloud-top extinction difference ($\delta\sigma_{ext}$, km^{-1})	-	11 ±25	-	36 ±12	52 ±42	37 ±6	34 ±7
Cloud-top shortwave radiative flux difference (δRF, W m^{-2})[f]	-	11 ±26	-	48 ±11	20 ±6	88 ±8	74±12
Simulated CDNC (cm^{-3})	135 ±16	60 ±12	105 ±18	88 ±12	105 ±31	86 ±10	171 ±17
Satellite estimated CDNC (cm^{-3})	109	-	85	58 (83)[i]	104	-	-
Simulated S_{max} (%)	0.45 ±0.09	0.45 ±0.18	0.36 ±0.15	0.36 ±0.09	0.40 ±0.20	0.76 ±0.04	0.33 ±0.06
Satellite estimated S_{max} (%)	0.34	-	0.27	0.48	0.34	-	-

[a] C/D – coupled / decoupled; xx – date in August 2015; Sc / Cu – stratocumulus / cumulus cloud

[b] Precipitation occurred on 10 Aug.

[c] Accounting for entrainment improves model / measurement closure (Table 2).

[d] The C21Cu case is susceptible to droplet coalescence due to it's high liquid water content (Feingold et al., 2013) .

[e] The error includes the potential error of ±20% in updraft velocity and the standard error of the CCN concentration measurements.

[f] The difference between the observed (calculated from UAV extinction measurements) and simulated radiative flux. The error includes the potential error of ±20% in updraft velocity and the standard error of the CCN concentration measurements.

[g] The measurements and results in this column represent the lower of the two clouds.

[h] Altitude of top cloud level that is used to calculate cloud radiative flux.

[i] Excluding the correction for the inhomogeneous entrainment assumption in parentheses

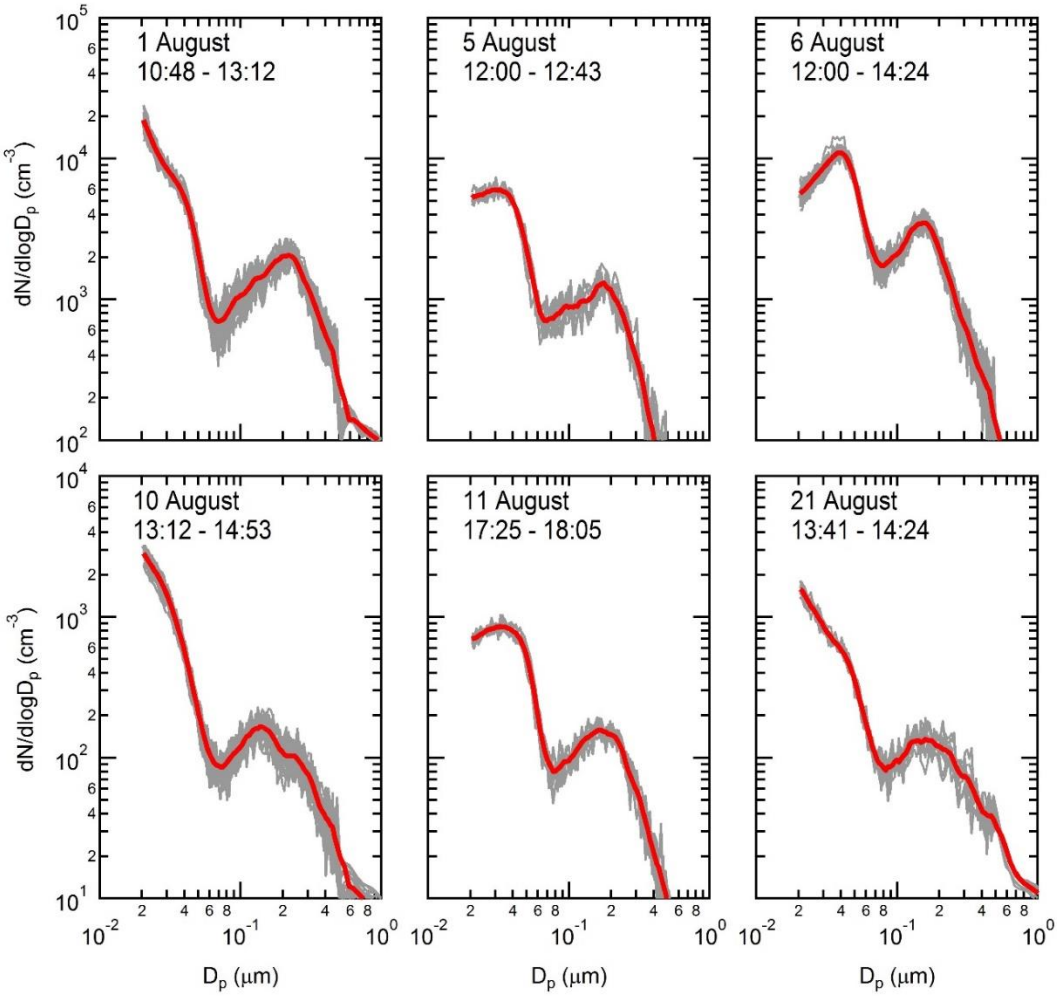

Figure 2.5: SMPS and APS derived size distributions used for each case study in Table 2. The 5 August size distribution is used for both the coupled and decoupled case. Individual distributions (grey) are from the indicated time ranges in the figure. The time ranges are in UTC. Average distributions are shown in red.

D_{min}. Figure 2.6 shows Hoppel-based CDNC estimates are within 30% of simulated CDNC for the 7 cases. The presence of the Hoppel minimum occurs on average at 80 nm diameter throughout the campaign (Figure 2.1b, 2.5) implying in-cloud supersaturations near 0.25 % using a campaign averaged hygroscopicity (K) of 0.42, which is in agreement with K values observed in the North Atlantic marine planetary boundary layer in Pringle et al. [2010].

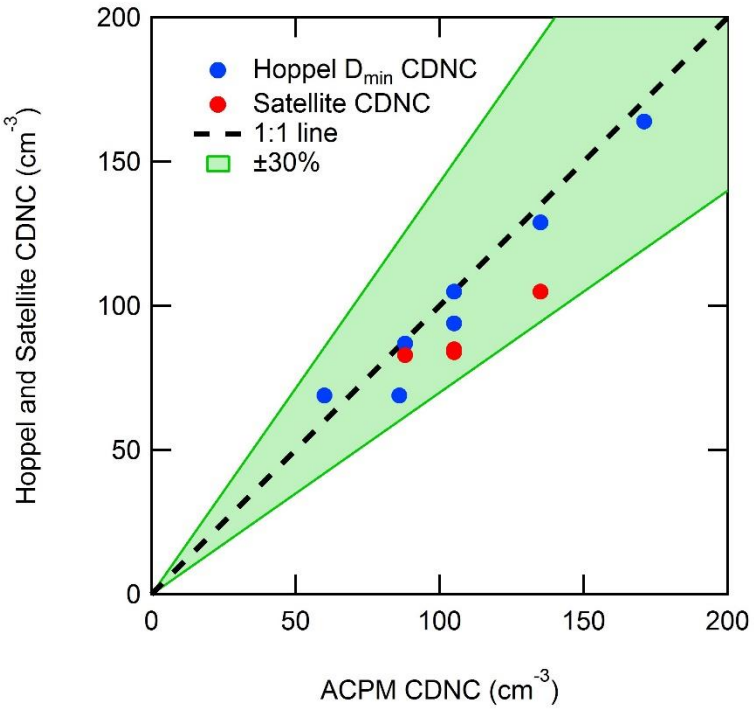

Figure 2.6: Comparison of simulated CDNC from ACPM with both Hoppel minimum diameter (D_{min}) derived CDNC (blue) and satellite estimated CDNC (red). CDNC plotted are from the listed cloud cases in Table 2.2. The green shaded region represents Hoppel and Satellite CDNCs within 30% of ACPM simulation CDNC.

2.3.1.2 UAV measurements closure

Figure 2.7 displays vertical profiles of meteorological parameters, as well as OPC aerosol number concentration (N_{OPC}; Dp > 0.3 μm) and cloud extinction from two flights (23 and 27) on 11 August. The UAV used on flight 23 (conducted between 12:00 UTC and 12:47 UTC), contained the cloud sensor for cloud extinction measurements and flight27 (conducted between 16:58 UTC and 17:33 UTC) contained the OPC for droplet size distribution measurements. During this time period the cloud base reduced from 1200 m on flight 23 to 980 m on flight 27, but cloud depth remained approximately the same. In the OPC vertical profiles, in Figure 2.7d, an aerosol layer is shown above the cloud at ~1400 m. OPC measurements are removed inside cloud layers (as aerosol data is contaminated by cloud droplets), hence the gap in OPC data in Figure 2.7d. The OPC and temperature measurements, in Figure 2.7a and d, are used to show if the boundary layer was coupled (well-mixed) or if it was decoupled. The state of the boundary layer and the OPC and temperature measurements are further discussed at the end of this section. The observed temperature and relative humidity profiles, in Figure 2.7a and b, are also used to initialize the ACPM. In-situ cloud extinction measurements, in Figure 2.7c, are then compared to the ACPM simulated cloud extinction (Figure 2.8c).

Figure 2.8a, c and e present the observed and simulated adiabatic cloud extinction profile for three of the case studies (C11Sc, D05Sc and C21Cu)[5]. The

[5] C/D – coupled / decoupled; xx – date in August 2015; Sc / Cu – stratocumulus / cumulus cloud

measurements are binned into in-cloud, cloud-free, and cloud-transition (or cloud-edge) samples. Many clouds had a small horizontal extent making it difficult for the UAVs to remain in cloud as they ascended and descended in a spiral pattern. Also, high horizontal winds ($10 – 15$ m s^{-1}) will generally move the cloud outside the field of measurement of the aircraft very quickly. For cases where the UAV did not remain in-cloud throughout the ascent or descent, the in-cloud samples are identified as the largest extinction values at each height and are seen in the measurements as a cluster of points (Figure 2.8e). Since lateral mixing with cloud-free air exerts an influence near the cloud edges, the cloud-transition air is not representative of the cloud core and adiabatic simulations. The amount of sampling within individual clouds varied from case to case, but the UAVs were generally able to make multiple measurements of the same cloud during each vertical profile. C11Sc was unique in that it involved stratocumulus clouds with a large horizontal extent, allowing the UAV to remain entirely in-cloud during the upward and downward vertical profiles around a fixed waypoint. Figure 2.8f shows how the difference between simulated and observed extinction ($\delta\sigma_{ext}$) is calculated throughout the cloud based on a discrete sampling of in-cloud measurements. It is not certain that the UAV measured the cloud core for cumulus cases so $\delta\sigma_{ext}$ is an upper limit (Table 2.2).

All ACPM simulation results, including those in Table 2.2, use the cloud radar updraft velocity as input and not the 5-hole probe updraft velocity because 5-hole probe updraft velocities are not available for all cases. Nonetheless, the differences in ACPM simulated shortwave radiative flux between using the 5-hole probe and cloud radar

updraft velocities (Figure 2.3) is less than 3 W m^{-2} for the four cases that had both measurements.

The integrated effect of $\delta\sigma_{ext}$ leads to a difference in cloud observed and simulated shortwave radiative flux (δRF) for both clouds that were coupled with and decoupled from the surface boundary layer (Table 2.2). Figure 2.9, presents a vertical profile of N_{OPC} and equivalent potential temperature. OPC measurements within a thin cloud layer at ~2000 m are removed. N_{OPC} and equivalent potential temperature (θ_e) clearly illustrate this decoupling as shown in an example vertical profile (Figure 2.9) at 900 and 2200 m.asl, with the latter representing the inversion between the boundary layer top and free troposphere. N_{OPC} decreases from an average of 31 cm^{-3} to 19 cm^{-3} at the same altitude as the weak inversion (700-1000 m). In this study, decoupled boundary layers are often observed and aerosol number concentrations (Dp > 0.3 μm) in the decoupled layer were 44% ±14% of those measured at the ground. While N_{OPC} are not directly representative of CCN concentrations, a reduction in aerosol number with height (and potential differences in hygroscopicity) will nonetheless affect aerosol-cloud closures, and ultimately, the cloud radiative properties. Similarly, Norton et al. [2006] showed results from the European Centre for Medium-Range Weather Forecasts (ECMWF) model re-analysis in which surface winds at Mace Head are often decoupled from synoptic flow and, therefore, the air masses in each layer have different origins and most likely different aerosol properties. Consequently, the CCN number concentrations measured at the surface do not represent those in the higher decoupled cloud layer, which ultimately dictates cloud shortwave radiative flux in the region and

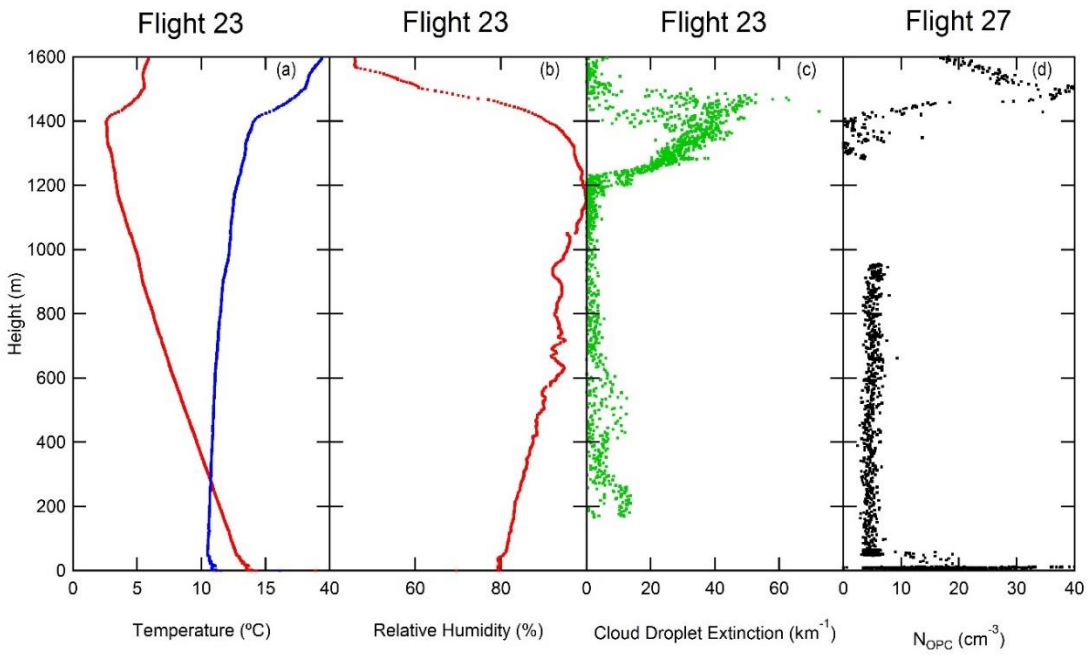

Figure 2.7: Vertical profiles of temperature, virtual potential temperature (θ_v), relative humidity, cloud droplet extinction and OPC total aerosol concentration. The figure consists of measurements collected from flights 23 and 27 on 11 August 2015 between 12:00 - 12:47 and 16:58 -17:33 respectively. The cloud level is between 1200 m to 1480 m in flight 23, and lowered to approximately 980 m to 1280 m in flight 27. OPC measurements that occurred in the cloud have been removed.

δRF in Table 2.2. While aerosol profiles were not collected by UAVs for the decoupled cases presented in Table 2.2, the θ_e profiles and ceilometer measurements show evidence of boundary layer decoupling. These two decoupled cases have larger $\delta\sigma_{ext}$ than the coupled boundary layer cases in this study, leading to larger cloud-top δRF as well. ACPM simulations were conducted using aerosol concentrations based on the approximate average decoupled to coupled aerosol concentration ratio (50%, Figure 2.9) to estimate the difference in shortwave radiative flux. For the D05Sc case, simulations with 50% decreased cloud-base aerosol concentrations show only slight

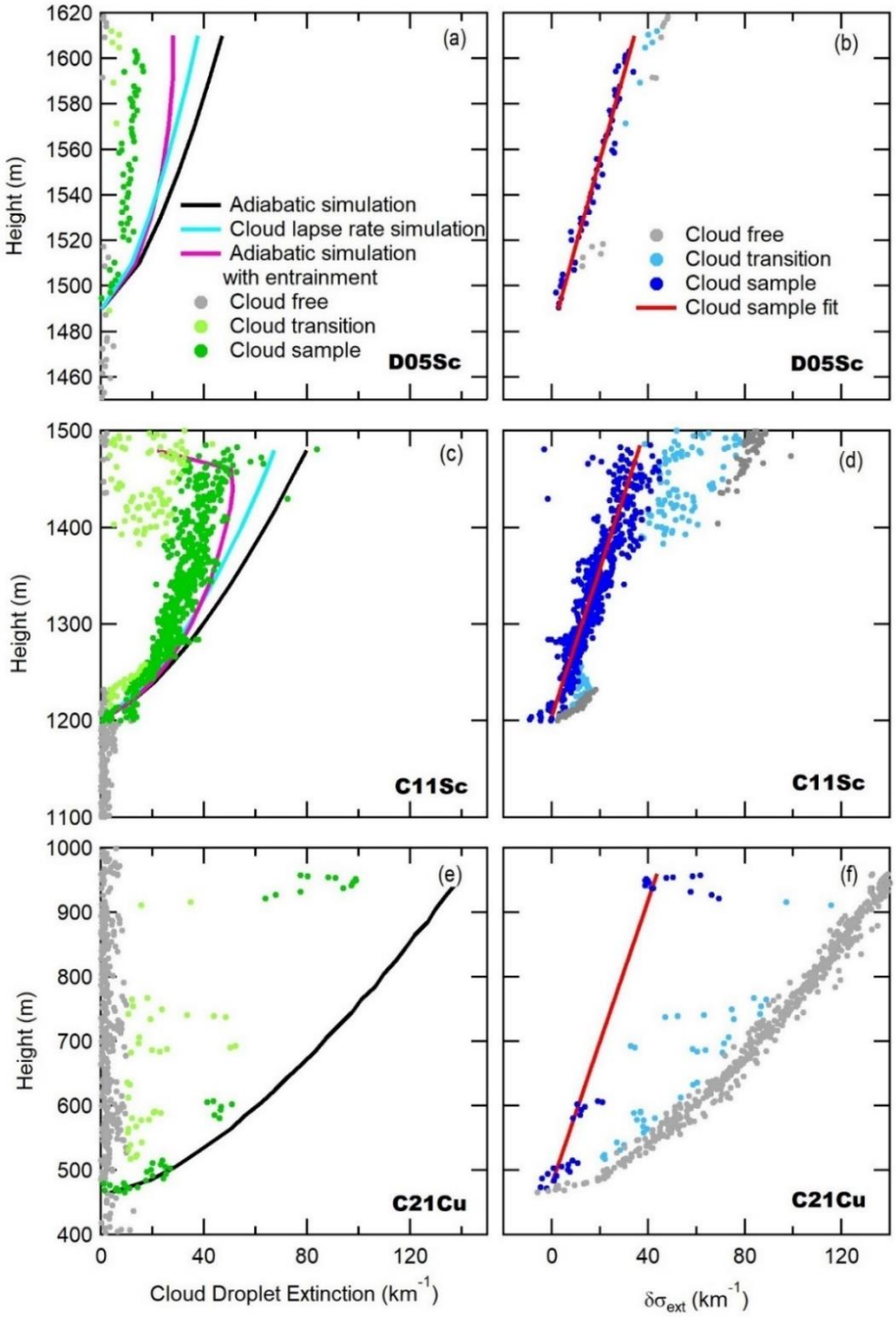

Figure 2.8: Vertical profiles of measured and simulated cloud extinction from flights D05Sc, C11Sc and C21Cu (a, c, e; Table 2.2). In-situ measurements are classified into cloud, cloud-transition and cloud-free observations. The difference between UAV-observed and ACPM-simulated cloud extinction (black line) on left figures (a, c, e) are used to calculate ($\sigma\delta_{ext}$) as a function of altitude in the right figures (b, d, f). The slope of the best fit through in-cloud measurements (red line) represents the increase in $\sigma\delta_{ext}$ as a function of cloud thickness.

differences in δRF of 2 Wm^{-2} and decreases in CDNC of 10%. The decrease in aerosol concentration resulted in increased supersaturation due to the low water uptake from fewer activating droplets. The increased supersaturation caused smaller aerosols to activate [*Raatikainen et al.*, 2013] and therefore, little change in CDNC. The D05Sc case has very low updraft velocities (0-0.3 m s^{-1}). At low updraft velocities, the CDNC is often updraft limited [*Reutter et al.*, 2009]. This means the CDNC is very sensitive to the updraft velocities and less sensitive to aerosol concentration. Small errors in updraft velocity and low modeled updraft resolution (0.1 m s^{-1}) likely contributes significantly

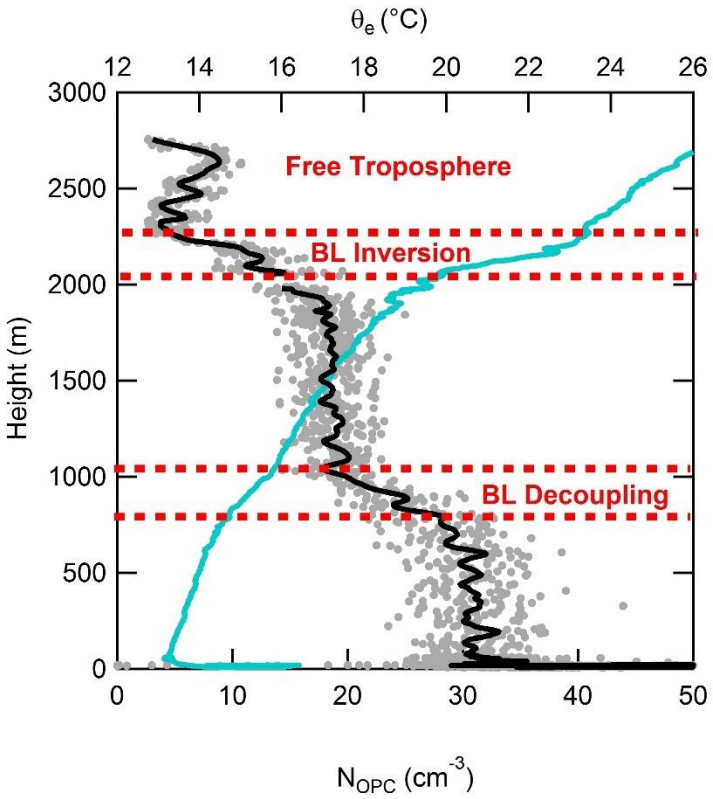

Figure 2.9: Flight 10 UAV vertical profile of OPC aerosol number concentrations (Dp > 0.3 um) (grey) with a 20 second running mean (black) and equivalent potential temperature (θ_e, light blue) illustrate decoupling of the boundary layer. In-cloud OPC measurements (2000 m- 2050 m) have been removed.

to the error in this case. The D06Cu was not influenced as much by low water uptake because the CDNC was much higher at 171 cm^{-3} compared to 86 cm^{-3} for D05Sc. The D06Cu the CDNC decreased by 42% and δRF decreased by 18 Wm^{-2}. The updraft velocity range for the D06Cu case is significantly higher than the D05Cu case (0-1.6 m s^{-1}). The higher velocities for the D05Sc and greater sensitivity to aerosol concentration suggest this case is aerosol limited [*Reutter et al.,* 2009]. Both decoupled cases still have a δRF greater than the coupled cases.

2.3.1.3 Satellite measurements closure

The satellite and simulated CDNC and S_{max} measurements are presented in the bottom of Table 2.2. The method for satellite retrieval of cloud properties could not be used for cases when cloud layers were too thin which, unfortunately was the situation during the flights with the decoupled cloud layers. Nonetheless, Figure 2.4 shows the satellite image used to identify the clouds to calculate CDNC for C11Sc. Satellite retrieved cloud-base height and temperature are verified by ground-based ceilometer and temperature measurements. Figure 2.6 shows the top-down closures demonstrate that satellite-estimated CDNC and simulated CDNC are within a ± 30% expected concentrations, which is limited by the retrieval of effective radius [*Rosenfeld et al.*, 2016]. The stratocumulus deck at the top of a well-mixed boundary layer (C11Sc) shows evidence of cloud-top inhomogeneous entrainment (see section 2.3.2). Freud et al. [2011] found that the inhomogeneous mixing assumption used to derive CDNC from satellite measurements resulted in an average over-estimate in CDNC of 30% (considering an adiabatic cloud droplet profile). Consequently, satellite-retrieved

CDNC is reduced by 30% to account for the inhomogeneous entrainment assumption, which does not necessarily reflect the actual magnitude of entrainment in the clouds. For the C11Sc case, before the correction, proposed by Freud et al. [2011] is applied, the satellite derived CDNC (83 cm^{-3}) is within 30% of the ACPM CDNC (88 cm^{-3}), similar to the other cases (Figure 2.6). However, if the correction is applied, the satellite derived CDNC (58 cm^{-3}) is not within 30% of the ACPM CDNC. This indicates cloud top entrainment for the C11Sc case is already inhomogeneous and the usual 30% reduction in CDNC, to correct for the inhomogeneous assumption, should not be applied. Both stratocumulus cases (C11Sc, D05Sc) with cloud-top entrainment (Table 2.2) are similar to a case studied by Burnet and Brenguier [2007], in which cloud-top entrainment resulted in inhomogeneous mixing. In the following section, C11Sc and D05Sc are reanalyzed to include the effect of cloud-top entrainment on simulated cloud properties using the inhomogeneous mixing assumption.

2.3.2 Entrainment

Based on the ground-based and UAV measurements, ACPM simulations over-estimate cloud shortwave radiative flux significantly for three cases (C11Sc, D05Sc, D06Cu). Section 2.3.1.2 identified that clouds in decoupled layers (D05Sc, D06Cu) have smaller radiative effects than predicted based on ground-based observations as aerosol (and CCN) number concentrations in the decoupled layer are often smaller than in the surface-mixed layer. In this section, cloud-top entrainment is also shown to influence the radiative properties of two sub-adiabatic stratocumulus clouds, C11Sc and D05Sc.

The UAV observations show that both C11Sc and D05Sc have sub-adiabatic lapse rate measurements, compared to simulated moist-adiabatic lapse rates within the cloud (Table 2.2). The difference between the observed and simulated lapse rates therefore suggests a source of heating in the cloud. The sub-adiabatic lapse rate is attributed to cloud-top entrainment by downward mixing of warmer air at cloud-top. The D06Cu case has a slightly sub-adiabatic observed lapse rate (Table 2.2), however the difference with respect to an adiabatic lapse rate is within instrument error. For this reason, cloud top entrainment is not explored for this case, though it may contribute to the error.

Further evidence of cloud-top entrainment is shown through conserved variable mixing diagram analysis. In previous studies, a conserved variable mixing diagram analysis was used to show lateral or cloud-top entrainment by showing linear relationships between observations of conserved variables [*Burnet and Brenguier*, 2007; *Neggers et al.*, 2002; *Paluch*, 1979]. Paluch [1979] first observed a linear relationship of conservative properties (total water content, q_t and liquid water potential temperature, θ_l) between cumulus cloud cores and cloud edge, to show the cloud-free source of entrained air. Paluch [1979], Burnet and Brenguier [2007], Roberts et al. [2008] and Lehmann et al. [2009] observed decreases in CDNC and liquid water content in cumulus clouds as a function of distance from the cloud cores that indicate inhomogeneous mixing at the cloud edge. Burnet and Brenguier [2007] also show that q_t is linearly proportional to liquid water potential temperature specifically for a stratocumulus cloud with cloud-top entrainment and inhomogeneous mixing. Direct

observations of CDNC and liquid water content were not measured at Mace Head, so direct comparisons of CDNC and q_t with Paluch [1979] and Burnet and Brenguier [2007] cannot be investigated here. However, UAV measurements of cloud extinction (Eq. 2.1), which are related to CDNC ($CDNC = \int_0^\infty n(r)\, dr$) and liquid water content ($LWC = \int_0^\infty \frac{4}{3}\rho\pi r^3 n(r)\, dr$, ρ is liquid water density), were measured and are found to be systematically lower than the adiabatic simulated cloud extinction (Figure 2.8).

To apply the cloud-top mixing, a fraction of air at cloud-base and a fraction of air above cloud-top are mixed, conserving q_t and θ_e. The fraction of air from cloud-base and cloud-top is determined with the measured equivalent potential temperature,

$$\theta_{e,c}(z) = \theta_{e,ent}X(z) + \theta_{e,CB}(1 - X(z)) \quad (2.4)$$

where $\theta_{e,c}(z)$ is the equivalent potential temperature in cloud as a function of height, $\theta_{e,ent}$ is the equivalent potential temperature of the cloud-top entrained air, $\theta_{e,CB}$ is the equivalent potential temperature of air at cloud base, and $X(z)$ is the fraction of cloud-top entrained air as a function of height (referred to as the entrainment fraction). $\theta_{e,ent}$ $\theta_{e,c}(z)$ and $\theta_{e,CB}$ are measured parameters by the UAV and are not affected by latent heating from evaporation or condensation. The equivalent potential temperature, by definition, accounts for the total water content by including the latent heat released by condensing all the water vapor. Eq. (2.4) takes into account latent heating caused by evaporation of droplets. By rearranging Eq. (2.4), the entrained fraction is calculated as

$$X(z) = \frac{\theta_{e,c}(z) - \theta_{e,CB}}{\theta_{e,ent} - \theta_{e,CB}} \quad (2.5)$$

Figure 2.10a and b present the relationships between two conservative variables measured by the UAV (water vapor content, q_v, and θ_e) for C11Sc and D05Sc. The q_v is derived from relative humidity measurements and is equivalent to the q_t for sub-saturated, cloud-free air (i.e., < 100% RH). The cloud-free air is shown in blue in Figure 2.10, where the below cloud measurements have lower θ_e than in-cloud and the above cloud measurements have higher θ_e than in-cloud.

Figure 2.11 shows the relative humidity and θ_e profiles used in Figure 2.10. For both C11Sc and D05Sc, $\theta_{e,c}(z)$ is directly measured in-cloud, and q_t and θ_e exhibit an approximately linear relationship (Figure 2.10; Eq. 2.4). The linear relationship of q_t and θ_e (between the non-mixed sources of air indicated by orange circles in Figure 2.10) is assumed to be a result of the cloud reaching a steady-state, with air coming from cloud-base and cloud-top (e.g. cloud lifetime >> mixing time). The observed in-cloud q_v in Figure2.10a and b is less than the conservative variable q_t, however, the figure also includes q_t based on simulated adiabatic (marked with an 'X') and cloud-top entrainment (dashed black line) conditions. Under adiabatic conditions q_t and θ_e do not change in the cloud, which is why the adiabatic simulations only consists of one point in Figure 2.10. Eq. (2.4) is used to derive the simulated cloud-top entrainment conditions (Figure 2.10a and b), where the fraction entrained is used to calculate q_t and shows a linear relationship between q_t and θ_e. Measurements above cloud-top (RH < 95%), labeled entrained air, with q_v > 5.1 g kg^{-1} and q_v > 6.5 g kg^{-1} are used to represent the properties of the entrained air for C11Sc and D05Sc, respectively (Figure 2.10). These

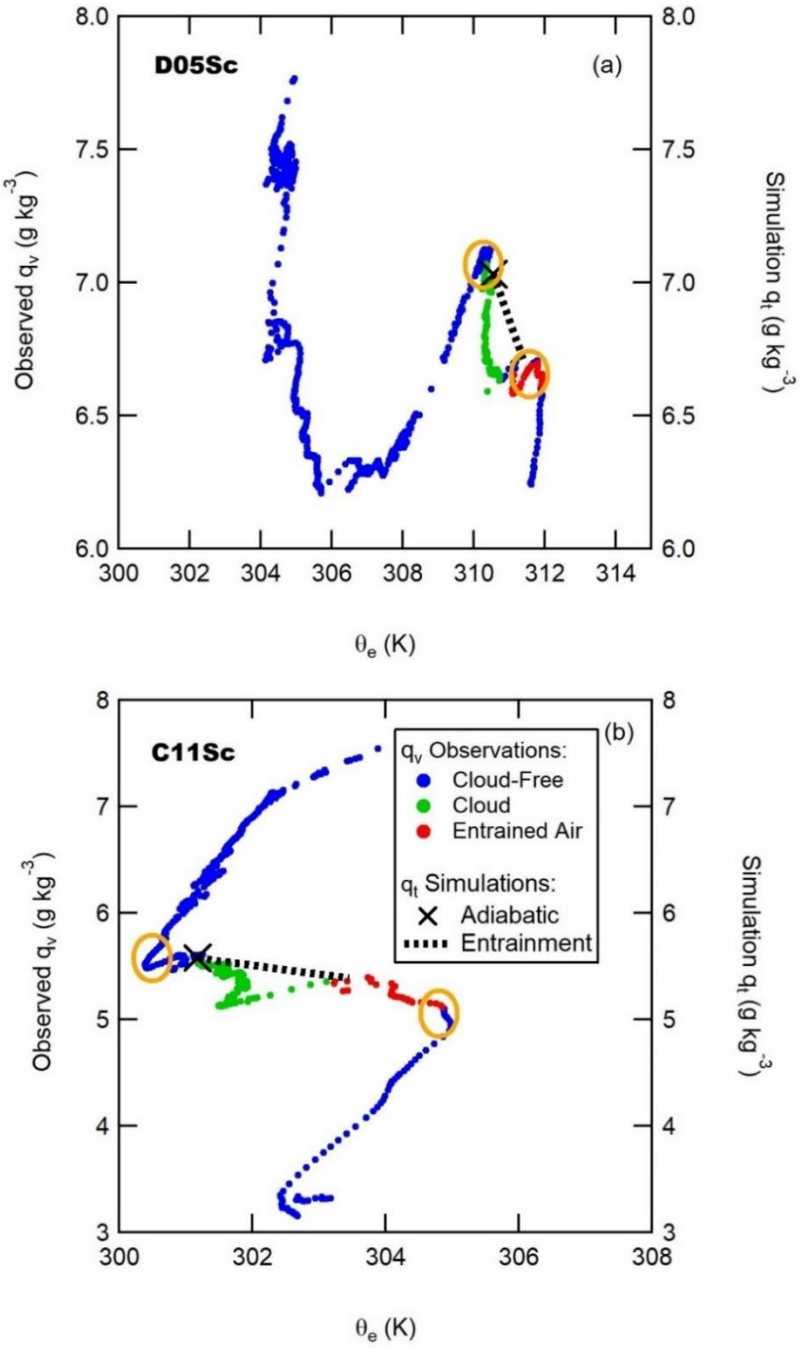

Figure 2.10: Conservative variables, water vapor content (q_v, conservative in subsaturated conditions and derived from RH measurements) and equivalent potential temperature (θ_e) identify mixing between cloud air and entrained air for flights D06Sc (top) and C11Sc (bottom). Measurements are defined as cloud-free (blue), in-cloud (green) or entrained air properties used in simulations (red). The orange circles highlight what is suggested to be the non-mixed sources of air.

conditions were chosen because these values are on the mixing line, between the non-mixed sources identified by the orange circles.

Figure 2.12 shows the sensitivity of the simulated cloud extinction profile, for the 11 August case, based on measurement uncertainties related to the entrained q_t and θ. The key variable for identifying the entrained fraction (Eq. 2.5), $\theta_{e,ent}$, is a function of q_t and θ, so a decrease in either parameter results in a proportional decrease in $\theta_{e,ent}$. Eq. (2.5) shows that entrainment fraction becomes more sensitive to the uncertainty related to the measurement of θ_e as the difference between $\theta_{e,ent}$ and $\theta_{e,CB}$ approaches zero. This is also shown in Figure 2.12 where σ_{ext} is more sensitive to lower entrained q_t and θ values.

Table 2.3 shows $\delta\sigma_{ext}$, δRF, and CDNC for two cases with cloud-top entrainment (C11Sc and D05Sc) using two methods of accounting for the cloud top entrainment. One method (labeled the 'inhomogeneous mixing entrainment method' in Table 2.3) applies the entrainment fraction calculated in Eq. (2.5) and the other an entrainment parameterization, presented by Sanchez et al. [2016]. The entrainment parameterization constrains the ACPM simulation to use the observed in-cloud lapse rate instead of assuming an adiabatic lapse rate. This is labeled the 'lapse rate adjustment' entrainment method in Table 2.3. In the sub-adiabatic cloud cases (C11Sc and D05Sc), the measured in-cloud lapse rate is lower than the adiabatic lapse rate, which leads to the condensation of less water vapor and subsequent activation of fewer droplets in the ACPM simulation. Similarly, when applying the inhomogeneous mixing entrainment method, the dryer and warmer entrained air (from above cloud-top) leads to evaporation of liquid water in the

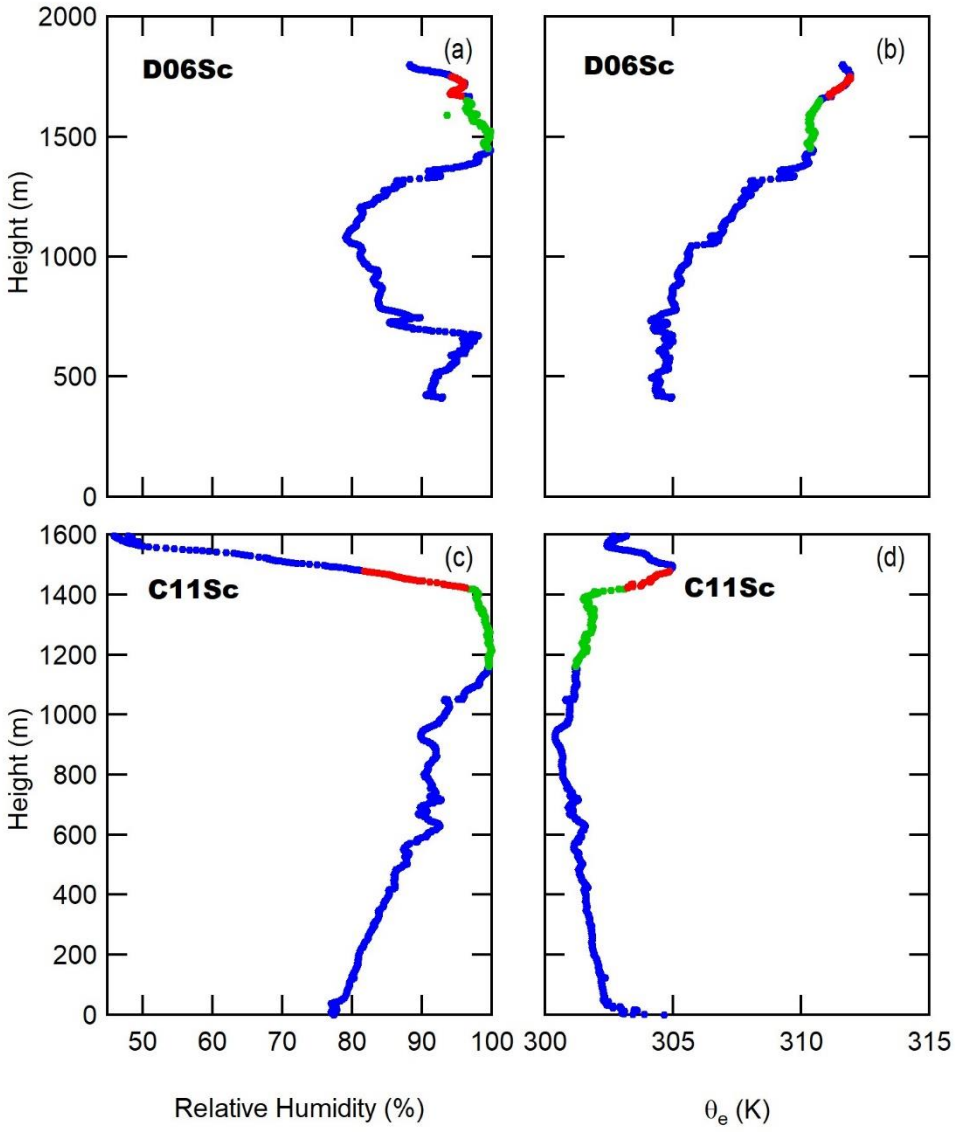

Figure 2.11: UAV vertical profiles of relative humidity (a, c) and θ_e (b, d) for flights D06Sc and C11Sc, used in Figure 2.10. Profiles are defined as cloud-free (blue), in-cloud (green) or entrained air sources (red).

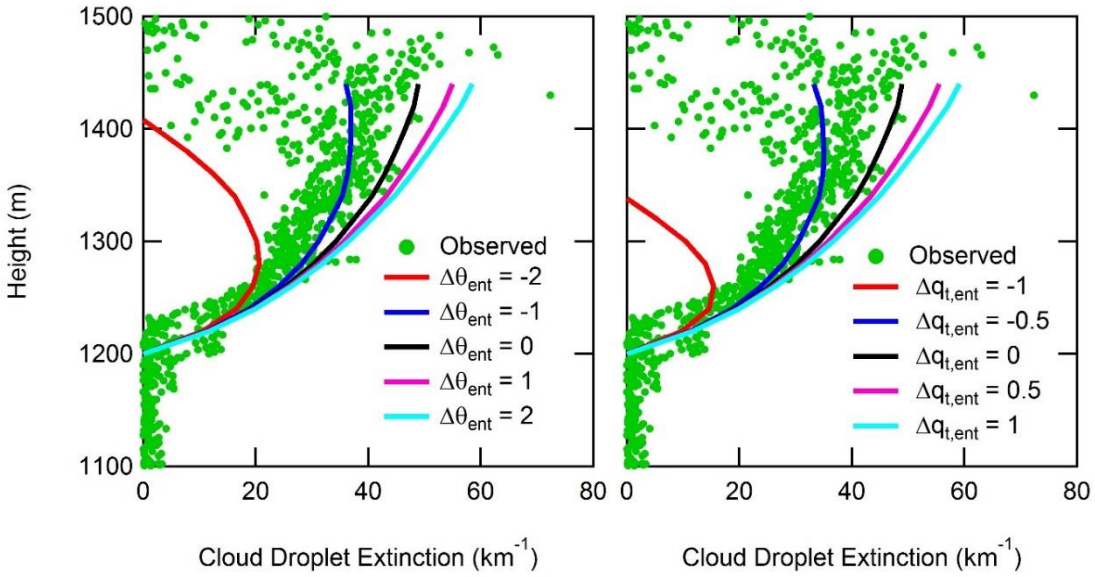

Figure 2.12: Sensitivity of simulated cloud extinction based on variability of entrained air potential temperature (θ_{ent}, K) and entrained air total water mixing ratio ($q_{t,ent}$, g kg^{-1}) for the C11Sc case. The $\Delta\theta_{ent}$ and $\Delta q_{t,ent}$ terms define the change in the entrained θ and q_t values where no change ($\Delta\theta_{ent} = 0$ and $\Delta q_{t,ent} = 0$) is equivalent to the adiabatic simulation with entrainment from Figure 2.8c.

cloud. Previous observations of stratocumulus cloud-top mixing suggest the entrainment is inhomogeneous [*Beals et al.*, 2015; *Burnet and Brenguier*, 2007], which implies that time scales of evaporation are much less than the time scales of mixing, such that a fraction of the droplets are evaporated completely and the remaining droplets are unaffected by the entrainment. The net decrease in CDNC subsequently results in less extinction of solar radiation compared to the purely adiabatic simulation.

Table 2.3: Results of the application of entrainment fraction and the measured lapse rate entrainment parameterization for two clouds with observed cloud-top entrainment.

	Coupled BL (C11Sc)		**Decoupled BL (D05Sc)**	
Entrainment method	Homogeneous mixing entrainment	Lapse rate adjustment	Homogeneous mixing entrainment	Lapse rate adjustment
Cloud-top extinction difference ($\delta\sigma_{ext}$, km^{-1})	16 ±10	23 ±11	16 ±5	26 ±6
Simulated cloud τ	10.1 ±1.5	10.3 ±1.6	2.2±0.3	3.5 ±0.5
Cloud-top shortwave radiative flux difference (δRF, W m^{-2})[a]	20 ±16	32 ±17	33 ±9	61 ±12
Cloud base simulated CDNC[b]	88 ±12	83 ±12	86 ±10	68 ±10

[a] The difference between the observed (calculated from UAV extinction measurements) and simulated shortwave radiative flux. The error includes the potential error of ±20% in updraft velocity and the standard error of the CCN concentration measurements.
[b] The simulated CDNC is unchanged at the cloud base for the entrainment fraction method, however the CDNC decreases with height.

The inclusion of inhomogeneous mixing entrainment improved the ACPM accuracy for both C11Sc and D05Sc using the measured lapse-rate and entrainment fraction methods (Figure 2.8, Table 2.3). After accounting for inhomogeneous entrainment, δRF decreased from 88 Wm^{-2} to 33 Wm^{-2} and 48 Wm^{-2} to 20 Wm^{-2} for D05Sc and D11Sc, respectively, using the entrainment fraction method. D05Sc simulations still yields significant δRF even after accounting for inhomogeneous mixing entrainment, likely because the cloud is in a decoupled BL, as noted in Section 2.3.1.2 to exhibit lower aerosol concentrations than those measured at the surface. The CDNC presented in Table 2.3 represents the CDNC at cloud base and did not change after applying the entrainment fraction method, however, the CDNC decreases with height

for the entrainment fraction method rather than remain constant with height. Finally, the lapse rate adjustment entrainment method [*Sanchez et al.*, 2016] does improve ACPM accuracy between in-situ and satellite-retrieved cloud optical properties relative to the adiabatic simulations, but has greater $\delta\sigma_{ext}$ throughout the cloud than the inhomogeneous mixing entrainment method. For the lapse rate adjustment entrainment method δRF decreased from 88 Wm^{-2} to 61 Wm^{-2} and 48 Wm^{-2} to 32 Wm^{-2} for D05Sc and D11Sc respectively. The lapse rate adjustment entrainment method resulted in lower δRF than the purely adiabatic simulations, however, δRF was minimized by directly accounting for the entrainment fraction.

2.4 Conclusions

This work presents measurements conducted in August 2015 at the Mace Head Research Station in Ireland, from multiple platforms including ground-based, airborne and satellites. As part of the BACCHUS (Impact of Biogenic versus Anthropogenic emissions on Clouds and Climate: towards a Holistic UnderStanding) European collaborative project, the goal of this study is to understand key processes affecting aerosol-cloud shortwave radiative flux interactions. Seven cases including cumulus and stratocumulus clouds were investigated to quantify aerosol-cloud interactions using ground-based and airborne measurements (bottom-up closure), as well as cloud microphysical and radiative properties using airborne measurements and satellite retrievals (top-down closure). An aerosol-cloud parcel model (ACPM) was used to link the ground-based, airborne and satellite observations, and to quantify uncertainties

related to aerosols, cloud microphysical properties, and resulting cloud optical properties.

ACPM simulations represent bottom-up and top-down closures within uncertainties related to satellite retrievals for conditions with a coupled boundary layer and adiabatic cloud development. For these conditions, the difference in shortwave radiative flux between simulations and *in-situ* observed parameters is no greater than 20 W m^{-2}. However, when entrainment and decoupling of the cloud layer occur, the ACPM simulations overestimate the cloud shortwave radiative flux. Of the seven cases, two of the observed clouds occurred in a decoupled layer, resulting in differences in observed and simulated shortwave radiative flux (δRF) of 88 Wm^{-2} and 74 Wm^{-2} for the decoupled stratocumulus case on 5 August (D05Sc) and the decoupled cumulus case on 6 August (D06Cu) cases respectively. Adiabatic ACPM simulations resulted in a maximum cloud-top δRF value of 20 W m^{-2} for coupled boundary layer cases and 74 W m^{-2} for the decoupled boundary layer cases, after accounting for cloud-top entrainment. The reduction in aerosol concentrations in the decoupled layer compared to ground-based measurements is a factor in overestimating decoupled cloud-top shortwave radiative flux with the ACPM, however simulations with 50% decreased aerosol concentrations show only slight differences δRF of 2 W m^{-2} and decreases in CDNC of 10% for D05Sc. For D06Cu δRF decreased by 18 Wm^{-2} and the CDNC decreased by 42%. Even after decreasing the aerosol concentration by 50% both decoupled cases have δRF values significantly higher than the coupled boundary layer cases (< 20 W m^{-2}).

For the cases with cloud-top entrainment, D05Sc and the coupled stratocumulus case on 11 August (C11Sc), liquid water content is one of the major factors in overestimating cloud-top shortwave radiative flux with the ACPM. For these cases, the measured in-cloud lapse rates are lower than adiabatic lapse rates, suggesting a source of heat due to entrainment of warmer, drier air from above the cloud. Furthermore, linear relationships between conservative variables, simulated total water vapor, q_t, and equivalent potential temperature, θ_e, also suggest mixing between air at cloud-base and cloud-top. For D05Sc, after accounting for cloud top entrainment by applying the entrainment fraction δRF decreased from 88 W m^{-2} to 33 Wm^{-2}. For the coupled boundary layer case with entrainment (C11Sc) the δRF decreases from 48 Wm^{-2} to 20 Wm^{-2} after accounting for cloud top entrainment with the entrainment fraction.

Based on airborne observations with UAVs, decoupling of the boundary layer occurred on four of the 13 flight days (two decoupled cloud cases were not discussed due to the lack of in-cloud measurements). However, cloud drop entrainment was only observed on two of those days, limited by the ability to make in-situ measurements. These measurements occurred during the summer, so additional measurements are needed to look at seasonal trends. These cases illustrate the need for *in-situ* observations to quantify entrainment mixing and cloud base CCN concentrations particularly when the mixing state of the atmosphere is not known. Using ground-based observations to model clouds in decoupled boundary layers and not including cloud top entrainment are shown to cause significant differences between observations and simulation radiative

forcing and therefore, should be included in large scale modeling studies to accurately predict future climate forcing.

UAV measurements were coordinated with 13 days of satellite overpasses and cloud microphysical properties were retrieved for four of the cases. When accounting for entrainment, the differences between simulated and satellite-retrieved CDNC are within the expected 30% accuracy of the satellite retrievals [*Rosenfeld et al.*, 2016]. However, in-situ measurements are necessary to refine satellite retrievals to allow cloud properties to be studied on larger spatial scales.

2.5 Acknowledgements

The research leading to these results received funding from the European Union's Seventh Framework Programme (FP7/2007-2013) project BACCHUS under grant agreement n°603445. EU H2020 project ACTRIS-2 under the grant agreement No. 654109 is also acknowledged for supporting the Mace Head Research Station. K.A. Nicoll acknowledges a NERC Independent Research Fellowship (NE/L011514/1). D. Ceburnis acknowledges the Irish EPA (2012-CCRP-FS.12). J. Preissler acknowledges the Irish EPA (2015-CCRP-FS.24). R. Calmer acknowledges financial support from Meteo France. K. J. Sanchez acknowledges the Chateaubriand Fellowship. We thank École Nationale de l'Aviation Civile (ENAC) for assistance with construction and operation of the UAVs. The authors also acknowledge Kirsten Fossum for the collection of SMPS data. We applied a sequence-defines-credit approach for the sequence of authorship. All data is available by contacting the corresponding author or through the following link: www.umr-cnrm.fr/spip.php?article1040.

Chapter 2, in full, is a reprint of the material as it appears in the *Atmospheric Chemistry and Physics* 2017 with slight modifications. Sanchez, K.J., G.C. Roberts, R. Calmer, K. Nicoll, E. Hashimshoni, D. Rosenfeld, J. Ovadnevaite, J. Preissler, D. Ceburnis, C. O'Dowd, and L.M. Russell, "Top-down and bottom-up aerosol–cloud closure: towards understanding sources of uncertainty in deriving cloud shortwave radiative flux." *Atmos. Chem. Phys*., 17, 9797-9814, https://doi.org/10.5194/acp-17-9797-2017, 2017. The dissertation author was the primary investigator and author of this paper.

References

Albrecht, B. A., Bretherton, C. S., Johnson, D., Scubert, W. H., and Frisch, A. S.: The Atlantic Stratocumulus Transition Experiment - ASTEX, Bulletin of the American Meteorological Society, 76, 889-904, 10.1175/1520-0477 (1995) 0762.0.CO ; 2, 1995.

Bahadur, R., Russell, L. M., Jacobson, M. Z., Prather, K., Nenes, A., Adams, P., and Seinfeld, J. H.: Importance of composition and hygroscopicity of BC particles to the effect of BC mitigation on cloud properties: Application to California conditions, Journal of Geophysical Research-Atmospheres, 117, 10.1029/2011jd017265, 2012.

Bates, T. S., Huebert, B. J., Gras, J. L., Griffiths, F. B., and Durkee, P. A.: International Global Atmospheric Chemistry (IGAC) project's first aerosol characterization experiment (ACE 1): Overview, Journal of Geophysical Research-Atmospheres, 103, 16297-16318, 10.1029/97jd03741, 1998.

Beals, M. J., Fugal, J. P., Shaw, R. A., Lu, J., Spuler, S. M., and Stith, J. L.: Holographic measurements of inhomogeneous cloud mixing at the centimeter scale, Science, 350, 87-90, 10.1126/science.aab0751, 2015.

Bohren, C. F., and Battan, L. J.: Radar Backscattering by Inhomogeneous Precipitation Particles, Journal of the Atmospheric Sciences, 37, 1821-1827, 10.1175/1520-0469(1980)037<1821:RBBIPP>2.0.CO;2, 1980.

Bretherton, C. S., Wyant, M. C., and Ams: Decoupling of subtropical stratocumulus-topped boundary layers as they warm and deepen, 12th Symposium on Boundary Layers and Turbulence, 56-57, 1997.

Burnet, F., and Brenguier, J.-L.: Observational study of the entrainment-mixing process in warm convective clouds, Journal of the Atmospheric Sciences, 64, 1995-2011, 10.1175/jas3928.1, 2007.

Calmer, R., Roberts, G. C., Sanchez, K. J., and Lothon, P. M.: Validation of 3D wind vector measurements using a 5-hole Probe with Remotely Piloted Aircraft, in, In Prep. ed., Atmospheric Measurement Techniques, 2017.

Coe, H., Allan, J. D., Alfarra, M. R., Bower, K. N., Flynn, M. J., McFiggans, G. B., Topping, D. O., Williams, P. I., O'Dowd, C. D., Dall'Osto, M., Beddows, D. C. S., and Harrison, R. M.: Chemical and physical characteristics of aerosol particles at a remote coastal location, Mace Head, Ireland, during NAMBLEX, Atmospheric Chemistry and Physics, 6, 3289-3301, 10.5194/acp-6-3289-2006, 2006.

Conant, W. C., VanReken, T. M., Rissman, T. A., Varutbangkul, V., Jonsson, H. H., Nenes, A., Jimenez, J. L., Delia, A. E., Bahreini, R., Roberts, G. C., Flagan, R. C., and

Seinfeld, J. H.: Aerosol-cloud drop concentration closure in warm cumulus, Journal of Geophysical Research-Atmospheres, 109, 10.1029/2003jd004324, 2004.

Dall'Osto, M., Ceburnis, D., Martucci, G., Bialek, J., Dupuy, R., Jennings, S. G., Berresheim, H., Wenger, J., Healy, R., Facchini, M. C., Rinaldi, M., Giulianelli, L., Finessi, E., Worsnop, D., Ehn, M., Mikkila, J., Kulmala, M., and O'Dowd, C. D.: Aerosol properties associated with air masses arriving into the North East Atlantic during the 2008 Mace Head EUCAARI intensive observing period: an overview, Atmospheric Chemistry and Physics, 10, 8413-8435, 10.5194/acp-10-8413-2010, 2010.

Feingold, G., McComiskey, A., Rosenfeld, D., and Sorooshian, A.: On the relationship between cloud contact time and precipitation susceptibility to aerosol, Journal of Geophysical Research-Atmospheres, 118, 10544-10554, 10.1002/jgrd.50819, 2013.

Fountoukis, C., Nenes, A., Meskhidze, N., Bahreini, R., Conant, W. C., Jonsson, H., Murphy, S., Sorooshian, A., Varutbangkul, V., Brechtel, F., Flagan, R. C., and Seinfeld, J. H.: Aerosol-cloud drop concentration closure for clouds sampled during the International Consortium for Atmospheric Research on Transport and Transformation 2004 campaign, Journal of Geophysical Research-Atmospheres, 112, 10.1029/2006jd007272, 2007.

Freud, E., Rosenfeld, D., and Kulkarni, J. R.: Resolving both entrainment-mixing and number of activated CCN in deep convective clouds, Atmospheric Chemistry and Physics, 11, 12887-12900, 10.5194/acp-11-12887-2011, 2011.

Geresdi, I., Meszaros, E., and Molnar, A.: The effect of chemical composition and size distribution of aerosol particles on droplet formation and albedo of stratocumulus clouds, Atmospheric Environment, 40, 1845-1855, 10.1016/j.atmosenv.2005.11.012, 2006.

Goersdorf, U., Lehmann, V., Bauer-Pfundstein, M., Peters, G., Vavriv, D., Vinogradov, V., and Volkov, V.: A 35-GHz Polarimetric Doppler Radar for Long-Term Observations of Cloud Parameters-Description of System and Data Processing, Journal of Atmospheric and Oceanic Technology, 32, 675-690, 10.1175/jtech-d-14-00066.1, 2015.

Hansen, J. E., and Travis, L. D.: Light-Scattering in Planetary Atmospheres, Space Science Reviews, 16, 527-610, 10.1007/bf00168069, 1974.

Harrison, R. G., and Nicoll, K. A.: Note: Active optical detection of cloud from a balloon platform, Review of Scientific Instruments, 85, 10.1063/1.4882318, 2014.

Heard, D. E., Read, K. A., Methven, J., Al-Haider, S., Bloss, W. J., Johnson, G. P., Pilling, M. J., Seakins, P. W., Smith, S. C., Sommariva, R., Stanton, J. C., Still, T. J., Ingham, T., Brooks, B., De Leeuw, G., Jackson, A. V., McQuaid, J. B., Morgan, R.,

Smith, M. H., Carpenter, L. J., Carslaw, N., Hamilton, J., Hopkins, J. R., Lee, J. D., Lewis, A. C., Purvis, R. M., Wevill, D. J., Brough, N., Green, T., Mills, G., Penkett, S. A., Plane, J. M. C., Saiz-Lopez, A., Worton, D., Monks, P. S., Fleming, Z., Rickard, A. R., Alfarra, M. R., Allan, J. D., Bower, K., Coe, H., Cubison, M., Flynn, M., McFiggans, G., Gallagher, M., Norton, E. G., O'Dowd, C. D., Shillito, J., Topping, D., Vaughan, G., Williams, P., Bitter, M., Ball, S. M., Jones, R. L., Povey, I. M., O'Doherty, S., Simmonds, P. G., Allen, A., Kinnersley, R. P., Beddows, D. C. S., Dall'Osto, M., Harrison, R. M., Donovan, R. J., Heal, M. R., Jennings, S. G., Noone, C., and Spain, G.: The North Atlantic Marine Boundary Layer Experiment (NAMBLEX). Overview of the campaign held at Mace Head, Ireland, in summer 2002, Atmospheric Chemistry and Physics, 6, 2241-2272, 10.5194/acp-6-2241-2006, 2006.

Heese, B., Flentje, H., Althausen, D., Ansmann, A., and Frey, S.: Ceilometer lidar comparison: backscatter coefficient retrieval and signal-to-noise ratio determination, Atmospheric Measurement Techniques, 3, 1763-1770, 10.5194/amt-3-1763-2010, 2010.

Hoppel, W. A.: MEASUREMENT OF THE SIZE DISTRIBUTION AND CCN SUPERSATURATION SPECTRUM OF SUB-MICRON AEROSOLS OVER THE OCEAN, Journal of the Atmospheric Sciences, 36, 2006-2015, 10.1175/1520-0469(1979)036<2006:motsda>2.0.co;2, 1979.

Jacobson, M. Z., Turco, R. P., Jensen, E. J., and Toon, O. B.: Modeling Coagulation Among Particles of Different Composition and Size, Atmospheric Environment, 28, 1327-1338, 10.1016/1352-2310(94)90280-1, 1994.

Jones, C. R., Bretherton, C. S., and Leon, D.: Coupled vs. decoupled boundary layers in VOCALS-REx, Atmospheric Chemistry and Physics, 11, 7143-7153, 10.5194/acp-11-7143-2011, 2011.

Kleefeld, C., O'Dowd, C. D., O'Reilly, S., Jennings, S. G., Aalto, P., Becker, E., Kunz, G., and de Leeuw, G.: Relative contribution of submicron and supermicron particles to aerosol light scattering in the marine boundary layer, Journal of Geophysical Research-Atmospheres, 107, 10.1029/2000jd000262, 2002.

Kunz, G. J., de Leeuw, G., Becker, E., and O'Dowd, C. D.: Lidar observations of atmospheric boundary layer structure and sea spray aerosol plumes generation and transport at Mace Head, Ireland (PARFORCE experiment), Journal of Geophysical Research-Atmospheres, 107, 10.1029/2001jd001240, 2002.

Lehmann, K., Siebert, H., and Shaw, R. A.: Homogeneous and Inhomogeneous Mixing in Cumulus Clouds: Dependence on Local Turbulence Structure, Journal of the Atmospheric Sciences, 66, 3641-3659, 10.1175/2009jas3012.1, 2009.

Lenschow, D. H., and Spyers-Duran, P.: Measurement Techniques: Air Motion Sensing, NCAR, 1989.

Lilly, D. K.: MODELS OF CLOUD-TOPPED MIXED LAYERS UNDER A STRONG INVERSION, Quarterly Journal of the Royal Meteorological Society, 94, 292-&, 10.1002/qj.49709440106, 1968.

Martucci, G., Milroy, C., and O'Dowd, C. D.: Detection of Cloud-Base Height Using Jenoptik CHM15K and Vaisala CL31 Ceilometers, Journal of Atmospheric and Oceanic Technology, 27, 305-318, 10.1175/2009jtecha1326.1, 2010.

Melchionna, S., Bauer, M., and Peters, G.: A new algorithm for the extraction of cloud parameters using multipeak analysis of cloud radar data - First application and preliminary results, Meteorologische Zeitschrift, 17, 613-620, 10.1127/0941-2948/2008/0322, 2008.

Milroy, C., Martucci, G., Lolli, S., Loaec, S., Sauvage, L., Xueref-Remy, I., Lavric, J. V., Ciais, P., Feist, D. G., Biavati, G., and O'Dowd, C. D.: An Assessment of Pseudo-Operational Ground-Based Light Detection and Ranging Sensors to Determine the Boundary-Layer Structure in the Coastal Atmosphere, Advances in Meteorology, 10.1155/2012/929080, 2012.

Neggers, R. A. J., Duynkerke, P. G., Rodts, S. M. A., and Ams, A. M. S.: Shallow cumulus convection: a validation of large-eddy simulation against aircraft and Landsat observations, 15th Symposium on Boundary Layers and Turbulence, 199-202, 10.1256/qj.02.93, 2002.

Nicholls, S., and Leighton, J.: An Observational Study of the Structure of Stratiform Cloud Sheets. 1. Structure, Quarterly Journal of the Royal Meteorological Society, 112, 431-460, 10.1002/qj.49711247209, 1986.

Nicoll, K., Harrison, R. G., and Brus, D.: Optical cloud detection from a disposable airborne sensor, EGU General Assembly, Vienna Austria, 2016.

Norton, E. G., Vaughan, G., Methven, J., Coe, H., Brooks, B., Gallagher, M., and Longley, I.: Boundary layer structure and decoupling from synoptic scale flow during NAMBLEX, Atmospheric Chemistry and Physics, 6, 433-445, 10.5194/acp-6-433-2006, 2006.

O'Connor, T. C., Jennings, S. G., and O'Dowd, C. D.: Highlights of fifty years of atmospheric aerosol research at Mace Head, Atmospheric Research, 90, 338-355, 10.1016/j.atmosres.2008.08.014, 2008.

O'Dowd, C., Ceburnis, D., Ovadnevaite, J., Vaishya, A., Rinaldi, M., and Facchini, M. C.: Do anthropogenic, continental or coastal aerosol sources impact on a marine aerosol

signature at Mace Head?, Atmospheric Chemistry and Physics, 14, 10687-10704, 10.5194/acp-14-10687-2014, 2014.

O'Dowd, C. D., Becker, E., and Kulmala, M.: Mid-latitude North-Atlantic aerosol characteristics in clean and polluted air, Atmospheric Research, 58, 167-185, 10.1016/S0169-8095(01)00098-9, 2001.

O'Dowd, C. D., Facchini, M. C., Cavalli, F., Ceburnis, D., Mircea, M., Decesari, S., Fuzzi, S., Yoon, Y. J., and Putaud, J. P.: Biogenically driven organic contribution to marine aerosol, Nature, 431, 676-680, 10.1038/nature02959, 2004.

Painemal, D., and Zuidema, P.: Assessment of MODIS cloud effective radius and optical thickness retrievals over the Southeast Pacific with VOCALS-REx in situ measurements, Journal of Geophysical Research-Atmospheres, 116, 10.1029/2011jd016155, 2011.

Paluch, I. R.: Entrainment Mechanism in Colorado Cumuli, Journal of the Atmospheric Sciences, 36, 2467-2478, 10.1175/1520-0469(1979)036<2467:temicc>2.0.co;2, 1979.

Petters, M. D., and Kreidenweis, S. M.: A single parameter representation of hygroscopic growth and cloud condensation nucleus activity, Atmospheric Chemistry and Physics, 7, 1961-1971, 10.5194/acp-7-1961-2007, 2007.

Pinsky, M., Khain, A., Mazin, I., and Korolev, A.: Analytical estimation of droplet concentration at cloud base, Journal of Geophysical Research-Atmospheres, 117, 10.1029/2012jd017753, 2012.

Pringle, K. J., Tost, H., Pozzer, A., Poschl, U., and Lelieveld, J.: Global distribution of the effective aerosol hygroscopicity parameter for CCN activation, Atmospheric Chemistry and Physics, 10, 5241-5255, 10.5194/acp-10-5241-2010, 2010.

Raatikainen, T., Nenes, A., Seinfeld, J. H., Morales, R., Moore, R. H., Lathem, T. L., Lance, S., Padro, L. T., Lin, J. J., Cerully, K. M., Bougiatioti, A., Cozic, J., Ruehl, C. R., Chuang, P. Y., Anderson, B. E., Flagan, R. C., Jonsson, H., Mihalopoulos, N., and Smith, J. N.: Worldwide data sets constrain the water vapor uptake coefficient in cloud formation, Proceedings of the National Academy of Sciences of the United States of America, 110, 3760-3764, 10.1073/pnas.1219591110, 2013.

Raes, F., Bates, T., McGovern, F., and Van Liedekerke, M.: The 2nd Aerosol Characterization Experiment (ACE-2): general overview and main results, Tellus Series B-Chemical and Physical Meteorology, 52, 111-125, 10.1034/j.1600-0889.2000.00124.x, 2000.

Reutter, P., Su, H., Trentmann, J., Simmel, M., Rose, D., Gunthe, S. S., Wernli, H., Andreae, M. O., and Poeschl, U.: Aerosol- and updraft-limited regimes of cloud droplet formation: influence of particle number, size and hygroscopicity on the activation of cloud condensation nuclei (CCN), Atmospheric Chemistry and Physics, 9, 7067-7080, 2009.

Rinaldi, M., Facchini, M. C., Decesari, S., Carbone, C., Finessi, E., Mircea, M., Fuzzi, S., Ceburnis, D., Ehn, M., Kulmala, M., de Leeuw, G., and O'Dowd, C. D.: On the representativeness of coastal aerosol studies to open ocean studies: Mace Head - a case study, Atmospheric Chemistry and Physics, 9, 9635-9646, 10.5194/acp-9-9635-2009, 2009.

Roberts, G. C., Andreae, M. O., Zhou, J. C., and Artaxo, P.: Cloud condensation nuclei in the Amazon Basin: "Marine" conditions over a continent?, Geophysical Research Letters, 28, 2807-2810, 10.1029/2000gl012585, 2001.

Roberts, G. C., and Nenes, A.: A continuous-flow streamwise thermal-gradient CCN chamber for atmospheric measurements, Aerosol Science and Technology, 39, 206-221, 10.1080/027868290913988, 2005.

Roberts, G. C., Ramana, M. V., Corrigan, C., Kim, D., and Ramanathan, V.: Simultaneous observations of aerosol-cloud-albedo interactions with three stacked unmanned aerial vehicles, Proceedings of the National Academy of Sciences of the United States of America, 105, 7370-7375, 10.1073/pnas.0710308105, 2008.

Rosenfeld, D., Williams, E., Andreae, M. O., Freud, E., Poeschl, U., and Renno, N. O.: The scientific basis for a satellite mission to retrieve CCN concentrations and their impacts on convective clouds, Atmospheric Measurement Techniques, 5, 2039-2055, 10.5194/amt-5-2039-2012, 2012.

Rosenfeld, D., Fischman, B., Zheng, Y., Goren, T., and Giguzin, D.: Combined satellite and radar retrievals of drop concentration and CCN at convective cloud base, Geophysical Research Letters, 41, 3259-3265, 10.1002/2014gl059453, 2014.

Rosenfeld, D., Zheng, Y., Hashimshoni, E., Poehlker, M. L., Jefferson, A., Poehlker, C., Yu, X., Zhu, Y., Liu, G., Yue, Z., Fischman, B., Li, Z., Giguzin, D., Goren, T., Artaxo, P., Barbosa, H. M. J., Poeschl, U., and Andreae, M. O.: Satellite retrieval of cloud condensation nuclei concentrations by using clouds as CCN chambers, Proceedings of the National Academy of Sciences of the United States of America, 113, 5828-5834, 10.1073/pnas.1514044113, 2016.

Russell, L. M., Lenschow, D. H., Laursen, K. K., Krummel, P. B., Siems, S. T., Bandy, A. R., Thornton, D. C., and Bates, T. S.: Bidirectional mixing in an ACE 1 marine boundary layer overlain by a second turbulent layer, J. Geophys. Res., 103, 16411-16432, 1998.

Russell, L. M., and Seinfeld, J. H.: Size- and composition-resolved externally mixed aerosol model, Aerosol Science and Technology, 28, 403-416, 10.1080/02786829808965534, 1998.

Russell, L. M., Seinfeld, J. H., Flagan, R. C., Ferek, R. J., Hegg, D. A., Hobbs, P. V., Wobrock, W., Flossmann, A. I., O'Dowd, C. D., Nielsen, K. E., and Durkee, P. A.: Aerosol dynamics in ship tracks, Journal of Geophysical Research-Atmospheres, 104, 31077-31095, 10.1029/1999jd900985, 1999.

Sanchez, K. J., Russell, L. M., Modini, R. L., Frossard, A. A., Ahlm, L., Corrigan, C. E., Roberts, G. C., Hawkins, L. N., Schroder, J. C., Bertram, A. K., Zhao, R., Lee, A. K. Y., Lin, J. J., Nenes, A., Wang, Z., Wonaschutz, A., Sorooshian, A., Noone, K. J., Jonsson, H., Toom, D., Macdonald, A. M., Leaitch, W. R., and Seinfeld, J. H.: Meteorological and aerosol effects on marine cloud microphysical properties, Journal of Geophysical Research-Atmospheres, 121, 4142-4161, 10.1002/2015jd024595, 2016.

Schubert, W. H., Wakefield, J. S., Steiner, E. J., and Cox, S. K.: MARINE STRATOCUMULUS CONVECTION .1. GOVERNING EQUATIONS AND HORIZONTALLY HOMOGENEOUS SOLUTIONS, Journal of the Atmospheric Sciences, 36, 1286-1307, 10.1175/1520-0469(1979)036<1286:mscpig>2.0.co;2, 1979.

Sollazzo, M. J., Russell, L. M., Percival, D., Osborne, S., Wood, R., and Johnson, D. W.: Entrainment rates during ACE-2 Lagrangian experiments calculated from aircraft measurements, Tellus Series B-Chemical and Physical Meteorology, 52, 335-347, 10.1034/j.1600-0889.2000.00010.x, 2000.

Stephens, G. L.: Radiation Profiles in Extended Water Clouds 2. Parameterization Schemes, Journal of the Atmospheric Sciences, 35, 2123-2132, 10.1175/1520-0469(1978)035<2123:rpiewc>2.0.co;2, 1978.

Stevens, B.: Entrainment in stratocumulus-topped mixed layers, Quarterly Journal of the Royal Meteorological Society, 128, 2663-2690, 10.1256/qj.01.202, 2002.

Stull, R. B.: An Introduction to Boundary Layer Meteorology, Kluwer Academic, Dordrecht, 574-576 pp., 1988.

Turton, J. D., and Nicholls, S.: A Study of the Diurnal-Variation of Stratocumulus Using a Multiple Mixed Layer Model, Quarterly Journal of the Royal Meteorological Society, 113, 969-1009, 10.1256/smsqj.47710, 1987.

Tzivion, S., Feingold, G., and Levin, Z.: An efficient numerical solution to the stochastic collection equation, Journal of the Atmospheric Sciences, 44, 3139-3149, 10.1175/1520-0469(1987)044<3139:aenstt>2.0.co;2, 1987.

Wildmann, N., Ravi, S., and Bange, J.: Towards higher accuracy and better frequency response with standard multi-hole probes in turbulence measurement with remotely piloted aircraft (RPA), Atmospheric Measurement Techniques, 7, 1027-1041, 10.5194/amt-7-1027-2014, 2014.

Zhou, X., Kollias, P., and Lewis, E. R.: Clouds, Precipitation, and Marine Boundary Layer Structure during the MAGIC Field Campaign, Journal of Climate, 28, 2420-2442, 10.1175/jcli-d-14-00320.1, 2015.

Chapter 3

Higher Contributions of Marine Sulfate than Sea Spray to Cloud Condensation Nuclei in Late Spring than in Late Autumn

Biogenic sources contribute to cloud condensation nuclei (CCN) in the clean marine atmosphere, but few measurements exist to constrain climate model simulations of their importance. The chemical composition of individual atmospheric aerosol particles showed two types of sulfate-containing particles in clean marine air masses in addition to mass-based Estimated Salt particles. Both types of sulfate particles lack combustion tracers and correlate, for some conditions to atmospheric or seawater dimethyl sulfide (DMS) concentrations, which means their source was largely biogenic. The first type is identified as New Sulfate because their large sulfate mass fraction (63% sulfate) and association with entrainment conditions means they could have formed by

nucleation in the free troposphere. The second type is Added Sulfate particles (38% sulfate), because they are preexisting particles onto which additional sulfate condensed. New Sulfate particles accounted for 31% (7 cm^{-3}) and 33% (36 cm^{-3}) CCN at 0.1% supersaturation in late-autumn and late-spring, respectively, whereas sea spray provided 55% (13 cm^{-3}) in late-autumn but only 4% (4 cm^{-3}) in late-summer. Our results show a clear seasonal difference in the marine CCN budget, which illustrate how important phytoplankton-produced DMS emissions are for CCN in the North Atlantic.

3.1 Introduction

Cloud condensation nuclei (CCN) provide the sites on which droplets form, resulting in clouds with radiative properties determined in part by CCN abundance and characteristics. The amount of water that is available to condense is described by the supersaturation, which is often 0.1% for the stratocumulus clouds that cover much of the ocean and reflect a large fraction of incoming sunlight [*Hoppel et al.*, 1996; *Hudson et al.*, 2010; *Leaitch et al.*, 1996; *Sanchez et al.*, 2016]. The number and chemical composition of CCN in the marine atmosphere depend on their emission sources and the contributing atmospheric growth processes. The ocean sources of submicron particles are sea spray, which is largely sea salt, and marine biogenic gases that can oxidize and condense, for which dimethyl sulfide (DMS) [*Bates et al.*, 1998b; *Bates et al.*, 2012; *Covert et al.*, 1992; *Frossard et al.*, 2014a; *Middlebrook et al.*, 1998; *Murphy et al.*, 1998b; *Pirjola et al.*, 2000; *Quinn et al.*, 2000; *Quinn et al.*, 2014; *Rinaldi et al.*, 2010; *Sievering et al.*, 1992; *Sievering et al.*, 1999; *Warren and Seinfeld*, 1985] contributes the most mass. Quantifying these sources for the marine boundary layer aerosol budget provides the framework necessary for predicting how changing ocean conditions will affect marine clouds [*Charlson et al.*, 1987; *Keene et al.*, 2007; *Shaw*, 1983; *Wood et al.*, 2015]. Model simulations that include parameterizations of marine sources and processes illustrate their effect on the budget of CCN over the remote open ocean. Combining parameterizations of DMS-derived sulfate [*Pandis et al.*, 1994; *Russell et al.*, 1994] and sea spray [*Odowd et al.*, 1997] emission models to simulate CCN contributions showed that DMS-derived sulfate accounted for over 70% of CCN

at low wind speeds (< 6 m s^{-1}) but that sea spray particles contributed more than 80% of CCN at high wind speeds (>12 m s^{-1}) [*Yoon and Brimblecombe,* 2002]. Adding primary marine sea spray particles to a sulfate-only global model increased CCN concentration by less than 20% over most of the North Atlantic, but up to 70% near Greenland (which is frequently influenced by Arctic air masses) [*Pierce and Adams*, 2006]. The CCN fraction attributed to primary particles (mostly sea spray) in a global transport model accounted for most CCN at high latitudes but for less than 40% in the mid North Atlantic [*Yu and Luo,* 2009]. These model results reflect substantial uncertainty about what sources are most important for CCN because there are effectively no observations to constrain which model is correct.

The reason for this is that existing measurements provide only limited information about where individual particles come from. Most chemical characterization of aerosol particles over open oceans quantify the mass of different components in particles but not their number [*Frossard et al.,* 2014a; *Grythe et al.*, 2014; *Kim et al.,* 2015; *Massling et al.,* 2003; *Quinn and Bates,* 2005; *Wood et al.,* 2011; *X L Zhang et al.,* 2014]. Because of this, indirect ways to estimate primary marine aerosol contributions have been developed [*Modini et al.,* 2015; *Odowd and Smith*, 1993; *Quinn et al.,* 2017]. For example, sea spray particles were shown to account for less than 35% of CCN (at 0.1% supersaturation) over most of the North Atlantic and as little as 8% in some regions [*Quinn et al.*, 2017]. However, sampling in clean Arctic air masses had as much as 75% of CCN attributed to sea salt particles [*Odowd and Smith*, 1993]. The same number concentrations of sea salt particles accounted for up to 47% of

CCN (at 0.1 % supersaturation) in clean polar air masses (with few continental sources and low biogenic DMS emissions) but only 8-25% in marine air masses at mid-latitudes (where continental sources contribute more particles and biological DMS sources are larger) [*de Leeuw et al.*, 2011; *Odowd and Smith*, 1993; *Quinn et al.*, 2015; *Warneck*, 1988]. These indirect approaches have both substantial uncertainty and limited information about particles other than sea spray.

Biogenic sulfate mass has been measured during many open ocean cruises in clean regions [*Bates et al.*, 1998b; *Quinn and Bates*, 2011; *Quinn et al.*, 2000; *Quinn et al.*, 2014; *Quinn et al.*, 2004; *Quinn et al.*, 1998; *Reus et al.*, 2000], with observations in the North Atlantic of 0.06±0.07 μg m^{-3} during winter and 0.45±0.37 μg m^{-3} during summer [*Ovadnevaite et al.*, 2014]. In the northeastern Pacific under clean marine conditions [*Quinn et al.*, 1993], a doubling of the non-sea salt sulfate mass was linked to a 40% increase in CCN concentration. Converting sulfate mass to CCN concentration requires assuming the size and sulfate mass fraction in the particles and does not separate the contributions of nucleation and condensation [*Kuang et al.*, 2009]. There is little evidence of particle nucleation in the boundary layer [*Andreae et al.*, 1995; *Ayers and Gras*, 1991; *Hegg et al.*, 1991; *Hegg et al.*, 1990; *Quinn et al.*, 2014], but the conditions in the free troposphere are often more consistent with DMS-derived H_2SO_4 nucleation [*Clarke*, 1993; *Raes et al.*, 1997]. In other words, the cold free troposphere (and clean winter MBL) has few pre-existing particles and these typically have lower particle surface area than in the boundary layer, making them less likely to compete against nucleation for DMS products [*Raes et al.*, 1997; *Yue and Deepak*, 1982]. This

may happen when buoyancy driven transport causes surface air to mix trace gases (such as DMS) throughout the marine boundary layer and sometimes penetrate the mixed layer inversion, transporting trace gases into the free troposphere [*Cotton et al.*, 1995; *Perry and Hobbs*, 1994; *Sorbjan*, 1996], which is supported by observations [*Bandy et al.*, 2002; *Conley et al.*, 2009; *Faloona et al.*, 2005; *Gregory et al.*, 1993; *Lenschow et al.*, 1999; *Russell et al.*, 1998; *Simpson et al.*, 2001; *Thornton et al.*, 1997].

In fact, observations to date indicate that high concentrations of newly formed sulfate particles (<10 nm in diameter) exist in outflow regions of clouds and are important in the nucleation of biogenic DMS products in the free troposphere [*Clarke et al.*, 1998; *Clarke et al.*, 1999; *Hegg et al.*, 1990; *Perry and Hobbs*, 1994], where they grow and eventually become entrained in the marine boundary layer [*Bates et al.*, 1998a; *Clarke et al.*, 1998; *Clarke et al.*, 2013; *Clarke et al.*, 1996; *Reus et al.*, 2000] to become an important new source of CCN [*Clarke et al.*, 1996; *Katoshevski et al.*, 1999] if rates of entrainment and growth are sufficiently high [*Katoshevski et al.*, 1999; *Korhonen et al.*, 2008; *Merikanto et al.*, 2009; *Raes*, 1995]. Global models estimate that the nucleation of DMS products in the free troposphere and entrainment into the boundary layer contribute less than 10% of CCN in the North Atlantic annually [*Korhonen et al.*, 2008]. However, direct observations confirming or refuting these modeling results are essentially non-existent. A primary challenge for field verification is the time lag that exists between DMS emission, transport to the free troposphere, oxidation, nucleation, entrainment back down to the boundary layer, and condensational growth to CCN [*Dzepina et al.*, 2015; *Korhonen et al.*, 2008; *Woodhouse et al.*, 2010]. One potential

solution to this problem is to use the chemical composition of individual particles in the marine boundary layer to identify CCN sources. Unfortunately, measurements to date have not quantified the sea salt, sulfate, and organic components in individual particles [*Gaston et al.*, 2015; *Middlebrook et al.*, 1998; *Murphy et al.*, 1998a; *Murphy et al.*, 1998b]. The current study addresses this issue.

To provide the direct observations of particle composition needed to constrain and evaluate model simulations of CCN, we measured and categorized the chemical compositions of individual marine boundary layer particles and used correlations of particle types to tracers for natural marine (DMS, NaCl, MSA) and non-marine (black carbon, radon, hydrocarbon fragment [*Zhang et al.*, 2005] $C_4H_9^+$) emission sources to associate measured particle types. Our measurements were conducted during the second Western Atlantic Climate Study (WACS2) and the first and second cruises of the North Atlantic Aerosols and Marine Ecosystems Study (NAAMES1 and NAAMES2). Boundary layer inversion strength (a proxy for entrainment rate) was used to distinguish sulfate condensing in the marine boundary layer (Added Sulfate) from sulfate that formed new particles after the lofting of DMS into the free troposphere and entraining back down into the marine boundary layer (New Sulfate). We also constrained sea salt particle number (Estimated Salt) using measured mass composition to get a complete accounting of particle sources for each study. Finally, we calculated the contributions of salt and sulfate particles to CCN using the size and composition of the different types of marine particles.

3.2 Results

The New Sulfate and Added Sulfate types are the most prevalent type of particles in all of the clean marine air masses that were sampled. For clean marine conditions, the Estimated Salt particles account for 57±22% of CN_{180} in November (NAAMES1) but only 4±3% in May-June (NAAMES2), respectively (Figure 3.1, 3.2). The ambient particle concentrations of each measured type is calculated by scaling the measured fraction of each type to the measured particle size-distribution (from combined Differential Mobility Particle Sizer and Aerodynamic Particle Sizer distributions) after subtracting the Estimated Salt distribution.

3.2.1 Marine Sulfate Sources of Atmospheric Particles

New Sulfate particles accounted for 25±29% and 28±22% of particles greater than 180 nm diameter (CN_{180}) for marine conditions during NAAMES1 and NAAMES2, respectively but less than 15% in continental conditions (Figure 3.1). Classification of ambient air as marine or continental is based on the radon concentration, particle concentration, and back trajectories (Section 3.6.2). Added Sulfate particles account for 31±20% of particles in NAAMES2 marine conditions but only 3±3% of particles in NAAMES1 (Figure 3.1, 3.2, and 3.8). While the marine measurements satisfy the "clean" criteria for radon, condensation nucleation concentrations, and back trajectories, contributions from ship emissions and long-range continental transport to the measured sulfate cannot be entirely ruled out. However, the absence of hydrocarbon fragments (m/z 41, 55, 57) in the sulfate particle composition and the lack or negative correlation of the sulfate particle types with black carbon and

hydrocarbon-like tracers make the contributions of non-biogenic sources small or unlikely. The continental air masses contain less than 10% Added Sulfate particles, consistent with Added Sulfate particles being of marine origin but still contributing a

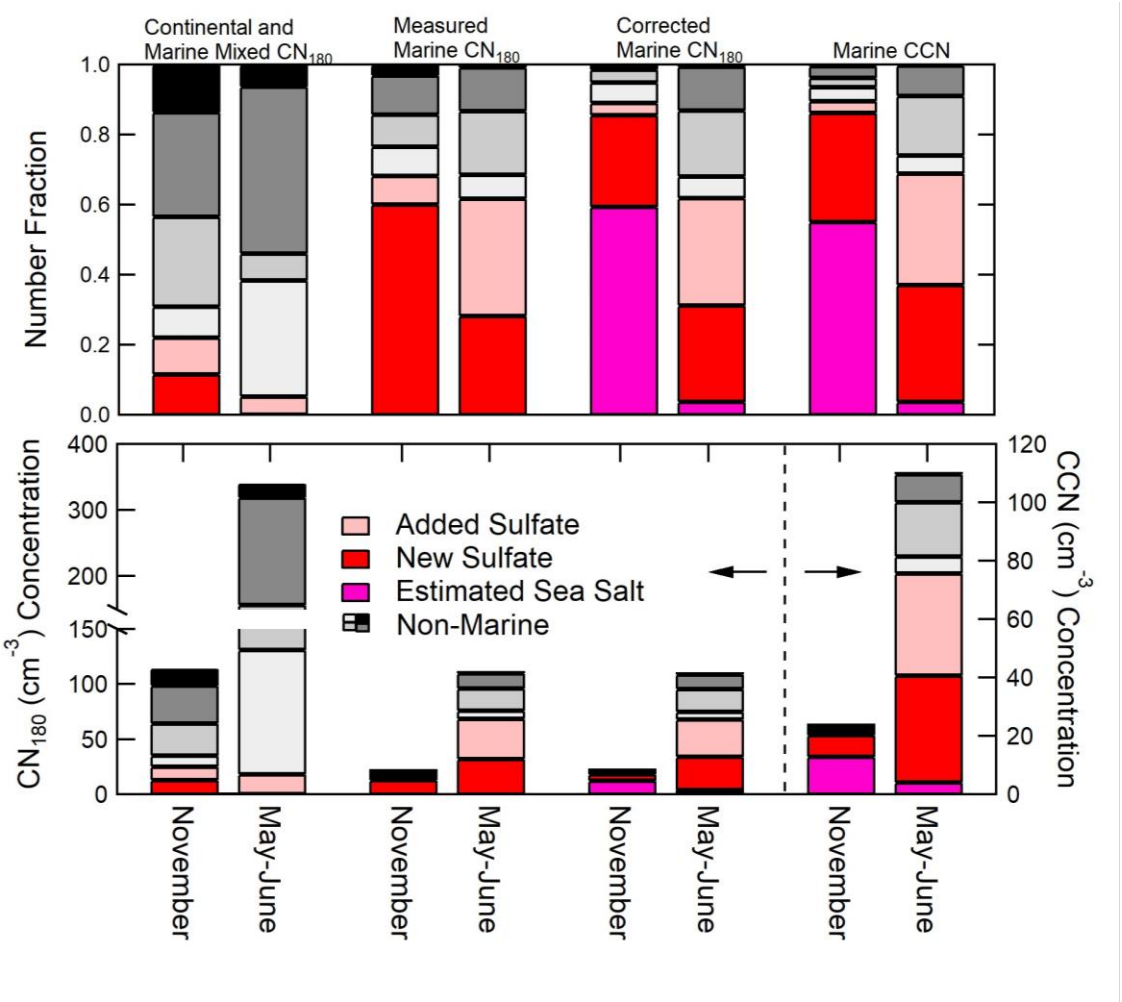

Figure 3.1: Relative (top) and absolute (bottom) contribution of particles with different chemical compositions measured by ET-AMS in NAAMES1 (November) and NAAMES2 (May-June) for air masses separated for continental (radon greater than 1000 mBq m-3) and marine (radon less than 500 mBq m-3 and CN concentrations less than 1000 cm-3) conditions. Contamination events from the ship stack are excluded. For marine conditions, the measured contributions are also corrected to include Estimated Salt particles (calculated from IC sodium) and the distributions are integrated to calculate CCN. For the lower panel, the bars to the left of the dotted line correspond to the left axis, and the bars to the right of the dotted line correspond to the right axis. Labels for both plots are found at the top of the figure.

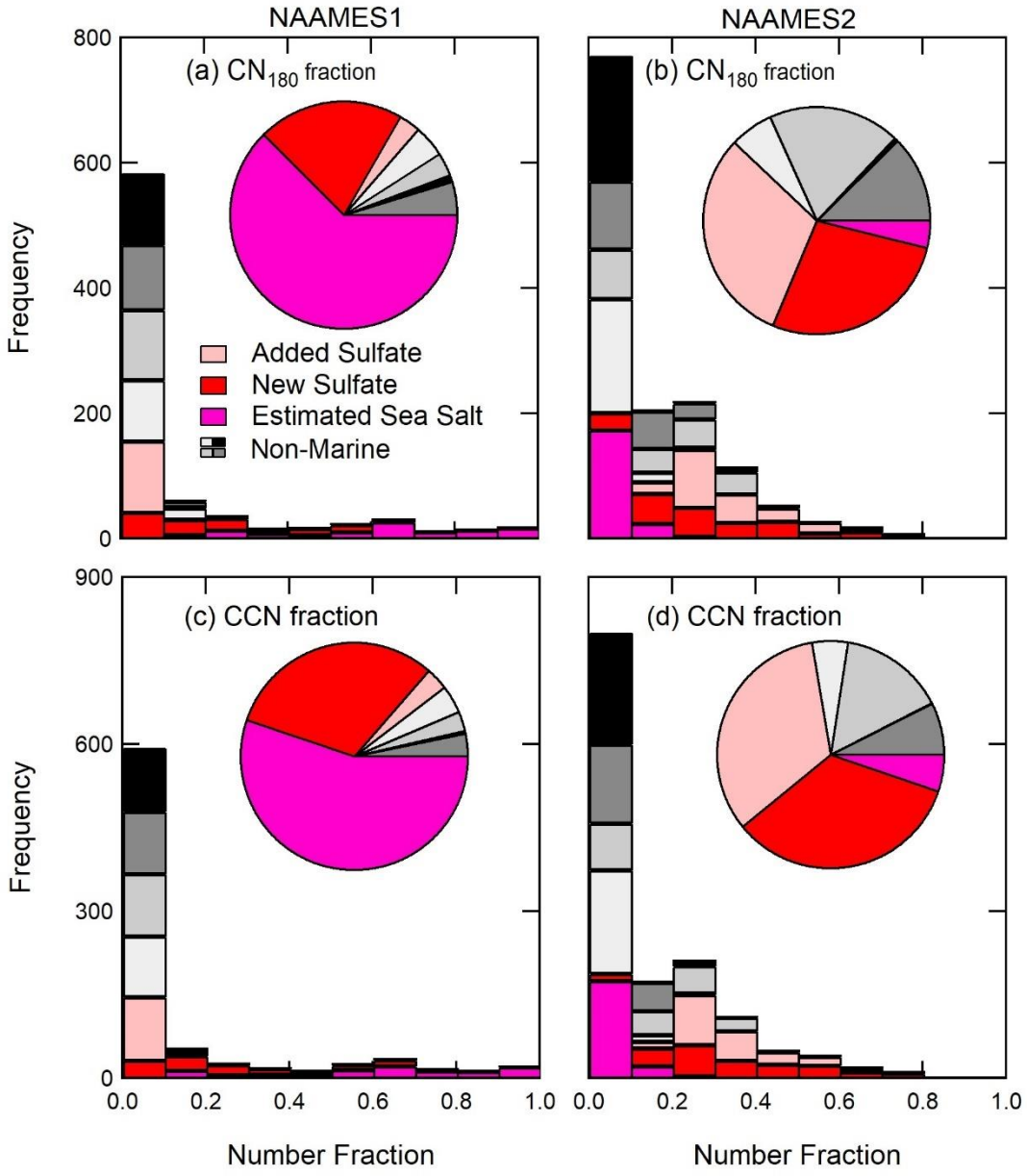

Figure 3.2: Contributions of seven particle types to (a, b) CN_{180} and (c, d) CCN (at 0.1% supersaturation) fraction from clean marine ET-AMS measurements during NAAMES1 and NAAMES2. The histogram frequency represents the number of hours that each particle type accounted for a given number fraction of observed CN_{180} and calculated CCN. WACS2 is excluded because the LS-AMS cut off diameter is 400 nm.

modicum of particles in polluted conditions. Overall these results provide strong evidence that the three most abundant particle types in the clean marine conditions (New Sulfate, Added Sulfate, and Estimated Salt) are produced by natural ocean sources.

Further support for the sulfate particles being not only marine but also biogenic is provided by their composition and their correlation to DMS and its products, which are known tracers of phytoplankton emissions. The New Sulfate particles consist of 63% sulfate by mass and the Added Sulfate particles have only 38% sulfate (Table 3.5). The remaining mass is mostly organic (36% for New Sulfate and 58% for Added Sulfate), but the organic fragments were not characteristic of combustion or other continental sources. Added Sulfate particle number fraction is correlated moderately with atmospheric DMS and MSA concentration during NAAMES2 (Table 3.4, Figure 3.3), indicating Added Sulfate particles are likely formed from the condensation of DMS products onto existing particles in the boundary layer. (Correlations are defined as weak for $|r| > 0.25$ and $|r| < 0.50$, moderate for $|r| >= 0.50$ and $|r| < 0.80$, and strong for $|r| >= 0.80$ [*Devore and Berk*, 2012]). The organic (and sea salt) components in Added Sulfate particles (Table 3.5) suggest that the source of the pre-existing smaller particles onto which sulfate is added could include continental, ship, and sea spray emissions, but the organic mass is too small and mixed to identify specific sources.

Interestingly, atmospheric DMS correlated weakly to New Sulfate particle fraction in NAAMES2 ($r = 0.28$) and did not correlate to any particle types in NAAMES1. This lack of correlation could result from the competition for DMS and its oxidation products with the competing sinks of condensation onto existing particles and

vertical transport to the free troposphere. In addition, the long time lag (12-24 hr) between emission, nucleation in the free troposphere, and entrainment to the marine boundary layer means that the time series of sulfate particles may not correlate with DMS even if DMS is the source. For NAAMES1, we find a weak correlation between the New Sulfate particle fraction and seawater DMS (r = 0.37; Figure 3.3, Table 3.4), while no correlation was observed during NAAMES2. The observed correlation during NAAMES1 may indicate that the cold temperatures (10.7 ±5.7 ºC), low particle numbers (114 ± 116 cm^{-3}), and low particle surface area (17.8 ±9.6 μm^2 cm^{-3}) allowed new sulfate particles to form from DMS products in the boundary layer without requiring the lofting to the free troposphere that otherwise precludes a correlation in time. We investigated lagged correlations but found nothing significant, likely because the time lag is variable and the transport distances can be large [*Korhonen et al.*, 2008].

The average (standard deviation) sea salt fraction of sulfate (ss-sulfate) mass on the three cruises varied by a factor nearly 8, with 12 (15%) for WACS2, 52 (28%) for NAAMES1, and 7 (28%) for NAAMES2 (Table 3.1). NAAMES1 had considerably lower particle concentrations (particle concentrations < 50 cm^{-3}) and frequent northerly winds as well as some periods with significant ss-sulfate mass fractions. The fraction of ss-sulfate correlates moderately and negatively with particle concentration in NAAMES1 (r = -0.71; Figure 3.11), showing that primary marine sea spray particles are a relatively large source in clean Arctic air but a small fraction of higher particle concentrations. During NAAMES2 and WACS2, the highest fractions of ss-sulfate mass were during or just after periods of elevated precipitation rates (Figure 3.12), likely

due to scavenging of particles by precipitation. Scavenging removes all particle types, but sea salt particles are replenished more quickly because sea spray produces particles locally and on shorter time scales than marine biogenic secondary particle production. In summary, these results suggest that the higher ss-sulfate fraction for NAAMES1, relative to NAAMES2, is mostly due the significantly lower biogenic sulfate during NAAMES1.

3.2.2 Entrainment of Particles into the Boundary Layer

Sources of particles measured at the surface in marine conditions include emissions in the boundary layer itself and transport from the free troposphere. To distinguish particles formed in the boundary layer from those entrained from the free troposphere, the strength of the boundary layer inversion (as indicated by Convective Inhibition or CIN, Section 3.6.7) was compared to the number fraction of measured particle types identified by LS-AMS and ET-AMS (Figure 3.4). We find that the New Sulfate particle fraction has a moderate and strong negative correlation to inversion strength for NAAMES1 and NAAMES2, respectively, but that the non-marine particle fractions have weak to strong positive correlations. The stronger negative correlation of New Sulfate particle fraction to CIN ($r = -0.76$) indicates that the New Sulfate number fraction is highest when the boundary layer inversion is weak (indicated by low CIN), providing evidence that New Sulfate particles are frequently entrained from the free troposphere (Figure 3.4). Low CIN may also allow increased mixing of DMS up to the

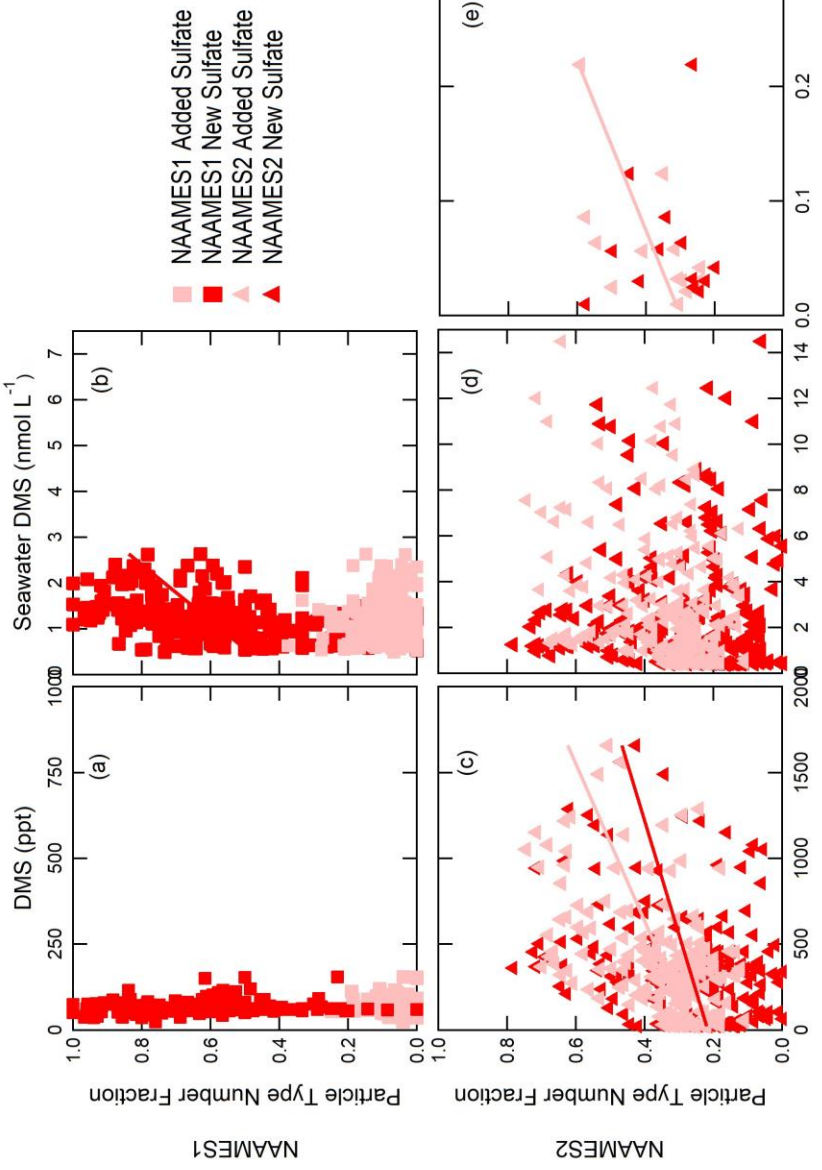

Figure 3.3: Correlations of NAAMES1 (November) and NAAMES2 (May-June) Added Sulfate and New Sulfate non-refractory particle number fraction to (a,c) atmospheric DMS, (b,d) seawater DMS, and (e) particle MSA. WACS2 measurements are too few to include. Pearson's coefficients of correlation are 0.50 and 0.28 for atmospheric DMS to Added Sulfate and New Sulfate particles in NAAMES2, respectively ($p < 0.01$), 0.37 ($p < 0.01$) for seawater DMS to NAAMES1 New Sulfate particles, and 0.60 ($p = 0.03$) for MSA to NAAMES2 Added Sulfate particles. The other relationships show no correlation ($r < 0.25$).

Table 3.1: Observed IC sea salt and sulfate concentrations and CN and CCN concentrations for clean marine ambient periods during WACS2, NAAMES1, and NAAMES2.

	WACS2	NAAMES1	NAAMES2
180 – 550 nm[1]			
Sulfate (μg m^{-3})	0.34 ±0.12	0.07 ±0.10	0.31 ±0.14
Sea salt (μg m^{-3})	0.05 ±0.02	0.25 ±0.15	0.17 ±0.14
Sulfate/Sea salt	7.30 ±3.65	0.25 ±0.25	3.85 ±3.66
Sub-1.1 μm[1]			
Sulfate (μg m^{-3})	0.45 ±0.15	0.14 ±0.15	0.46 ±0.22
Sea salt (μg m^{-3})	0.13 ±0.09	0.99 ±0.63	0.23 ±0.20
Sulfate/Sea salt	11.6 ±16.8	0.39 ±0.89	3.82 ±3.35
CN (cm^{-3})	421 ±127	116 ±114	423 ±239
CN_{180} (cm^{-3})[2]	-	22 ±14	110 ±81
CCN (cm^{-3})[3]	-	22 ±12	71 ±38
Calculated CCN (cm^{-3})[3]	-	26 ±22	90 ±54

[1] Only IC measurements that are in clean marine air >75% of the time are included in the mean and standard deviation calculation.
[2] CN_{180} are calculated from DMPS and APS combined distributions.
[3] Averaged CCN and Calculated CCN are from clean marine periods where CCN, IC, DMPS, and ET-AMS measurements are all available.

free troposphere, providing the source of sulfate [*Bandy et al.*, 2002].

To investigate further these results, we evaluated results from airborne (NASA C-130 aircraft) atmospheric measurements conducted on 20 May 2016 almost directly above the ship (R/V *Atlantis*). These aircraft data indicated surface and free troposphere dry particle size distributions with a mode at approximately 25 nm (Figure 3.5a,b). This particle mode is characteristic of recently formed particles since they have a short lifetime and are too small for combustion or other transported primary emissions [*Williams et al.*, 2002]. Furthermore, we find that these particles are associated with elevated DMS concentrations in the lower free troposphere (Figure 3.5d) and give peak concentrations at 25 nm that are almost three times higher at 1-1.5 km than at the surface

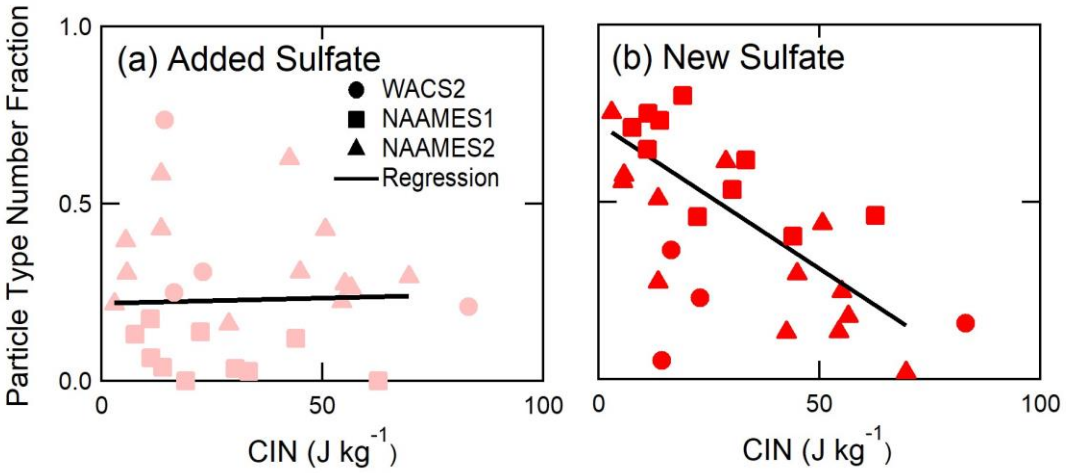

Figure 3.4: Dependence of WACS2 LS-AMS and NAAMES1 and NAAMES2 ET-AMS non-refractory particle number fractions during clean marine conditions on CIN calculated from radiosonde measurements. Pearson correlation coefficients for NAAMES1 and NAAMES2 for CIN are, (a) 0.03 for the Added Sulfate type, and (b) -0.76 for the New Sulfate type ($N = 24$, $p < 0.01$).

(measured both on the aircraft and the ship). This finding provides evidence that the source of these particles is the free troposphere and that they were entrained down into the boundary layer (Figure 3.5a,b and Section 3.6.7). At 25 nm diameter, such particles are not large enough to be active as CCN, but condensational growth from volatile organic compounds and DMS oxidation products can grow them into CCN-sized particles. This process would be consistent with an increase to larger sized particles over time and the observed increase in concentration of the 150 nm mode. For particles with the average chemical composition of New Sulfate (Table 3.6 and 3.7), the minimum (or activation) diameter of CCN at 0.1% supersaturation is 156 nm [*Kohler*,

1936; *Petters and Kreidenweis*, 2007]. Size distributions of pToF-AMS mass and ET-AMS number show that the accumulation mode consisted largely of sulfate mass and, specifically, of New Sulfate particles (Figure 3.5c). This finding provides additional evidence that the entrained particles formed from lofted and oxidized DMS continue to grow to CCN sizes.

Since the New Sulfate particles formed by nucleation of H_2SO_4 in the free troposphere are initially smaller than 3 nm [*Kulmala et al.*, 2004; *Reus et al.*, 2000], condensation of secondary inorganic or organic compounds is needed to grow them to sufficiently large diameters to have lifetimes long enough to be entrained in the boundary layer and to potentially serve as CCN [*Russell et al.*, 2007]. Substantial contributions from organic components would explain why the New Sulfate particles have a significant fraction of organic mass (36%) (Figure 3.6 and Table 3.5).

Furthermore, we suggest that condensation of secondary organic components onto the New Sulfate particles accounts for the New Sulfate particle organic mass fraction, similar to evidence provided by the diurnal cycle of organic components (Figure 3.10).

3.2.3 CCN Source Contributions

Natural marine particle sources can affect atmospheric radiative properties indirectly by modifying cloud properties [*Charlson et al.*, 1987; *Quinn et al.*, 2017; *Shaw*, 1983]. To quantify these radiative effects accurately, climate models need to be able to correctly simulate natural particle number and CCN budgets. The challenge here

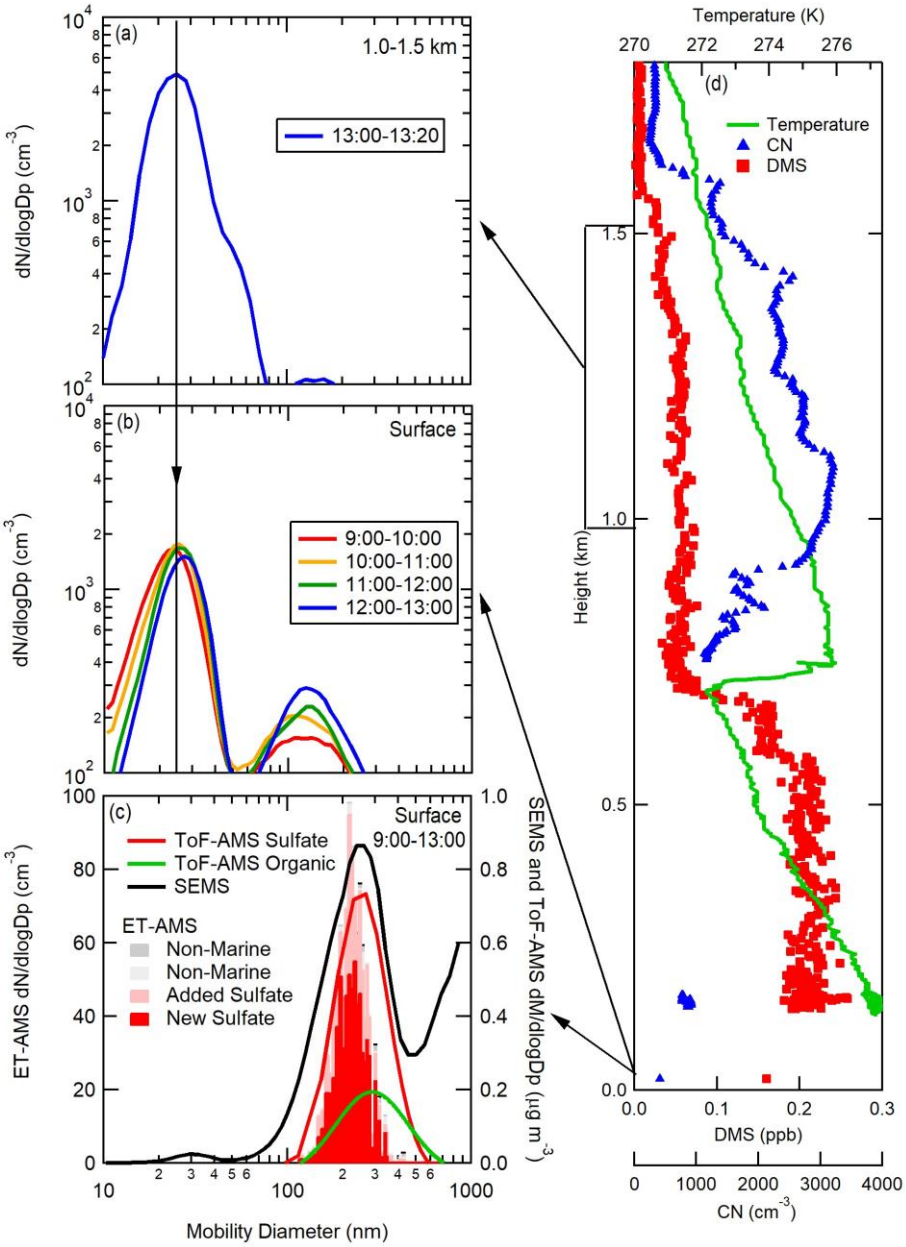

Figure 3.5: Free troposphere (a) and near-surface (b, c) particle size distributions collected on the NASA C-130 aircraft and R/V Atlantis on 20 May 2016 during NAAMES2 (times shown are UTC). The composition of surface measured ET-AMS size distributions are compared to lognormal fits of the sulfate and organic pToF-AMS mass distributions and SEMS mass distributions (c). SEMS number distribution was converted to mass using the campaign average density (1.33 g cm^{-3}). Vertical profiles (d) show temperature, and CN from the MCPC and DMS concentrations from the PTR-MS. The two lowest-altitude CN and DMS values in (d) were collected on board the R/V *Atlantis*. Particle concentrations have been corrected to cm^{-3} volumes at STP. In-cloud measurements of CN are excluded.

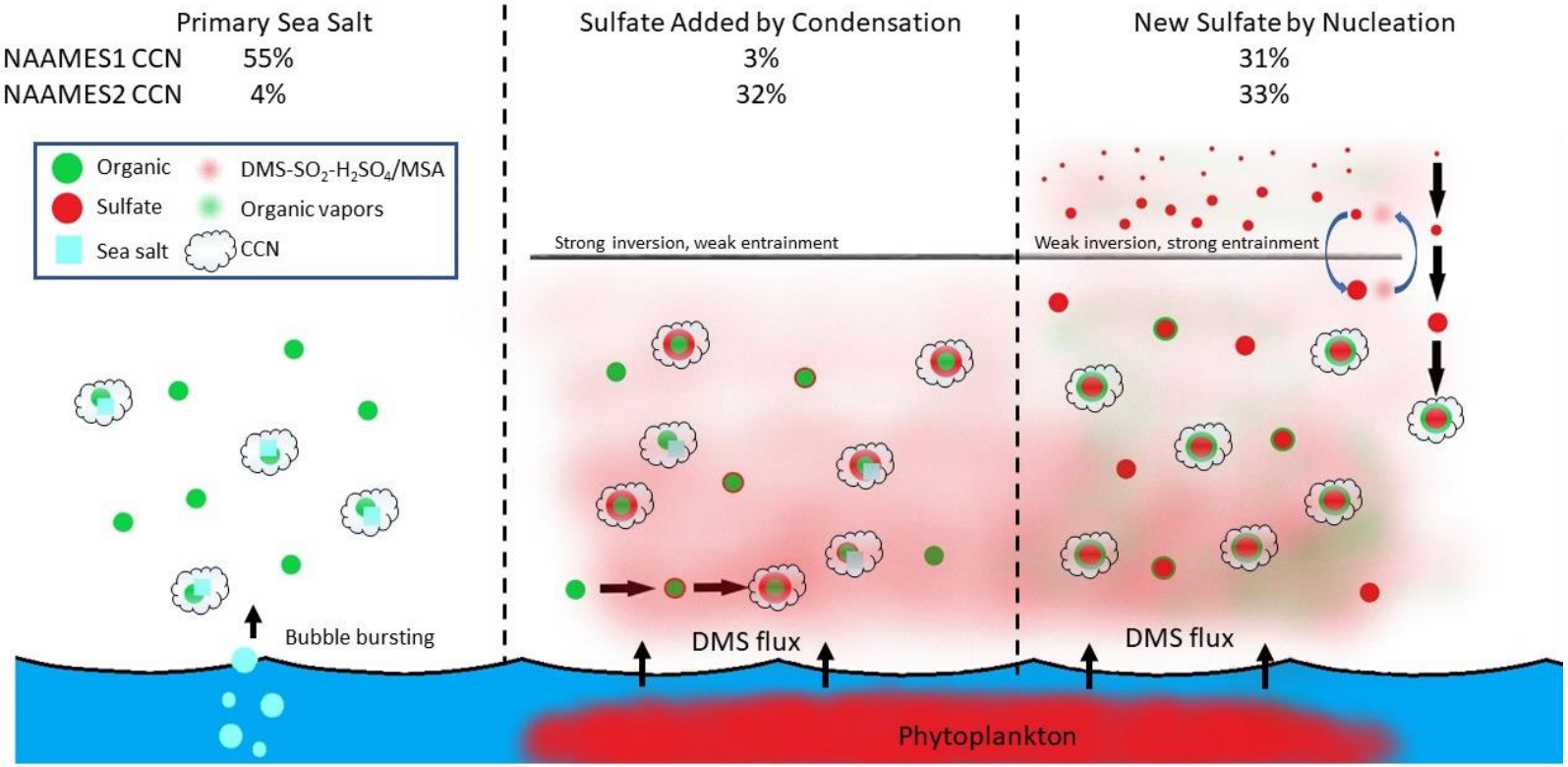

Figure 3.6: Diagram illustrating the three marine sources of particles, namely primary sea salt (Estimated Salt) from bubble bursting, condensation of DMS oxidation products onto existing particles (Added Sulfate particles) in the boundary layer, and nucleation of DMS oxidation products in the free troposphere before entrainment down to the boundary layer (New Sulfate particles). CCN contributions for NAAMES1 (November 2015) and NAAMES2 (May-June 2016) illustrate the substantial seasonal differences.

is that particle budgets are not uniform across oceans or seasons because marine particle sources are controlled by both physical conditions (wind and sea state) and biological processes (DMS emission) (Figure 3.6). In other words, variations in meteorology and ecosystem properties produce different contributions from each of the particle sources. The fraction of those particles that are CCN further depends on particle size and composition-dependent water uptake properties (or hygroscopicity).

We calculated the CCN concentration at 0.1% supersaturation by integrating the number of particles of each type that are larger than the activation diameter of that type (Figure 3.16 and Section 3.6.6). The hygroscopicity parameter (κ) that is needed for calculating the activation diameter of each particle type was estimated from the chemical composition (Table 3.6) as a volume-weighted average of the density and component-specific hygroscopicity of the organic, sulfate, nitrate and sea salt mass (Table 3.7) [*Mochida et al.*, 2011; *Petters and Kreidenweis*, 2007]. We find that the activation diameters at 0.1% supersaturation for Added Sulfate, New Sulfate, and Estimated Salt particles have similar values, ranging from 130 to 183 nm (Table 3.6). For CCN spectra collected at 0.1% intervals, the activation diameter differs by 50 to 68 nm between 0.1% and 0.2% [*Quinn et al.*, 2017; *Schill et al.*, 2015]. What this means is that all three particle types activate in the same supersaturation bin, thus giving a sharp step change in spectra despite their differing chemical compositions. Our calculated CCN concentrations are on average within 16% and 22% of measured CCN concentrations for NAAMES1 and NAAMES2, respectively (Figures 3.1 and 3.2).

From a seasonal perspective, we find that Estimated Salt particles account for 57±22% of CCN in November (NAAMES1), but only 4±3% during the clean marine conditions sampled in May-June (NAAMES2). Since the Estimated Salt particles account for a smaller mass fraction at smaller diameters (<100 nm) [*Quinn et al.*, 2014], these particles would account for fewer CCN at supersaturations higher than 0.1% [*Modini et al.*, 2015]. Excluding the organic component from the Estimated Salt type had no effect on the Estimated Salt CCN concentration because the increase in particle hygroscopicity offsets the decrease in particle size. The significance of these findings is that clouds with higher updraft velocities (such as cumulus) would have larger fractions of New Sulfate and Added Sulfate.

New Sulfate particles accounted for an average of 33±24% of CCN (at 0.1% supersaturation) during NAAMES2 clean marine sampling and for an even greater percentage (55±19%) at times when the boundary layer inversion was weak. For NAAMES1, the New Sulfate particles accounted for 31±37% of CCN for all clean marine air masses and only slightly more (36±24%) during weak boundary layer inversions. Since the New Sulfate particles are small when formed by nucleation, they could frequently represent a larger fraction of particles smaller than the ET-AMS cutoff diameter (145-180 nm, Figure 3.13 and Table 3.3). What these findings suggest is that New Sulfate particles would represent more than 31% and 33% of CCN at supersaturations higher than 0.1% for NAAMES1 and NAAMES2, respectively. Finally, we found that Added Sulfate particles account for 32±20% of CCN (Figure 3.2) and, at higher atmospheric DMS concentrations (>500 ppt), they account for the

majority of CCN for NAAMES2. This same class of particles only accounted for 3±3% of CCN during NAAMES1.

3.3 Discussion

One important finding of this study was that sea spray particles are a large fraction (>50%) of a very small number (25 cm^{-3}) of natural marine CCN at 0.1% supersaturation in November (NAAMES1), largely because the low phytoplankton productivity emits little DMS and consequently few New or Added Sulfate particles. In contrast, the phytoplankton bloom conditions of May-June (NAAMES2) in the North Atlantic provide three times more CCN (90 cm^{-3}), of which less than 5% are from sea spray (Figure 3.1, Table 3.1). Nearly one-third of these CCN (32%) in May-June are produced from DMS oxidation products that nucleate New Sulfate particles, and another third (31%) is from Added Sulfate on pre-existing particles. These substantial seasonal differences in number concentrations provide constraints for models to test their process parameterizations.

An interesting consequence of measuring specific marine particle types is the new evidence for nucleation of DMS products in the free troposphere that is provided by the negative correlation of New Sulfate particles to weak boundary layer inversions (low CIN). This result provides substantial evidence for particle nucleation occurring after lofting DMS to the free troposphere. Going further on this point, the weaker correlation to seawater DMS in NAAMES1 suggests that the colder temperatures and lower particle concentrations of November may have supported nucleation of DMS-derived H_2SO_4 in the boundary layer rather than the free troposphere. This possibility

could also explain the small number (3%) of Added Sulfate particles because New Sulfate formation is a faster sink of DMS oxidation products if transport to the free troposphere is not required. If this interpretation is further substantiated by future studies, it provides strong evidence for the biogenic contribution to cloud radiative properties.

Based on these results, we can also consider what would happen if DMS emissions from phytoplankton were decreased. Removing the DMS oxidation products that nucleate would eliminate all New Sulfate particles to lower CCN by more than 30% in both November and May-June, with the expectation that the organic components would redistribute and condense onto existing particles without increasing CCN. We find that removing the sulfate mass from the Added Sulfate particles (using densities in Table 3.5) results in 60% fewer Added Sulfate CCN at 0.1% supersaturation, indicating that without the condensation of DMS oxidation products there would be 19% fewer CCN in May-June (NAAMES2) but little change (2%) in November (NAAMES1). The summed effects of removing DMS contributions to both Added Sulfate and New Sulfate particles eliminates an average of 9 cm^{-3} CCN (33%) in November (NAAMES1) and 47 cm^{-3} CCN (52%) in May-June (NAAMES2). Alternatively, if we double the biogenic sulfate in November as a hypothetical response to warmer temperatures and more productive phytoplankton, CCN would increase by 33%.

These DMS-driven changes in CCN concentration are expected to influence cloud droplet concentrations, but cloud processes can buffer their impact on cloud properties [*Stevens and Feingold*, 2009]. For example, increased CCN concentrations

could reduce precipitation, which could increase or decrease cloud lifetime [*Albrecht*, 1989; *Stevens and Seifert*, 2008]. But if we consider only the initial changes in cloud drop number concentration associated with the CCN differences for an idealized cloud (100 m thick, 283 K, 0.3 g/kg liquid water at cloud top) that activates all CCN at 0.1%, then the increase in albedo from adding 50% more DMS-related CCN is 13% in November but eliminating biogenic DMS decreases the albedo by 52% in May-June. These results provide the most direct evidence to date of the proposed link between greater DMS emissions and more CCN [*Charlson et al.*, 1987; *Shaw*, 1983] and moreover provide season-specific constraints on the magnitude of its impact on CCN.

3.4 Methods

WACS2, NAAMES1, and NAAMES2 included comprehensive chemical and physical characterization of atmospheric aerosol particles. WACS2 sampled in the northwestern Atlantic aboard the R/V *Knorr* from 20 May to 5 June 2014 between 33°N and 42°N and between 61°W and 71°W. NAAMES1 and NAAMES2 sampled in the North Atlantic from 6 November to 1 December 2015 and 11 May to 5 June 2016, respectively. During NAAMES1 the R/V *Atlantis* transited approximately to the northeast until 55°N at 40°W then headed southward to 40.5°N, 40°W. For NAAMES2, the R/V *Atlantis* followed a similar track, from 56.5°N, 47°W to 44°N, 43°W.

3.4.1 Aerosol Particle Measurements

On all three cruises, ambient particles were collected with a temperature-controlled isokinetic inlet at approximately 18 m above sea level and dried in diffusion

driers before being transported to the instruments reported here. Supermicron particles were removed by a 1.0 µm sharp cut cyclone (SCC 2.229, BGI Inc. US). A condensation particle counter (CPC 3010, TSI Inc., St. Paul, MN) was used to identify contamination from ship exhaust. Submicron particles were analyzed with a high-resolution time-of-flight aerosol mass spectrometer (AMS, Aerodyne Research Inc., Billerica, MA) [*Peter F. DeCarlo et al.,* 2006] that measures non-refractory inorganic (sulfate, ammonium, nitrate, chloride) and organic components.

During WACS2, the AMS included LS-AMS mode to analyze the composition of individual particles [*S Liu et al.*, 2013] for particles with mobility diameter greater than 400 nm [*Frossard et al.*, 2014b]. During NAAMES1 and NAAMES2, the AMS included the ET-AMS mode, which extracted mass spectra for individual particles that had ion signals exceeding pre-set thresholds for three m/z regions [*Price et al.*, 2017]. NAAMES1 ET-AMS thresholds were typically set to 4.5 ions/extraction at m/z 55-79, 6 ions/extraction at m/z 48-150, and 4 ions/extraction at m/z 43 or 2.5 ions/extraction at m/z 48. NAAMES2 used the same m/z regions (excluding m/z 48) but with trigger levels of 8, 9, and 3.5 ions/extraction. Higher trigger levels were chosen for NAAMES2 to account for the higher single ion baseline and air beam intensity associated with the higher particle concentrations. The thresholds were determined using particle-free air. The LS and ET measurements were processed by Sparrow software version 1.04E and Tofware version 2.5.3.b (TOFWERK and Aerodyne Research, Inc.). The pre-processed data were clustered using the clustering input preparation panel (CIPP) v1.2 and the clustering analysis panel (CAP) v1.2 (developed by A. Lee, National University of

Singapore, and M. Willis, University of Toronto), which applies a k-means clustering algorithm to the mass spectra of the particles [*Lee et al.*, 2015; *Lee et al.*, 2016]. Only particles with mass spectra signal-to-noise ratio of greater than 5 were used in the clustering analysis (Table 3.3). WACS2 also included a second AMS with a soot-particle module (SP-AMS, Aerodyne Research Inc., Billerica, MA) operated in standard AMS mode (with tungsten vaporizer on and laser vaporizer off) to evaluate the effect of volatility temperature on salt detection. All diameters from the ET-AMS, LS-AMS and HR-AMS were converted to mobility diameter using a shape factor of 1 and campaign average particle type densities (Table 3.3).

Mass spectra of ambient single particles with diameters greater than 180 nm from the Event-Trigger AMS (ET-AMS) during NAAMES1 (in November 2015) and NAAMES2 (in May and June 2016) were grouped by k-means clustering to identify three types of spectra, all of which are similar to spectra identified by AMS ensemble (non-single-particle) mode measurements: hydrocarbon-like organic aerosols (HOA), oxygenated organic aerosols (OOA), and sulfate-containing particles [*Aiken et al.*, 2008; *Crippa et al.*, 2014; *Frossard et al.*, 2014b; *Lee et al.*, 2015; *Ulbrich et al.*, 2009; *Q Zhang et al.*, 2011] (Figure 3.1, 3.7 and 3.13, and Table 3.3 and 3.4). WACS2 particle type fractions from the Light-Scattering Aerosol-Mass-Spectrometer (LS-AMS) are shown separately (Figure 3.8) for particles greater than 400 nm diameter. The collection efficiency of the HR-AMS sea salt (CE_{SS}) is calculated as $3.26*Na^{+}$, which account for the mass of sodium chloride, magnesium sulfate and other inorganic salts present in seawater, where Na^{+} is the sodium concentration from ion chromatography (IC)

measurements. Non-marine particles are described in Section 3.6.2. The refractory sea salt particles missed by the HR-AMS are calculated as "Estimated Salt" particle number concentration from the ET-AMS number size distribution scaled to the collection-efficiency-corrected HR-AMS sea salt mass (Figure 3.1, 3.2, Section 3.6.4). Sea salt (ss) sulfate is calculated by dividing the amount of sulfate associated with sea salt (7.7% of sea salt mass) [*Holland*, 1978] from the total sulfate mass measured by IC (Table 3.1).

On all three cruises, ambient particles were collected on pre-scanned 37 mm Teflon filters (Pall Inc., 1 μm pore size) for 4 to 24 hr for Fourier transform infrared (FTIR) spectroscopy (Tensor 27 spectrometer, Bruker, Billerica, MA). The particles were dried in diffusion driers and passed through either a 1 μm sharp cut cyclone (SCC 2.229 BGI Inc., U.S.) or a 1.1 μm cut Berner impactor. The FTIR spectrum from each filter was baselined and integrated at specific peak locations to determine the peak areas of the organic functional groups using an automated algorithm [*Maria et al.*, 2002; *Russell et al.*, 2009; *Takahama et al.*, 2013]. Ambient particles were also collected on Millipore Fluoropore filters with a 1.1 μm cut Berner impactor for extraction and IC for sodium, chloride, sulfate, nitrate, and ammonium mass [*Quinn et al.*, 1998].

On all three cruises, a Differential Mobility Particle Sizer (DMPS, University of Vienna [*Winklmeyer et al.*, 1991]) was used to measure the number size distribution of dry submicron (0.02–0.8 μm diameter) ambient particles [*Bates et al.*, 2002]. Radon was measured with a dual-flow-loop two-filter 103 radon detector [*Whittlestone and Zahorowski*, 1998]. During NAAMES1 and NAAMES2, a Scanning Electrical Mobility

Sizer (SEMS, Model 138, 2002, BMI, Hayward, CA) measured particle size distributions and a Single-Particle Soot Photometers (SP2, DMT, Boulder, CO) measured refractory black carbon number and mass concentration [*Betha et al.*, 2017]. Continuous DMS measurements were made by atmospheric pressure chemical ionization mass spectrometers [*Bell et al.*, 2015; *Bell et al.*, 2013]. One instrument was dedicated to air measurements and the other analyzed gas that had been equilibrated with seawater. During NAAMES1 and NAAMES2, a Cloud Condensation Nuclei Counter (CCNC, DMT, Boulder, CO) measured ambient CCN concentrations at 0.1% supersaturation [*Quinn et al.*, 2008].

3.4.2 Aircraft and Balloon Microphysical and Meteorological Measurements

The NASA C-130 aircraft collected aerosol particle measurements between 100 m and 3000 m near the location of the R/V *Atlantis* during NAAMES1 and NAAMES2. A Scanning Mobility Particle Sizer (SMPS TSI, Shoreview, MN) measured ambient aerosol number size distribution (0.01 to 0.3 μm diameter) at multiple heights. A Condensation Particle Counter (CPC 3772, TSI Inc., St. Paul, MN) measured the particle concentration. Both SMPS and CPC measurements are reported at standard temperature and pressure (T = 0 ºC, P = 1013 mb). A Proton-Transfer-Reaction Time-of-Flight Mass Spectrometer [*Muller et al.*, 2014] was used to measure volatile organic compounds including DMS.

Radiosondes (iMet-1) were launched twice daily typically between 1000 and 1200 UTC and between 1800 and 2000 UTC for NAAMES1, NAAMES2 and WACS2.

The radiosondes directly measure temperature, pressure, and relative humidity, which were used to calculate the inversion strength at the top of the marine boundary layer (Section 3.6.7) [*Berkes et al.*, 2016; *Ouwersloot and de Arellano*, 2013]. The inversion strength is useful because it has been shown to be correlated negatively to the entrainment rate [*Lilly*, 1968; *Myers and Norris*, 2013; *B. Stevens*, 2002].

3.5 Acknowledgements

This work was funded by NSF AGS-1360645 and NASA NNX15AE66G. DMS measurements aboard the NASA C-130 were supported by the Austrian Federal Ministry for Transport, Innovation and Technology (bmvit) through the Austrian Space Applications Programme (ASAP) of the Austrian Research Promotion Agency (FFG). We thank Tim Onasch, Bill Brooks and Leah Williams for assistance with AMS operation and maintenance. We thank Amanda Frossard for advice on the analysis of marine AMS measurements. We thank Derek Coffman, Jim Johnson, Cyril McCormick and the crew of *R/V Atlantis*, and the crew of the *R/V Knorr* for their contributions to successful measurements at sea.

Chapter 3, in full, has been submitted to *Nature: Scientific Reports*. Sanchez, K.J., C. Chen, L.M. Russell, R. Betha, J. Liu, D.J. Price, P. Massoli, L.D. Ziemba, E.C. Crosbie, R.H. Moore, M. Müller, S.A. Schiller, A. Wisthaler, A.K.Y. Lee, P.K. Quinn, T.S. Bates, J. Porter, T.G. Bell, E.S. Saltzman, R.D. Vaillancourt, M.J. Behrenfeld, "Higher Contributions of Marine Sulfate than Sea Spray to Cloud Condensation Nuclei in Late Spring than in Late Autumn." The dissertation author was the primary investigator and author of this paper.

3.6 Appendix

This section provides additional details on the particle type clustering criteria, the Non-Marine particle types, the sea salt mass correction, the Estimated Salt correction, the HR-AMS vaporizer temperature effects, the hygroscopicity and CCN calculations, and the inversion strength calculations.

3.6.1 Particle Type Clustering Criteria

Table 3.3 summarizes the single particle measurements from WACS2, NAAMES1, and NAAMES2. The individual particle mass spectra were grouped using k-means clustering into 7-10 clusters, which were then compared and similar clusters were identified and combined. NAAMES1 and NAAMES2 ET-AMS ambient particles included one HOA, three OOA and two sulfate clusters; WACS2 LS-AMS types were the same but had no HOA type (Figure 3.7). The sulfate particle types have peaks at m/z marine aerosol [Frossard et al., 2014b]. The HOA cluster was similar to primary emissions from fossil fuel (FF) combustion [Lanz et al., 2007; Q Zhang et al., 2011]. The three OOA clusters include one with mostly less oxidized (LO) organic components, one with more oxidized (MO) organic components, and a third considered to be “mixed continental” (MC) because it contains both sulfate and organic mass and

Table 3.2: Selected references on DMS as a marine aerosol source.

Relevant Findings	Ref.	Location	Observations or Model
Relationship between DMS and CCN			
DMS-derived sulfate aerosol account for most of the CCN in the remote marine boundary layer.	[*Charlson et al.*, 1987]	Global	Model plus Observations
MSA and CCN vary seasonally and have a non-linear relationship.	[*Ayers and Gras*, 1991]	Cape Grim	Observations
DMS and CCN in boundary layer are strongly (non-linearly) correlated.	[*Hegg et al.*, 1991]	NE Pacific	Observations
CCN and DMS are correlated but relationship can be nonlinear because of SO_2 sinks.	[*Russell et al.*, 1994]	N/A	Model
CN correlates strongly with atmospheric DMS and DMS flux but weakly with CCN.	[*Andreae et al.*, 1995]	S. Atlantic	Observations
Modeled CN and CCN correlate with DMS flux; free tropospheric entrainment affects CN and CCN concentration in the marine boundary layer.	[*Raes*, 1995]	N/A	Model
New Particle Formation from DMS Products			
The number of particles formed by homogeneous nucleation depends on the preexisting aerosol concentration.	[*Warren and Seinfeld*, 1985]	N/A	Model
Particle number concentration increases rapidly after a decrease in particle surface area and increase in SO_2 concentration.	[*Covert et al.*, 1992]	NE Pacific	Observations
After precipitation, marine boundary layer aerosol particles can be replenished from new particles formed by nucleation if DMS concentrations are high.	[*Pirjola et al.*, 2000]	N/A	Model
Evidence of New Particle Formation in the Free Troposphere			
Vertical profiles of Aitken mode aerosol concentrations showed maximum values just above cloud tops.	[*Hegg et al.*, 1990]	NW and NE Pacific	Observations
Aerosol nucleation is observed above cloud top and downwind of cloud outflows.	[*Perry and Hobbs*, 1994]	N. Pacific	Observations
CN and CCN were replenished on time scales of 2-4 days with transported nuclei from the free troposphere after precipitation scavenging.	[*Clarke et al.*, 1996]	Christmas Island	Observations
Variability in marine boundary layer aerosol concentration is closely linked to changes in vertical transport.	[*Raes et al.*, 1997]	NE Atlantic	Observations
Nucleation is observed in the free troposphere but not the marine boundary layer, and it is observed more frequently for particle surface area less than 5-10 μm^2 cm^{-3}.	[*Clarke et al.*, 1998]	Southern Ocean	Observations
CN concentration in the marine boundary layer is controlled by the rate of entrainment from the free troposphere in most conditions.	[*Katoshevski et al.*, 1999]	N/A	Model
Observed growth rates of new particles in the free troposphere cannot be explained by SO_2 products and water vapor so other components must contribute to condensation.	[*Reus et al.*, 2000]	NE Atlantic	Model/Observations
New sulfate particles do not form in the marine boundary layer but instead in the free troposphere and then are entrained downward.	[*Kazil et al.*, 2006]	Global	Model
Entrainment of nucleated sulfate particles from the free troposphere account for 43-65% of CCN, but only 7-20% in the winter; long range transport of marine CCN results in a time lag between CCN and DMS concentrations.	[*Korhonen et al.*, 2008]	Southern Ocean	Model
45% of marine boundary layer CCN (at 0.2%) are from nucleation that occurred in the free troposphere.	[*Merikanto et al.*, 2009]	Global	Model
Sulfate particles from DMS mixed up to the free troposphere are a source of marine boundary layer CCN.	[*Clarke et al.*, 2013]	Tropical Pacific	Observations

Table 3.3: Cumulative number of single particle measurements for WACS2, NAAMES1 and NAAMES2.

Statistic	WACS2 (LS-AMS)	NAAMES1 (ET-AMS)	NAAMES2 (ET-AMS)
Total triggers	1471	2460399	2392300
Prompt particles[1]	362	85909	159359
D_{min} (nm)[2]	400	145	180

[1]Prompt particles are those that have above the minimum S/N of 5 and greater than 10 ions measured within 200 μs of impacting the vaporizer surface.
[2]The minimum mobility particle diameter is defined as the smallest diameter with a 5% collection efficiency.

correlates moderately with radon during NAAMES2 (r = 0.55). The MO, LO, FF and MC particle number concentrations correlate with one or more continental tracers and are typically higher fractions of particle number in continental air masses and therefore are identified as Non-Marine particles (Figure 3.1, 3.8 and Table 3.4). The FF, LO and MO organic and two sulfate particle types were similar to previously measured mass spectra (Table 3.4), with cosine similarity ranging from 0.6 to 0.8. The main differences among the sulfate particle mass spectra were the relative amounts of sulfate and organic peaks, which was likely caused by differences in fragmentation associated with matrix effects and vaporizer inhomogeneities rather than differences in composition. Consequently, the sulfate spectra were grouped into two types, one that contained mostly sulfate mass and one that contained mostly organic mass (Table 3.5). The time series of the two sulfate clusters were correlated weakly (r < 0.4).

3.6.2 Non-Marine Particle Types

The Non-Marine particle types identified from the ET-AMS and LS-AMS mass spectra are likely from different primary and secondary emission contributions [*Cross et al.*, 2009; *Lee et al.*, 2015; *S Liu et al.*, 2013]. Radon is a continental tracer (the main source is soil) that has been shown to be correlated to other emissions from land-based sources [*Dorr and Munnich*, 1988]. We use the level of radon and CN to separate marine (radon < 500 mBq m^{-3}, CN < 1000 cm^{-3}) and continental (radon > 1000 mBq m^{-3}, CN > 1000 cm^{-3}) air masses for the three campaigns (Figure 3.1 and 3.8) [*Bates et al.*, 2008]. Marine conditions also had back trajectories that spent more than 75% of the preceding 5 days over the ocean. Continental measurements are not shown for WACS2, because very few measurements had high radon concentrations. The clean marine periods with IC measurements that are used in Table 3.1, Figure 3.1, 3.8, 3.11 and 3.12 are 17:35 21 May 2014 – 22:04 21 May 2014, 23:24 28 May 2014 – 10:41 31 May 2014, 22:18 11 November 2015 – 08:00 17 November 2015, 19:00 18 November 2015 – 08:00 20 November 2015, 19:36 22 November 2015 – 06:41 24 November 2015, 10:30 15 May 2016 – 7:55 17 May 2015, and 18:17 24 May 2016 – 09:10 01 June 2015.

The LO particle type contributes the largest fraction of particle number to continental air masses (Figure 3.1) and correlates moderately with radon in both NAAMES1 (r = 0.40) and NAAMES2 (r = 0.49). The FF particle type is also more abundant in continental air than marine air for both NAAMES1 and NAAMES2. This FF particle type correlates moderately to a previously identified AMS marker fragment associated with fossil fuel combustion C_4H_9 (r = 0.70) [*Q Zhang et al.*, 2005] and to

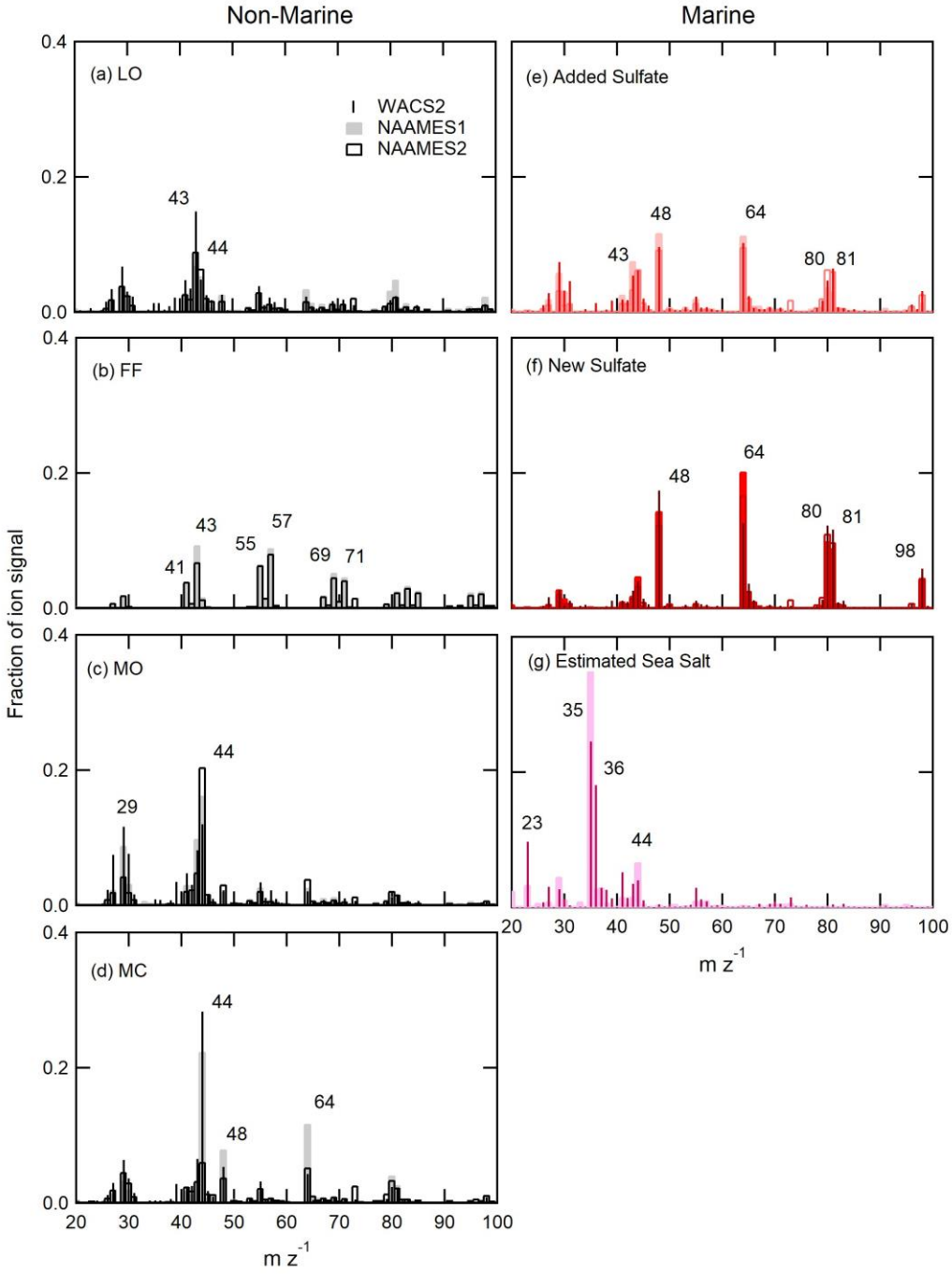

Figure 3.7: The average mass spectra for particle types from LS-AMS during WACS2 and the ET-AMS during NAAMES1 and NAAMES2. All mass spectra are from ambient measurements except for the Estimated Salt type, which is from SeaSweep measurements. There are no mass spectra for the FF particle type in WACS2 because it was not measured in that project. There are no mass spectra for the Estimated Salt particle type in NAAMES2 because the ET-AMS regions of interest did not include m/z 23, 35 or 58.

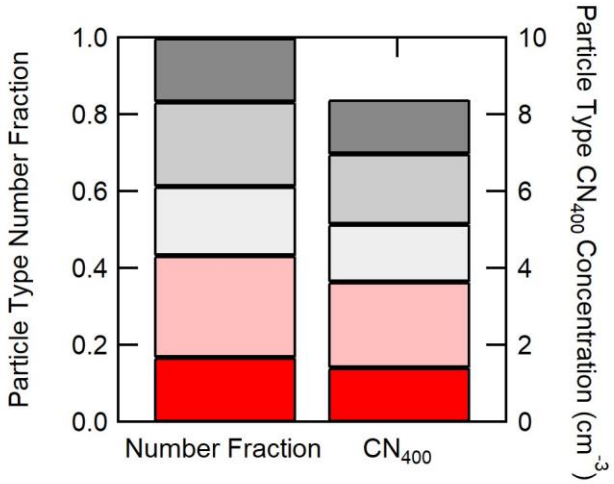

Figure 3.8: WACS2 non-refractory LS-AMS particle type number fraction and CN greater than the LS-AMS minimum cut diameter of 400 nm (CN_{400}) for clean marine periods. WACS2 included only limited time for sampling ambient air and so only four times were available for LS-AMS measurements (more than 3 hr).

black carbon number concentration (r = 0.54) [*Price et al.*, 2017], suggesting these particles come from anthropogenic fossil fuel combustion sources that could include ships (Figure 3.9).The FF particles were also measured at high concentrations when the ship stack was upwind of the sampling line (time periods with ship stack contamination are excluded from both the continental and clean marine periods). The FF particle type was not identified in the WACS2 LS-AMS measurements, likely because there were no periods with continentally-influenced air masses or with ship stack emissions. The MC particle type also likely has a continental source because of the moderate correlation to radon in NAAMES2 (r = 0.55, Table 3.4) and its higher concentration during continental conditions in NAAMES2 (Figure 3.1). The MC particle type contributes a much smaller fraction of particles during continental periods in NAAMES1 than NAAMES2, in line

Table 3.4: NAAMES1 and NAAMES2 single particle aerosol types identified by ET-AMS and their compositions and correlations to tracers. The characteristic m/z peaks for each particle type (shown in Figure 3.7) are listed in order of abundance. WACS2 is not included because there were not enough measurements to correlate time series. Weak correlations (|r| >= 0.25 and |r| < 0.50), moderate correlations (|r| >= 0.50 and |r| < 0.80) and strong correlations (|r| >= 0.80) are in bold. Correlations are for all ambient measurements, except for MSA and DMS, which were only correlated with measurements in clean marine air masses.

Particle Types	Correlations (r) Radon	Black Carbon	fC_4H_9	$fC_2H_4O_2$	MSA[1]	CIN	DMS: Atmospheric (Seawater)	References for Comparison
NAAMES1								
Non-Marine MO	**0.30**	0.05	**0.32**	**0.32**	-	**0.40**	0.05 (-0.27)	[*Ulbrich et al.*, 2009] (OOA-1), [*Crippa et al.*, 2013] (LV-OOA)
MC	0.05	0.12	0.04	0.04	-	**0.48**	0.22 (-0.16)	[*J Liu et al.*, 2017] (cluster82), [*Budisulistiorini et al.*, 2015] (IEPOX OA)
LO	**0.40**	-0.06	**0.40**	**0.40**	-	**0.81**	0.15 (-0.22)	[*Ulbrich et al.*, 2009] (OOA-2), [*Crippa et al.*, 2013] (SV-OOA)
FF	0.07	0.23	0.11	0.11	-	**0.59**	0.01 (-0.11)	[*Lanz et al.*, 2007] (HOA), [*Q Zhang et al.*, 2011] (HOA)
Added Sulfate	0.09	-0.01	0.16	0.16	-	**-0.42**	0.00 (-0.13)	[*Schmale et al.*, 2013] (MSA-OA)
New Sulfate	**-0.44**	-0.05	**-0.46**	**-0.45**	-	**-0.74**	-0.17 (**0.37**)	This study
NAAMES2								
Non-Marine MO	-0.20	0.04	0.13	**0.49**	**-0.60**	**0.62**	**-0.51** (-0.28)	[*Ulbrich et al.*, 2009] (OOA-1), [*Crippa et al.*, 2013] (LV-OOA)
MC	**0.55**	-0.06	0.04	0.08	0.06	**0.61**	0.03 (0.29)	[*J Liu et al.*, 2017] (cluster82), [*Budisulistiorini et al.*, 2015] (IEPOX OA)
LO	**0.49**	0.01	0.16	**0.43**	**-0.63**	**0.83**	**-0.56** (-0.29)	[*Ulbrich et al.*, 2009] (OOA-2), [*Crippa et al.*, 2013] (SV-OOA)
FF	0.01	**0.48**	**0.70**	0.04	**-0.36**	**0.52**	-0.03 (0.07)	[*Lanz et al.*, 2007] (HOA), [*Q Zhang et al.*, 2011] (HOA)
Added Sulfate	**-0.25**	-0.24	0.15	**-0.48**	**0.60**	-0.16	**0.50** (**0.32**)	[*Schmale et al.*, 2013] (MSA-OA)
New Sulfate	**-0.32**	-0.15	0.16	**-0.28**	**0.30**	**-0.81**	**0.28** (0.01)	This study

[1] MSA measurements in NAAMES1 were below detection limit so no correlations are reported.

Table 3.5: The high m/z peaks and measured mass fractions of organic, sulfate, nitrate and sea salt components in the average or centroids of the clusters of single-particle mass spectra.

Particle Types	Organic (%)	Sulfate[1] (%)	Nitrate (%)	Salt (%)	Major m/z Fragments
WACS2					
Non-Marine More Oxidized organics (MO)	80.7	7.6	8.6	3.0	44, 29, 43
Continental Mixed (MC)	79.0	15.1	4.6	1.4	44, 29, 48
Less Oxidized organics (LO)	79.5	10.7	4.8	5.0	43, 29, 41
Fossil Fuel combustion (FF)	-	-	-	-	-
Added Sulfate	57.8	35.3	4.2	2.7	48, 64, 29
New Sulfate	37.9	60.6	1.0	0.5	48, 64, 80
Estimated Salt	-	-	-	-	-
NAAMES1					
Non-Marine More Oxidized organics (MO)	85.5	9.6	4.4	0.5	44, 43, 29
Continental Mixed (MC)	65.5	31.2	2.7	0.6	44, 64, 48
Less Oxidized organics (LO)	74.5	20.9	3.7	0.9	43, 44, 55
Fossil Fuel combustion (FF)	93.1	5.7	0.7	0.5	43, 57, 55
Added Sulfate	60.4	34.8	4.1	0.7	48, 64, 43
New Sulfate	35.3	62.3	1.9	0.5	64, 48, 80
Estimated Salt	20.8	6.0	1.5	71.7	35, 36, 23
NAAMES2					
Non-Marine More Oxidized organics (MO)	81.1	15.1	3.4	0.5	44, 43, 29
Continental Mixed (MC)	71.3	22.5	5.9	0.3	44, 64, 29
Less Oxidized organics (LO)	81.8	12.0	5.7	0.5	43, 44, 29
Fossil Fuel combustion (FF)	92.8	5.7	0.8	0.6	57, 43, 55
Added Sulfate	55.2	42.2	2.1	0.5	64, 48, 44
New Sulfate	35.7	62.7	1.3	0.3	64, 48, 80
Estimated Salt[2]	20.8	6.0	1.5	71.7	35, 36, 23

[1]Sulfate mass fraction is corrected as described in Section 3.6.3.
[2] The Estimated Salt particle type for NAAMES1 is used for NAAMES2 because the ROIs for the ET-AMS were not optimized to collect sea salt particles during NAAMES2.

with the generally lower concentrations and cleaner conditions during NAAMES1 in both continental air (1070 ± 720) and marine air (116 ± 114). Note that there is still approximately 10 times higher number concentration of MC particles in continental conditions than in marine conditions.

The MO particle type is not consistently higher or lower in continental air masses than in marine air masses, suggesting a particle type that forms in both marine and continental air masses. The MO particle type has almost the same ET-AMS chemical composition as the LO particle type (Table 3.5) but a higher fraction of oxidized organic fragments (m/z 44, CO_2; m/z 29, CHO) than the LO type. This suggests that the MO particle type consists of marine or continental particles that have had a longer residence time in the atmosphere and have accumulated a substantial amount of

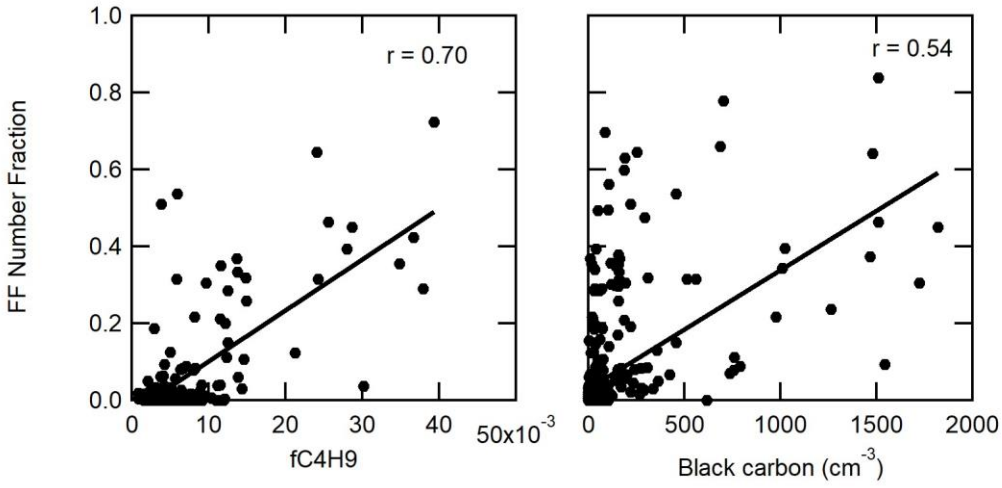

Figure 3.9: The correlation of the fraction of the FF particle type to AMS organic fraction of C_4H_9 (a fossil fuel combustion tracer; left) and to black carbon number concentration (right) for NAAMES2. WACS2 LS-AMS measurements did not have FF particles and NAAMES1 contained too few FF particle measurements for correlation so are excluded.

photochemically-produced secondary organic aerosol. This long residence time in the atmosphere would also explain the lack of association with either marine or continental emission tracers. In NAAMES2, the MO and LO types both correlate weakly to an AMS biomass burning marker fragment (m/z 60, $C_2H_4O_2$), suggesting the transported particles may include contributions from wildfire emissions [*Crippa et al.*, 2014] with longer (MO) or shorter (LO) residence times. The diurnal variation of the ratio of MO to LO particles also provides evidence of condensation of secondary organic compounds onto particles in the marine boundary layer (Figure 3.10). The greater MO particle fraction in the afternoon suggests secondary organics are condensing onto LO particle types. In effect, MO particles cannot be identified with specific emissions because their source signatures are largely atmospheric rather than marine or continental. The ratio of the MO to LO particle concentration has a peak in late afternoon, suggesting that LO particles are being oxidized to form more MO particles (Figure 3.10).

MO, MC, LO and FF particles account for 1%, 1%, 1% and 0%, respectively, for NAAMES1 and 11%, 4%, 6%, and 0%, respectively, for NAAMES2. MC and FF particles have small contributions to CCN because they are from continental and anthropogenic sources that are largely excluded during clean marine conditions. The small but consistent fraction of the MC and LO particles that account for up to 11% of CCN are consistent with contributions from non-marine sources observed in other clean marine conditions [*Frossard et al.*, 2014a; *Shank et al.*, 2012].

3.6.3 Sea Salt Mass Calculation

The sea salt in all particle types is estimated using the sum of chloride peaks in their mass spectra. WACS2, NAAMES1, and NAAMES2 included comprehensive chemical and physical characterization of particles from SeaSweep [Bates et al., 2012] which generates particles on the sea surface, free of influence from or processing in ambient air [Bates et al., 2012]. The sea salt type measured from SeaSweep (Figure 3.7) for NAAMES1 has a lower sulfate/chloride ratio than expected (0.16) [Holland, 1978] for seawater. The sulfate ion fraction was corrected from1% to 5% for consistency with the expected sulfate/chloride ratio of 0.16 (Table 3.5). The chloride and corrected sulfate ion fraction is divided by 0.627, the mass fraction of chloride and sulfate in seawater [Holland, 1978]. During NAAMES1 SeaSweep measurements, the ET-AMS m/z 43 region, used for ambient measurements, was replaced by m/z 23, 35 or 58 to measure sea salt particles. The sea salt type was not observed in NAAMES2 because the ET-AMS did not select for m/z 23, 35 or 58. NAAMES1 sea salt composition was used for NAAMES2 sea salt because the campaigns contain similar sea salt mass concentrations (Table 3.1).

SeaSweep particles were also collected on Millipore Fluoropore filters with a 1.1 µm cut Berner impactor for extraction and IC for sodium [Quinn et al., 1998]. The IC measurements of Na^+ collected on PM1 filters were used to calculate the mass of sea salt as $3.26*Na^+$ (based on calculations from Quinn et al. [2014] and the ratio of sea salt ions in seawater [Holland, 1978]). The HR-AMS sea salt collection efficiency (CE_{ss})

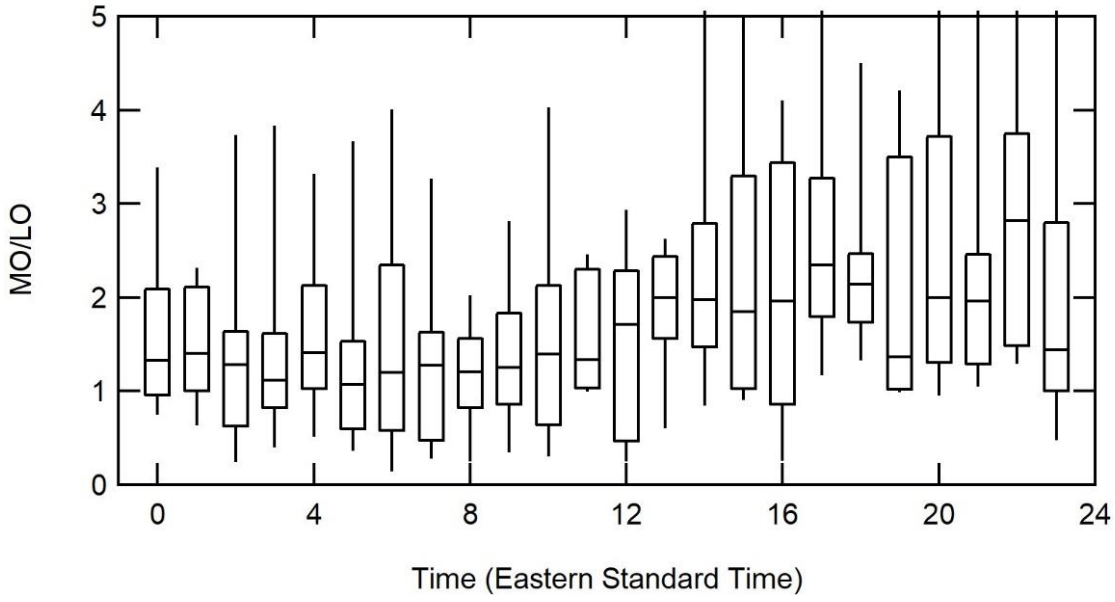

Figure 3.10: Diurnal averaged number ratio of MO to LO particles for clean marine periods during NAAMES2. There are insufficient measurements of MO and LO during WACS2 and NAAMES1 so they are not shown.

[*Frossard et al.*, 2014b] was calculated as the ratio of the summed salt masses (Cl^+, HCl^+, $NaCl^+$, Na_2Cl^+, KCl^+, $MgCl^+$, $^{37}Cl^+$, $H^{37}Cl^+$, $Na^{37}Cl^+$, $Na_2\ ^{37}Cl^+$, $K^{37}Cl^+$, $^{41}KCl^+$, $^{41}K^{37}Cl^+$ and $Mg^{37}Cl^+$) to the IC sea salt mass. The Berner impactor stages for the 180 nm – 550 nm diameter range are used because salt below 180 nm was below detection and HR-AMS does not measure 50% of particles above 700 nm (Figure 3.13).

3.6.4 Estimated Salt Correction

The Estimated Salt particle concentration is determined by apportioning the sea salt mass calculated from the HR-AMS salt mass after correction by CE_{ss} to the ET number distribution as follows:

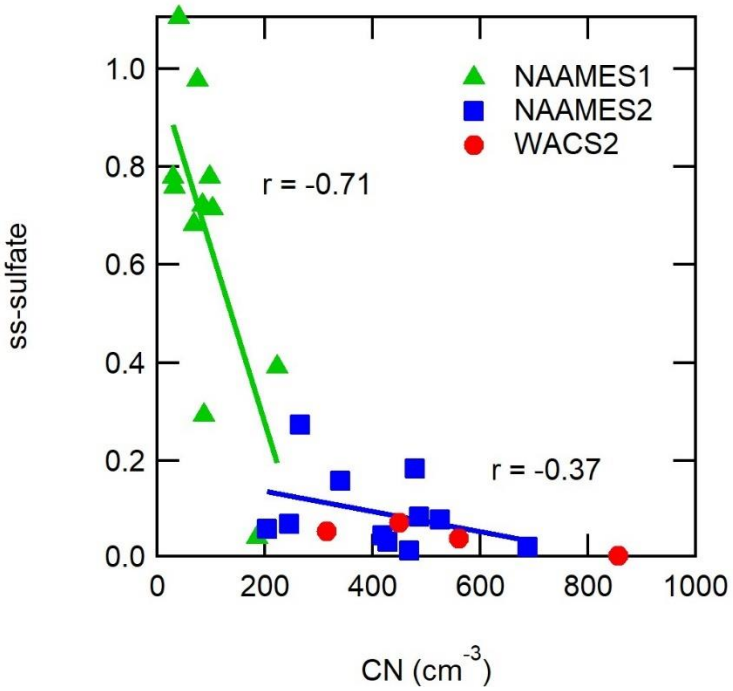

Figure 3.11: The ss-sulfate fraction, calculated from measurements of IC sodium, chloride and sulfate, is compared to condensation nuclei (CN) concentrations for each campaign during clean marine periods. Linear regressions are shown for NAAMES1 and NAAMES2, which have correlation coefficients of -0.71 and -0.37, respectively.

$$N_{ETsalt,j} = (1 + X_{sweep}) \frac{M_{HRSS}}{CE_{SS}} \frac{N_{ET,j}}{\sum M_{ET,j}} \quad (3.1)$$

$N_{ET,j}$ is the number concentration of the campaign average ET-AMS particle number concentration of all ET-AMS types at particle diameter j. $M_{ET,j}$ is the ET-AMS particle mass calculated from $N_{ET,j}$ using a density of 1.73 g cm^{-3} (from 70% sodium chloride, 10% sulfate, and 20% organic components based on the SeaSweep sea salt particle composition). The limits on the $M_{ET,j}$ summation are the size cuts of the IC samples (180 nm to 550 nm) to which the HR-AMS CEss is calibrated. The small number of salt

particles larger than the 550 nm mobility Diameter cutoff of ET-AMS (< 3 cm^{-3} for NAAMES1 and < 6 cm^{-3} for NAAMES2) was not included. M_{HRSS} is the HR-AMS sea salt mass, and X_{sweep} is the sea salt organic mass fraction observed during SeaSweep (Table 3.5). $CE_{SS} = M_{HRSS}/M_{ICSS}$ where M_{ICSS} is the mass of IC sea salt, which is calculated from 3.26* Na^+ to account for the mass of sodium chloride, magnesium sulfate and other inorganic salts present in seawater. The activation diameter for the Estimated Salt at 0.1% supersaturation is 130 nm (Table 3.6).

3.6.5 HR-AMS Vaporizer Temperature Effects

WACS2 sampled with SeaSweep deployed at five stations with a range of chlorophyll-a concentrations. Phytoplankton pigments (chlorophyll *a*, Chl-a) in seawater samples were collected from the R/V *Knorr* underway line (depth = 5m) and

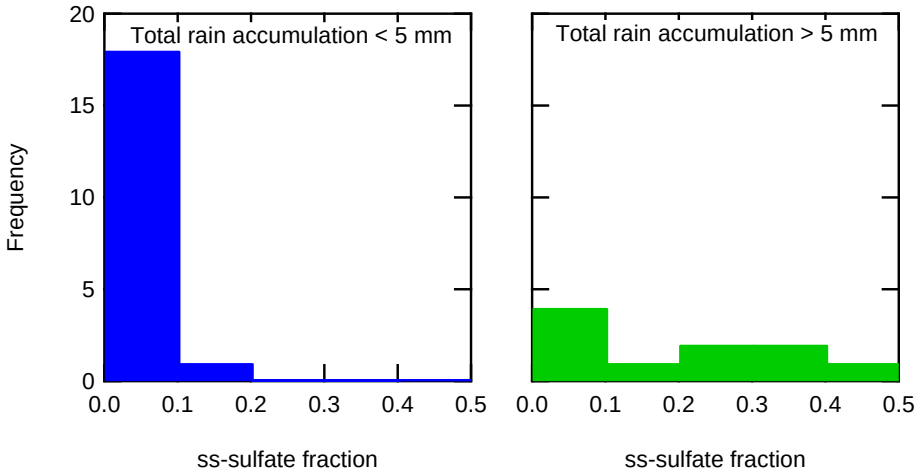

Figure 3.12: The ss-sulfate fraction is calculated from sub 1.1 µm measurements of IC sodium and sulfate. Total rain accumulation is calculated by integrating the rain accumulation from six hours before the IC filter sample start time to the filter sample end time for the NAAMES2 and WACS2 campaigns.

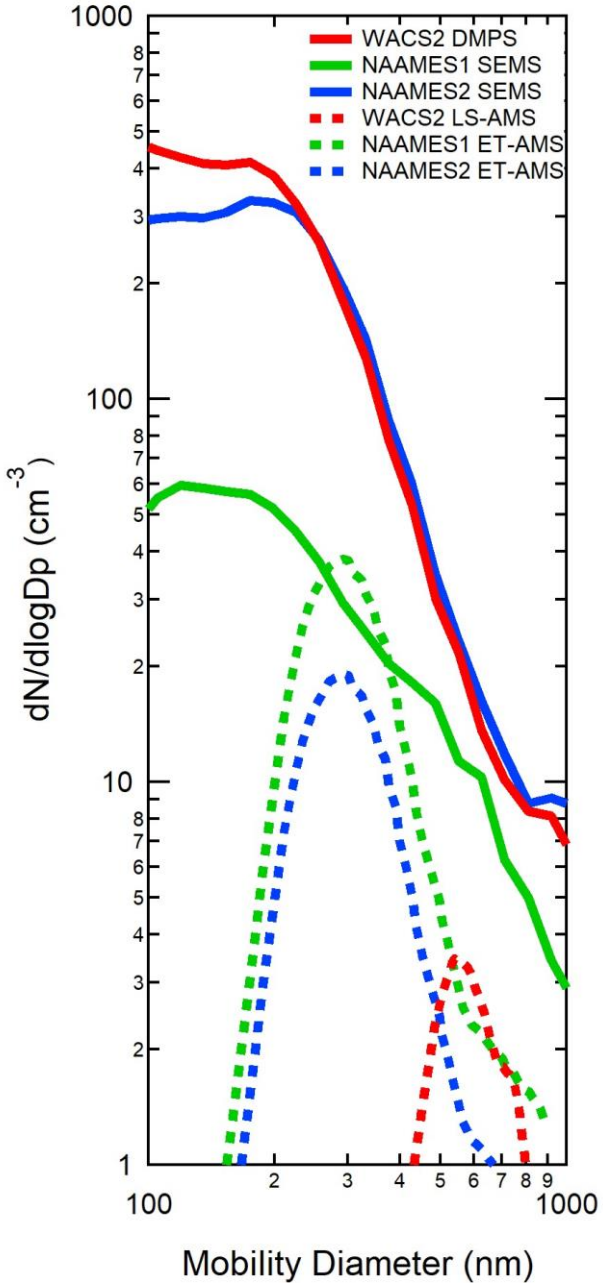

Figure 3.13: Measurement range for LS-AMS and ET-AMS are compared to averaged SEMS and DMPS size distributions for clean marine conditions. The AMS aerodynamic diameter is converted to mobility diameter to compare with the SEMS (WACS2) or DMPS (NAAMES1 and NAAMES2) [DeCarlo et al., 2004]. Campaign average particle densities derived from AMS particle time of flight, and SEMS or DMPS measurements are 1.26, 1.27, and 1.33 g cm^{-3} for WACS2, NAAMES1, and NAAMES2, respectively.

Table 3.6: Chemical composition and physical properties used for calculating hygroscopicity from AMS measured components.

AMS Ions	Molecular Composition	Density (g cm^{-3})	Hygroscopicity (κ)
Organic	-	1	(0.01-0.2, see Table 3.3)
Sulfate	NH_4HSO_4	1.77	0.84
Nitrate	NH_4NO_3	1.72	0.78
Salt	NaCl	2.16	1.33

filtered through 25 mm glass-fiber filters (GF/F) with a nominal pore size of 700 nm under low vacuum pressure (< 5 psi) and dim light. Filters were placed in 100% methanol to extract at -20°C for 24 hr prior to measuring and the Chl-a was measured using a Turner 10AU fluorometer calibrated using pure Chl-a standard [*Coad*, 2014].

Two HR-AMS instruments were operated simultaneously at different temperatures during WACS2 SeaSweep deployments. This approach increased the fraction of refractory sea salt particles and associated organic mass measured relative to a single instrument held at 650°C [*Bates et al.*, 2012; *Frossard et al.*, 2014a; *Frossard et al.*, 2014b; *Keene et al.*, 2007]. The first AMS vaporizer was continuously held at approximately 560°C (referred to as AMS560), while the SP-AMS was set at approximately 660°C (referred to as AMShot) then increased to 700°C for 5 hours at station 3, and 800°C for 3 hours at station 5. CE_{ss} and high O/C organic mass fraction increase with the AMS vaporizer temperature (Figure 3.14). SeaSweep particles were also collected for FTIR analysis, but the samples were dehydrated to remove interference of sea salt hydrate bound water with the organic signal in the FTIR spectra [*Frossard and Russell* 2012]. The CE_{org} of the SeaSweep sea spray particles calculated from the FTIR organic mass concentration is 0.23 for the AMS560 and 0.18 for AMShot

at 660^{o}C. At higher vaporizer temperatures, the AMS measured a larger fraction of the IC-measured sea salt mass. The organic oxygenated mass fraction and O/C increased with vaporizer temperature. This supports the hypothesis that the lower volatility of salt particles accounts for the lower O/C measured by AMS (relative to the FTIR) [*Frossard et al.,* 2014b]. However, the change in organic composition may also be due to differences in organic fragmentation at higher vaporizer temperatures or difference in organic composition in large particles (>700 nm) that are not measured by the AMS. SeaSweep sea spray particle detection varied at the different WACS2 stations with an apparent dependence on the measured Chl-a concentration, even though organic properties showed no dependence on Chl-a (Figure 3.14). These limitations of measuring sea salt particles by HR-AMS are addressed by calibration to filter-based IC measurements of sea salt.

Fourier Transform Infrared (FTIR) spectroscopy and AMS showed submicron particles contain two types of functional group composition, one with high and the other with low ratios of oxygen to carbon (O/C) [*Frossard et al.*, 2014b; *Russell et al.*, 2010]. Frossard et al. [2014b] explicitly compared the organic chemical composition of SeaSweep marine particles using multiple measurement methods, including FTIR and AMS, and showed that the apparent discrepancy was due to the large fraction of refractory salt particles in the generated sea spray. Also, the AMS high O/C organic mass fraction is 11% lower than in the FTIR for SeaSweep sea spray particles, suggesting that the high O/C organic mass is more likely to be on refractory sea salt particles but the low O/C organic mass components are on particles with less salt. FTIR

shows a greater fraction of high O/C organic components than the AMS for all stations, consistent with Frossard et al. [2014b]. Figure 3.15c shows an increase in AMS high O/C OM fraction at higher vaporizer temperatures. The AMS high O/C OM fraction at higher vaporizer temperatures is still significantly lower than it is for the FTIR, as is expected given that even at higher vaporizer temperatures the CE of refractory sea salt is well below 0.1. Figure 3.15b shows that the ratio of OM to sea salt decreases with greater vaporizer temperatures, with the exception of station 2, because the sea salt

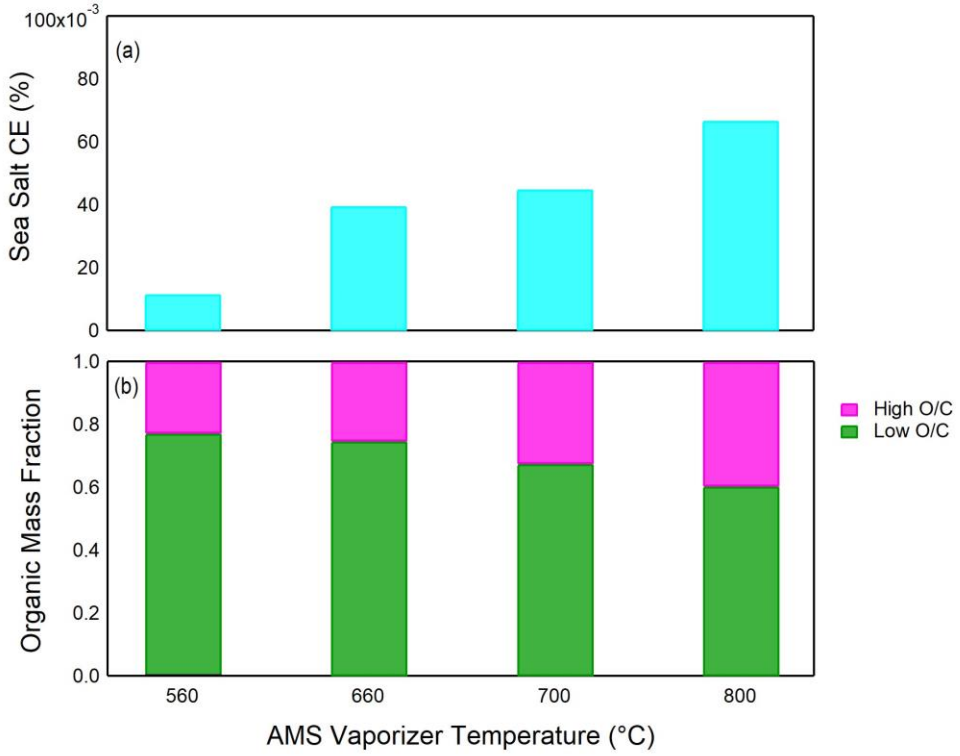

Figure 3.14: Dependence of WACS2 HR-AMS measurements of SeaSweep particles on vaporizer temperature as shown by (a) the collection efficiency of sea salt calculated from IC measurements of sodium and chloride [*Frossard et al.,* 2014b] and (b) the organic mass fraction composition, where high O/C organic mass includes mass fragment groups C_XH_YO and $C_XH_YO_{>1}$ and low O/C mass includes mass fragment group C_XH_Y.

concentration increases more than the OM as vaporizer temperature was increased since sea salt was disproportionally on particles that were more refractory. Figure 3.15a shows the ratio of OM is fairly consistent at stations 2 and 3 even when the vaporizer temperature is increased at station 3. Stations 4 and 5 have higher OM ratios when AMShot is at 660ºC, which could result from the higher particle mass concentration at these stations. At station 5, the OM ratio increases when the AMShot vaporizer temperature is increased from 660ºC to 800ºC, possibly due to the increase in vaporization of OM on sea salt particles.

3.6.6 Hygroscopicity and CCN Calculations

The hygroscopicity parameter is calculated from

$$\kappa = \sum_j v_j \kappa_j \quad (3.2)$$

where v_j is the volume fraction of each component (j) and κ_j is the hygroscopicity parameter for the component. The four components used are in Table 3.7. The volume fraction is calculated by multiplying the mass fraction (Table 3.5) by the density (Table 3.7) of each component.

The organic hygroscopicity in New Sulfate, Added Sulfate, MO, and LO particles is assumed to be 0.1, consistent with the range identified by Mochida et al. [2011] (Table 3.6). The organic hygroscopicity for the Estimated Salt type was assumed to be 0.2 based on the high fraction of oxygenated mass fragments associated with sea spray particles [*Frossard et al.*, 2014b]. The organic hygroscopicity of the FF type was assumed to be 0.01, consistent with low O/C organic particles in urban areas [*Petters et al.*, 2016].

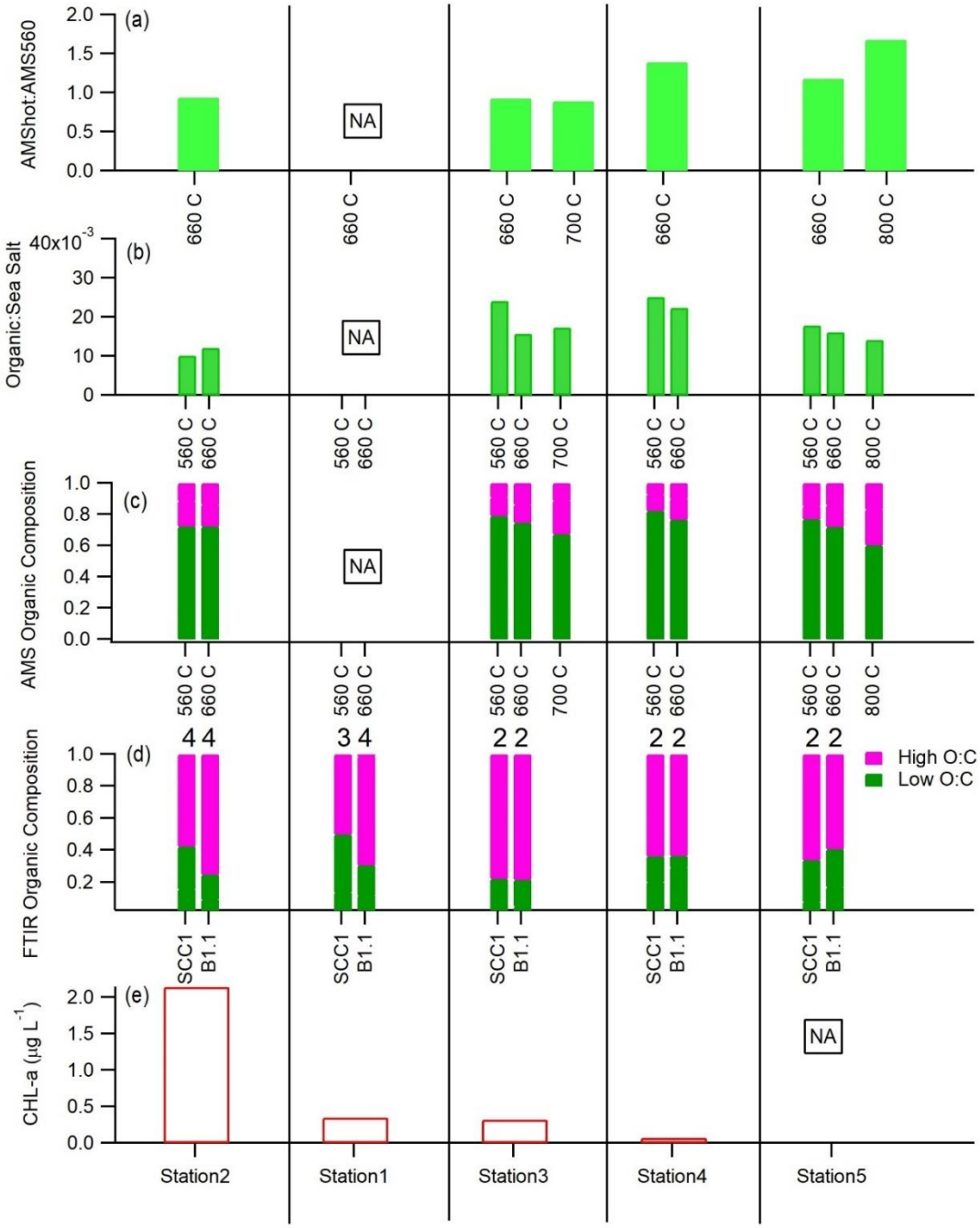

Figure 3.15: For each SeaSweep station and each AMShot vaporizer temperature, (a) the ratio of the AMS organic mass, (b) the ratio of organic mass to sea salt mass, (c) the high and low O/C organic mass fraction, (d) FTIR high and low O/C organic mass fraction for particles collected after a 1 µm sharp cut cyclone (SCC1) or a 1.1 µm cut Berner impactor (B1.1), and (e) Chl-a concentration. The number of FTIR samples is given above each bar in (d).

Table 3.7: The ambient hygroscopicity, activation diameter and fraction of particles that contain salt ions for each aerosol type, based on the chemical composition in Table 3.5. The non-marine particle types, More Oxygenated (MO), Less Oxygenated (LO), Mixed Continental (MC), and Fossil Fuel (FF), are discussed in Section 3.6.2.

Particle Types	Organic Hygroscopicity [2] (κ_{org})	Total Hygroscopicity (κ)	Minimum Activation Diameter[3] (nm)	Salt Containing (m/z 35+ m/z 36) Fraction
NAAMES1				
Non-Marine				
MO	0.2	0.27	198	0.23
MC	0.1	0.31	189	0.12
LO	0.1	0.25	203	0.14
FF	0.01	0.05	346	0.13
Added Sulfate	0.1	0.34	183	0.12
New Sulfate	0.1	0.56	155	0.12
Estimated Salt[1]	0.2	0.95	130	1.00
NAAMES2				
Non-Marine				
MO	0.2	0.29	193	0.22
MC	0.1	0.26	200	0.19
LO	0.1	0.20	219	0.19
FF	0.01	0.05	346	0.16
Added Sulfate	0.1	0.38	177	0.18
New Sulfate	0.1	0.55	156	0.15
Estimated Salt[4]	0.2	0.95	130	0.86

[1] The sea salt particle type is based on ET-AMS single particle chemical composition of SeaSweep sea salt particles measured.
[2] The organic hygroscopicity for FF is based on Sanchez et al. [2016], MO is based on Chang et al. [2010]. The organic hygroscopicity of Estimated Salt is consistent with Mochida et al. [2011] and Quinn et al. [2014].
[3] The minimum activation diameter is the mobility diameter and is calculated for a supersaturation of 0.1% [*Petters and Kreidenweis*, 2007].
[4] The Estimated Salt particle type for NAAMES1 is used for NAAMES2 because the ROIs for the ET-AMS were not optimized to collect sea salt particles during NAAMES2.

The resulting κ values (Table 3.6) were used to calculate the minimum activation diameter (D_{act}) for each particle type [*Petters and Kreidenweis*, 2007], and the number of particles of each type that were larger than D_{act} were summed to give CCN at 0.1% supersaturation (Figure 3.16). The size bin that included D_{act} was linearly interpolated so that only the fraction of particles in each bin with sizes greater than D_{act} were included. D_{act} for some of the particle types is below the ET-AMS lower cut off diameter (Table 3.3). The particle range below the 180 nm ET-AMS cut off diameter are included but account for a small fraction of the CCN (Figure 3.16).

3.6.7 Inversion Strength Calculations

The inversion strength was estimated by integrating the convective inhibition (CIN) over the inversion layer for $\mathrm{CIN} = \int_{z_b}^{z_t} -g * \frac{T_{v,ap} - T_v}{T_v} dz$, where z_t and z_b are the top and bottom of the inversion layer, respectively, g is the acceleration due to gravity, T_v is the virtual temperature in units of degrees Kelvin, calculated from the radiosonde measured temperature and relative humidity, and $T_{v,ap}$ is the virtual temperature of a theoretical parcel that rises adiabatically. This definition of CIN is slightly different from the traditional definition where z_t would instead be equivalent to the level of free convection. The bottom of the inversion layer is defined by a minimum in the temperature profile, just below a temperature increase in the inversion. Radiosonde profiles that showed evaporative cooling at cloud top are not included in the analysis because the minimum temperature does not accurately define the bottom of the inversion layer which makes CIN ill-bounded. The top of the inversion layer is defined

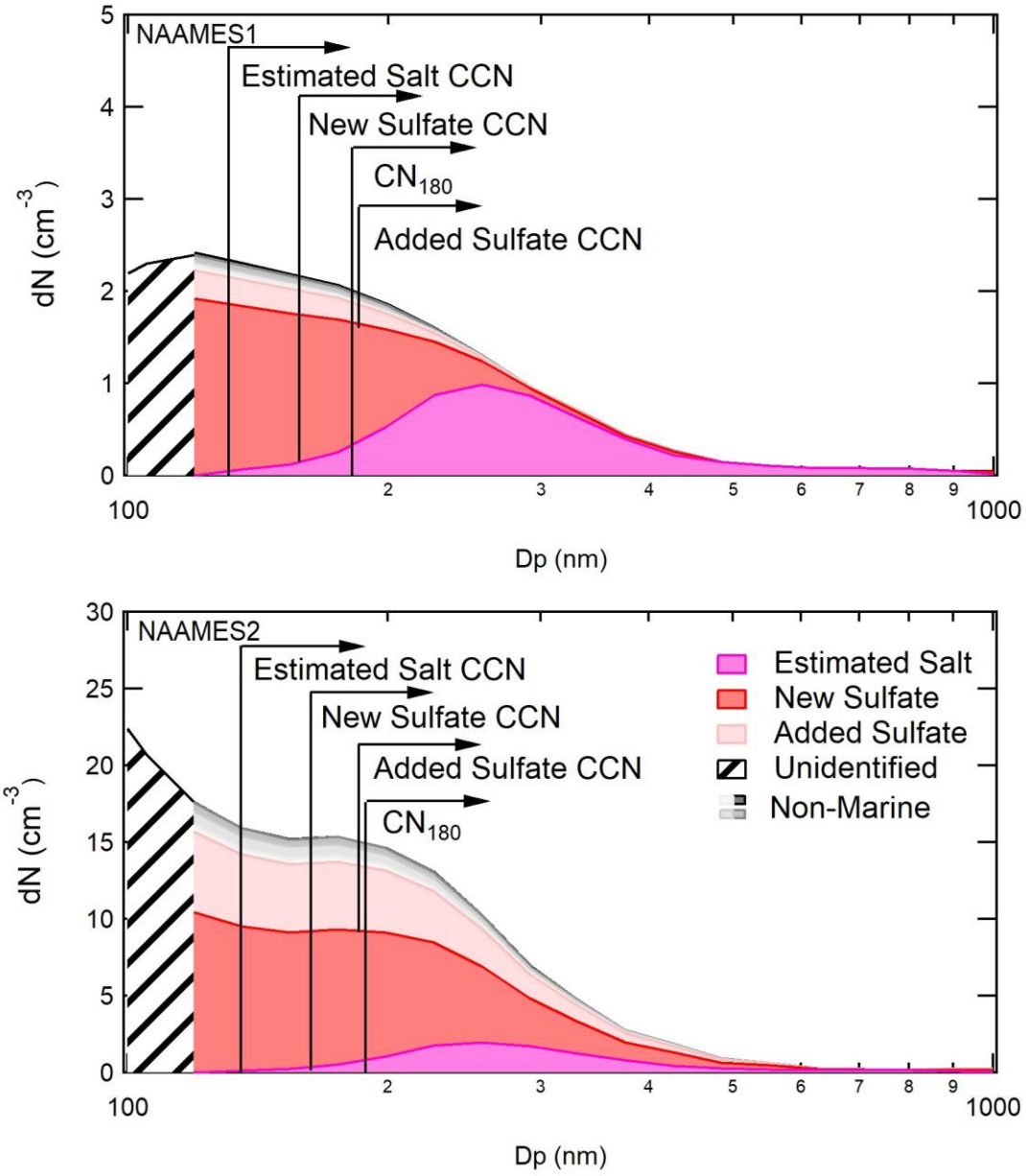

Figure 3.16: Particle type size distributions for sample NAAMES1 and NAAMES2 cases. Black arrows identify the 0.1% supersaturation activation diameters for the Estimated Salt, New Sulfate, and Added Sulfate types.

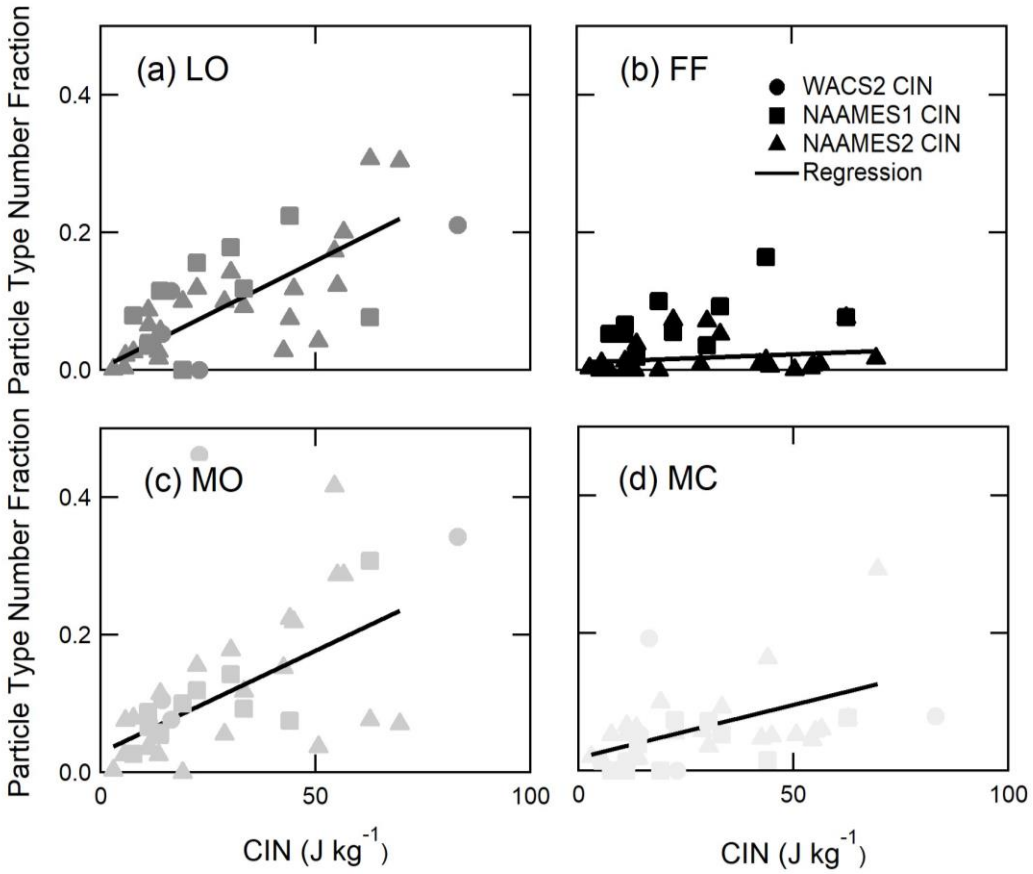

Figure 3.17: Dependence of WACS2 LS-AMS and NAAMES1 and NAAMES2 ET-AMS particle number fractions during clean marine conditions on CIN calculated from radiosonde measurements. Pearson correlation coefficients for NAAMES1 and NAAMES2 for CIN are (a) 0.77, (b) 0.21, (c) 0.58, and (d) 0.54 for the non-marine types. Added Sulfate and New Sulfate are included in Figure 3.

by a maximum in the measured temperature just below the free troposphere, at which temperature decreases consistently with altitude. In cases with weak inversions, the vertical temperature profile does not have a minimum or maximum temperature at the inversion, but instead a change in slope at the top and bottom of the inversion. The second variable used to identify the inversion strength is the buoyancy jump, given by

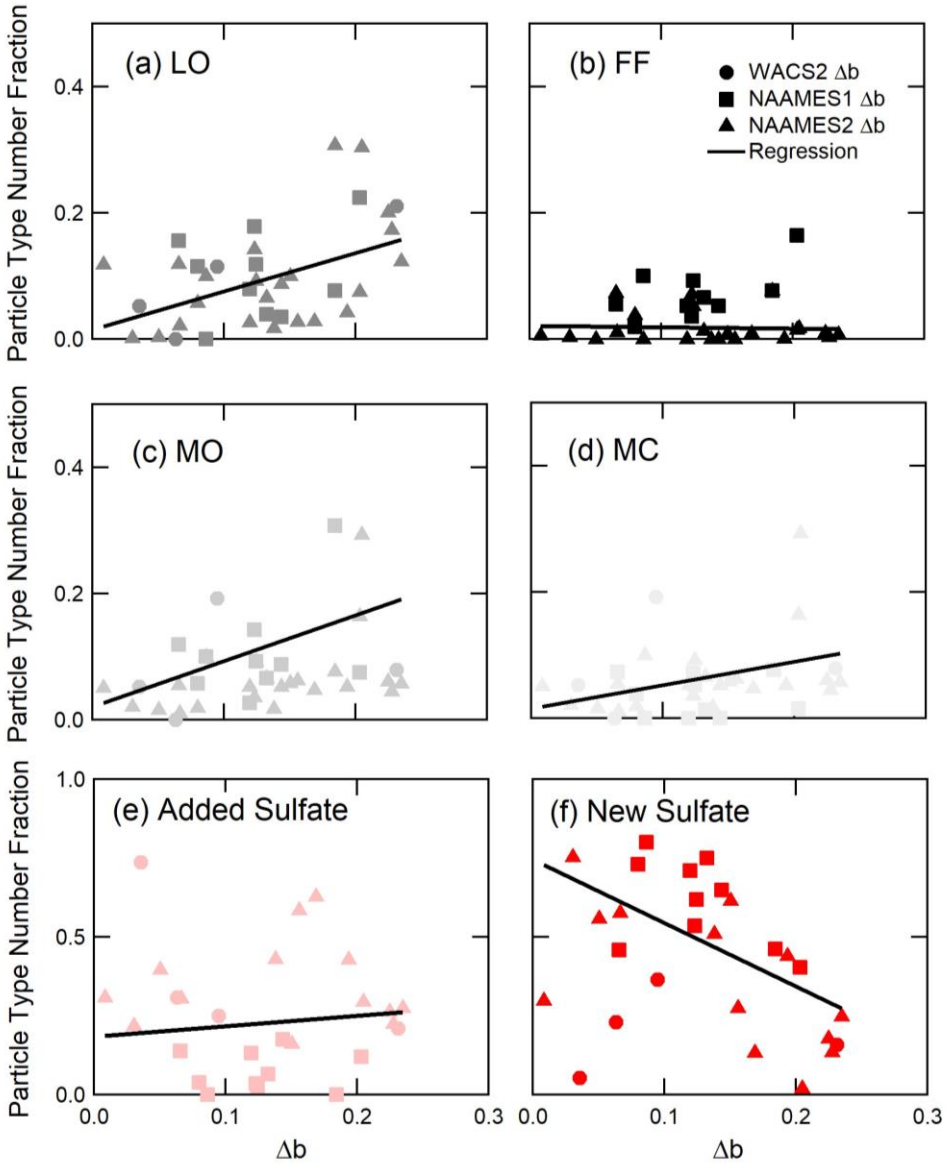

Figure 3.18: Dependence of WACS2 LS-AMS and NAAMES1 and NAAMES2 ET-AMS particle number fractions during clean marine conditions on Δb calculated from radiosonde measurements. Pearson correlation coefficients for NAAMES1 and NAAMES2 for Δb are (a) 0.47 for LO, (b) -0.06 for FF, (c) 0.44 for MO, (d) 0.41 for MC, (e) 0.01 for the Added Sulfate, and (f) -0.58 for the New Sulfate particles.

$\Delta b = g\frac{\Delta T_v}{T_v}$, where ΔT_v is the change in the virtual potential temperature across the inversion layer.

Correlations of particle types with CIN are shown in Figure 3.3 and 3.17. The correlation of particle types with CIN are stronger than correlations with Δb (Figures 3.3, 3.18), consistent with the expectation that CIN is a more accurate representation of the inversion strength because it integrates across the inversion the difference between the temperature of an adiabatic parcel and the observed temperature, whereas Δb only depends on the temperature difference above and below the inversion. The CIN from the two radiosondes collected on this day are low (6 J kg^{-1} and 13 J kg^{-1}), indicating a higher rate of entrainment from the free troposphere to the boundary layer.

References

Aiken, A. C., Decarlo, P. F., Kroll, J. H., Worsnop, D. R., Huffman, J. A., Docherty, K. S., Ulbrich, I. M., Mohr, C., Kimmel, J. R., Sueper, D., Sun, Y., Zhang, Q., Trimborn, A., Northway, M., Ziemann, P. J., Canagaratna, M. R., Onasch, T. B., Alfarra, M. R., Prevot, A. S. H., Dommen, J., Duplissy, J., Metzger, A., Baltensperger, U., and Jimenez, J. L.: O/C and OM/OC ratios of primary, secondary, and ambient organic aerosols with high-resolution time-of-flight aerosol mass spectrometry, Environmental Science & Technology, 42, 4478-4485, 10.1021/es703009q, 2008.

Albrecht, B. A.: AEROSOLS, CLOUD MICROPHYSICS, AND FRACTIONAL CLOUDINESS, Science, 245, 1227-1230, 10.1126/science.245.4923.1227, 1989.

Andreae, M. O., Elbert, W., and Demora, S. J.: BIOGENIC SULFUR EMISSIONS AND AEROSOLS OVER THE TROPICAL SOUTH-ATLANTIC .3. ATMOSPHERIC DIMETHYLSULFIDE, AEROSOLS AND CLOUD CONDENSATION NUCLEI, Journal of Geophysical Research-Atmospheres, 100, 11335-11356, 10.1029/94jd02828, 1995.

Ayers, G. P., and Gras, J. L.: SEASONAL RELATIONSHIP BETWEEN CLOUD CONDENSATION NUCLEI AND AEROSOL METHANESULFONATE IN MARINE AIR, Nature, 353, 834-835, 10.1038/353834a0, 1991.

Bandy, A. R., Thornton, D. C., Tu, F. H., Blomquist, B. W., Nadler, W., Mitchell, G. M., and Lenschow, D. H.: Determination of the vertical flux of dimethyl sulfide by eddy correlation and atmospheric pressure ionization mass spectrometry (APIMS), Journal of Geophysical Research-Atmospheres, 107, 9, 10.1029/2002jd002472, 2002.

Bates, T. S., Huebert, B. J., Gras, J. L., Griffiths, F. B., and Durkee, P. A.: International Global Atmospheric Chemistry (IGAC) project's first aerosol characterization experiment (ACE 1): Overview, Journal of Geophysical Research-Atmospheres, 103, 16297-16318, 10.1029/97jd03741, 1998a.

Bates, T. S., Kapustin, V. N., Quinn, P. K., Covert, D. S., Coffman, D. J., Mari, C., Durkee, P. A., De Bruyn, W. J., and Saltzman, E. S.: Processes controlling the distribution of aerosol particles in the lower marine boundary layer during the First Aerosol Characterization Experiment (ACE 1), Journal of Geophysical Research-Atmospheres, 103, 16369-16383, 10.1029/97jd03720, 1998b.

Bates, T. S., Coffman, D. J., Covert, D. S., and Quinn, P. K.: Regional marine boundary layer aerosol size distributions in the Indian, Atlantic, and Pacific Oceans: A comparison of INDOEX measurements with ACE-1, ACE-2, and Aerosols99, Journal of Geophysical Research-Atmospheres, 107, 10.1029/2001jd001174, 2002.

Bates, T. S., Quinn, P. K., Coffman, D., Schulz, K., Covert, D. S., Johnson, J. E., Williams, E. J., Lerner, B. M., Angevine, W. M., Tucker, S. C., Brewer, W. A., and Stohl, A.: Boundary layer aerosol chemistry during TexAQS/GoMACCS 2006: Insights into aerosol sources and transformation processes, Journal of Geophysical Research-Atmospheres, 113, 10.1029/2008jd010023, 2008.

Bates, T. S., Quinn, P. K., Frossard, A. A., Russell, L. M., Hakala, J., Petaja, T., Kulmala, M., Covert, D. S., Cappa, C. D., Li, S. M., Hayden, K. L., Nuaaman, I., McLaren, R., Massoli, P., Canagaratna, M. R., Onasch, T. B., Sueper, D., Worsnop, D. R., and Keene, W. C.: Measurements of ocean derived aerosol off the coast of California, Journal of Geophysical Research-Atmospheres, 117, 13, 10.1029/2012jd017588, 2012.

Bell, T. G., De Bruyn, W., Miller, S. D., Ward, B., Christensen, K. H., and Saltzman, E. S.: Air-sea dimethylsulfide (DMS) gas transfer in the North Atlantic: evidence for limited interfacial gas exchange at high wind speed, Atmospheric Chemistry and Physics, 13, 11073-11087, 10.5194/acp-13-11073-2013, 2013.

Bell, T. G., De Bruyn, W., Marandino, C. A., Miller, S. D., Law, C. S., Smith, M. J., and Saltzman, E. S.: Dimethylsulfide gas transfer coefficients from algal blooms in the Southern Ocean, Atmospheric Chemistry and Physics, 15, 1783-1794, 10.5194/acp-15-1783-2015, 2015.

Berkes, F., Hoor, P., Bozem, H., Kunkel, D., Sprenger, M., and Henne, S.: Airborne observation of mixing across the entrainment zone during PARADE 2011, Atmospheric Chemistry and Physics, 16, 6011-6025, 10.5194/acp-16-6011-2016, 2016.

Betha, R., Russell, L. M., Sanchez, K. J., Liu, J., Price, D. J., Lamjiri, M. A., Chen, C. L., Kuang, X. M., da Rocha, G. O., Paulson, S. E., Miller, W., and Cocker, D. R.: Lower NOx but higher particle and black carbon emissions from renewable diesel compared to ultra low sulfur diesel in at-sea operations of a research vessel, Aerosol Science and Technology, 51, 123-134, 10.1080/02786826.2016.1238034, 2017.

Budisulistiorini, S. H., Li, X., Bairai, S. T., Renfro, J., Liu, Y., Liu, Y. J., McKinney, K. A., Martin, S. T., McNeill, V. F., Pye, H. O. T., Nenes, A., Neff, M. E., Stone, E. A., Mueller, S., Knote, C., Shaw, S. L., Zhang, Z., Gold, A., and Surratt, J. D.: Examining the effects of anthropogenic emissions on isoprene-derived secondary organic aerosol formation during the 2013 Southern Oxidant and Aerosol Study (SOAS) at the Look Rock, Tennessee ground site, Atmospheric Chemistry and Physics, 15, 8871-8888, 10.5194/acp-15-8871-2015, 2015.

Chang, R. Y. W., Slowik, J. G., Shantz, N. C., Vlasenko, A., Liggio, J., Sjostedt, S. J., Leaitch, W. R., and Abbatt, J. P. D.: The hygroscopicity parameter (kappa) of ambient organic aerosol at a field site subject to biogenic and anthropogenic influences:

relationship to degree of aerosol oxidation, Atmospheric Chemistry and Physics, 10, 5047-5064, 10.5194/acp-10-5047-2010, 2010.

Charlson, R. J., Lovelock, J. E., Andreae, M. O., and Warren, S. G.: OCEANIC PHYTOPLANKTON, ATMOSPHERIC SULFUR, CLOUD ALBEDO AND CLIMATE, Nature, 326, 655-661, 10.1038/326655a0, 1987.

Clarke, A. D.: ATMOSPHERIC NUCLEI IN THE PACIFIC MIDTROPOSPHERE - THEIR NATURE, CONCENTRATION, AND EVOLUTION, Journal of Geophysical Research-Atmospheres, 98, 20633-20647, 10.1029/93jd00797, 1993.

Clarke, A. D., Li, Z., and Litchy, M.: Aerosol dynamics in the equatorial Pacific Marine boundary layer: Microphysics, diurnal cycles and entrainment, Geophysical Research Letters, 23, 733-736, 10.1029/96gl00778, 1996.

Clarke, A. D., Davis, D., Kapustin, V. N., Eisele, F., Chen, G., Paluch, I., Lenschow, D., Bandy, A. R., Thornton, D., Moore, K., Mauldin, L., Tanner, D., Litchy, M., Carroll, M. A., Collins, J., and Albercook, C.: Particle nucleation in the tropical boundary layer and its coupling to marine sulfur sources, Science, 282, 89-92, 10.1126/science.282.5386.89, 1998.

Clarke, A. D., Kapustin, V. N., Eisele, F. L., Weber, R. J., and McMurry, P. H.: Particle production near marine clouds: Sulfuric acid and predictions from classical binary nucleation, Geophysical Research Letters, 26, 2425-2428, 10.1029/1999gl900438, 1999.

Clarke, A. D., Freitag, S., Simpson, R. M. C., Hudson, J. G., Howell, S. G., Brekhovskikh, V. L., Campos, T., Kapustin, V. N., and Zhou, J.: Free troposphere as a major source of CCN for the equatorial pacific boundary layer: long-range transport and teleconnections, Atmospheric Chemistry and Physics, 13, 7511-7529, 10.5194/acp-13-7511-2013, 2013.

Coad, T.: Chlorophyll a data collected during the SIPEX II voyage of the Aurora Australis, 2012, Australian Antarctic Data Centre, 2014.

Conley, S. A., Faloona, I., Miller, G. H., Lenschow, D. H., Blomquist, B., and Bandy, A.: Closing the dimethyl sulfide budget in the tropical marine boundary layer during the Pacific Atmospheric Sulfur Experiment, Atmospheric Chemistry and Physics, 9, 8745-8756, 2009.

Cotton, W. R., Alexander, G. D., Hertenstein, R., Walko, R. L., McAnelly, R. L., and Nicholls, M.: Cloud venting - A review and some new global annual estimates, Earth-Science Reviews, 39, 169-206, 10.1016/0012-8252(95)00007-0, 1995.

Covert, D. S., Kapustin, V. N., Quinn, P. K., and Bates, T. S.: NEW PARTICLE FORMATION IN THE MARINE BOUNDARY-LAYER, Journal of Geophysical Research-Atmospheres, 97, 20581-20589, 10.1029/92jd02074, 1992.

Crippa, M., El Haddad, I., Slowik, J. G., DeCarlo, P. F., Mohr, C., Heringa, M. F., Chirico, R., Marchand, N., Sciare, J., Baltensperger, U., and Prevot, A. S. H.: Identification of marine and continental aerosol sources in Paris using high resolution aerosol mass spectrometry, Journal of Geophysical Research-Atmospheres, 118, 1950-1963, 10.1002/jgrd.50151, 2013.

Crippa, M., Canonaco, F., Lanz, V. A., Aijala, M., Allan, J. D., Carbone, S., Capes, G., Ceburnis, D., Dall'Osto, M., Day, D. A., DeCarlo, P. F., Ehn, M., Eriksson, A., Freney, E., Hildebrandt Ruiz, L., Hillamo, R., Jimenez, J. L., Junninen, H., Kiendler-Scharr, A., Kortelainen, A. M., Kulmala, M., Laaksonen, A., Mensah, A., Mohr, C., Nemitz, E., O'Dowd, C., Ovadnevaite, J., Pandis, S. N., Petaja, T., Poulain, L., Saarikoski, S., Sellegri, K., Swietlicki, E., Tiitta, P., Worsnop, D. R., Baltensperger, U., and Prevot, A. S. H.: Organic aerosol components derived from 25 AMS data sets across Europe using a consistent ME-2 based source apportionment approach, Atmospheric Chemistry and Physics, 14, 6159-6176, 10.5194/acp-14-6159-2014, 2014.

Cross, E. S., Onasch, T. B., Canagaratna, M., Jayne, J. T., Kimmel, J., Yu, X. Y., Alexander, M. L., Worsnop, D. R., and Davidovits, P.: Single particle characterization using a light scattering module coupled to a time-of-flight aerosol mass spectrometer, Atmospheric Chemistry and Physics, 9, 7769-7793, 2009.

de Leeuw, G., Andreas, E. L., Anguelova, M. D., Fairall, C. W., Lewis, E. R., O'Dowd, C., Schulz, M., and Schwartz, S. E.: PRODUCTION FLUX OF SEA SPRAY AEROSOL, Reviews of Geophysics, 49, 10.1029/2010rg000349, 2011.

DeCarlo, P. F., Slowik, J. G., Worsnop, D. R., Davidovits, P., and Jimenez, J. L.: Particle morphology and density characterization by combined mobility and aerodynamic diameter measurements. Part 1: Theory, Aerosol Science and Technology, 38, 1185-1205, 10.1080/027868290903907, 2004.

DeCarlo, P. F., Kimmel, J. R., Trimborn, A., Northway, M. J., Jayne, J. T., Aiken, A. C., Gonin, M., Fuhrer, K., Horvath, T., Docherty, K. S., Worsnop, D. R., and Jimenez, J. L.: Field-deployable, high-resolution, time-of-flight aerosol mass spectrometer, Analytical Chemistry, 78, 8281-8289, 10.1021/ac061249n, 2006.

Devore, J. L., and Berk, K. N.: Modern Mathematical Statistics with Application, 2nd ed., Springer Science+Business Media, New York, 2012.

Dorr, H., and Munnich, K. O.: SOIL RN-222 AS A TRACER FOR GAS-TRANSPORT IN THE UNSATURATED SOIL ZONE, Chemical Geology, 70, 97-97, 10.1016/0009-2541(88)90469-x, 1988.

Dzepina, K., Mazzoleni, C., Fialho, P., China, S., Zhang, B., Owen, R. C., Helmig, D., Hueber, J., Kumar, S., Perlinger, J. A., Kramer, L. J., Dziobak, M. P., Ampadu, M. T., Olsen, S., Wuebbles, D. J., and Mazzoleni, L. R.: Molecular characterization of free tropospheric aerosol collected at the Pico Mountain Observatory: a case study with a long-range transported biomass burning plume, Atmospheric Chemistry and Physics, 15, 5047-5068, 10.5194/acp-15-5047-2015, 2015.

Faloona, I., Lenschow, D. H., Campos, T., Stevens, B., van Zanten, M., Blomquist, B., Thornton, D., Bandy, A., and Gerber, H.: Observations of entrainment in eastern Pacific marine stratocumulus using three conserved scalars, Journal of the Atmospheric Sciences, 62, 3268-3285, 10.1175/jas3541.1, 2005.

Frossard, A. A., and Russell, L. M.: Removal of Sea Salt Hydrate Water from Seawater-Derived Samples by Dehydration, Environmental Science & Technology, 46, 13326-13333, 10.1021/es3032083, 2012.

Frossard, A. A., Russell, L. M., Burrows, S. M., Elliott, S. M., Bates, T. S., and Quinn, P. K.: Sources and composition of submicron organic mass in marine aerosol particles, Journal of Geophysical Research-Atmospheres, 119, 12977-13003, 10.1002/2014jd021913, 2014a.

Frossard, A. A., Russell, L. M., Massoli, P., Bates, T. S., and Quinn, P. K.: Side-by-Side Comparison of Four Techniques Explains the Apparent Differences in the Organic Composition of Generated and Ambient Marine Aerosol Particles, Aerosol Science and Technology, 48, V-X, 10.1080/02786826.2013.879979, 2014b.

Gaston, C. J., Furutani, H., Guazzotti, S. A., Coffee, K. R., Jung, J., Uematsu, M., and Prather, K. A.: Direct Night-Time Ejection of Particle-Phase Reduced Biogenic Sulfur Compounds from the Ocean to the Atmosphere, Environmental Science & Technology, 49, 4861-4867, 10.1021/es506177s, 2015.

Gregory, G. L., Warren, L. S., Davis, D. D., Andreae, M. O., Bandy, A. R., Ferek, R. J., Johnson, J. E., Saltzman, E. S., and Cooper, D. J.: AN INTERCOMPARISON OF INSTRUMENTATION FOR TROPOSPHERIC MEASUREMENTS OF DIMETHYL SULFIDE - AIRCRAFT RESULTS FOR CONCENTRATIONS AT THE PARTS-PER-TRILLION LEVEL, Journal of Geophysical Research-Atmospheres, 98, 23373-23388, 10.1029/93jd00688, 1993.

Grythe, H., Strom, J., Krejci, R., Quinn, P., and Stohl, A.: A review of sea-spray aerosol source functions using a large global set of sea salt aerosol concentration measurements, Atmospheric Chemistry and Physics, 14, 1277-1297, 10.5194/acp-14-1277-2014, 2014.

Hegg, D. A., Radke, L. F., and Hobbs, P. V.: PARTICLE-PRODUCTION ASSOCIATED WITH MARINE CLOUDS, Journal of Geophysical Research-Atmospheres, 95, 13917-13926, 10.1029/JD095iD09p13917, 1990.

Hegg, D. A., Ferek, R. J., Hobbs, P. V., and Radke, L. F.: DIMETHYL SULFIDE AND CLOUD CONDENSATION NUCLEUS CORRELATIONS IN THE NORTHEAST PACIFIC-OCEAN, Journal of Geophysical Research-Atmospheres, 96, 13189-13191, 10.1029/91jd01309, 1991.

Holland, H. D.: The Chemistry of the Atmosphere and Oceans, Jon Wiley New York, 1978.

Hoppel, W. A., Frick, G. M., and Fitzgerald, J. W.: Deducing droplet concentration and supersaturation in marine boundary layer clouds from surface aerosol measurements, Journal of Geophysical Research-Atmospheres, 101, 26553-26565, 10.1029/96jd02243, 1996.

Hudson, J. G., Noble, S., and Jha, V.: Stratus cloud supersaturations, Geophysical Research Letters, 37, 10.1029/2010gl045197, 2010.

Katoshevski, D., Nenes, A., and Seinfeld, J. H.: A study of processes that govern the maintenance of aerosols in the marine boundary layer, Journal of Aerosol Science, 30, 503-532, 10.1016/s0021-8502(98)00740-x, 1999.

Kazil, J., Lovejoy, E. R., Barth, M. C., and O'Brien, K.: Aerosol nucleation over oceans and the role of galactic cosmic rays, Atmospheric Chemistry and Physics, 6, 4905-4924, 10.5194/acp-6-4905-2006, 2006.

Keene, W. C., Maring, H., Maben, J. R., Kieber, D. J., Pszenny, A. A. P., Dahl, E. E., Izaguirre, M. A., Davis, A. J., Long, M. S., Zhou, X. L., Smoydzin, L., and Sander, R.: Chemical and physical characteristics of nascent aerosols produced by bursting bubbles at a model air-sea interface, Journal of Geophysical Research-Atmospheres, 112, 10.1029/2007jd008464, 2007.

Kim, G., Cho, H. J., Seo, A., Kim, D., Gim, Y., Lee, B. Y., Yoon, Y. J., and Park, K.: Comparison of Hygroscopicity, Volatility, and Mixing State of Subnnicrometer Particles between Cruises over the Arctic Ocean and the Pacific Ocean, Environmental Science & Technology, 49, 12024-12035, 10.1021/acs.est.5b01505, 2015.

Kohler, H.: The nucleus in and the growth of hygroscopic droplets, Transactions of the Faraday Society, 32, 1152-1161, 10.1039/tf9363201152, 1936.

Korhonen, H., Carslaw, K. S., Spracklen, D. V., Mann, G. W., and Woodhouse, M. T.: Influence of oceanic dimethyl sulfide emissions on cloud condensation nuclei concentrations and seasonality over the remote Southern Hemisphere oceans: A global model study, Journal of Geophysical Research-Atmospheres, 113, 10.1029/2007jd009718, 2008.

Kuang, C., McMurry, P. H., and McCormick, A. V.: Determination of cloud condensation nuclei production from measured new particle formation events, Geophysical Research Letters, 36, 10.1029/2009gl037584, 2009.

Kulmala, M., Vehkamaki, H., Petaja, T., Dal Maso, M., Lauri, A., Kerminen, V. M., Birmili, W., and McMurry, P. H.: Formation and growth rates of ultrafine atmospheric particles: a review of observations, Journal of Aerosol Science, 35, 143-176, 10.1016/j.jaerosci.2003.10.003, 2004.

Lanz, V. A., Alfarra, M. R., Baltensperger, U., Buchmann, B., Hueglin, C., and Prevot, A. S. H.: Source apportionment of submicron organic aerosols at an urban site by factor analytical modelling of aerosol mass spectra, Atmospheric Chemistry and Physics, 7, 1503-1522, 2007.

Leaitch, W. R., Banic, C. M., Isaac, G. A., Couture, M. D., Liu, P. S. K., Gultepe, I., Li, S. M., Kleinman, L., Daum, P. H., and MacPherson, J. I.: Physical and chemical observations in marine stratus during the 1993 North Atlantic Regional Experiment: Factors controlling cloud droplet number concentrations, Journal of Geophysical Research-Atmospheres, 101, 29123-29135, 10.1029/96jd01228, 1996.

Lee, A. K. Y., Willis, M. D., Healy, R. M., Onasch, T. B., and Abbatt, J. P. D.: Mixing state of carbonaceous aerosol in an urban environment: single particle characterization using the soot particle aerosol mass spectrometer (SP-AMS), Atmospheric Chemistry and Physics, 15, 1823-1841, 10.5194/acp-15-1823-2015, 2015.

Lee, A. K. Y., Willis, M. D., Healy, R. M., Wang, J. M., Jeong, C. H., Wenger, J. C., Evans, G. J., and Abbatt, J. P. D.: Single-particle characterization of biomass burning organic aerosol (BBOA): evidence for non-uniform mixing of high molecular weight organics and potassium, Atmospheric Chemistry and Physics, 16, 5561-5572, 10.5194/acp-16-5561-2016, 2016.

Lenschow, D. H., Krummel, P. B., and Siems, S. T.: Measuring entrainment, divergence, and vorticity on the mesoscale from aircraft, Journal of Atmospheric and Oceanic Technology, 16, 1384-1400, 10.1175/1520-0426(1999)016<1384:medavo>2.0.co;2, 1999.

Lilly, D. K.: MODELS OF CLOUD-TOPPED MIXED LAYERS UNDER A STRONG INVERSION, Quarterly Journal of the Royal Meteorological Society, 94, 292-&, 10.1002/qj.49709440106, 1968.

Liu, J., Russell, L. M., Lee, A. K. Y., McKinney, K. A., Surratt, J. D., and Ziemann, P. J.: Observational Evidence for Pollution-influenced Selective Uptake Contributing to Biogenic Secondary Organic Aerosols in the Southeastern US, 10.1002/2017gl074665, 2017.

Liu, S., Russell, L. M., Sueper, D. T., and Onasch, T. B.: Organic particle types by single-particle measurements using a time-of-flight aerosol mass spectrometer coupled with a light scattering module, Atmospheric Measurement Techniques, 6, 187-197, 10.5194/amt-6-187-2013, 2013.

Maria, S. F., Russell, L. M., Turpin, B. J., and Porcja, R. J.: FTIR measurements of functional groups and organic mass in aerosol samples over the Caribbean, Atmospheric Environment, 36, 5185-5196, 10.1016/s1352-2310(02)00654-4, 2002.

Massling, A., Wiedensohler, A., Busch, B., Neususs, C., Quinn, P., Bates, T., and Covert, D.: Hygroscopic properties of different aerosol types over the Atlantic and Indian Oceans, Atmospheric Chemistry and Physics, 3, 1377-1397, 10.5194/acp-3-1377-2003, 2003.

Merikanto, J., Spracklen, D. V., Mann, G. W., Pickering, S. J., and Carslaw, K. S.: Impact of nucleation on global CCN, Atmospheric Chemistry and Physics, 9, 8601-8616, 10.5194/acp-9-8601-2009, 2009.

Middlebrook, A. M., Murphy, D. M., and Thomson, D. S.: Observations of organic material in individual marine particles at Cape Grim during the First Aerosol Characterization Experiment (ACE 1), Journal of Geophysical Research-Atmospheres, 103, 16475-16483, 10.1029/97jd03719, 1998.

Mochida, M., Nishita-Hara, C., Furutani, H., Miyazaki, Y., Jung, J., Kawamura, K., and Uematsu, M.: Hygroscopicity and cloud condensation nucleus activity of marine aerosol particles over the western North Pacific, Journal of Geophysical Research-Atmospheres, 116, 10.1029/2010jd014759, 2011.

Modini, R. L., Frossard, A. A., Ahlm, L., Russell, L. M., Corrigan, C. E., Roberts, G. C., Hawkins, L. N., Schroder, J. C., Bertram, A. K., Zhao, R., Lee, A. K. Y., Abbatt, J. P. D., Lin, J., Nenes, A., Wang, Z., Wonaschuetz, A., Sorooshian, A., Noone, K. J., Jonsson, H., Seinfeld, J. H., Toom-Sauntry, D., Macdonald, A. M., and Leaitch, W. R.: Primary marine aerosol-cloud interactions off the coast of California, Journal of Geophysical Research-Atmospheres, 120, 4282-4303, 10.1002/2014jd022963, 2015.

Muller, M., Mikoviny, T., Feil, S., Haidacher, S., Hanel, G., Hartungen, E., Jordan, A., Mark, L., Mutschlechner, P., Schottkowsky, R., Sulzer, P., Crawford, J. H., and Wisthaler, A.: A compact PTR-ToF-MS instrument for airborne measurements of volatile organic compounds at high spatiotemporal resolution, Atmospheric Measurement Techniques, 7, 3763-3772, 10.5194/amt-7-3763-2014, 2014.

Murphy, D. M., Anderson, J. R., Quinn, P. K., McInnes, L. M., Brechtel, F. J., Kreidenweis, S. M., Middlebrook, A. M., Posfai, M., Thomson, D. S., and Buseck, P. R.: Influence of sea-salt on aerosol radiative properties in the Southern Ocean marine boundary layer, Nature, 392, 62-65, 10.1038/32138, 1998a.

Murphy, D. M., Thomson, D. S., Middlebrook, A. M., and Schein, M. E.: In situ single-particle characterization at Cape Grim, Journal of Geophysical Research-Atmospheres, 103, 16485-16491, 10.1029/97jd03281, 1998b.

Myers, T. A., and Norris, J. R.: Observational Evidence That Enhanced Subsidence Reduces Subtropical Marine Boundary Layer Cloudiness, Journal of Climate, 26, 7507-7524, 10.1175/jcli-d-12-00736.1, 2013.

Odowd, C. D., and Smith, M. H.: PHYSICOCHEMICAL PROPERTIES OF AEROSOLS OVER THE NORTHEAST ATLANTIC - EVIDENCE FOR WIND-SPEED-RELATED SUBMICRON SEA-SALT AEROSOL PRODUCTION, Journal of Geophysical Research-Atmospheres, 98, 1137-1149, 10.1029/92jd02302, 1993.

Odowd, C. D., Smith, M. H., Consterdine, I. E., and Lowe, J. A.: Marine aerosol, sea-salt, and the marine sulphur cycle: A short review, Atmospheric Environment, 31, 73-80, 1997.

Ouwersloot, H. G., and de Arellano, J. V. G.: Analytical Solution for the Convectively-Mixed Atmospheric Boundary Layer, Boundary-Layer Meteorology, 148, 557-583, 10.1007/s10546-013-9816-z, 2013.

Ovadnevaite, J., Ceburnis, D., Leinert, S., Dall'Osto, M., Canagaratna, M., O'Doherty, S., Berresheim, H., and O'Dowd, C.: Submicron NE Atlantic marine aerosol chemical composition and abundance: Seasonal trends and air mass categorization, Journal of Geophysical Research-Atmospheres, 119, 11850-11863, 10.1002/2013jd021330, 2014.

Pandis, S. N., Russell, L. M., and Seinfeld, J. H.: THE RELATIONSHIP BETWEEN DMS FLUX AND CCN CONCENTRATION IN REMOTE MARINE REGIONS, Journal of Geophysical Research-Atmospheres, 99, 16945-16957, 10.1029/94jd01119, 1994.

Perry, K. D., and Hobbs, P. V.: FURTHER EVIDENCE FOR PARTICLE NUCLEATION IN CLEAR-AIR ADJACENT TO MARINE CUMULUS CLOUDS, Journal of Geophysical Research-Atmospheres, 99, 22803-22818, 10.1029/94jd01926, 1994.

Petters, M. D., and Kreidenweis, S. M.: A single parameter representation of hygroscopic growth and cloud condensation nucleus activity, Atmospheric Chemistry and Physics, 7, 1961-1971, 10.5194/acp-7-1961-2007, 2007.

Petters, M. D., Kreidenweis, S. M., and Ziemann, P. J.: Prediction of cloud condensation nuclei activity for organic compounds using functional group contribution methods, Geoscientific Model Development, 9, 111-124, 10.5194/gmd-9-111-2016, 2016.

Pierce, J. R., and Adams, P. J.: Global evaluation of CCN formation by direct emission of sea salt and growth of ultrafine sea salt, Journal of Geophysical Research-Atmospheres, 111, 10.1029/2005jd006186, 2006.

Pirjola, L., O'Dowd, C. D., Brooks, I. M., and Kulmala, M.: Can new particle formation occur in the clean marine boundary layer?, Journal of Geophysical Research-Atmospheres, 105, 26531-26546, 10.1029/2000jd900310, 2000.

Price, D. J., Chen, C. L., Russell, L. M., Lamjiri, M. A., Betha, R., Sanchez, K., Liu, J., Lee, A. K. Y., and Cocker, D. R.: More unsaturated, cooking-type hydrocarbon-like organic aerosol particle emissions from renewable diesel compared to ultra low sulfur diesel in at-sea operations of a research vessel, Aerosol Science and Technology, 51, 135-146, 10.1080/02786826.2016.1238033, 2017.

Quinn, P. K., Covert, D. S., Bates, T. S., Kapustin, V. N., Ramseybell, D. C., and McInnes, L. M.: DIMETHYLSULFIDE CLOUD CONDENSATION NUCLEI CLIMATE SYSTEM - RELEVANT SIZE-RESOLVED MEASUREMENTS OF THE CHEMICAL AND PHYSICAL-PROPERTIES OF ATMOSPHERIC AEROSOL-PARTICLES, Journal of Geophysical Research-Atmospheres, 98, 10411-10427, 10.1029/93jd00467, 1993.

Quinn, P. K., Coffman, D. J., Kapustin, V. N., Bates, T. S., and Covert, D. S.: Aerosol optical properties in the marine boundary layer during the First Aerosol Characterization Experiment (ACE 1) and the underlying chemical and physical aerosol properties, Journal of Geophysical Research-Atmospheres, 103, 16547-16563, 10.1029/97jd02345, 1998.

Quinn, P. K., Bates, T. S., Miller, T. L., Coffman, D. J., Johnson, J. E., Harris, J. M., Ogren, J. A., Forbes, G., Anderson, T. L., Covert, D. S., and Rood, M. J.: Surface submicron aerosol chemical composition: What fraction is not sulfate?, Journal of Geophysical Research-Atmospheres, 105, 6785-6805, 10.1029/1999jd901034, 2000.

Quinn, P. K., Coffman, D. J., Bates, T. S., Welton, E. J., Covert, D. S., Miller, T. L., Johnson, J. E., Maria, S., Russell, L., Arimoto, R., Carrico, C. M., Rood, M. J., and Anderson, J.: Aerosol optical properties measured on board the Ronald H. Brown during ACE-Asia as a function of aerosol chemical composition and source region, Journal of Geophysical Research-Atmospheres, 109, 10.1029/2003jd004010, 2004.

Quinn, P. K., and Bates, T. S.: Regional aerosol properties: Comparisons of boundary layer measurements from ACE 1, ACE 2, aerosols99, INDOEX, ACE asia, TARFOX, and NEAQS, Journal of Geophysical Research-Atmospheres, 110, 10.1029/2004jd004755, 2005.

Quinn, P. K., Bates, T. S., Coffman, D. J., and Covert, D. S.: Influence of particle size and chemistry on the cloud nucleating properties of aerosols, Atmospheric Chemistry and Physics, 8, 1029-1042, 10.5194/acp-8-1029-2008, 2008.

Quinn, P. K., and Bates, T. S.: The case against climate regulation via oceanic phytoplankton sulphur emissions, Nature, 480, 51-56, 10.1038/nature10580, 2011.

Quinn, P. K., Bates, T. S., Schulz, K. S., Coffman, D. J., Frossard, A. A., Russell, L. M., Keene, W. C., and Kieber, D. J.: Contribution of sea surface carbon pool to organic matter enrichment in sea spray aerosol, Nature Geoscience, 7, 228-232, 10.1038/ngeo2092, 2014.

Quinn, P. K., Collins, D. B., Grassian, V. H., Prather, K. A., and Bates, T. S.: Chemistry and Related Properties of Freshly Emitted Sea Spray Aerosol, Chemical Reviews, 115, 4383-4399, 10.1021/cr5007139, 2015.

Quinn, P. K., Coffman, D. J., Johnson, J. E., Upchurch, L. M., and Bates, T. S.: Small fraction of marine cloud condensation nuclei made up of sea spray aerosol, Nature Geoscience, 10.1038/ngeo3003, 2017.

Raes, F.: ENTRAINMENT OF FREE TROPOSPHERIC AEROSOLS AS A REGULATING MECHANISM FOR CLOUD CONDENSATION NUCLEI IN THE REMOTE MARINE BOUNDARY-LAYER, Journal of Geophysical Research-Atmospheres, 100, 2893-2903, 10.1029/94jd02832, 1995.

Raes, F., VanDingenen, R., Cuevas, E., VanVelthoven, P. F. J., and Prospero, J. M.: Observations of aerosols in the free troposphere and marine boundary layer of the subtropical Northeast Atlantic: Discussion of processes determining their size distribution, Journal of Geophysical Research-Atmospheres, 102, 21315-21328, 10.1029/97jd01122, 1997.

Reus, M., Strom, J., Curtius, J., Pirjola, L., Vignati, E., Arnold, F., Hansson, H. C., Kulmala, M., Lelieveld, J., and Raes, F.: Aerosol production and growth in the upper free troposphere, Journal of Geophysical Research-Atmospheres, 105, 24751-24762, 10.1029/2000jd900382, 2000.

Rinaldi, M., Decesari, S., Finessi, E., Giulianelli, L., Carbone, C., Fuzzi, S., O'Dowd, C. D., Ceburnis, D., and Facchini, M. C.: Primary and Secondary Organic Marine Aerosol and Oceanic Biological Activity: Recent Results and New Perspectives for Future Studies, Advances in Meteorology, 10.1155/2010/310682, 2010.

Russell, L. M., Pandis, S. N., and Seinfeld, J. H.: AEROSOL PRODUCTION AND GROWTH IN THE MARINE BOUNDARY-LAYER, Journal of Geophysical Research-Atmospheres, 99, 20989-21003, 10.1029/94jd01932, 1994.

Russell, L. M., Lenschow, D. H., Laursen, K. K., Krummel, P. B., Siems, S. T., Bandy, A. R., Thornton, D. C., and Bates, T. S.: Bidirectional mixing in an ACE 1 marine boundary layer overlain by a second turbulent layer, Journal of Geophysical Research-Atmospheres, 103, 16411-16432, 10.1029/97jd03437, 1998.

Russell, L. M., Mensah, A. A., Fischer, E. V., Sive, B. C., Varner, R. K., Keene, W. C., Stutz, J., and Pszenny, A. A. P.: Nanoparticle growth following photochemical alpha- and beta-pinene oxidation at Appledore Island during International Consortium for Research on Transport and Transformation/Chemistry of Halogens at the Isles of Shoals 2004, Journal of Geophysical Research-Atmospheres, 112, 10.1029/2006jd007736, 2007.

Russell, L. M., Takahama, S., Liu, S., Hawkins, L. N., Covert, D. S., Quinn, P. K., and Bates, T. S.: Oxygenated fraction and mass of organic aerosol from direct emission and atmospheric processing measured on the R/V Ronald Brown during TEXAQS/GoMACCS 2006, Journal of Geophysical Research-Atmospheres, 114, 10.1029/2008jd011275, 2009.

Russell, L. M., Hawkins, L. N., Frossard, A. A., Quinn, P. K., and Bates, T. S.: Carbohydrate-like composition of submicron atmospheric particles and their production from ocean bubble bursting, Proceedings of the National Academy of Sciences of the United States of America, 107, 6652-6657, 10.1073/pnas.0908905107, 2010.

Sanchez, K. J., Russell, L. M., Modini, R. L., Frossard, A. A., Ahlm, L., Corrigan, C. E., Roberts, G. C., Hawkins, L. N., Schroder, J. C., Bertram, A. K., Zhao, R., Lee, A. K. Y., Lin, J. J., Nenes, A., Wang, Z., Wonaschutz, A., Sorooshian, A., Noone, K. J., Jonsson, H., Toom, D., Macdonald, A. M., Leaitch, W. R., and Seinfeld, J. H.: Meteorological and aerosol effects on marine cloud microphysical properties, Journal of Geophysical Research-Atmospheres, 121, 4142-4161, 10.1002/2015jd024595, 2016.

Schill, S. R., Collins, D. B., Lee, C., Morris, H. S., Novak, G. A., Prather, K. A., Quinn, P. K., Sultana, C. M., Tivanski, A. V., Zimmermann, K., Cappa, C. D., and Bertram, T. H.: The Impact of Aerosol Particle Mixing State on the Hygroscopicity of Sea Spray Aerosol, Acs Central Science, 1, 132-141, 10.1021/acscentsci.5b00174, 2015.

Schmale, J., Schneider, J., Nemitz, E., Tang, Y. S., Dragosits, U., Blackall, T. D., Trathan, P. N., Phillips, G. J., Sutton, M., and Braban, C. F.: Sub-Antarctic marine aerosol: dominant contributions from biogenic sources, Atmospheric Chemistry and Physics, 13, 8669-8694, 10.5194/acp-13-8669-2013, 2013.

Shank, L. M., Howell, S., Clarke, A. D., Freitag, S., Brekhovskikh, V., Kapustin, V., McNaughton, C., Campos, T., and Wood, R.: Organic matter and non-refractory aerosol over the remote Southeast Pacific: oceanic and combustion sources, Atmospheric Chemistry and Physics, 12, 557-576, 10.5194/acp-12-557-2012, 2012.

Shaw, G. E.: BIO-CONTROLLED THERMOSTASIS INVOLVING THE SULFUR CYCLE, Climatic Change, 5, 297-303, 10.1007/bf02423524, 1983.

Sievering, H., Boatman, J., Gorman, E., Kim, Y., Anderson, L., Ennis, G., Luria, M., and Pandis, S.: REMOVAL OF SULFUR FROM THE MARINE BOUNDARY-LAYER BY OZONE OXIDATION IN SEA-SALT AEROSOLS, Nature, 360, 571-573, 10.1038/360571a0, 1992.

Sievering, H., Lerner, B., Slavich, J., Anderson, J., Posfai, M., and Cainey, J.: O-3 oxidation of SO2 in sea-salt aerosol water: Size distribution of non-sea-salt sulfate during the First Aerosol Characterization Experiment (ACE 1), Journal of Geophysical Research-Atmospheres, 104, 21707-21717, 10.1029/1998jd100086, 1999.

Simpson, I. J., Colman, J. J., Swanson, A. L., Bandy, A. R., Thornton, D. C., Blake, D. R., and Rowland, F. S.: Aircraft measurements of dimethyl sulfide (DMS) using a whole air sampling technique, Journal of Atmospheric Chemistry, 39, 191-213, 10.1023/a:1010608529779, 2001.

Sorbjan, Z.: Effects caused by varying the strength of the capping inversion based on a large eddy simulation model of the shear-free convective boundary layer, Journal of the Atmospheric Sciences, 53, 2015-2024, 10.1175/1520-0469(1996)053<2015:ecbvts>2.0.co;2, 1996.

Stevens, B.: Entrainment in stratocumulus-topped mixed layers, Quarterly Journal of the Royal Meteorological Society, 128, 2663-2690, 10.1256/qj.01.202, 2002.

Stevens, B., and Seifert, A.: Understanding macrophysical outcomes of microphysical choices in simulations of shallow cumulus convection, Journal of the Meteorological Society of Japan, 86A, 143-162, 10.2151/jmsj.86a.143, 2008.

Stevens, B., and Feingold, G.: Untangling aerosol effects on clouds and precipitation in a buffered system, Nature, 461, 607-613, 10.1038/nature08281, 2009.

Takahama, S., Johnson, A., and Russell, L. M.: Quantification of Carboxylic and Carbonyl Functional Groups in Organic Aerosol Infrared Absorbance Spectra, Aerosol Science and Technology, 47, 310-325, 10.1080/02786826.2012.752065, 2013.

Thornton, D. C., Bandy, A. R., Blomquist, B. W., Bradshaw, J. D., and Blake, D. R.: Vertical transport of sulfur dioxide and dimethyl sulfide in deep convection and its role in new particle formation, Journal of Geophysical Research-Atmospheres, 102, 28501-28509, 10.1029/97jd01647, 1997.

Ulbrich, I. M., Canagaratna, M. R., Zhang, Q., Worsnop, D. R., and Jimenez, J. L.: Interpretation of organic components from Positive Matrix Factorization of aerosol

mass spectrometric data, Atmospheric Chemistry and Physics, 9, 2891-2918, 10.5194/acp-9-2891-2009, 2009.

Warneck, P.: Chemistry of the natural atmosphere: International geophysical series, Academic Press, San Diego, 1988.

Warren, D. R., and Seinfeld, J. H.: PREDICTION OF AEROSOL CONCENTRATIONS RESULTING FROM A BURST OF NUCLEATION, Journal of Colloid and Interface Science, 105, 136-142, 10.1016/0021-9797(85)90356-x, 1985.

Whittlestone, S., and Zahorowski, W.: Baseline radon detectors for shipboard use: Development and deployment in the First Aerosol Characterization Experiment (ACE 1), Journal of Geophysical Research-Atmospheres, 103, 16743-16751, 10.1029/98jd00687, 1998.

Williams, J., de Reus, M., Krejci, R., Fischer, H., and Strom, J.: Application of the variability-size relationship to atmospheric aerosol studies: estimating aerosol lifetimes and ages, Atmospheric Chemistry and Physics, 2, 133-145, 2002.

Winklmeyer, W., Reischl, G. P., Lindner, A. O., and Berner, A.: New electromobility spectrometer for the measurement of aerosol size distributions in the size range 1 to 1000 nm, J. Aerosol. Sci., 22, 289 - 296, 1991.

Wood, R., Mechoso, C. R., Bretherton, C. S., Weller, R. A., Huebert, B., Straneo, F., Albrecht, B. A., Coe, H., Allen, G., Vaughan, G., Daum, P., Fairall, C., Chand, D., Klenner, L. G., Garreaud, R., Grados, C., Covert, D. S., Bates, T. S., Krejci, R., Russell, L. M., de Szoeke, S., Brewer, A., Yuter, S. E., Springston, S. R., Chaigneau, A., Toniazzo, T., Minnis, P., Palikonda, R., Abel, S. J., Brown, W. O. J., Williams, S., Fochesatto, J., Brioude, J., and Bower, K. N.: The VAMOS Ocean-Cloud-Atmosphere-Land Study Regional Experiment (VOCALS-REx): goals, platforms, and field operations, Atmospheric Chemistry and Physics, 11, 627-654, 10.5194/acp-11-627-2011, 2011.

Wood, R., Wyant, M., Bretherton, C. S., Remillard, J., Kollias, P., Fletcher, J., Stemmler, J., de Szoeke, S., Yuter, S., Miller, M., Mechem, D., Tselioudis, G., Chiu, J. C., Mann, J. A. L., O'Connor, E. J., Hogan, R. J., Dong, X. Q., Ghate, V., Jefferson, A., Min, Q. L., Minnis, P., Palikonda, R., Albrecht, B., Luke, E., Hannay, C., and Lin, Y. L.: CLOUDS, AEROSOLS, AND PRECIPITATION IN THE MARINE BOUNDARY LAYER An ARM Mobile Facility Deployment, Bulletin of the American Meteorological Society, 96, 419-439, 10.1175/bams-d-13-00180.1, 2015.

Woodhouse, M. T., Carslaw, K. S., Mann, G. W., Vallina, S. M., Vogt, M., Halloran, P. R., and Boucher, O.: Low sensitivity of cloud condensation nuclei to changes in the sea-air flux of dimethyl-sulphide, Atmospheric Chemistry and Physics, 10, 7545-7559, 10.5194/acp-10-7545-2010, 2010.

Yoon, Y. J., and Brimblecombe, P.: Modelling the contribution of sea salt and dimethyl sulfide derived aerosol to marine CCN, Atmospheric Chemistry and Physics, 2, 17-30, 2002.

Yu, F., and Luo, G.: Simulation of particle size distribution with a global aerosol model: contribution of nucleation to aerosol and CCN number concentrations, Atmospheric Chemistry and Physics, 9, 7691-7710, 2009.

Yue, G. K., and Deepak, A.: TEMPERATURE-DEPENDENCE OF THE FORMATION OF SULFATE AEROSOLS IN THE STRATOSPHERE, Journal of Geophysical Research-Oceans, 87, 3128-3134, 10.1029/JC087iC04p03128, 1982.

Zhang, Q., Alfarra, M. R., Worsnop, D. R., Allan, J. D., Coe, H., Canagaratna, M. R., and Jimenez, J. L.: Deconvolution and quantification of hydrocarbon-like and oxygenated organic aerosols based on aerosol mass spectrometry, Environmental Science & Technology, 39, 4938-4952, 10.1021/es048568l, 2005.

Zhang, Q., Jimenez, J. L., Canagaratna, M. R., Ulbrich, I. M., Ng, N. L., Worsnop, D. R., and Sun, Y. L.: Understanding atmospheric organic aerosols via factor analysis of aerosol mass spectrometry: a review, Analytical and Bioanalytical Chemistry, 401, 3045-3067, 10.1007/s00216-011-5355-y, 2011.

Zhang, X. L., Massoli, P., Quinn, P. K., Bates, T. S., and Cappa, C. D.: Hygroscopic growth of submicron and supermicron aerosols in the marine boundary layer, Journal of Geophysical Research-Atmospheres, 119, 10.1002/2013jd021213, 2014.

Conclusions

Observations from several field studies are compared to simulations to quantify the relative importance of aerosol particle sources and physical processes that influence cloud condensation nuclei (CCN) concentration and cloud radiative forcing. The first chapter focuses on the effects of polluted air on marine clouds and a method for accurately simulating the cloud droplet distribution [*Sanchez et al.,* 2016]. The second chapter quantifies errors in cloud radiative forcing due to decoupling in the boundary layer and cloud top entrainment [*Sanchez et al.,* 2017]. The third chapter identifies seasonal differences in biologically derived CCN concentrations [*Sanchez et al.,* Submitted]. The objective of each of these studies is identifying aerosol processes that affect marine cloud optical properties. The motivation for these studies is that the ability to simulate marine clouds accurately is vital to predicting future changes in the Earth's net radiative forcing and consequently its changes in temperature and precipitation.

The first chapter used measurements collected in the marine boundary layer off the coast of California as part of the Eastern Pacific Emitted Aerosol Cloud Experiment (EPEACE) and on Mt. Soledad in San Diego in the Stratocumulus Observations of Los-Angeles Emission Derived Aerosol-Droplets (SOLEDAD) campaigns. These studies were designed to identify the influence of continental and polluted air on marine clouds and identify differences between cloud simulations and observations. Simulated cloud

droplet spectral widths from an aerosol cloud parcel model (ACPM), were narrow relative to observed droplet distributions of marine boundary layer clouds in the Eastern Pacific. The discrepancy affected the calculated albedo of the cloud. A weighted ensemble of simulations based on the observed updraft velocity distribution and cloud base height distribution broaden the droplet spectral widths to within 9% of the observed value with the exception of the generated smoke plume case. The increase in the cloud droplet spectral width, from using a distribution of updraft velocities and cloud base heights, resulted in an increase in the cloud reflectivity of ~0.01 to 0.03 when the cloud droplet number concentration (CDNC) is equivalent to the observed value. The sensitivity of organic hygroscopicity on CDNC was low for clean marine aerosol because the organic components are internally mixed with hygroscopic salts. The smoke generated plume particles were approximately 100% organic mass, and were the most sensitive to the organic hygroscopicity. Changing the organic hygroscopicity of the smoke generated plume from 0.01 to 0.2 increased the CDNC by a factor of 6 and lead to an increase in the cloud reflectivity from 0.09 to 0.16. The same change in the cargo ship plume's organic hygroscopicity resulted in a relatively small increase in cloud reflectivity from 0.26 to 0.28, which was calculated using the ACPM. The remaining cases result in an increase in cloud reflectivity of less than 0.01 because they had a significantly smaller organic mass fraction [*Sanchez et al.*, 2016].

In the second chapter measurements from the Biogenic versus Anthropogenic emissions on Clouds and Climate: towards a Holistic UnderStanding (BACCHUS) campaign were used with the objective of comparing observed cloud optical properties

with simulations in a bottom-up and top-down aerosol-cloud-satellite closure study to identify physical processes that prevented agreement between the observations and the model, or so-called "closure". For cases when the boundary layer was well-mixed and not influenced by entrainment, the difference between adiabatic simulated and observed shortwave radiative forcing (δRF), was less than 20 W m^{-2}. Observations form one case showed that the boundary layer is decoupled and not well-mixed. The δRF for this case is 74 W m^{-2} because the simulation was initialized with particle distributions measured at the surface, which are not representative of the particles in the decoupled layer. Decreasing the simulated particle concentration by 50% (as per observed aerosol gradients in the decoupled layer), decreased the δRF from 74 W m^{-2} to 56 W m^{-2}. Another case that had a well-mixed boundary layer and was influenced by cloud-top entrainment had a δRF of 48 W m^{-2}. The cloud top entrainment was identified by the sub-adiabatic lapse rate and total water content in the cloud. A method was used to account for cloud-top inhomogeneous entrainment using the measured adiabatic lapse rate and the δRF was reduced from 48 W m^{-2} to 20 W m^{-2}. Finally, a case with both a decoupled boundary layer and cloud-top entrainment had a δRF of 88 W m^{-2}. Applying the measured lapse rate method to account for cloud-top inhomogeneous entrainment reduced the δRF from 88 W m^{-2} to 33 W m^{-2} with the remaining bias resulting from the impact of the decoupled layer.

Entrainment from the free troposphere also contributes to the marine boundary layer CCN budget by enhancing particle concentrations. In the third chapter, measurements collected during the second Western Atlantic Climate Study (WACS2)

and the first and second North Atlantic Aerosol and Marine Ecosystems Study (NAAMES1 and NAAMES2) were used to identify marine biological contributions to marine aerosol particle concentrations from measurements collected in the North Atlantic at times corresponding to maxima and minima in phytoplankton production (late spring and late fall, respectively). Six particle types were identified from clustered single particle mass spectra, two of which were associated with marine sources. Of the two marine particle types, one was found to be entrained from the free troposphere. The two marine particle types, referred to as Added Sulfate and New Sulfate particles, correlated weakly to moderately to dimethyl-sulfide (DMS) concentrations. The New Sulfate particle type contains an average sulfate mass fraction of 60% and is associated with new particles formed in the free troposphere and entrained into the boundary layer. This process first requires DMS to be entrained from the marine boundary layer into the free troposphere. The New Sulfate particle type only weakly correlated with atmospheric DMS likely because the concentrations are also influenced by entrainment rate and requires substantial growth for single particle analysis. The New Sulfate particle fraction has a strong negative correlation with the inversion strength, which is used here as a proxy for the entrainment rate and is determined from the convective inhibition (CIN). The Added Sulfate particle type is associated with the condensation of DMS oxidation products onto existing particles and contains an average sulfate mass fraction of 40%. The Added Sulfate particle type correlates moderately to atmospheric DMS in the late spring. The Added Sulfate particle type also had a weak negative correlation with CIN in the late fall, but no correlation in late spring, suggesting this

type is not exclusively from entrainment from the free troposphere. The remaining particle types positively correlated to the inversion strength indicating they have boundary layer sources. The Added Sulfate and New Sulfate particle types accounted for 3 ±3% and 22 ±13% of CCN (at 0.1% supersaturation), respectively, in the late fall and 32 ±16% and 33 ±15% of CCN, respectively, in the late spring. Sea salt particles account for 68 ±43% and 7 ±5% of CCN in the late fall and the late spring respectively. In the absence of DMS contributions to both the New Sulfate and Added Sulfate types, CCN concentrations decrease by 52% in the late spring, but only by 26% in the late fall, reducing clean marine sources of CCN to mostly sea spray. While this result does not rely solely on DMS products nucleating new particles, it provides evidence for the link between greater DMS emissions and greater CCN concentrations proposed by Charlson et al. [1987] and Shaw [1983].

The results presented in this dissertation identify processes and variables that are important for accurately simulate cloud optical properties in the marine boundary layer. Organic hygroscopicity is found to significantly influence optical properties under polluted conditions when the organic volume fraction is high. Under clean marine conditions the cloud droplet spectral width and organic aerosol hygroscopicity affect cloud optical properties with similar magnitudes. In addition, cloud top entrainment and decoupling of the boundary layer can drastically reduce the cloud radiative forcing. The marine particle and CCN concentrations from DMS derived sulfate mass vary seasonally in the North Atlantic. New sulfate particles are shown to have enhanced

concentrations when the boundary layer inversion is weak, indicating new particles are forming in the free troposphere and entrained into the boundary layer.

Future work will expand on the results presented here to explore similar studies in climatically different regions to identify regional differences in aerosol-cloud interactions. Ultimately, such case studies identify the key parameters and frequency of the atmospheric processes to resolve differences between simulations and observations. These findings will be used to improve marine cloud parameterizations in climate models by including accurate marine particle composition, cloud droplet spectral width, cloud top entrainment, decoupling of the marine boundary layer, and entrainment of new free tropospheric particles. These studies strive to quantify the relative importance of aerosol and CCN particle sources, and atmospheric processes that impact cloud radiative forcing to better quantify the role of aerosol-cloud interactions on climate change.

References

Charlson, R. J., Lovelock, J. E., Andreae, M. O., and Warren, S. G.: OCEANIC PHYTOPLANKTON, ATMOSPHERIC SULFUR, CLOUD ALBEDO AND CLIMATE, Nature, 326, 655-661, 10.1038/326655a0, 1987.

Sanchez, K. J., Russell, L. M., Modini, R. L., Frossard, A. A., Ahlm, L., Corrigan, C. E., Roberts, G. C., Hawkins, L. N., Schroder, J. C., Bertram, A. K., Zhao, R., Lee, A. K. Y., Lin, J. J., Nenes, A., Wang, Z., Wonaschutz, A., Sorooshian, A., Noone, K. J., Jonsson, H., Toom, D., Macdonald, A. M., Leaitch, W. R., and Seinfeld, J. H.: Meteorological and aerosol effects on marine cloud microphysical properties, Journal of Geophysical Research-Atmospheres, 121, 4142-4161, 10.1002/2015jd024595, 2016.

Sanchez, K. J., Roberts, G. C., Calmer, R., Nicoll, K., Hashimshoni, E., Rosenfeld, D., Ovadnevaite, J., Preissler, J., Ceburnis, D., O'Dowd, C., and Russell, L. M.: Top-down and bottom-up aerosol-cloud closure: towards understanding sources of uncertainty in deriving cloud shortwave radiative flux, Atmospheric Chemistry and Physics, 17, 9797-9814, 10.5194/acp-17-9797-2017, 2017.

Sanchez, K.J., C. Chen, L.M. Russell, R. Betha, J. Liu, D.J. Price, P. Massoli, L.D. Ziemba, E.C. Crosbie, R.H. Moore, M. Müller, S.A. Schiller, A. Wisthaler, A.K.Y. Lee, P.K. Quinn, T.S. Bates, J. Porter, T.G. Bell, E.S. Saltzman, R.D. Vaillancourt, M.J. Behrenfeld. (in review), Higher Contributions of Marine Sulfate than Sea Spray to Cloud Condensation Nuclei in Late Spring than in Late Autumn.

Shaw, G. E.: BIO-CONTROLLED THERMOSTASIS INVOLVING THE SULFUR CYCLE, Climatic Change, 5, 297-303, 10.1007/bf02423524, 1983.